TIME: A Millimeter-Wavelength Grating Spectrometer Array for [CII] / CO Intensity Mapping

Thesis by
Jonathon Hunacek

In Partial Fulfillment of the Requirements for the
Degree of
Doctor of Philosophy

CALIFORNIA INSTITUTE OF TECHNOLOGY
Pasadena, California

2020
Defended April 21, 2020

Jonathon Hunacek
ORCID: 0000-0001-7066-226X

Acknowledgements

I have been very fortunate in being able to work with the TIME collaboration, all of whom are fantastic and without whom the work in this thesis would not have been possible. This includes Jamie Bock, Matt Bradford, Victoria Butler, Tzu-Ching Chang, Yun-Ting Cheng, Abby Crites, Nick Emerson, Clifford Frez, Ryan Keenan, Chao-Te Li, Paolo Madonia, Dan Marrone, Lorenzo Moncelsi, Guochao (Jason) Sun, Isaac Trumper, Anthony Turner, Tashun Wei, and Mike Zemcov as well as former TIME team members Roger O'Brient and Zak Staniszewski.

I want to especially thank my advisor Jamie Bock for his continued support and guidance, and TIME PI Abby Crites for teaching me so much and for making the lab my favorite place to be.

Collaborators from outside the TIME team are listed in certain section headers where relevant, and I thank them for their time, effort, and wisdom. I also want to thank the BICEP collaboration generally, who have provided a great deal of knowledge and support to TIME.

On a personal note, I want to thank my partner for standing by me and being my rock through difficult times. I could not have done this without you.

Abstract

In this thesis I review the design, fabrication, and initial engineering deployment of the TIME (Tomographic Ionized-carbon Mapping Experiment) instrument. TIME seeks to make a first detection of the clustering amplitude of the power spectrum of redshifted [CII] emission from the Epoch of Reionization ($z = 5 - 9$). [CII], the 157.7 μm fine-structure line of singly ionized carbon, traces star formation on large scales, providing a new method for constraining the contribution of star formation to the Reionization process. [CII] intensity mapping complements traditional galaxy surveys by using spatially-broad beams to integrate signal from the many faint sources thought to be responsible for the bulk of the integrated emission from galaxies. TIME covers the 200-300 GHz atmospheric window, which also enables the study of lower-redshift CO emission ($z = 0.5 - 2$), a tracer of molecular gas in the period following the peak of cosmic star formation. The full TIME instrument consists of 32 single-polarization grating spectrometers with a resolution $R \sim 100$. Each spectrometer consists of an input feedhorn coupled to parallel plate waveguide with a curved diffraction grating, which focuses the diffracted light onto an output arc populated by 60 transition-edge sensor (TES) bolometers at 250 mK. The 1920 total detectors couple to the output of the parallel plate waveguide with a direct-absorbing micro-mesh and are organized into buttable arrays covering 4 spatial by either 12 (HF) or 8 (LF) spectral pixels. A partial TIME instrument was field tested in early 2019 on the ARO APA 12m dish at Kitt Peak. We intend to return to Kitt Peak in late 2020 to begin initial science observations.

Published Content and Contributions

J. Hunacek, J. Bock, C. M. Bradford, V. Butler, T. C. Chang, Y. T. Cheng, A. Cooray, A. Crites, C. Frez, S. Hailey-Dunsheath, B. Hoscheit, D. W. Kim, C. T. Li, D. Marrone, L. Moncelsi, E. Shirokoff, B. Steinbach, G. Sun, I. Trumper, A. Turner, B. Uzgil, A. Weber, and M. Zemcov (2018). "Hafnium Films and Magnetic Shielding for TIME, A mm-Wavelength Spectrometer Array". In: *Journal of Low Temperature Physics*, 193(5-6):893–900. DOI: 10.1007/s10909-018-1906-3.
Figures 3, 4, 5, and 7 from said publication have been reprinted here with permission from the publisher. J.R.H. wrote the manuscript and performed the simulations used to generate the figures in question.

Table of Contents

List of Illustrations

List of Tables

Chapter 1

Motivation

1.1 Probing Cosmology with Line Intensity Mapping

Galaxy surveys have been crucial to the advancement of astrophysics and cosmology [e.g. 3, 33, 38, 77, 96, 99]. As we seek to extend the reach of our understanding of the universe to earlier epochs, we are driven toward observations of ever more faint and distant galaxies. Surveys in this regime are biased toward detecting only the brightest objects, which may not accurately reflect the sources accounting for the bulk of the integrated emission from galaxies. Intensity Mapping (IM) seeks to extract information statistically by mapping the integrated emission from all sources. Because sources need not be resolved individually, the detection thresholds and source confusion limitations present in traditional galaxy surveys are circumvented, enabling the use of instruments with low spatial resolution for rapid mapping of large cosmological volumes. Every astronomical photon detected contributes to the final result, ensuring faint galaxies are represented accurately. Continuum Intensity Mapping produces a two-dimensional fluctuation map of the sky [e.g. 12, 105], as demonstrated in Fig. 1.1; Line Intensity Mapping (LIM) takes this concept a step further by observing a single emission line spectroscopically. The use of a known emission frequency maps the observed spectral range to a range of cosmological redshifts, allowing one to map emission fluctuations in three dimensions over cosmic time. Besides probing for potential redshift evolution in emission parameters, the addition of spectral information allows for improved foreground discrimination and removal. Line intensity mapping is a nascent field, but several recent limits and detections show great promise for the future [e.g. 22, 54, 55, 58, 71, 86].

The luminosity function $\phi(L)$ describes the galaxy count per unit volume per unit luminosity at a given redshift. The characteristics of this function depend on the type of emission being observed, the sampling criteria of the objects, and the epoch under study. A generic luminosity function at luminosity L is often parameterized as a Schechter function, where L^* describes luminosity below

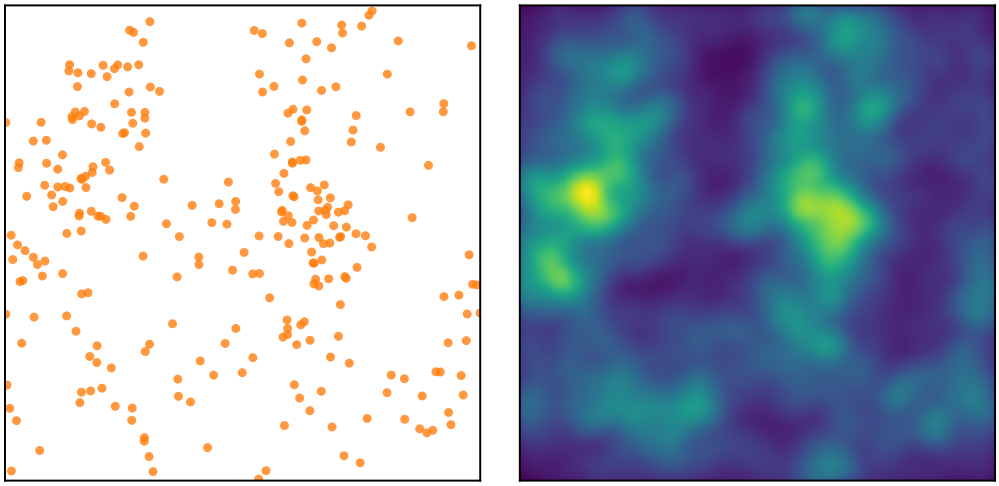

Figure 1.1: A conceptual illustration showing (*left*) a simulated galaxy catalog with some luminosity cutoff and (*right*) a low-resolution intensity field including contributions from faint galaxies as observed by a hypothetical intensity mapping experiment. This point source realization was generated with `powerbox` [73] using a dark matter power spectrum calculated by CAMB [63] assuming the Planck [79] cosmology.

which a power law dominates and α describes the faint-end slope [94, 101]:

$$\phi(L) \equiv \frac{\mathrm{d}n}{\mathrm{d}L} = \frac{\phi^*}{L^*} \left(\frac{L}{L^*}\right)^{\alpha} \mathrm{e}^{-L/L^*} \tag{1.1}$$

The total luminosity density in units of luminosity per volume is the first moment of this function [16].

$$\rho \equiv \int L \frac{\mathrm{d}n}{\mathrm{d}L} \mathrm{d}L \tag{1.2}$$

Here the limits of integration formally extend over all values for luminosity, implying that for large negative value of the faint end slope ($\alpha <= -2$) the integral diverges. In reality, some reasonable limits can be placed on the largest and smallest possible emission sources. However, at high redshifts dominated by fainter galaxies (ex: $\alpha \approx -2$ for UV luminosity at redshift $z \sim 7$ [15]), the assumptions and models used to choose the appropriate limits of integration have a significant impact on the resulting total luminosity density (see Fig. 1.3). Because the faint end is difficult to constrain observationally with a traditional galaxy survey, line intensity mapping is a valuable complement to existing measurements.

For a generic line intensity mapping experiment, the observed quantity is a map of intensity fluctuations ΔI. On very large scales (small values of the spatial frequency k) and at fixed redshift, the emission can be modeled as a tracer of the underlying dark matter overdensity δ_{dm} with some tracer-dependent cosmological mean bias $b \equiv \langle \delta_{tr} \,/\, \delta_{dm} \rangle$ (where $\delta_{tr} = \Delta I / \langle I \rangle$ is the overdensity of the tracer) [42]. In this regime the intensity fluctuations can be written in terms of the cosmological mean line intensity $\langle I \rangle$.

$$\Delta I = \langle I \rangle \, b \, \delta_{dm}(\vec{r}) \tag{1.3}$$

The large-scale clustering term of the power spectrum of the observed intensity fluctuations can therefore be written as follows, where P_{dm} is the full non-linear dark matter power spectrum including intra-halo clustering.

$$P_{clustering}(k) = \langle I \rangle^2 \; b^2 \, P_{dm}(k) \tag{1.4}$$

On small spatial scales (large k) we expect a white shot noise power arising from the fact that sources are discrete. As illustrated in Fig. 1.2, the total power spectrum can taken to be the sum of these two terms.

$$P = P_{clustering} + P_{shot} \tag{1.5}$$

For many LIM experiments (including TIME), a primary goal is to measure the power spectrum of the line intensity fluctuations on large (clustering-dominated) scales, and, through knowledge of the underlying dark matter power spectrum and with models for the tracer bias, to extract the mean line intensity in one or more redshift bins. This mean intensity is proportional to the first moment of the luminosity function [98].

$$\langle I \rangle \propto \int L \, \frac{\mathrm{d}n}{\mathrm{d}L} \, \mathrm{d}L \tag{1.6}$$

The shot noise term provides an additional constraint on the second moment of the luminosity function [60], which is dominated by the bright sources that are probed by traditional galaxy surveys.

$$P_{shot} \propto \int L^2 \, \frac{\mathrm{d}n}{\mathrm{d}L} \, \mathrm{d}L \tag{1.7}$$

Systematic and foreground controls are a top priority for line intensity mapping. In particular, alternate emission lines at different redshifts can be difficult to distinguish from the target line. Cross-correlations between two different emission lines at the same redshift (or between an emission line and a point source catalog) can provide an important measurement of this interloper line contamination [60].

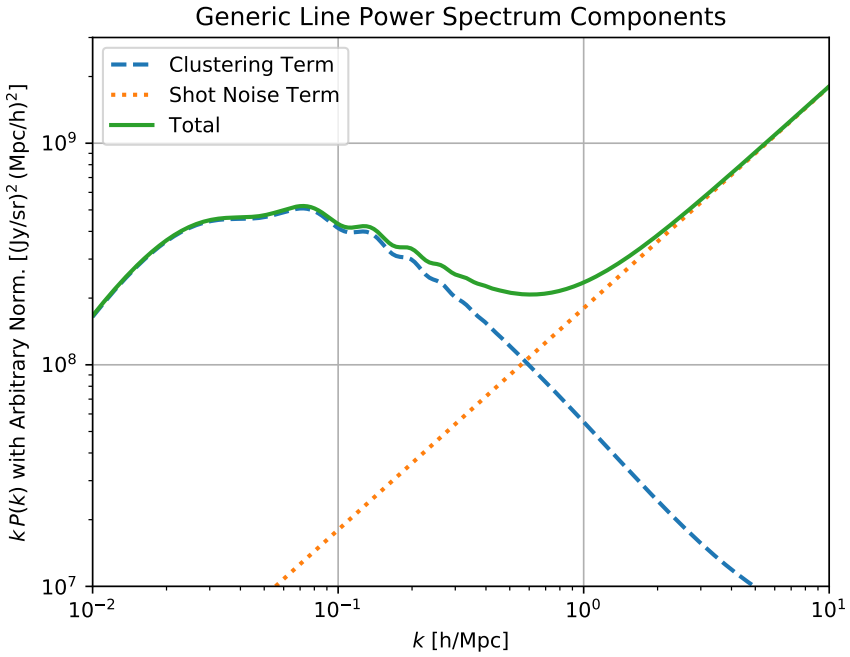

Figure 1.2: The clustering and shot noise terms of a generic emission line power spectrum with representative units but arbitrary relative and overall normalization (to illustrate the concept). The dark matter power spectrum was generated using CAMB [63] and the Planck 2018 cosmology [79]. Note that $k\,P(k)$ is plotted instead of the more common $k^3\,P(k)$ or $P(k)$ to reduce the y-axis scale range.

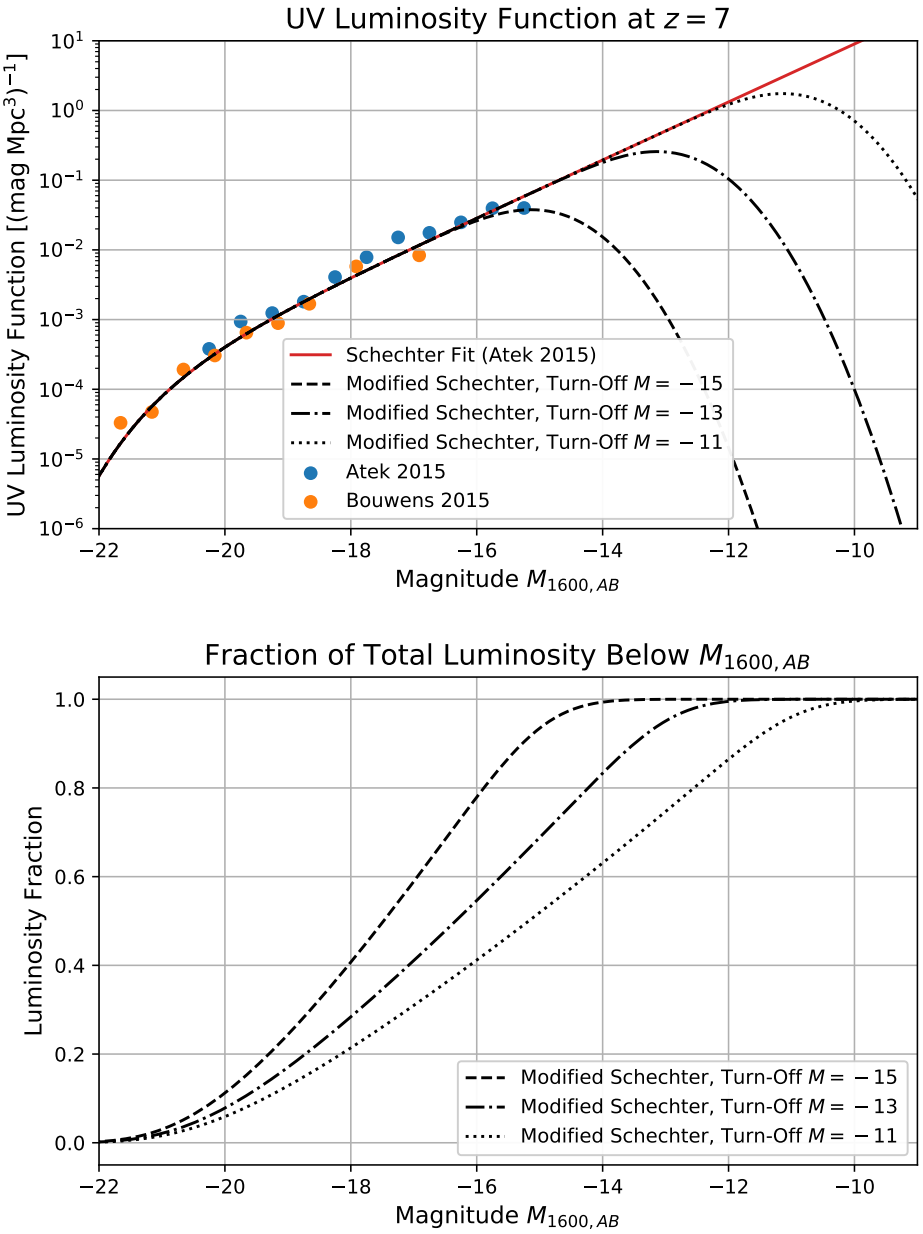

Figure 1.3: *Upper:* The UV luminosity function at redshift $z \sim 7$. Measurements (without error bars) are shown from Hubble deep fields as presented in Bouwens 2015 [15] and from lensed fields as presented in Atek 2015 [8]. A Schechter function fit is shown with the best-fit parameters from Atek 2015 [8], whose total luminosity integral formally diverges ($\alpha < -2$). Computing the total luminosity requires imposing a faint-end cutoff, for which I use the parameterization presented in Yue 2018 [110]. *Lower:* The total luminosity in sources brighter than a selected magnitude threshold for the three modified Schechter functions shown above.

1.2 [CII] in the Epoch of Reionization

Reionization

In the period following the Big Bang and cosmic inflation the universe was hot, dense, opaque plasma. After 370,000 years the universe had expanded and cooled to the point where the plasma could condense into neutral hydrogen. This major phase change in the universe, referred to as Recombination, allowed photons (observed today as the Cosmic Microwave Background) to freely stream through a mostly transparent medium. In the ensuing Dark Ages, overdensities in the matter distribution began to collapse into the first galaxies and the first stars were ignited. Ionizing radiation produced in these galaxies began driving a second major phase change in the history of the universe: Reionization [e.g. 88, 101]. Today the once-neutral hydrogen gas in the intergalactic medium is nearly completely ionized. Questions remain about the timing and duration of this process, and the contributions to the ionizing radiation field from sources other than galactic star formation remain uncertain [e.g. 68, 89, 101].

The process of Reionization depends on the production rate of photons that ionize the intergalactic medium (IGM) per unit volume, $\dot{n}$. When $\dot{n}$ exceeds the rate of recombination (which depends on the temperature and density of the IGM) there is a net ionization of the IGM; the difference between the production and recombination rates integrated over the history of the universe must produce at least one ionizing photon per hydrogen atom to fully reionize the universe. In this context an ionizing photon has $\lambda \leq 91.2\,\mathrm{nm}$, which is in the UV spectrum. Assuming photon production arises only from cosmic star formation, $\dot{n}$ is often interpreted in the literature [88] as the product of three parameters: the mean cosmic star formation rate density (ρ_{sfr}), the number of Lyman continuum photons produced per second per unit SFR (ξ_{ion}), and the mean fraction of photons that escape galaxies into the IGM (f_{esc}).

$$\dot{n} = f_{esc}\ \rho_{sfr}\ \xi_{ion} \tag{1.8}$$

Understanding Reionization can therefore be considered an exercise in constraining these parameters and their evolution in redshift. In addition, one must assess the contribution of sources of high-energy photons besides star formation to the overall ionizing background, including active galactic nuclei [68] and dark matter annihilation [53].

Existing Constraints and Methods

Existing constraints on Reionization come from a variety of observational sources:

The optical depth to Reionization τ is one of six independent variables in the ΛCDM model of cosmology and is constrained by measurements of CMB anisotropies as measured by Planck [79] and WMAP [48]. τ is set by the integrated impact of the free electrons generated by Reionization across cosmic time scattering and dampening CMB anisotropies, and therefore constraints on the timing of Reionization depend on the model assumed for its progression. Current results are compatible with a relatively late and quick Reionization process occurring between redshift $z \sim 10$ and $z \sim 6$ [79]. Separate constraints on the duration of Reionization can be extracted from the kinetic Sunyaev-Zel'dovich effect, where CMB photons scatter off of free electrons and gain energy from their bulk velocity; results from the South Pole Telescope are consistent with a Reionization duration $\Delta z \leq 4.4$ [111].

Because neutral hydrogen absorbs the Lyman series, the presence or absence of signal in an otherwise known reference emission spectrum can constrain the quantity of neutral hydrogen along a line of sight. Quasars have a bright, broad-band emission spectrum that is observable at high redshift; at $z \gtrsim 6$ near-total absorption in the redshifted Lyα line is observed in their spectra [10, 108], indicating the presence of neutral hydrogen at those redshifts. Similarly, the observed fraction of strongly Lyα-emitting galaxies reduces significantly at $z > 6$, which can be interpreted as an increasing opacity to the Lyα line resulting from the presence of neutral hydrogen [34, 44]. Only small neutral fractions are required to fully absorb Lyα emission, so these probes only tell us about the end of Reionization when the neutral hydrogen fraction was approaching zero.

Measurements of the UV luminosity function of high redshift galaxies allow for a direct census of the ionizing radiation field. However, the large distances and faint sources involved constrict galaxy surveys to only the brightest sources over small observing fields. Hubble Space Telescope observations across various deep field programs result in a few hundred galaxies from $z > 7.5$, and find a formally divergent faint end slope $\alpha \approx -2$ at $z \sim 7$ [15]. This leaves significant uncertainty in the integrated UV output of star forming galaxies during the Epoch of Reionization. As an example see Fig. 1.3, which also

includes measurements from gravitationally lensed fields [8]. Depending on the assumptions made for the inevitable turn-over at the faint end [110], galaxies accounting for approximately half of the UV luminosity at $z \sim 7$ remain unconstrained.

An exciting, though challenging, method for placing constraints on Reionization is mapping the fluctuations in the 21 cm emission or absorption from neutral hydrogen at high redshift, directly probing the neutral medium. However, bright astronomical foregrounds dominate the expected signal by several orders of magnitude [58], requiring careful systematic error control. Upper limits on the 21 cm power spectrum during the Epoch of Reionization have been published by PAPER [58]; a successor experiment, HERA, is currently being fielded and predicts significantly improved sensitivity [56, 57].

[CII] Intensity Mapping

TIME (Tomographic Ionized-carbon Mapping Experiment) focuses on a relatively new probe of Reionization: mapping fluctuations in the redshifted 157.7 μm (1.9 THz, 91K) emission line of singly ionized carbon [26, 42, 98]. (I will hereafter refer to singly ionized carbon as CII, and the specific fine structure line ${}^2P_{j=3/2} \rightarrow {}^2P_{j=1/2}$ as [CII].) With an ionization energy of 11.3 eV, CII is produced in radiation fields similar to those required to ionize hydrogen and therefore traces star formation on super-galactic scales [14, 36]. As shown in Fig. 1.4, this relation been found to extend out to the redshifts of interest for the Epoch of Reionization [11, 93]. Scatter in the relationship between [CII] luminosity and star formation rate is mitigated by the fact that we are seeking to measure a mean cosmological star formation rate, not the star formation rate of individual sources. On sub-galactic scales much of the [CII] emission originates from photodissociation regions at the boundaries of neutral molecular gas clouds, where it provides a cooling mechanism for the warm gas [14, 100]. [CII] is generally bright, being responsible for $\sim 0.3\%$ of the total IR luminosity of star-forming galaxies [42, 62, 100]. From $z \sim 5-9$ [CII] emission is redshifted into the 200-300 GHz atmospheric window, enabling ground-based observations that leverage existing CMB detector technologies.

Published models for [CII] emission at high redshift, such as those shown in Fig. 1.5, vary greatly and are poorly constrained by observations. TIME seeks to make a first detection of the clustering-scale ($k \sim 0.1$ h/Mpc) amplitude of

the [CII] power spectrum at high redshift ($z = 5 - 9$), laying the groundwork for future [CII] experiments to place tighter constraints on star formation activity during the Epoch of Reionization. As a basic proof of concept, I adopt as a fiducial model the [CII] power spectrum presented in Serra 2016 [97] and compute the expected errors on the measured power spectrum following the formalism presented in Gong 2012 [42], which includes cosmic variance and instrument noise. For the purposes of this demonstration I assume ideal foreground cleaning such that the measured power spectrum is the model [CII] power spectrum; CO line interlopers are discussed in the following section. I use a TIME-like survey geometry with a $\sim 1^\circ$ degree line scan spanning the 200-300 GHz atmospheric window with 1000 hr on a 12 m telescope and a per-detector NEI of 15 MJy/(sr $\sqrt{\text{Hz}}$). Channels from the high frequency band are coadded to improve sensitivity. As reported in published projections [28, 60] and indicated by Fig. 1.6, TIME expects a detection of clustering power for optimistic [CII] models, and expects to place upper limits sufficient to discriminate against those models in the pessimistic case.

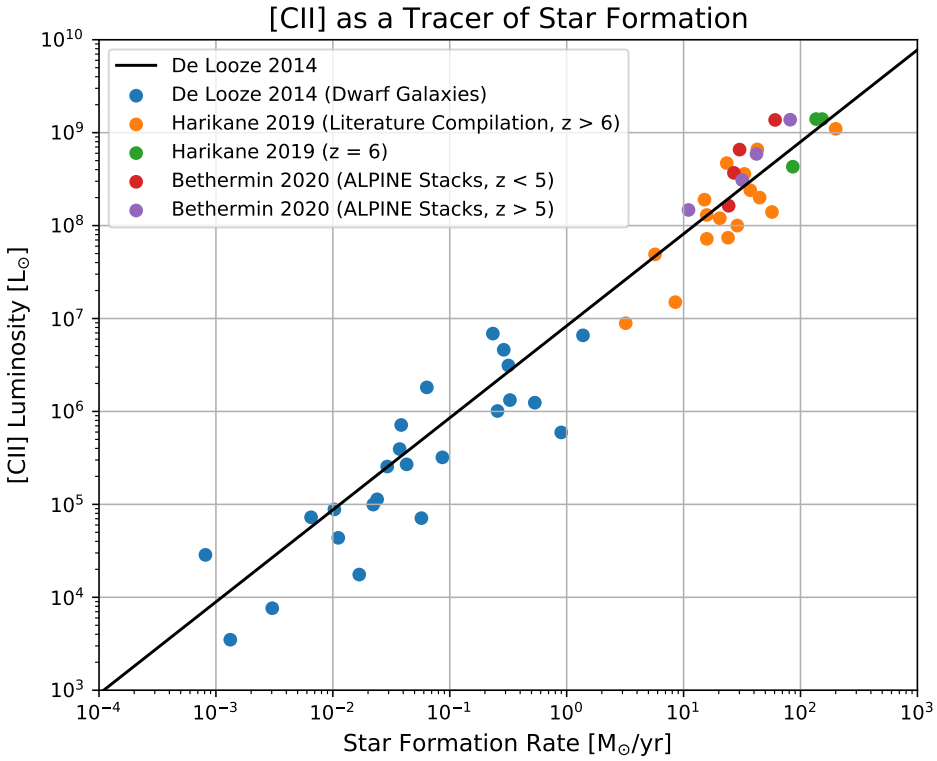

Figure 1.4: Measurements of [CII] luminosity and star formation rate are well correlated at a range of redshifts. The primary relation presented in De Looze 2014 [37] is compared here to low-redshift low-metallicity dwarf galaxies (as presented in the same paper) and to recent high redshift measurements with ALMA [11, 46].

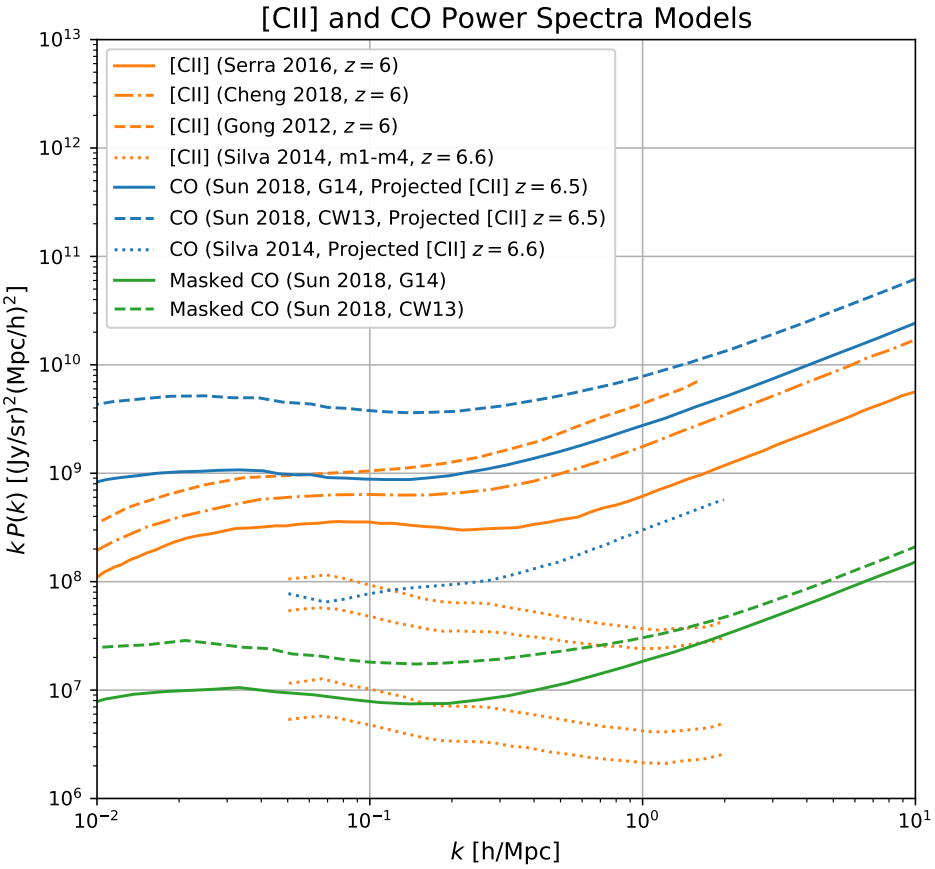

Figure 1.5: Models from the literature [23, 42, 97, 98, 102] for the [CII] and CO power spectrum at redshift $z \sim 6$, adapted from Fig. 6 of Sun et al. 2018 [102]. CO power spectra are projected into the k-space of [CII] at the indicated redshift and include contributions from multiple CO transitions. Masked CO power spectra, as presented by Sun et al. 2018 [102], represent the residual signal remaining after masking $8 - 18\%$ of TIME-like survey voxels using a low redshift galaxy tracer.

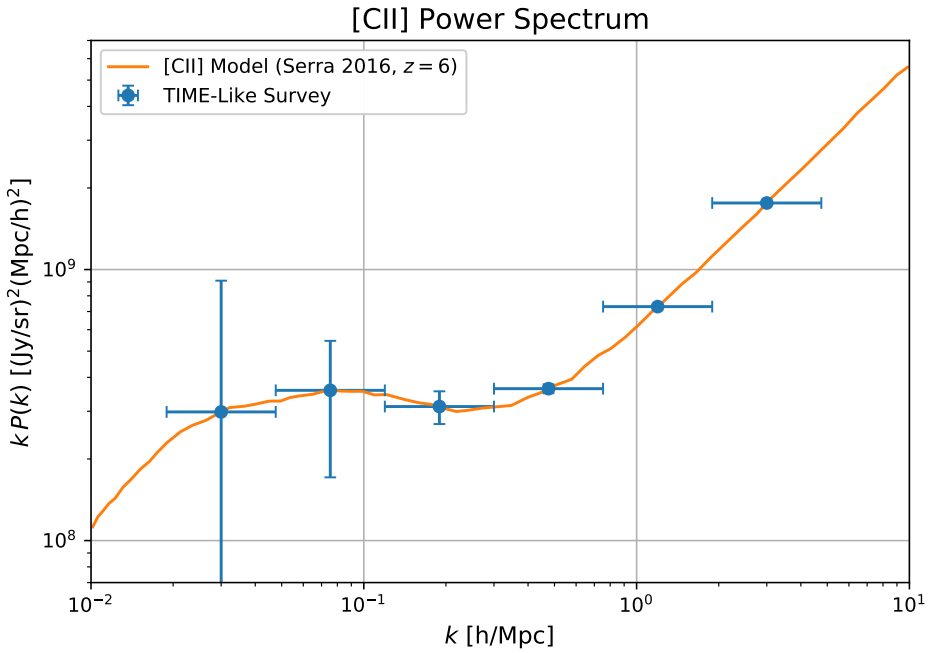

Figure 1.6: Power spectrum error projections following the formalism presented in Gong 2012 [42], including cosmic variance and a per-detector NEI of 15 MJy/(sr $\sqrt{\text{Hz}}$) for the high frequency band of a TIME-like survey. A single model [97] for [CII] is shown as a proof of concept.

1.3 CO During Peak Cosmic Star Formation

The 200-300 GHz atmospheric window observed by TIME also contains redshifted CO rotational ladder emission lines from $z = 0-2$, providing a valuable opportunity to study the abundance of molecular gas during and following the peak of cosmic star formation ($z \sim 2$) [89, 98]. As shown in Fig. 1.7, overlapping CO line coverage within the TIME band allows for CO constraints to be derived purely from cross-correlations. Measurements of the CO cross-power are robust against foreground contamination and are expected to place competitive constraints on the evolution of the cosmic molecular hydrogen density from redshift $z = 0.5 - 2$ (see Kovetz 2017 [60] for projections).

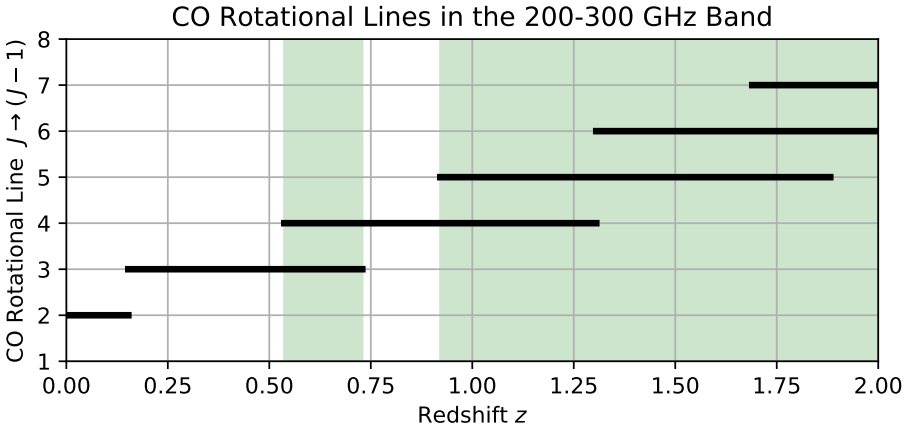

Figure 1.7: CO rotational lines redshifted into the 200-300 GHz atmospheric window. Green shaded regions indicate redshifts for which multiple CO lines are observed.

Depending on the models assumed, intermediate redshift CO emission is expected to be greater than or comparable to the [CII] emission at high redshift, presenting a complication for Epoch of Reionization science extraction [98, 102]. A few published models for the total CO power spectrum from all redshifts as mapped into the 200-300 GHz atmospheric window are shown in Fig. 1.5. Note that the CO models shown are projected into the [CII] k-space for direct comparison with the [CII] power spectra from a foreground-removal standpoint. TIME is considering two distinct methods for [CII] component separation. The first method, detailed in Sun 2018 [102], uses a tracer of low redshift galaxy CO emission to mask the survey voxels containing the brightest CO emitters. The author examines the use of K-band magnitude and photo-

metric redshift as a tracer for low-redshift CO emission, estimating the mean and the scatter in the relation and projecting voxel cut fractions necessary for a TIME-like survey. The residual CO power spectrum post-masking as presented Sun 2018 [102] is shown in Fig. 1.5 and corresponds to a removal of $8 - 18\%$ of survey voxels. Note that because the CO and [CII] are uncorrelated, this approach of proxy-guided masking does not introduce bias into the [CII] measurements. Sun 2018 [102] estimates that ancillary data on of order 200 low-redshift sources is needed to sufficiently mask the TIME survey geometry. The second component separation method, presented in Cheng 2016 [23], uses the distortion in power along the line of sight introduced by projecting low-redshift CO emission into high-redshift k space. Instead of looking only at the spherically averaged k, the measured power spectrum is viewed in two dimensional k-space, parallel and perpendicular to the line of sight. [CII] power is isotropic in this space, but lower-redshift interloper lines will appear anisotropic due to the incorrect redshift mapping. Two-dimensional templates can then be fit to extract the separate components. A complication of this method is that at a given frequency each CO transition arises from a different redshift and is thus uniquely distorted in this space, requiring several components to be removed. In summary, the combination of [CII] and CO emission from different redshifts into the same range of observing frequencies presents a challenge to Epoch of Reionization science extraction, but this challenge is surmountable.

Chapter 2

Instrument Design

In this chapter I will review the overall design of the TIME instrument, discussing hardware, readout, optics, and on-sky sensitivity projections. Detector design is covered separately in the following chapter.

2.1 Cryogenics

Fridge Configuration

TIME repurposes an existing cryostat produced by High Precision Devices for the BLISS experiment [18]. A Cryomech PT415 pulse tube cooler provides the 50K and 4K temperature stage, with a specified capacity of 40 W at 45K and 1.5 W at 4.2K with a load-free base temperature of 2.8K [29]. A ^{4}He Joule-Thompson fridge provides a continuous 1K stage with a capacity of 20 mW at 1.1K [84]. Helium is injected from a room temperature reservoir, precooled by the 50K stage head, and condensed at the 4K stage head before passing through a narrow impedance and collecting in a pot at the 1K stage; the vapor pressure in the pot is held down by an external vacuum pump, which recycles helium back into the room temperature reservoir. A pair of ^{3}He sorption fridges (Pumps 1 and 2 in Fig. 2.2) condense off of the 1K stage and provide the IC (intermediate-cold) stage, each with a capacity exceeding 100 μW at 350 mK [85]. The two IC fridges connect to the IC stage through gas-gap heat switches, allowing each evaporator to be disconnected and cycled while the alternate evaporator maintains a continuously-cold IC stage. The original Adiabatic Demagnetization Refrigerator (ADR) used in the BLISS testbed [83] has been removed and replaced with an additional ^{3}He sorption fridge, which serves as the UC (ultra-cold) stage. This fridge is buffered by the IC stage, providing a capacity of 8 μW at our nominal base temperature of 250 mK (or 25 μW at an elevated base temperature of 275 mK) [85].

Radiative Loading

The TIME cryostat consists of a nested series of aluminum cylindrical shields which radiatively exchange power based on their emissivity and surface area. Approximate geometries of the TIME radiation shields can be found in Table

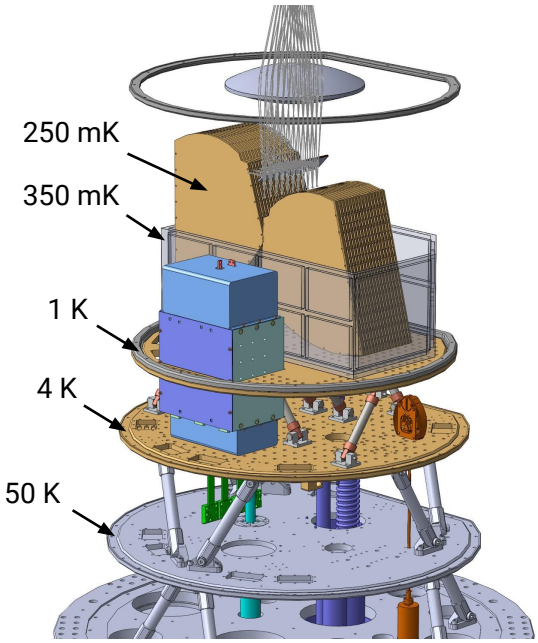

Figure 2.1: A rendering of the TIME cryostat with the radiation shields removed. Individual stages are marked with their nominal temperatures. Note that the cryostat is upward-facing in this diagram for illustrative purposes; the orientation of the pulse tube cooler requires that the cryostat be downward-facing while in operation.

2.1. In Table 2.2 I estimate the radiative loading between stages assuming bare aluminum shields with an emissivity of $\epsilon = 0.1$. Note that the expected loading on 50K from 300K is several times the capacity of the 50K stage, and that the expected loading on 4K uses two thirds of the capacity of the 4K stage. To reduce the effective emissivity, we surround the 50K and 4K shields with multi-layer insulation (MLI) consisting of approximately 30 sheets of aluminized Mylar each with a low-thermal-conductivity fibrous backing layer. These layers are held in place by Kevlar thread, minimizing conductivity between layers and allowing each layer to reach its own radiatively-driven equilibrium temperature. Assuming that the bare metal and aluminized Mylar have similar emissivities, that the layers are seamless, and that the layers are only radiatively coupled, then the effect of $N = 30$ radiation shields is to reduce the heat load on the colder stage by a factor of $N + 1 = 31$ [21].

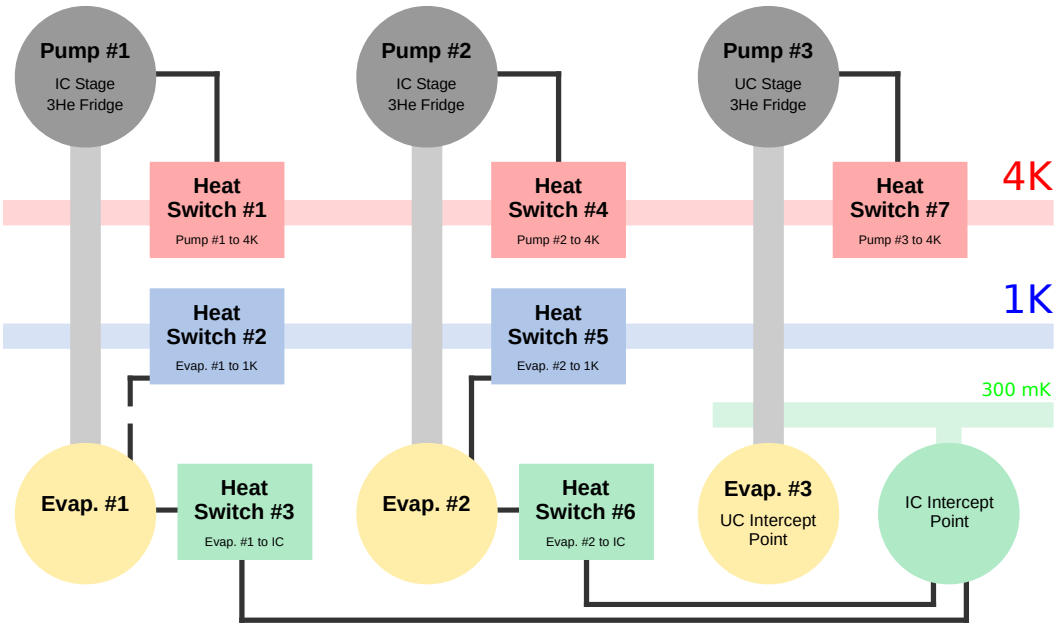

Figure 2.2: A schematic diagram of the three ^{3}He sorption fridges and seven gas-gap heat switches used in TIME. A break in the connection for Heat Switch #2 indicates a connection that was removed due to poor off-state conductance.

	Length [cm]	**Radius [cm]**	**Surface Area [m^2]**
300K	150	35	4.1
50K	120	33	3.2
4K	86	30	2.2
1K	60	28	1.5

Table 2.1: Approximate dimensions of the TIME cylindrical radiation shields.

Parasitic Loading

The geometry and composition of the mechanical legs connecting adjacent temperature stages are detailed in Table 2.3. The choice of materials at each stage is a compromise between thermal conductivity and mechanical strength; TIME uses thick G10 [69] legs for 300K-50K and 50K-4K, thin-walled stainless steel [69] from 4K-1K, and carbon fiber [91] from 1K-350mK and 350mK-250mK. These legs are the dominant source of parasitic non-radiative loading for TIME under normal conditions. Additional sources of loading include the

	$\mathbf{T_{hot\ shield}}$ [K]	Raw Radiation Loading
300K-50K	295	175 W
50K-4K	85	950 mW
4K-1K	8	50 μW

Table 2.2: Raw (uninsulated) radiation loading between the TIME shields, assuming an emissivity for aluminum of $\epsilon = 0.1$. Multi-layer insulation (MLI) covers the 50K and 4K shields to reduce this load by a factor of ~ 30 in the ideal case.

stainless steel pump line of the Joule-Thompson fridge (running from 300K to 1K) and the graphite passive heat switches (used to improve the cool-down time of the 1K stage by thermally shorting it to 4K at high temperatures); the geometry of both of these elements as well as the cryogenic thermal conductivity of graphite are described in Prouve 2012 [84]. The detector wiring, which runs from 300K to the FPU, is detailed in Table 2.4. Superconducting NbTi cabling is used between the series-array SQUIDs at 4K and the focal plane at 250mK; Manganin [2] wiring is used between warmer stages.

In Fig. 2.3 I estimate the parasitic load from the 4K stage to the 1K stage as a function of the 4K plate temperature. Note that at high temperatures the passive graphite heat switches become the dominant loading source (and a significant fraction of the cooling capacity of the 1K fridge). Parasitic loading from 50K onto 4K is seen in Fig. 2.4. Between room temperature and the 50K stage, I expect 880 mW from the six G10 legs, 780 mW from the JT pump line, and 110 mW from the detector wiring for a total of 1.8 W. The carbon fiber legs are expected to contribute 2 μW to the IC stage and 0.3 μW to the UC stage.

	Material	Count	L [mm]	OD [mm]	ID [mm]
300K-50K	G10	6	68.3	19.05	22.23
50K-4K	G10	6	101.6	19.05	22.23
4K-1K	Stainless Steel	6	81.3	15.87	14.45
1K-IC	Carbon Fiber	10	140	2.7	-
IC-UC	Carbon Fiber	10	50	2.7	-

Table 2.3: Materials and geometries (length L, outer diameter OD, and inner diameter ID) for the mechanical legs supporting the various temperature stages in TIME.

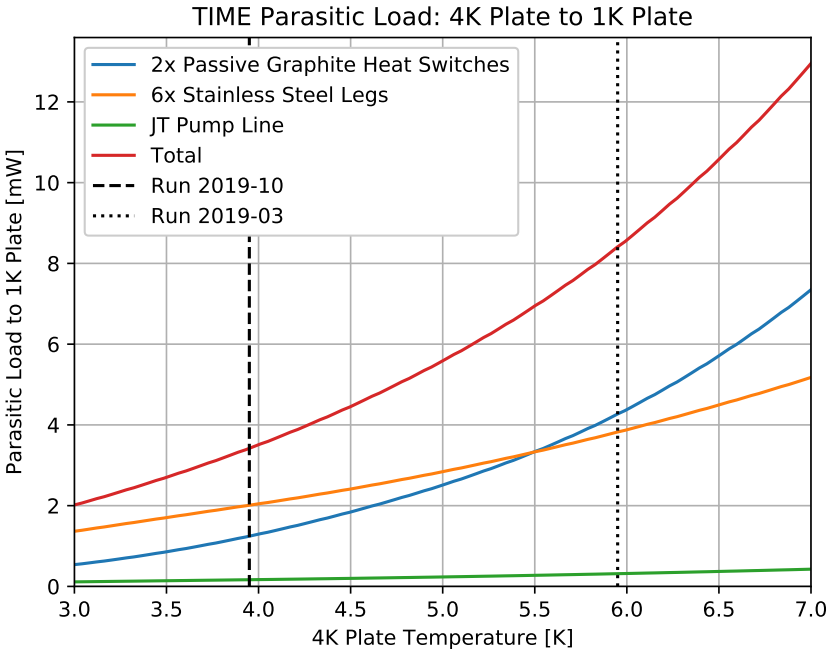

Figure 2.3: Parasitic load on the 1K stage in the TIME cryostat.

	Line Count	**Material**	**D [AWG]**	**L [cm]**
300K-50K	1000	Manganin	38	28
50K-4K	1000	Manganin	38	31-46
4K Isothermal	1000	Copper	38	40
4K-1K	592	NbTi	38	30
1K-FPU	592	NbTi	38	30

Table 2.4: Dimensions (diameter D and length L) of the detector wiring in TIME.

Precooling

Because the stage temperatures are poorly coupled by design, a series of heat switches are use to reduce the cool-down time of the TIME instrument. A pair of graphite rods (25 mm diameter, 25 mm exposed length) couple the 4K and 1K stages, acting as a passive switch with a thermal conductivity near 1 W/(cm K) at room temperature and 10^{-5} W/(cm K) a 1K [84]. A pair of mechanical heat switches (Fig. 2.5) produced by High Precision Devices connect the 4K stage directly to the spectrometer blocks (UC stage) by means of a cold strap penetrating the IC and 1K stages. These switches are driven

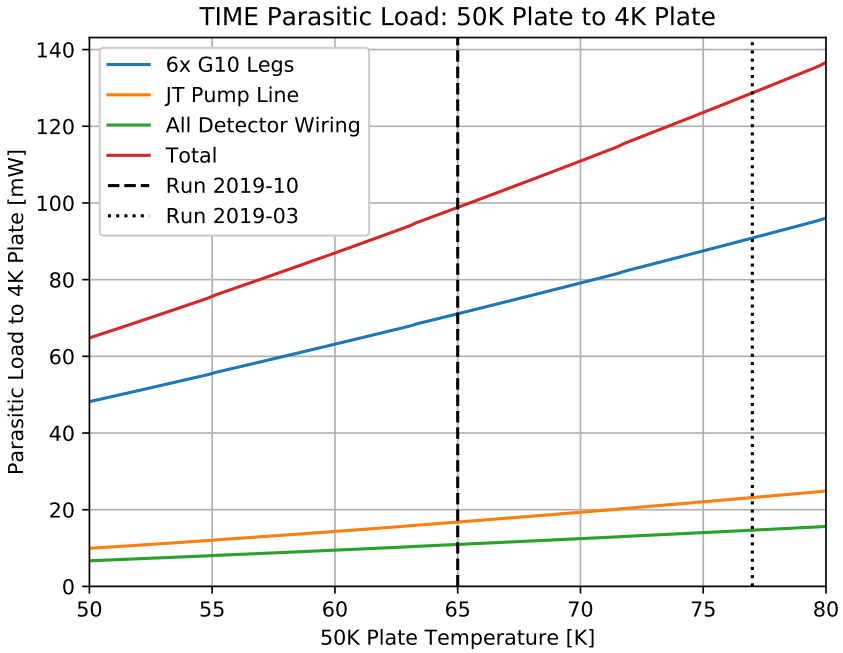

Figure 2.4: Parasitic load on the 4K stage in the TIME cryostat.

by motors located on the vacuum-side of the 300K plate. We measured the thermal conductance of one of these switches with the strap disconnected from the spectrometer; a thermometer and heater were installed on the floating strap, and the heater was chopped between 0 and 150 mW every 25 minutes during a normal cryostat cool-down. Results are shown in Fig. 2.6 down to 100K, where the measurement ended due to a wiring failure.

Figure 2.5: One of two mechanical heat switches connecting the 4K stage to the focal plane during the cool-down process. *Heat switches from High Precision Devices. Heat strap suspension system by Yun-Ting Cheng.*

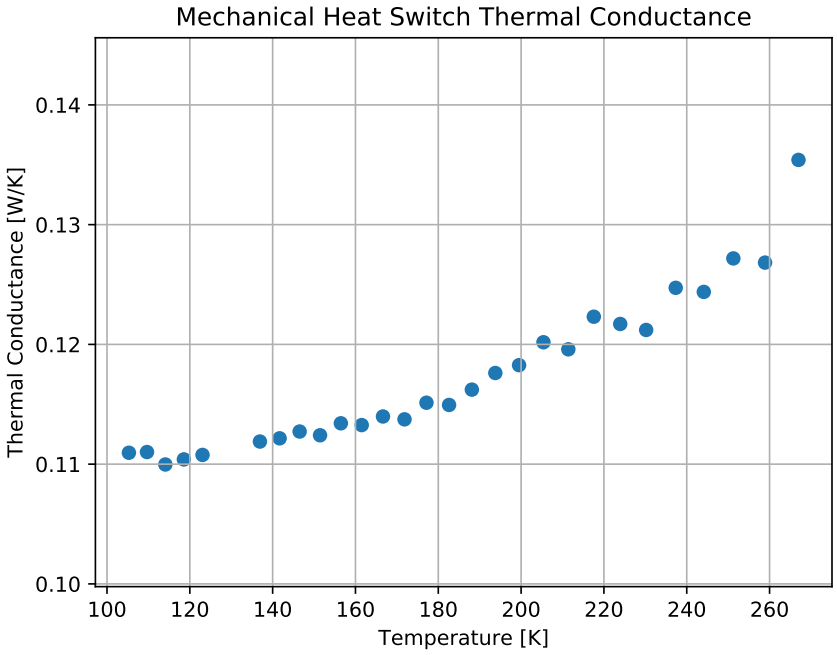

Figure 2.6: Thermal conductance measurement for one of the two HPD mechanical heat switches used in TIME. The strap to the heat switch was disconnected from the focal plane and replaced with a heater chopped between 0 and 150 mW every 25 minutes. Thermometers on either end measured the temperature drop across the heat switch from room temperature down to 100K.

2.2 Focal Plane

TIME consists of two banks of 16 single-polarization grating spectrometers (shown in Fig. 2.7). Each spectrometer is fed by a split-block smooth-wall multi-flare-angle conical feedhorn coupled to the TE01 mode of a rectangular waveguide. A constricted portion of the waveguide functions as a low frequency choke to reject out-of-band signals. The two spectrometer banks are fed with orthogonal polarizations, so a 90° twist in the rectangular waveguide is used to rotate the polarization in one of the two banks. At the mounting interface of the feedhorn, 3 mm rectangular waveguide launches into the spectrometer's 3 mm parallel plate waveguide, exciting (ideally only) its TE1 mode (which exactly matches the electric field distribution and impedance of the TE01 rectangular mode [81]). With a cutoff frequency of 50 GHz, the TE1 mode propagates with low loss in the target 200-300 GHz band. All parts are directly machined from aluminum and gold-plated to reduce conductor loss. A curved diffraction grating (similar to that used in Z-Spec [19, 39], but at lower resolution) is used to produce a compact instrument. Designed by TIME team member C.M. Bradford, the grating is a numerically optimized [17] perturbation of the Rowland spectrometer geometry [90]. At zeroth order, the input feedhorn and output detector arc lie along a Rowland circle of radius 133 mm, and the grating facets lie along a circle of radius 266 mm which is tangent to the Rowland circle. Two stigmatic frequencies are chosen near the band edges (see Fig. 2.8) at which aberration-free performance is demanded, providing constaints that allow one to solve for the individual facet positions [17]. The final TIME grating uses 190 facets whose blaze angles (optimized seperately) vary from 23° to 26° (see Fig. 2.9). Sample spectral profiles for a warm TIME grating spectrometer coupled to a diode detector are presented in Li et al. 2016 [64], one of which is shown in Fig. 2.10. Results generally agree with ray tracing expectations.

As indicated in Fig. 2.8, the output arc of the spectrometer is approximated by six 28 mm linear facets populated with detector arrays. A total of 60 TES bolometers populate the output arc of each spectrometer. The diffraction grating as designed provides a resolution $R \sim 170$, but detectors sample the output at $R \sim 100$, relaxing the detector count and noise level requirements while maintaining access to large-scale sky modes. Detectors are organized into subarrays corresponding to either 4 spatial by 12 spectral pixels (high frequency) or 4 spatial by 8 spectral pixels (low frequency). The baseline

detector design is described in detail in Ch. 3, with an alternate design presented in Ch. 4. Groups of four subarrays corresponding to 16 spatial pixels are housed in a gold-plated aluminum detector module as shown in Fig. 2.11. Spring-loaded tile clips located between subarrays (tensioned from the rear of the module) hold the subarrays against the gold module surface (which is not the backshort in this design); copper tile clips mounted from the front hold the free edges of the outer two subarrays. Two pins register the position of each subarray, and an additional two pins register the position of the module on the spectrometer bank. Six modules (three high frequency, three low frequency) are mounted to each spectrometer bank (Fig. 2.12). Aluminum wire bonds link detector wiring pads on the subarrays down to gold-plated copper traces on removable flex circuits mounted below. These traces quickly transition to superconducting tinned-copper to limit the TES series resistance. A set of four (low frequency) or six (high frequency) flex circuits (Fig. 2.14) each carry wiring for 32 detectors to an accompanying SQUID board (Fig. 2.13). Two removable caps spanning the short edges of the module set the mounting distance from the spectrometer face, which can be tuned depending on the detector wafer thickness. Pockets in the spectrometer faces accommodate the tile clips and wire bonds, allowing the detectors to be mounted arbitrarily close to the parallel plate waveguide. Because we operate far above the waveguide cutoff frequency, the impedance is very close to that of free space and thus mounting distance is generally not critical for absorbing-sheet detectors.

The SQUID board (Fig. 2.13) houses the first-stage SQUID (SQ1), bias resistor, and filter inductor for each channel. The SQ1s are organized into chips with 11 channels each; three chips are daisy-chained to produce a column of 33 channels that are time-domain multiplexed on a single second-stage SQUID (SSA, SQUID series array) and ADC. Each incoming flex circuit is screwed down to the SQUID board, and a series of aluminum wire bonds connect each of the 32 line pairs to corresponding pads on an interface chip containing the $3-4\,\mathrm{m}\Omega$ bias resistor and $2\,\mu$H filter inductor. One channel per column does not have a detector attached (a "dark SQUID") and is used to monitor certain types of dark noise pickup. The interface chips are linked to the SQ1 chips and ultimately to the underlying circuit board. The interface and SQ1 chips for each column are epoxied to 1 mm thick Al_2O_3 carriers, which approximately match the thermal contraction of silicon. These carriers are held down to the PCB with screws and are removable (at the cost of redoing the wire

bonds). Pads on the sides of the chips are transferred to the carrier edge via 10 μm thick AuPd traces. A set of three 37 pin micro-d connectors connect the multiplexing row address lines, TES bias lines, etc. to the distribution board (Fig. 2.18).

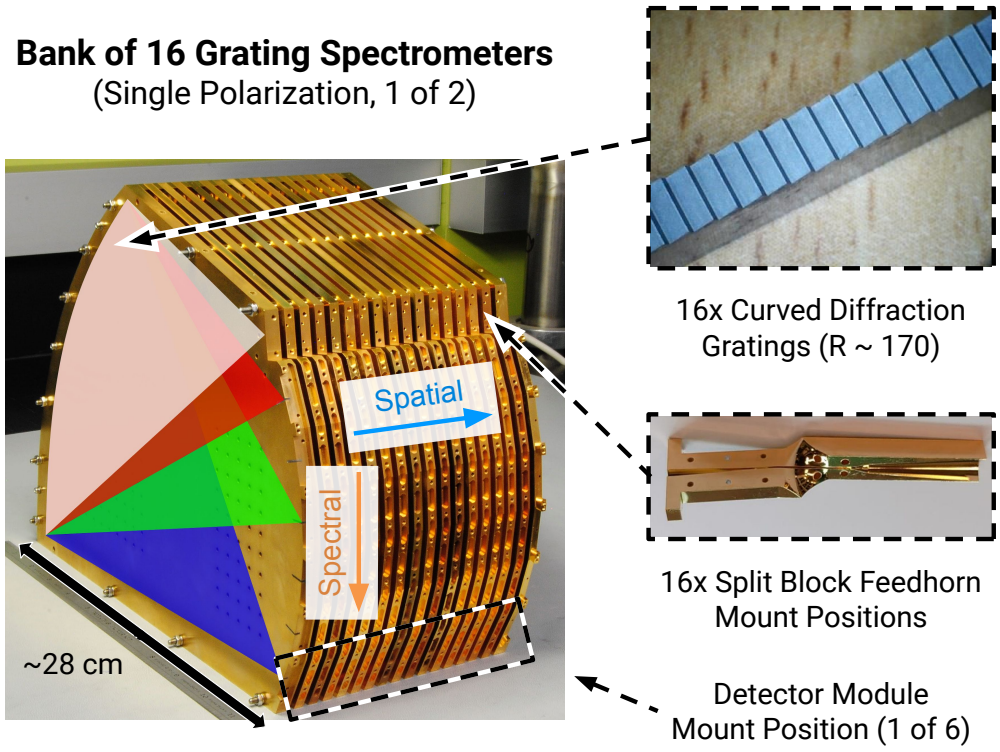

Figure 2.7: One of two banks of 16 grating spectrometers used in TIME. Mounting positions for feedhorns and detector modules are indicated but not populated here. A cartoon diagram of the light path is shown on the side of the bank.

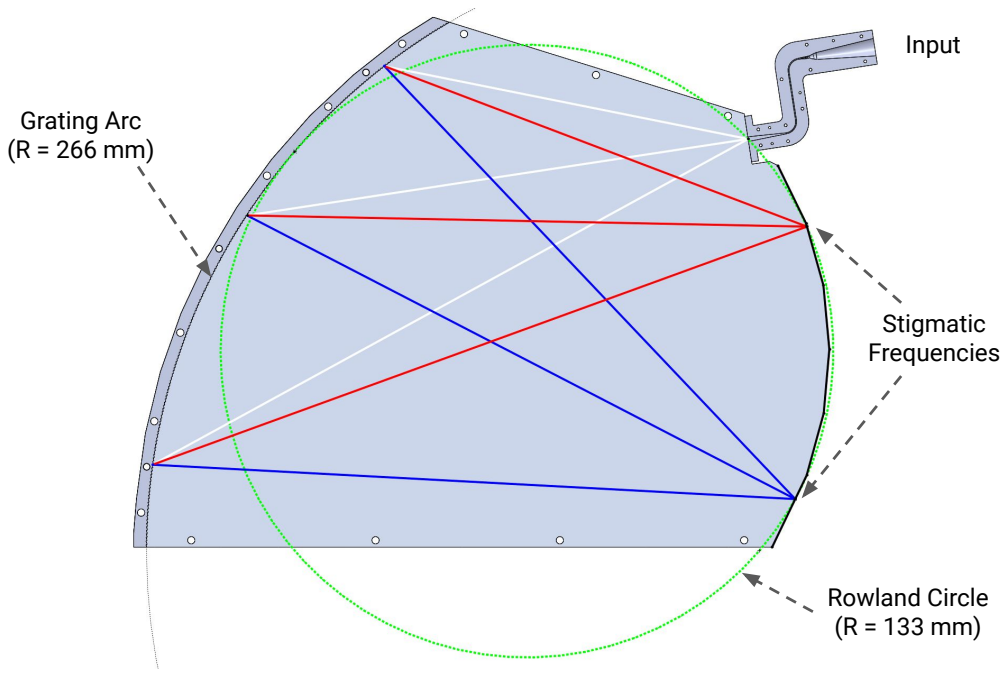

Figure 2.8: Layout of the TIME spectrometer grating (left), input horn (upper right), and output arc (right, solid black lines). *Adapted from Fig. 3 of Bradford et al. 2003 [17]. TIME grating spectrometer design by C.M. Bradford.*

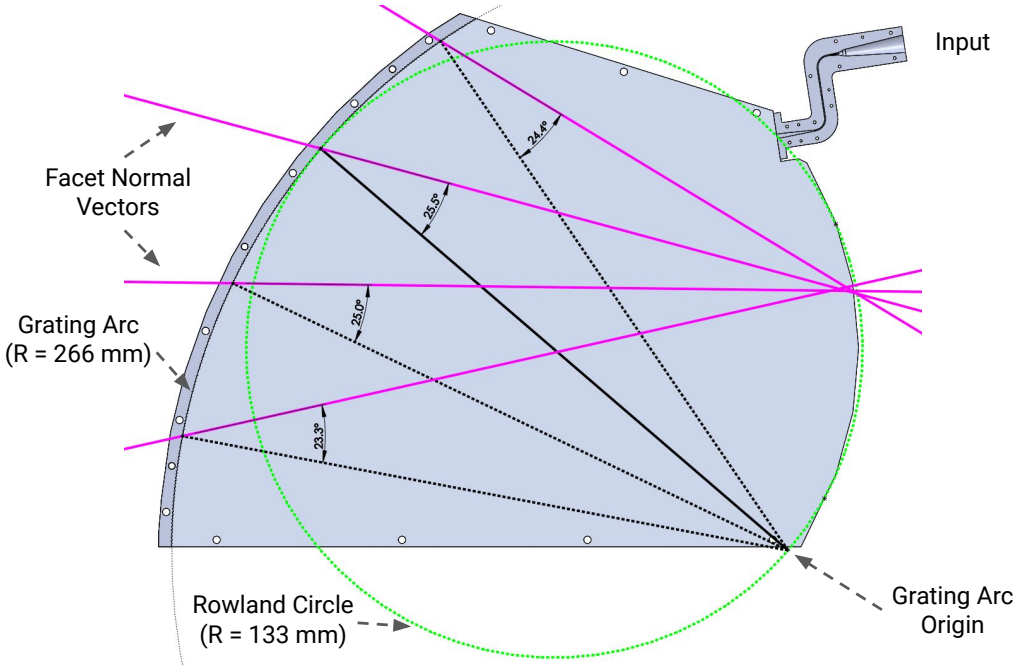

Figure 2.9: Facet blaze angles for the TIME spectrometer. Magenta lines indicate vectors normal to the facet surfaces, and broken black lines indicate vectors normal to the grating arc (with the solid black line indicating the pole of the grating). Blaze angles vary per facet and are near 25°. *TIME grating spectrometer design by C.M. Bradford.*

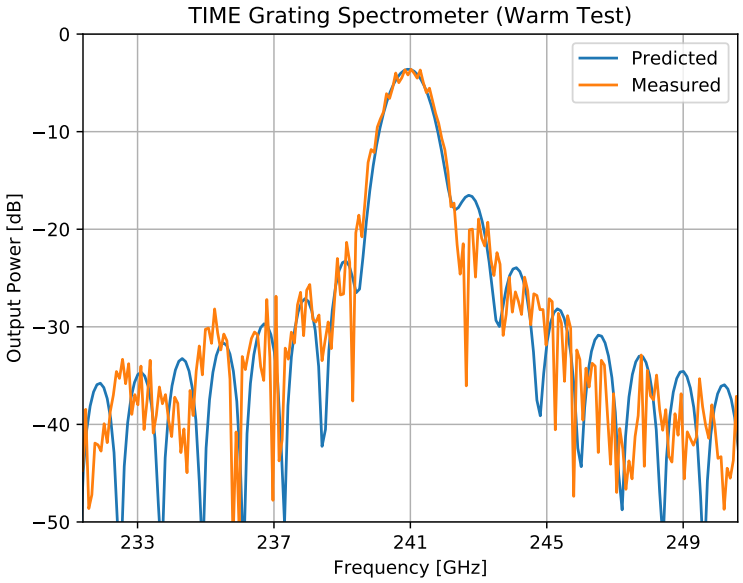

Figure 2.10: Measurement of a TIME grating spectrometer with a swept coherent source and a room temperature diode detector compared to ray tracing expectations (accounting for known coupling efficiencies in the test setup), as reported in Li 2016 [64]. *Prediction and measurements by C.T. Li, adapted from Fig. 7 of Li 2016 [64].*

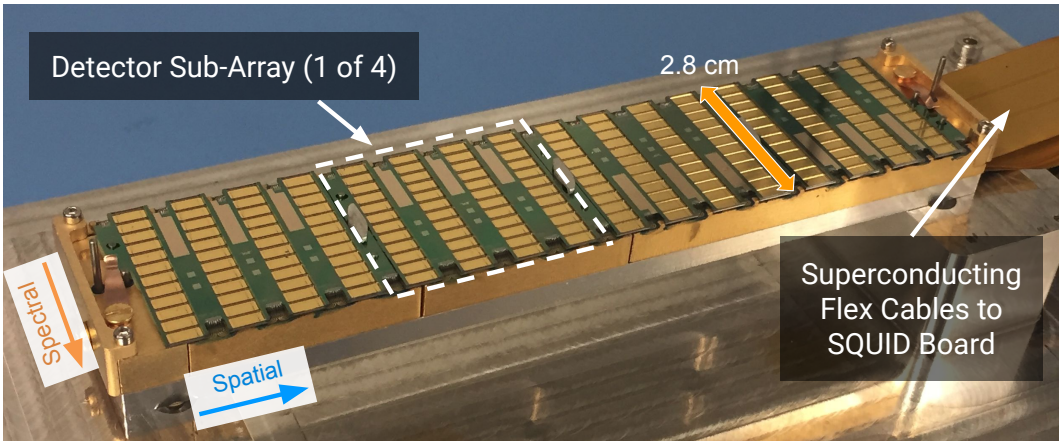

Figure 2.11: One of twelve detector modules needed for a full TIME instrument. Four HF detector subarrays are mounted, covering 16 spatial by 12 spectral pixels.

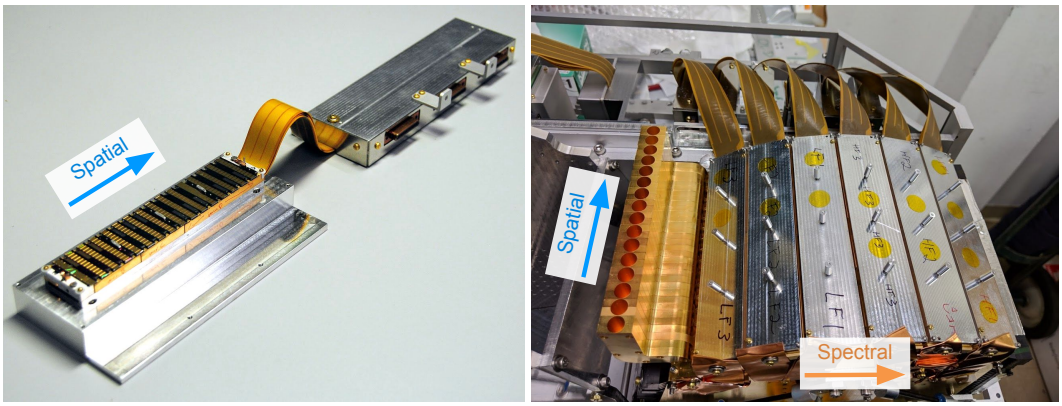

Figure 2.12: *Left:* A single detector module with its polyimide readout cables and SQUID board. *Right:* A fully populated grating spectrometer bank with all 16 feedhorns and 6 detector modules.

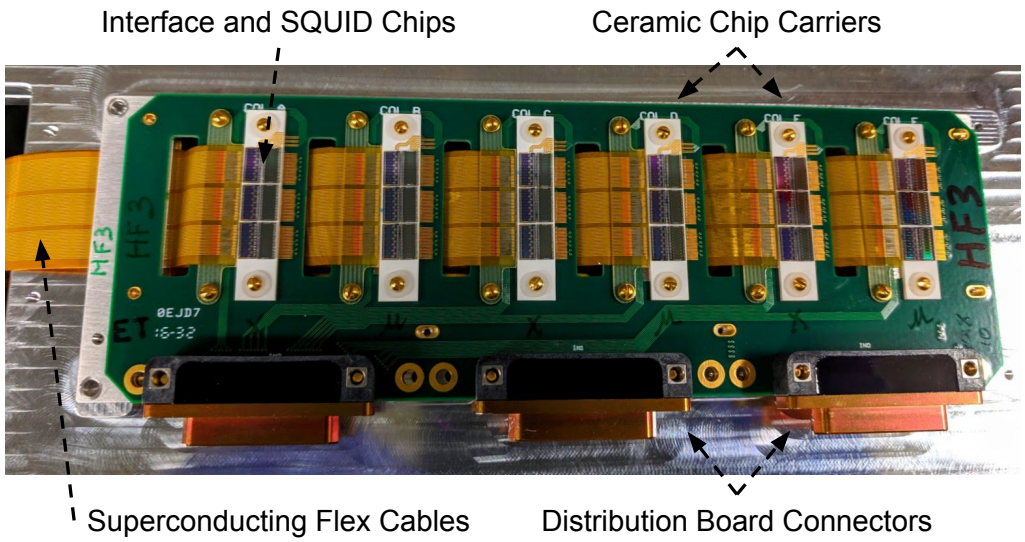

Figure 2.13: A photo of the SQUID board for a single HF detector module without its magnetic shielding box. Six polyimide readout cables, each carrying signals from 32 detectors, terminate on SQUID and interface chips. Three connectors attach to the readout distribution board.

2.3 Detector Readout

Wiring and Electronics

TIME sensor currents are amplified by two stages of superconducting quantum inference device (SQUID) amplifiers fabricated by NIST [35, 47]. The resulting signal is digitized by one of two Multi-Channel Electronics (MCE) crates produced at the University of British Columbia [9]. Each MCE crate corresponds to a TIME spectrometer bank and contains 32 independent readout chains (multiplexing columns) with a 50 MHz raw sampling rate. Each multiplexing column is time domain multiplexed across 33 multiplexing rows; detectors on a multiplexing column share an ADC, a TES bias, and a second stage SQUID (SSA, SQUID series array). All channels have unique first stage SQUIDs (SQ1s) that are enabled or disabled with flux-activated switches.

A high-level schematic diagram of the detector readout wiring can be seen in Fig. 2.15. The MCE crates are mounted on the outside of the cryostat; each crate runs five 100 pin shielded cables into the cryostat via hermetic circular connectors at the vacuum flange. Inside the cryostat, a total of ten 100 pin Manganin cables connect from the vacuum flange to the 4K electronics box; the cables have heat sinks connected to the 50K flange, but are not connectorized there. All wiring entering the 4K cavity (detectors and thermometry alike) passes through a LC RF low pass filter (Π-configuration, manufactured by Cristek). Inside the 4K electronics box, copper cables connect the filtered lines to one of four SQUID series array (SSA) boards, shown in Fig. 2.16. These boards each house two NIST-produced SSA modules covering 8 multiplexing columns each; a bare SSA for one column can be seen in Fig. 2.17. A set of 16 superconducting NbTi 37 pin cables join the 4K SSA boards (via 1K heat sinks) to two UC-stage distribution boards (one per spectrometer, shown in Fig. 2.18). Each distribution board accommodates six SQUID boards (Fig. 2.13), which are connected to detector modules via superconducting flex circuits.

Channel Mapping

Mapping from detector space (spectral and spatial pixels) to multiplexing space (row and column) is complicated by various hardware limitations, including the inability to cross lines on detector subarrays and flex circuits; this leads to a non-intuitive but well-defined coordinate mapping. Additionally, because all detectors on the same multiplexing column must share a common

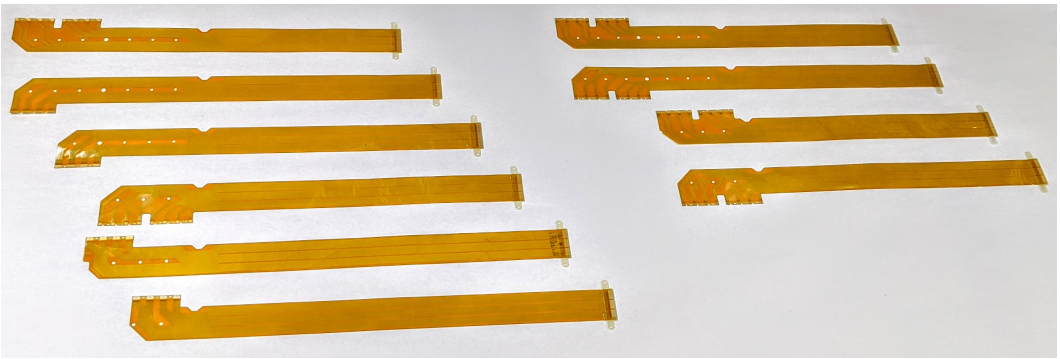

Figure 2.14: A photo of the superconducting (tinned copper) readout flex cables used to connect the detectors to the SQUID board in TIME. The left six are used for a HF module, and the right four are used for a LF module; the first and fourth cable are identical in the HF and LF modules.

TES bias line, optimal multiplexing column assignments group detectors that are close to each other in frequency space where possible (similar loading is expected at similar frequencies). Below I define three coordinate systems used for TIME, with relationships between coordinates illustrated in the following figures (for $p = 0$). Conversion is abstracted from the user by a simple Python library in a shared code repository.

- MCE/Multiplexing Coordinates (`mux` Space)
  - `c`: multiplexing column (0 to 31)
  - `r`: multiplexing row (0 to 32)
  - `p`: MCE number / feedhorn polarization (0 for no-twist feedhorn, 1 for twist)
- Spectrometer Coordinates (`xf` Space)
  - `x`: spatial index (0 to 15, with 0 being the spectrometer closest to the SQUID boards)
  - `f`: frequency index (0 to 59, with 0 being the lowest frequency)
  - `p`: MCE number / feedhorn polarization (0 for no-twist feedhorn, 1 for twist)
- Module Coordinates (`msbd` Space)

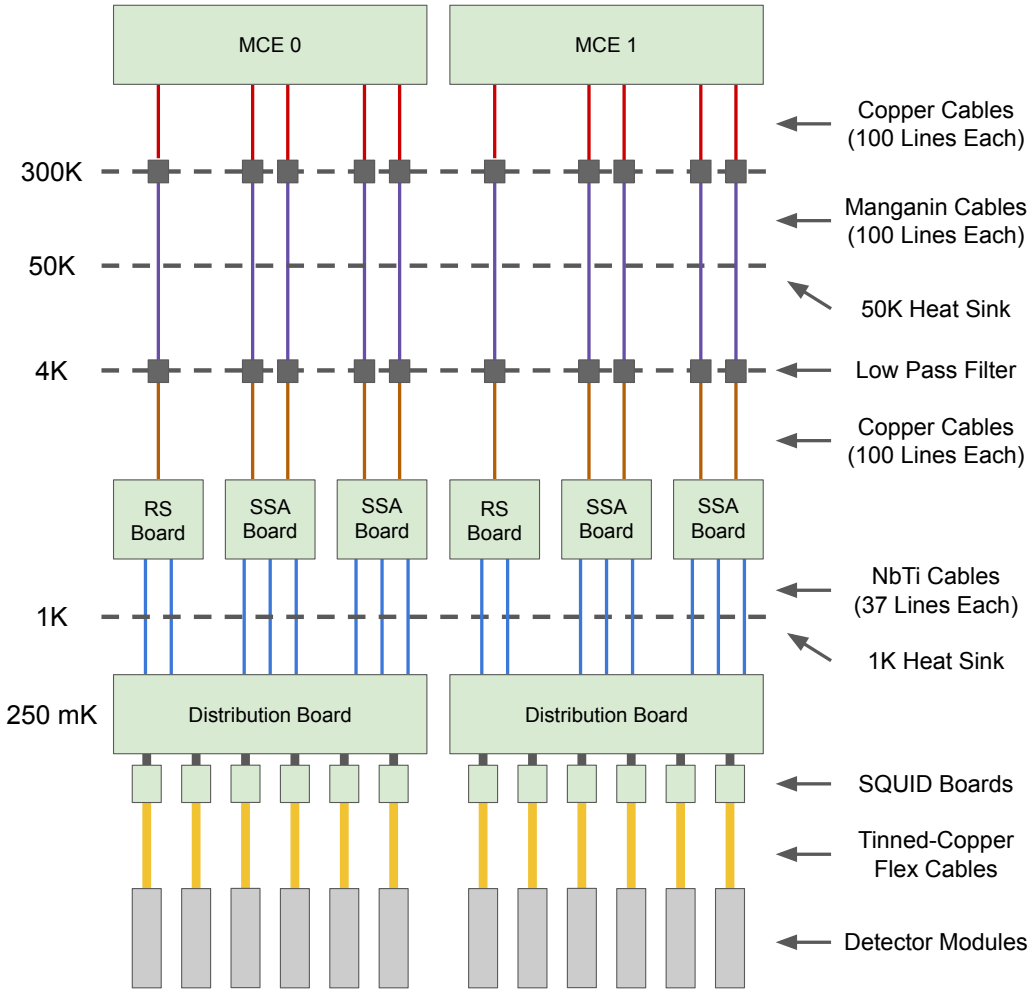

Figure 2.15: A simplified detector wiring and readout chain diagram for TIME, indicating thermal breaks, circuit boards, and connectors.

- `m`: detector module index (0 to 5, with 0 being the lowest low frequency module)
- `s`: detector subarray index within a module, (0 to 3, with 0 nearest the point where the polyimide cables exit the module)
- `b`: detector bank index within a subarray (0 to 3, with 0 nearest the side of the subarray with the pin hole)
- `d`: detector index within a bank (0 to 8 or 12 for low and high frequency modules respectively, with 0 nearest the side of the subarray

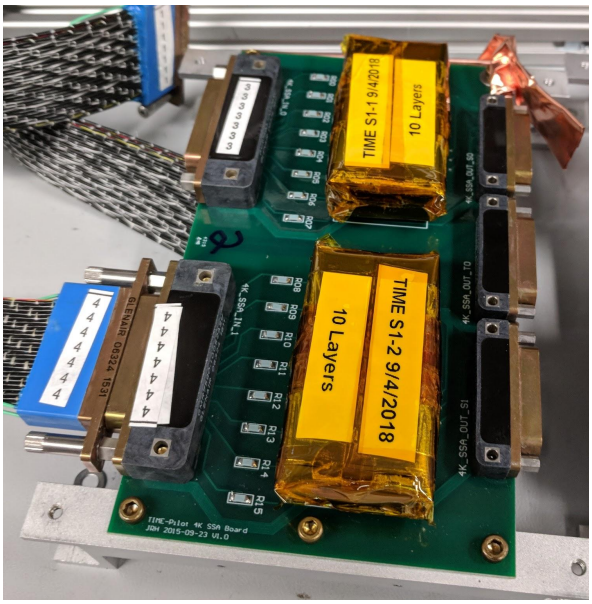

Figure 2.16: One of four SSA boards housed at 4K. Each board contains the SQUID series array for 16 multiplexing columns.

with the pin hole)

– p: MCE number / feedhorn polarization (0 for no-twist feedhorn, 1 for twist)

Timing

Multiple MCEs are synchronized using a MCE Sync Box (also developed by UBC), which generates frame identification numbers that are transmitted over optical fiber to the MCE crates. These sync numbers can serve as a master time source for synchronizing the detector data, thermometry data, and telescope positions if they can be propagated to all of the relevant data streams. However, because the signal (a continuous 25 MHz Manchester-encoded bit stream) is not easily digestible by other systems, synchronizing the telescope with the MCE Sync Box can be challenging. The BICEP team has explored using a Meinberg SyncBox/N2X to allow a Network Time Protocol (NTP) server to serve as the master time source. The Meinberg timing box is capable of synthesizing a square wave of variable frequency that is phase-locked to NTP time, which is fed into the MCE Sync Box to trigger detector sampling; this guarantees the detector frame rate is phase-locked to network time.

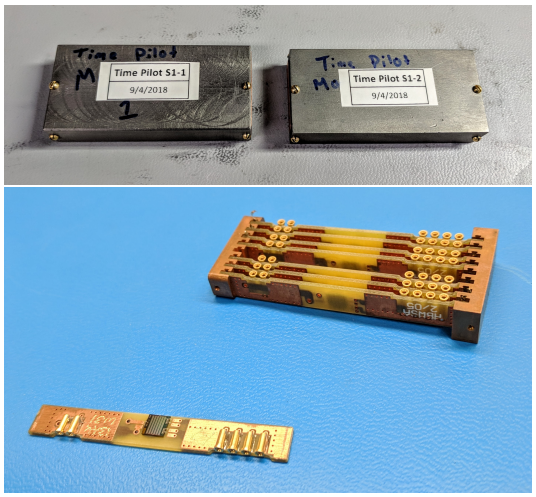

Figure 2.17: *Upper:* Two modules of eight SSAs each as provided by NIST (in a Nb housing). TIME uses a total of eight such modules, for a total of 64 SSAs. *Lower:* An exposed SSA module, showing the SQUID series array for a single multiplexing column.

However, there remains an absolute time offset that isn't known (N frames occur each second, but one cannot say which second corresponds to frame M). TIME has chosen to solve this problem by integrating into our housekeeping readout electronics (designed in-house, see Appendix C) the ability to read both MCE Sync Box time stamps and the Meinberg timing box's current time simultaneously. MCE sync numbers are carried over RS485 via DB-25 cable from the MCE Sync Box, and the Meinberg time is transferred as IRIG-B007 over coaxial cable. From these two sources the housekeeping electronics generate a 1 Hz timestream with sync number and NTP time pairs. When the Meinberg box is fully warmed up and stable a single time pair determines the mapping from sync number to NTP time indefinitely; however, during the initial Meinberg box warm-up period (many days in practice) the mapping will drift slowly, highlighting the need to constantly be monitoring this offset.

To verify the timing offset reported by the housekeeping electronics, I compare the output to the pulse-per-second and pulse-per-minute outputs of the Meinberg box. These signals are carried via coaxial cable to the MCE digital auxiliary input (a single bit sampled and reported with each detector frame). Results can be seen in Fig. 2.26 and 2.27, indicating accurate alignment within each second or minute; alignment on timescales longer than a minute is verified

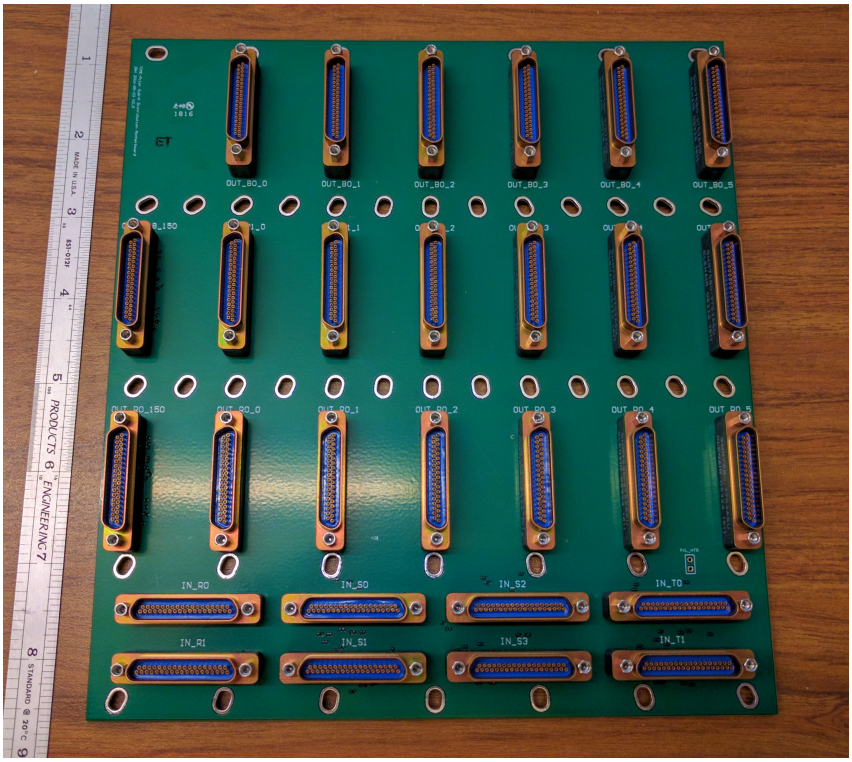

Figure 2.18: One of two identical detector wiring distribution boards for TIME. The board is mounted next to the spectrometers at the UC stage and routes lines from the 4K SSA boards to the detector module SQUID boards.

manually.

Figure 2.19: *Upper:* Four of the ten 100 pin Manganin detector cables running from the 300K vacuum flange to the 4K electronics box. *Lower:* A set of 37 pin superconducting NbTi cables joining the 4K electronics box to the UC distribution board.

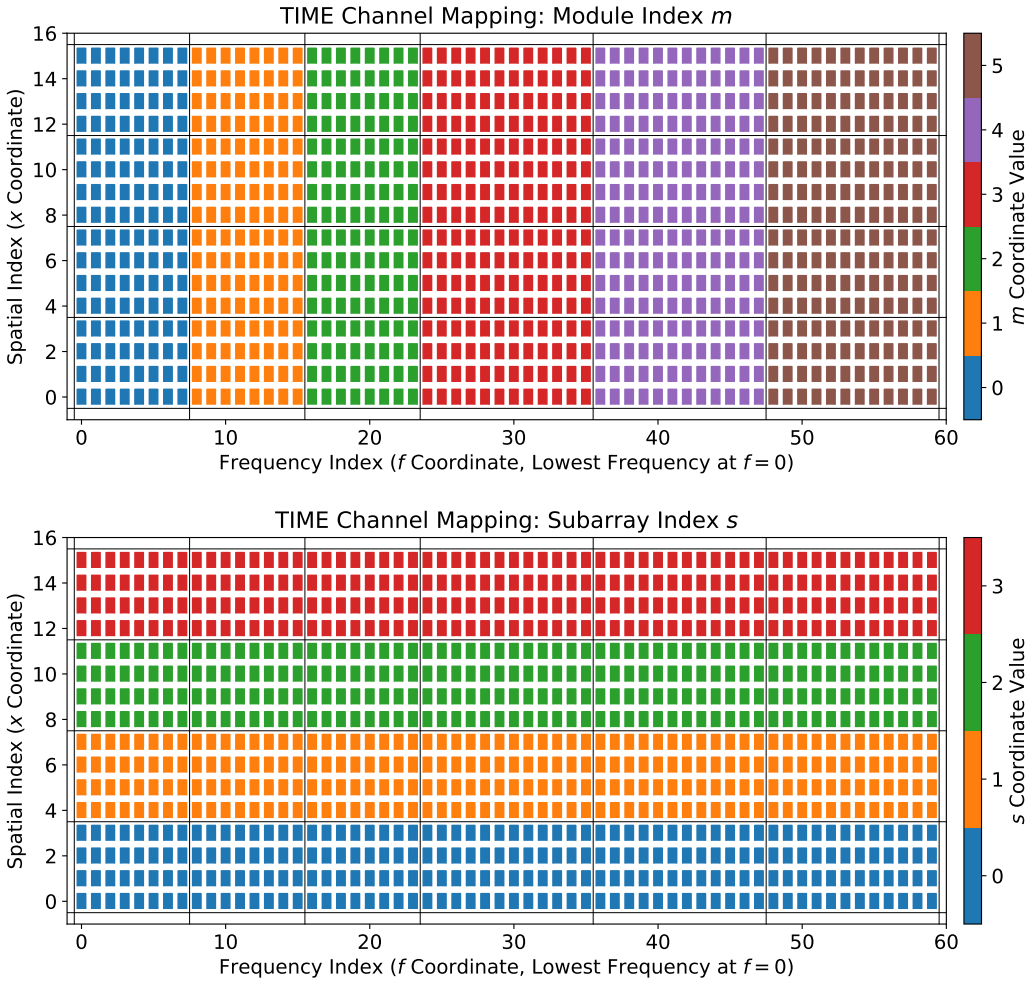

Figure 2.20: Coordinate mapping from `xf` space to `msbd` space.

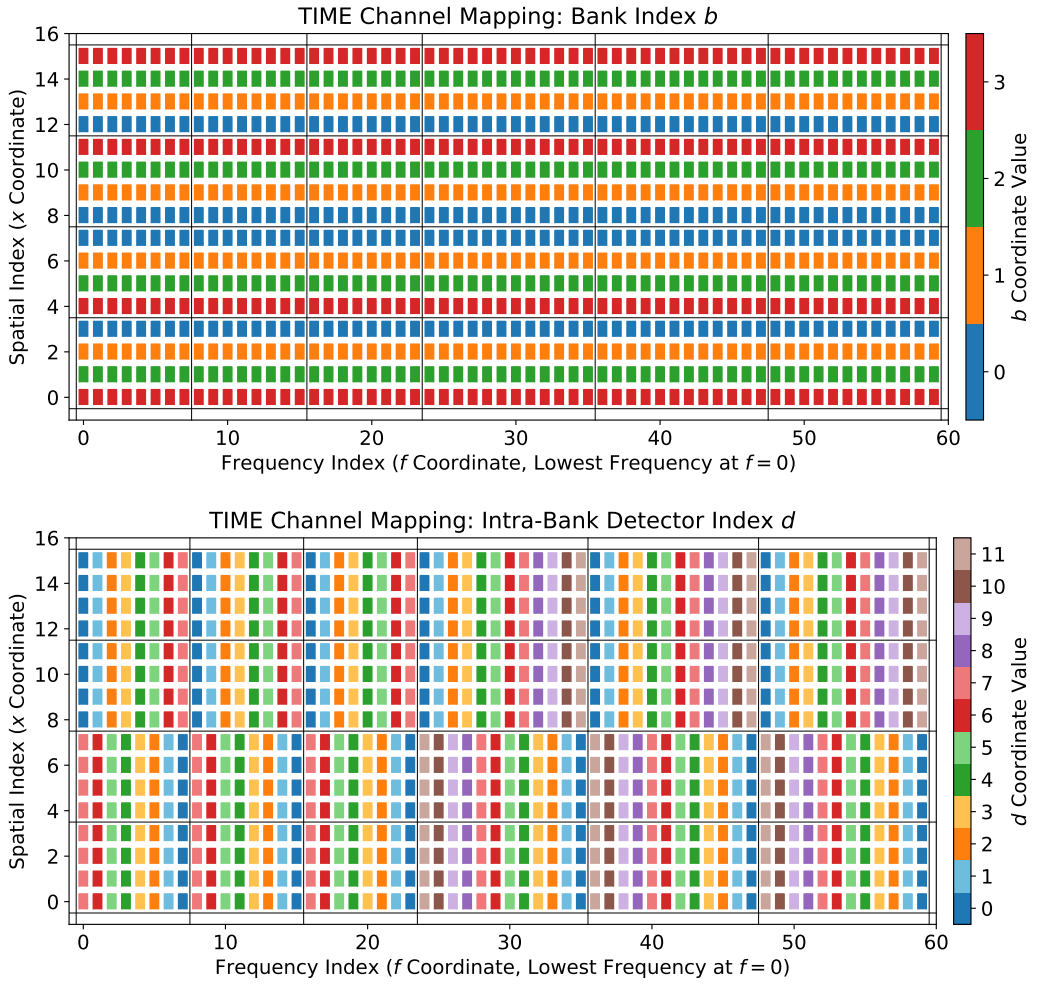

Figure 2.21: Coordinate mapping from `xf` space to `msbd` space. Note that subarrays $s = [0, 1]$ are mounted in reverse with respect to subarrays $s = [2, 3]$, leading to the difference in bank/detector order; the b and d coordinates refer to the physical locations on the (possibly rotated) subarray, not the module.

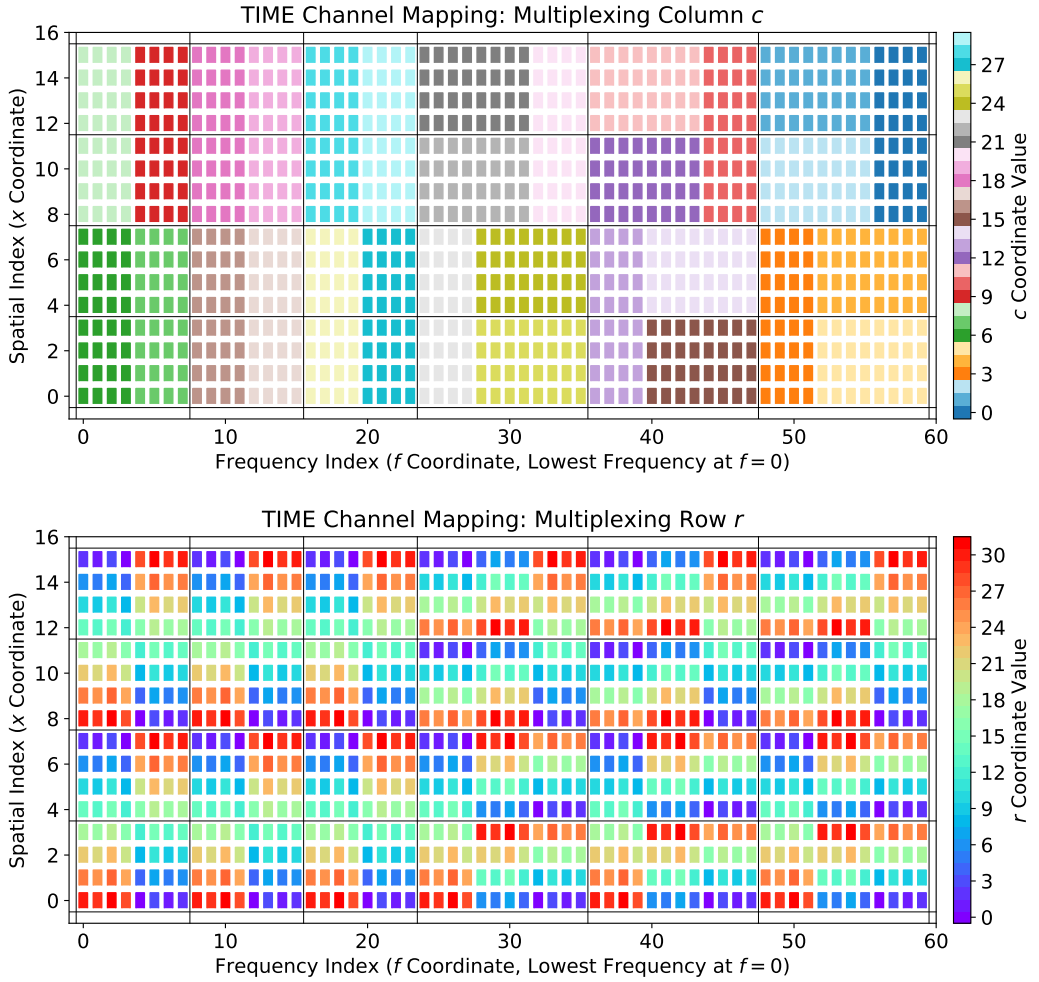

Figure 2.22: Coordinate mapping from `xf` space to `mux` space. Columns (which share a TES bias line) are assigned to blocks of similar frequency to the degree that is possible; rows are assigned based on hardware limitations that prevent lines from crossing each other.

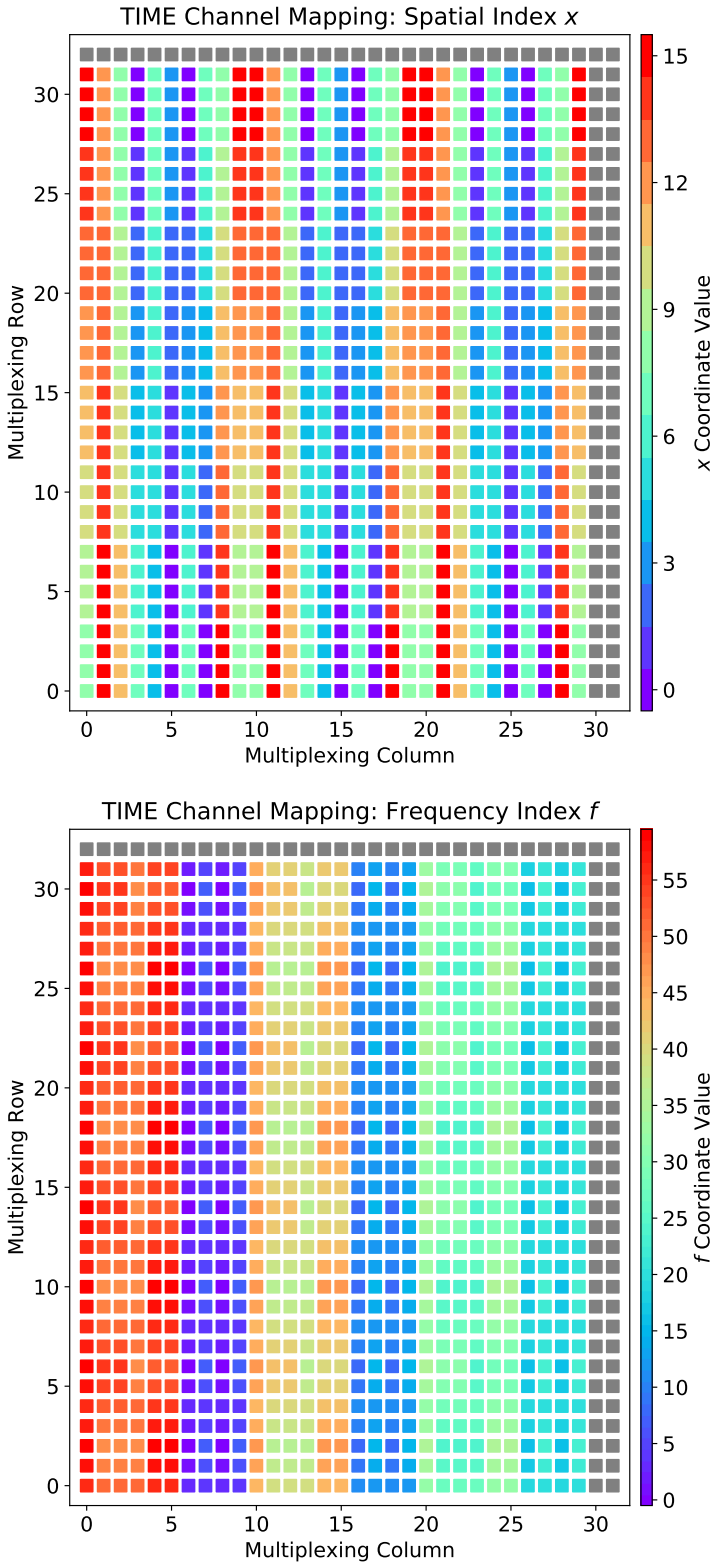

Figure 2.23: Coordinate mapping from `mux` space to `xf` space.

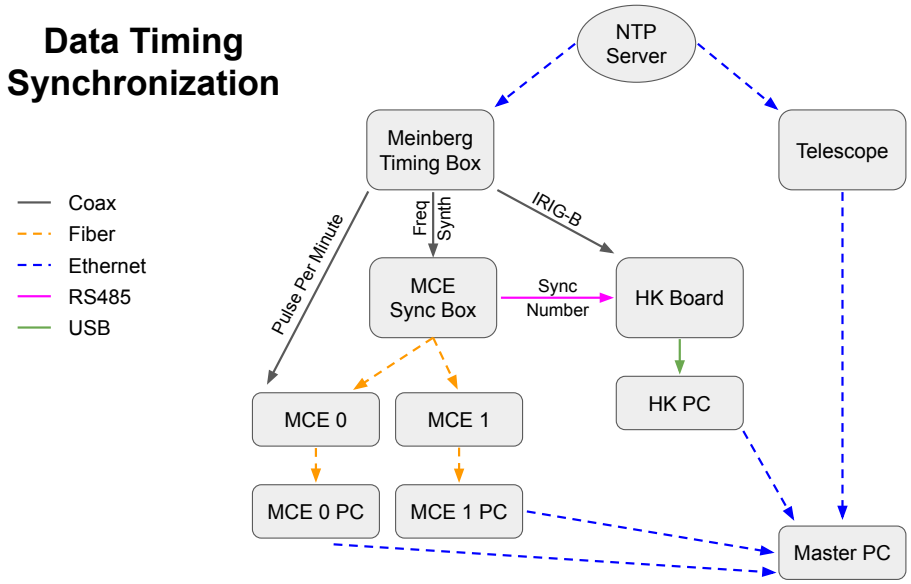

Figure 2.24: A diagram indicating the flow of time stamps for TIME. The NTP server is the master time source, and detector sampling is phase locked to this time by the Meinberg timing box via the MCE Sync Box. The housekeeping electronics monitor and report the absolute timing by matching MCE sync numbers to NTP time stamps.

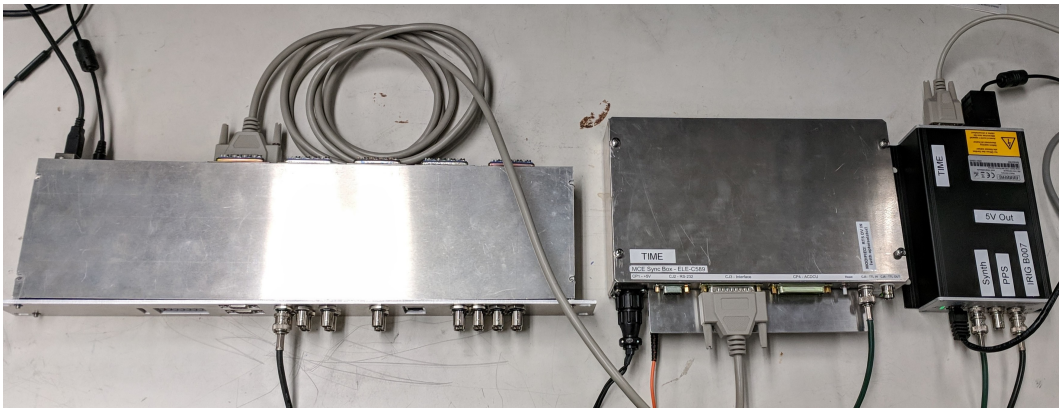

Figure 2.25: The key timing boxes used in TIME. *Left to right: HKMBv1 housekeeping readout box, MCE Sync Box, Meinberg SyncBox/N2X*

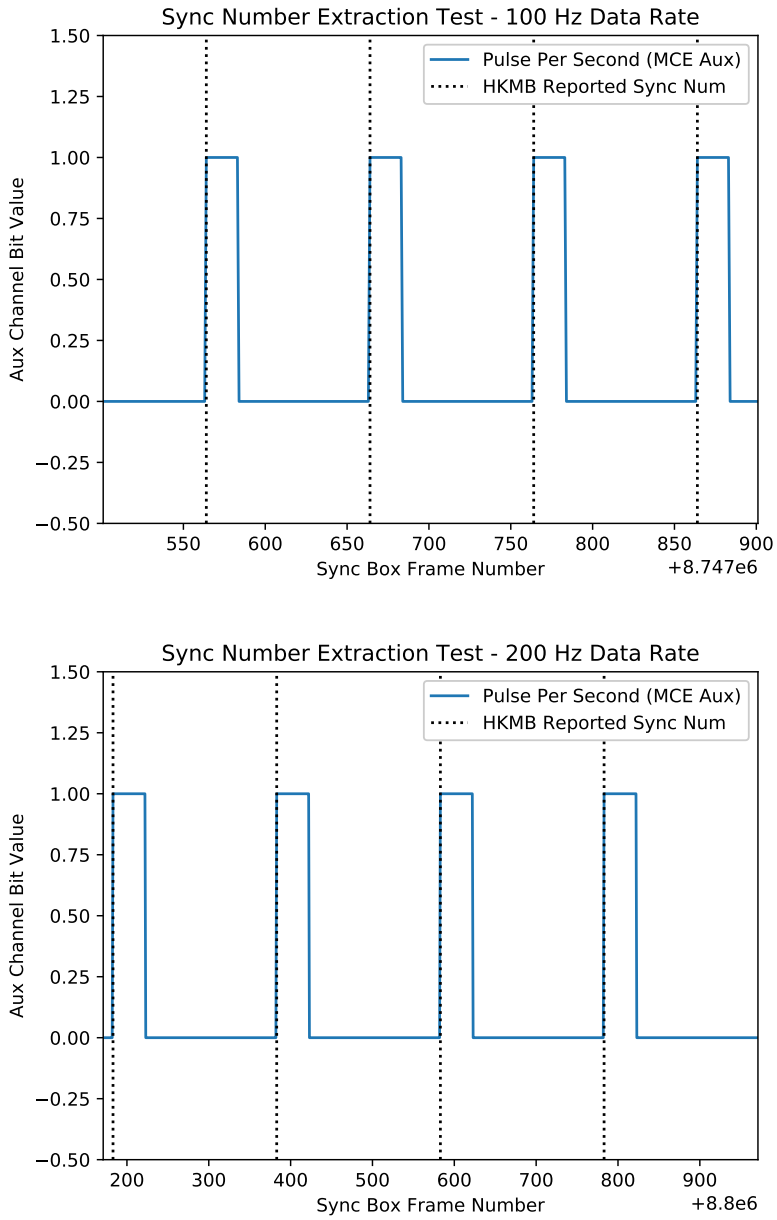

Figure 2.26: Verification at the sub-second level of the timing alignment reported by the housekeeping electronics at two different MCE frame rates.

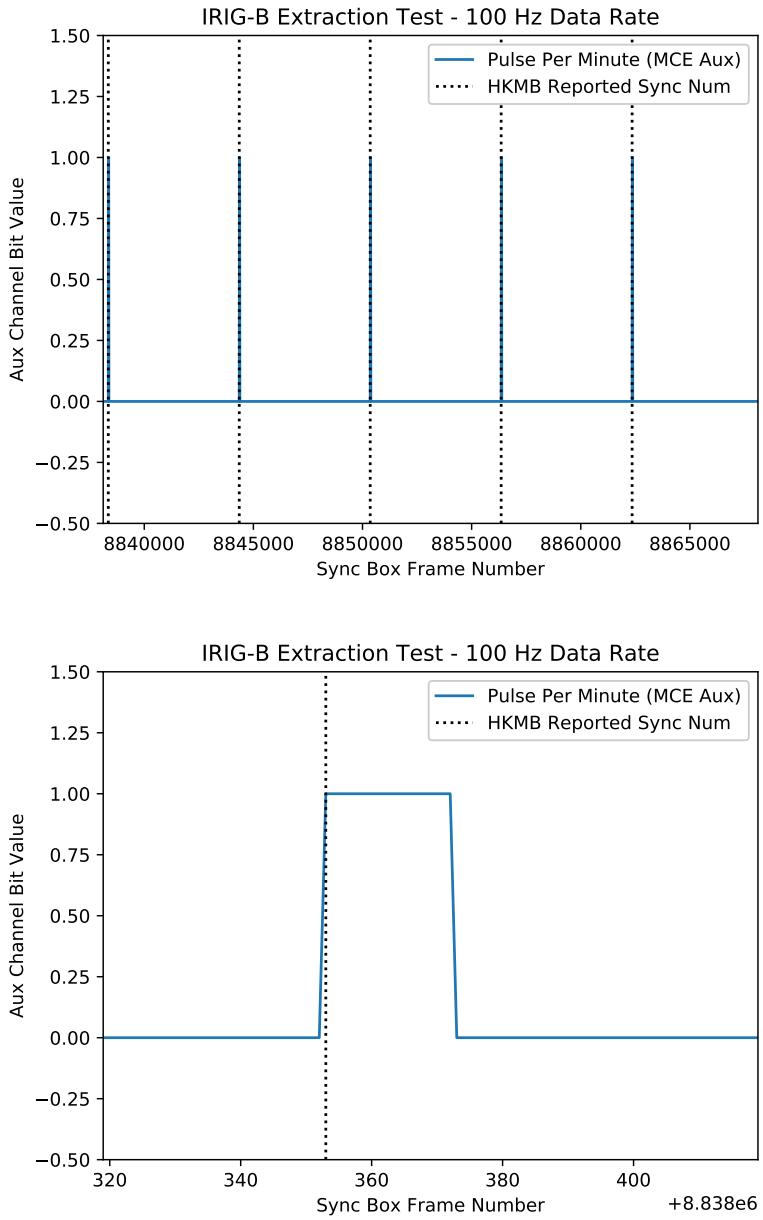

Figure 2.27: Verification at the sub-minute level of the timing alignment reported by the housekeeping electronics.

2.4 Magnetic Shielding

Because the SQUIDs used to amplify detector signals are essentially highly sensitive magnetometers, instruments such as TIME require significant magnetic shielding both at the DC and AC level for proper operation [74, 95]. Below I present magnetic shielding simulations carried out with COMSOL 5.2a.

Cryostat Level

TIME uses a high-μ open-ended cylinder as its first stage of magnetic shielding. The shield sits just within the 300K vacuum jacket, facing the 50K shield. It has a length of 150 cm, a radius of 69 cm, and wall thickness of 1.57 mm; it is made from Amuneal Amumetal with an advertised $\mu_r = 60000$ at 300K in 0.5 μT magnetic fields [6]. The detector modules and first stage SQUID boards are roughly centered within this shield with their normal axis orthogonal to the central axis of the shield. A Mag-03MC1000 three-axis magnetic field sensor was used to measure the suppression of Earth's field, and is compared to COMSOL simulations in Fig. 2.28.

Module Level

As shown in Fig. 2.29, the first stage of SQUIDs are mounted on ceramic carriers that attach to a printed circuit board. The board is housed inside of a superconducting aluminum shield (mounted off of the 250 mK stage, which does not rise above the transition temperature of aluminum during typical fridge cycles due to the continuous 350 mK stage). This superconducting layer is used primarily to reject AC magnetic fields; DC fields not attenuated by the high-μ 300K shield have the potential to become pinned as the aluminum passes through its transition temperature, but they should not modulate as the telescope moves. Ideally, the superconducting shield surrounding the SQUIDs would be continuous and without holes. In practice, we require large cutouts for the connectors and flex-circuits. Initial simulations showed significant magnetic field ingress originating near these cutouts. To draw the magnetic field away from the openings in the superconducting shield, we mount a 1 mm thick plate of high-permeability (high-μ) metal on the non-continuous faces; these plates are represented in magenta in Fig. 2.29.

To approximate superconducting shielding I apply magnetic insulation to all superconducting model surfaces and choose $\mu_r = 10^{-5}$. I model the high-mu

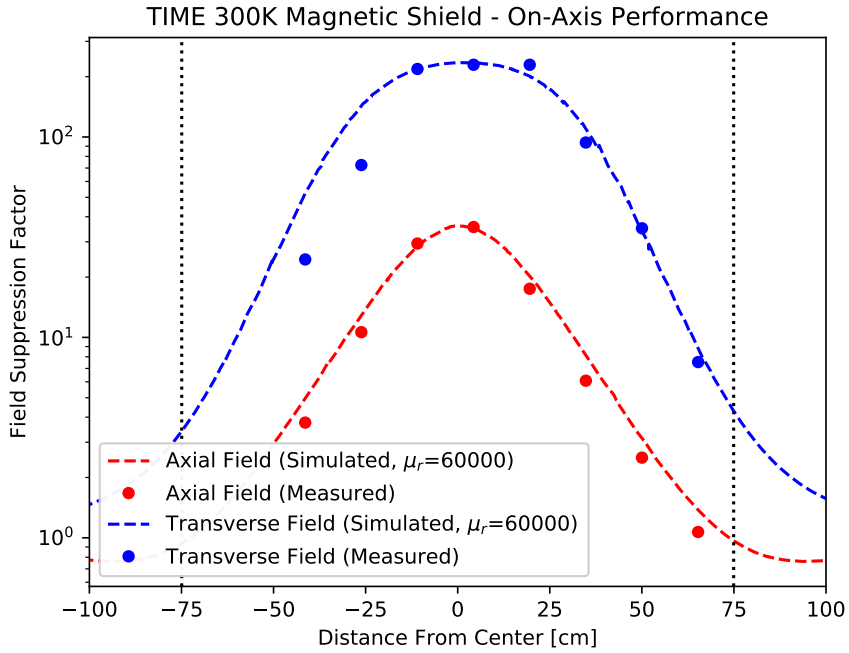

Figure 2.28: Measurements of the TIME high-μ over-shield compared to COMSOL simulations with $\mu_r = 60000$. *Reprinted by permission from Springer Nature: Hunacek et al. J Low Temp Phys [50], © 2018*

material with $\mu_r = 52000$, which corresponds to low temperature Amuneal A4K [92]. The simulation mesh was composed of 3.7 million elements for the results presented here. Fig. 2.30 shows the residual magnetic for three different orientations of the input field; only the component of the magnetic field normal to the plane of the SQUIDs is reported, as the SQUIDs are not sensitive to transverse fields. Residual field intrusion at the connector ports is evident, but the SQUIDs are mounted far enough from the edge that it is not an issue. The field suppression factor along the length of a single multiplexing column (three linear arrays of 11 SQUID channels) for an axial input field is shown in Fig. 2.31. Suppression factors (assuming only the module-level shield) exceed 5000 for all SQUID positions. Additionally, Fig. 2.31 demonstrates the order of magnitude reduction in the shielding factor if the high-μ cover plates are removed.

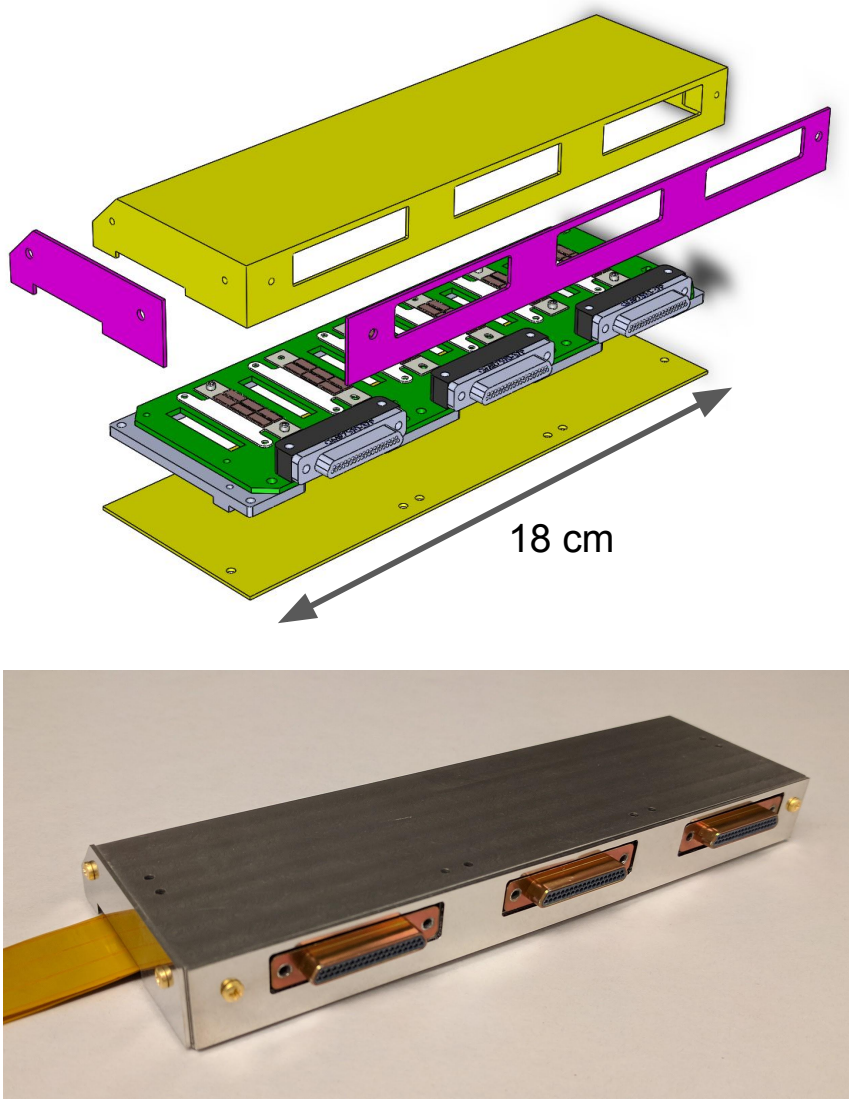

Figure 2.29: *Top:* An exploded render of a TIME SQUID board housing. Superconducting material (Al) is shown in yellow and high-μ metal (A4K) is shown in magenta. *Bottom:* One of 12 TIME SQUID boards. *Reprinted by permission from Springer Nature: Hunacek et al. J Low Temp Phys [50], © 2018*

SQUID Series-Array Level

The SQUID series arrays (SSAs) are located on the 4K stage, outside of the focal plane magnetic shielding. Sets of eight SSAs (corresponding to eight multiplexing columns) are packaged by NIST in a niobium enclosure (shown in Fig. 2.17), which acts as a superconducting magnetic shield at these temperatures. To supplement this, we wrap the enclosure in ten layers of high-

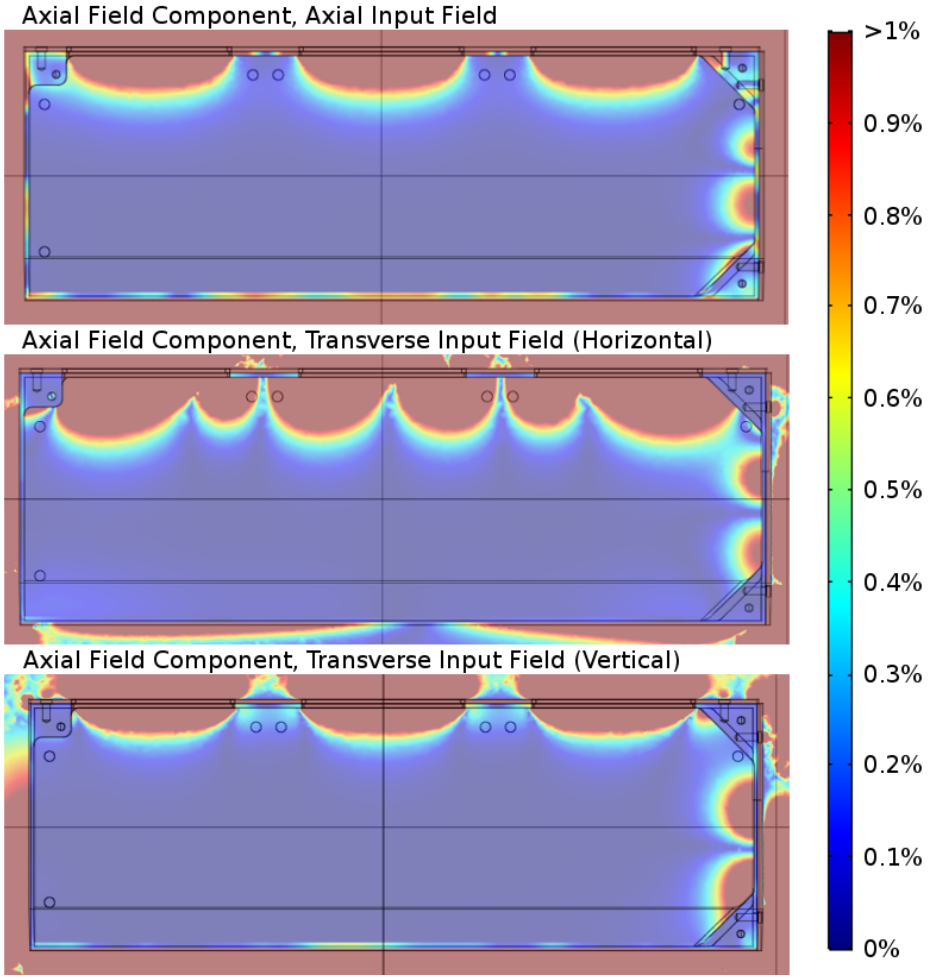

Figure 2.30: COMSOL simulations of the magnetic field suppression of the first stage SQUID board enclosure (superconducting box with high-μ connector plates). The axial component of the magnetic field in the plane of the SQUIDs is shown. The three connector holes are located at the top in this view, and the entrance for the superconducting flex-circuit is on the right. *Reprinted by permission from Springer Nature: Hunacek et al. J Low Temp Phys [50], © 2018*

permeability (high-μ) metal foil, as shown in Fig. 2.16.

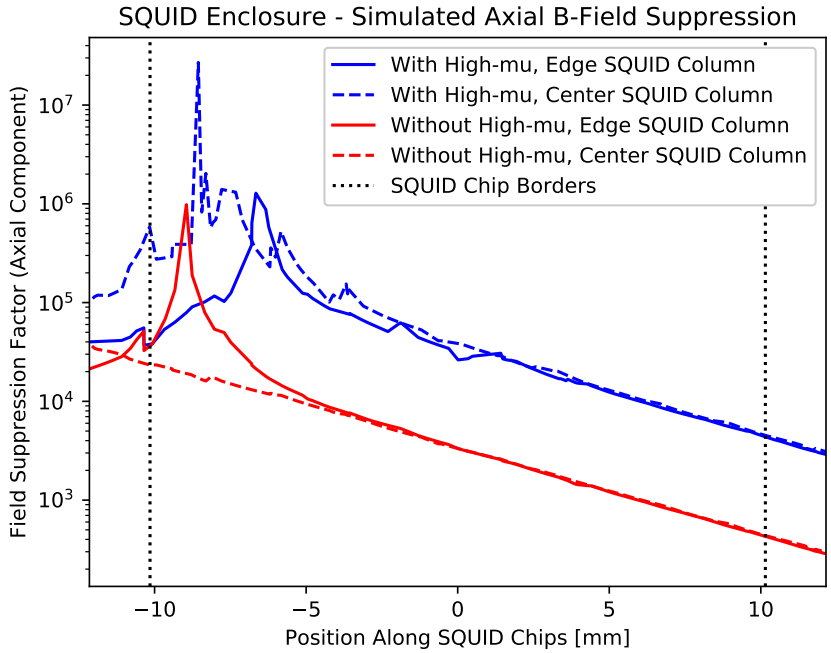

Figure 2.31: COMSOL simulations of the magnetic field suppression of the first stage SQUID board enclosure along the SQUID chips. The addition of high-μ connector plates (shown in magenta in Fig. 2.29) increases field suppression by a factor of 10. *Reprinted by permission from Springer Nature: Hunacek et al. J Low Temp Phys [50], © 2018*

2.5 Optics and Filter Stack

Thermal Simulations

In this section I simulate the TIME thermal filter stack being implemented after the first engineering run (cryogenic issues in late 2018 led to the use of very thick absorptive filters initially). Based on the heritage of the BICEP/Keck program [5, 95, 104], I consider absorptive polytetrafluoroethylene (PTFE), high-density polyethylene (HDPE), and nylon thermal filters in the optical path at various temperature interfaces. At low temperatures we consider reflective low-pass edge (LPE) metal mesh filters as a lower-loss supplement or replacement for nylon filters. At high temperatures we consider a radiatively-coupled multi-layer foam filter stack, which is transparent in-band but strongly absorptive in the IR [4, 25]; 0.125 inch sheets of Flextech LD24 are chosen based on reported spectral properties [103].

I define the filter stack model as a list of elements each with at most one state

variable. In the case of a floating-temperature filter in radiative equilibrium (such as the LD24 foam stack filter), that variable is a single temperature which is assumed to be uniform across the surface and unrelated to the temperature at its base (it is thermally isolated). For a plastic absorptive/conductive filter (PTFE, HDPE, or nylon), the state variable is the fraction of the total absorbed power that is conducted away instead of re-radiated. Reflective filters (used only at the IC stage in this model) have no state variable, and reflected power is assumed to provide negligible contributions to the overall power balance when computing state variables. Beginning with a simple guess for each state variable, I compute the power balance for each element (updating state values as needed) and iterate until all state variables converge. For a floating radiative filter, the temperature for iteration n is computed to balance the power absorbed from the preceding (nominally hotter) filter's output in iteration n and the power absorbed from the following (nominally colder) filter's back-radiation from iteration $n-1$. The process is similar for a conductive filter, except that for each global iteration the conducted power fraction is varied iteratively (locally) to balance absorbed, radiated, and conducted power. For a given conducted power, the radial temperature profile of the filter is computed (ex: Fig. 2.35) from the temperature-dependent thermal conductivity of the material. The base of the filter is at fixed temperature regardless of power flow, and input power is assumed to be uniformly distributed across the filter (the power conducted between adjacent radial elements approaches 0 at the center of the filter, and is maximal at the edge). The total filter emission is computed as the sum of emission from each of the radial elements (at different temperatures) weighted by surface area. Global iteration continues until convergence is achieved, defined as the point where the integrated output radiation at each filter element has changed by less than a chosen fraction of the previous iteration (Fig. 2.36).

Temperature-dependent thermal conductivity for PTFE and nylon are taken from the NIST cryogenic materials database [69]; for HDPE low-temperature data from the literature [20] is supplemented with known room temperature values [1]. For consistency with previous work I assume absorption in PTFE (Fig. 2.32) and nylon (Fig. 2.33) follows Halpern 1986 [45] (even though nylon in this paper is suspect). For reference only I compare these results with a best fit to data from the literature [31, 52, 61, 78]. HDPE (Fig. 2.32), being unavailable in Halpern, is taken from a fit to the Lamb data points [61].

Transmission in LD24 foam (Fig. 2.34) is extracted from data presented by the BICEP team [103]; I extrapolate by fitting a separate power law to the absorption coefficient near each end (in the formalism of Halpern 1986 [45]).

Fig. 2.37 and Fig. 2.38 show the results for the chosen filter stack: a 15-layer LD24 foam filter and two 0.5 cm PTFE filters at the 50K stage, a 0.5 cm PTFE filter and a 12 icm metal mesh LPE filter at the 4K stage, a 1K HDPE filter/lens at the 1K stage, and two metal mesh LPE filters of different cutoffs (to reduce high frequency leakage) at the IC stage. Note that the edge temperatures of the two PTFE filters at the 50K stage differ; the warm-side filter in this design conducts power through the 50K shield body with an expected edge temperature of 95K, while the cold-side filter conducts through an independent copper heat strap to the pulse tube head with an expected edge temperature of 75K. The load absorbed at 4K is strongly dependent on the center temperatures of the 50K filters, and using a pair of 0.5 cm PTFE filters instead of a single 1.0 cm filter results in lower loading on the 4K stage (due to the finite thermal conductivity of the available heat paths). The load absorbed at 1K is dominated by transmission through 4K, not the temperature at the base of the 4K optics. Due to its shallow absorption slope a thick filter with high in-band loss would be required to shield 1K with PTFE alone. A thin (< 1 mm) nylon filter at the cold side of the 4K stage can provide adequate shielding for the 1K stage (a few milliwatts absorbed at 1K), but a 12 icm metal mesh filter provides an order of magnitude better shielding at 1K with comparable in-band loss.

The column headers presented in Fig. 2.38 are described below. Energy is conserved when the cold and warm side absorption matches the conducted power plus the two-sided emission. Note that the final power out of the IC stage into the UC stage (dominated by in-band transmission from 300K) is high due to the overly-conservative assumption of 2π steradians coupling between each stage; the actual power absorbed on the UC will be a fraction of this and is not the focus of these particular results.

- *Element Name*: The name of the element, including the temperature stage, material, and thickness if relevant.
- *Center Temperature*: The temperature at the center of the element. For conductive filters, this is the peak of the computed radial temperature

profile. For reflective filters, this is the same as the edge temperature. For radiative filters, this is the equilibrium temperature (uniform across the filter).

- *Edge Temperature*: The temperature at the edge of the element. For conductive/reflective filters, this is set by the temperature at the mounting point. For radiative filters, this is floating and equal to the center temperature.
- *Absorption (Warm Side)*: The absorbed emission from the previous (hotter) filter over 2π sr (not the net absorption, the back-emission is accounted for separately).
- *Absorption (Cold Side)*: The absorbed emission from the next (colder) filter over 2π sr
- *Conducted Power*: The net power absorbed and conducted away at all frequencies by the filter, accounting for absorption and emission from adjacent filters.
- *Transmitted*: The total power that was incident on this element from elements further up the chain that is neither absorbed or reflected by this element.
- *Emission (One Side)*: Defined here as the single-sided thermal emission into 2π sr from the element itself as seen by a lower 0K element (this is not the net power flow).

Anti-reflection Coatings

The PTFE thermal filters and HDPE lens used for TIME are AR coated at both interfaces with a single layer of 0.25 mm Porex PM23DR expanded PTFE attached with a thin melted LDPE layer. Fig. 2.39 shows the transmission across the band for many realizations assuming $\sigma = 5\%$ Gaussian random fluctuations in the material index and thickness. Alternate coating schemes using dual-layer AR coatings are shown in Fig. 2.40 and Fig. 2.41, which do not perform well enough to justify the added complexity and which may be more sensitive to material property variation.

Warm Optics

The warm optics for TIME were designed for the Arizona Radio Observatory 12m ALMA Prototype Antenna (APA) at Kitt Peak in southern Arizona

(Fig. 2.42). Six room-temperature aluminum coupling mirrors are installed in the Cassegrain focus cabin for TIME, three of which form a K-mirror used as a field rotator. Mirror alignment is achieved with a laser tracking system. TIME's linear focal plane of 16 spatial pixels maps to an instantaneous field of view spanning 14 by 0.43 arcmin near the center of the band.

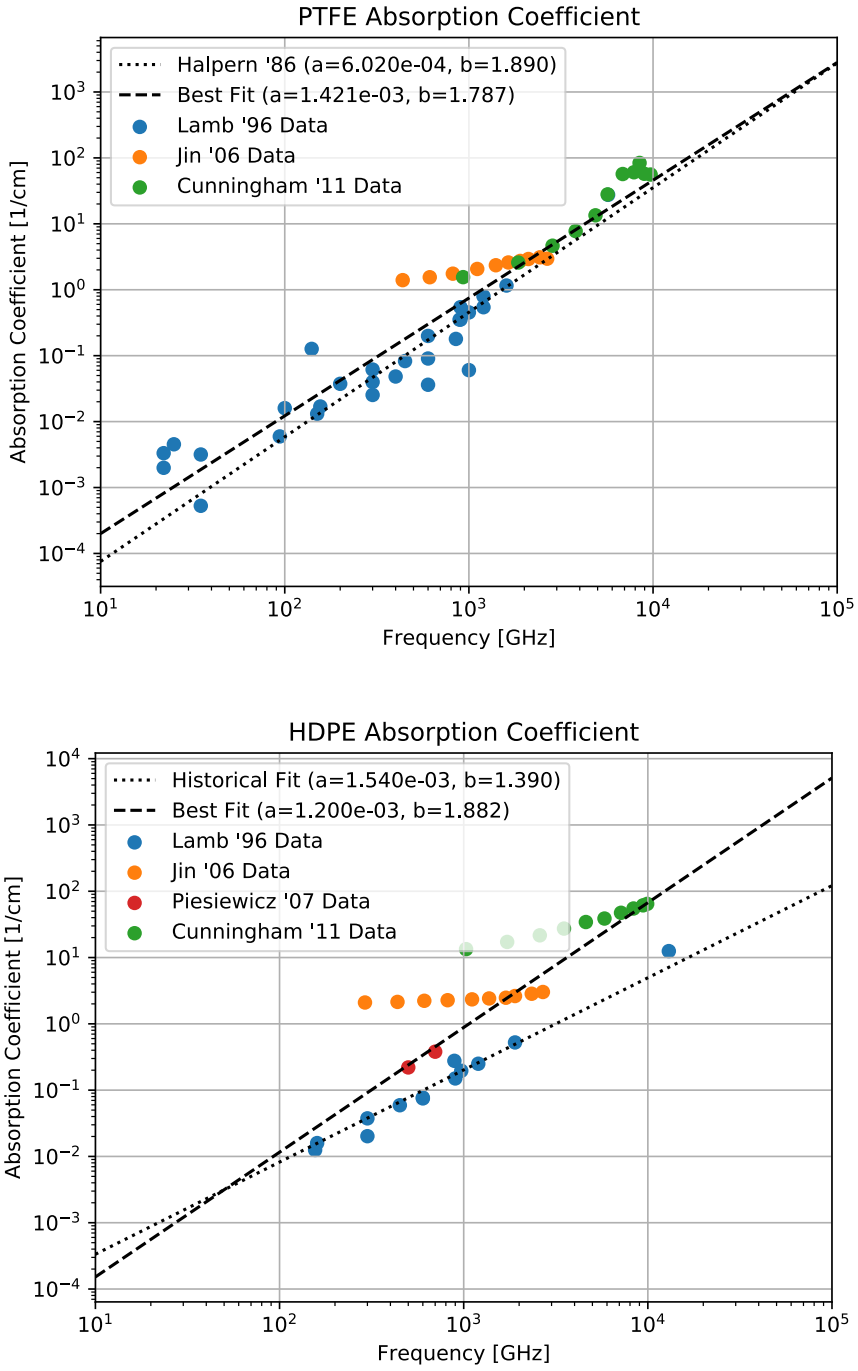

Figure 2.32: Measurements of the absorption coefficient for polytetrafluoroethylene (PTFE) and high-density polyethylene (HDPE) from the literature [31, 52, 61, 78] are presented, along with a best fit using the parameterization presented in Halpern 1986 [45]. For consistency with previous TIME calculations, I choose as my fiducial model the Halpern results for PTFE and a fit to the Lamb data (labeled Historical Fit) for HDPE.

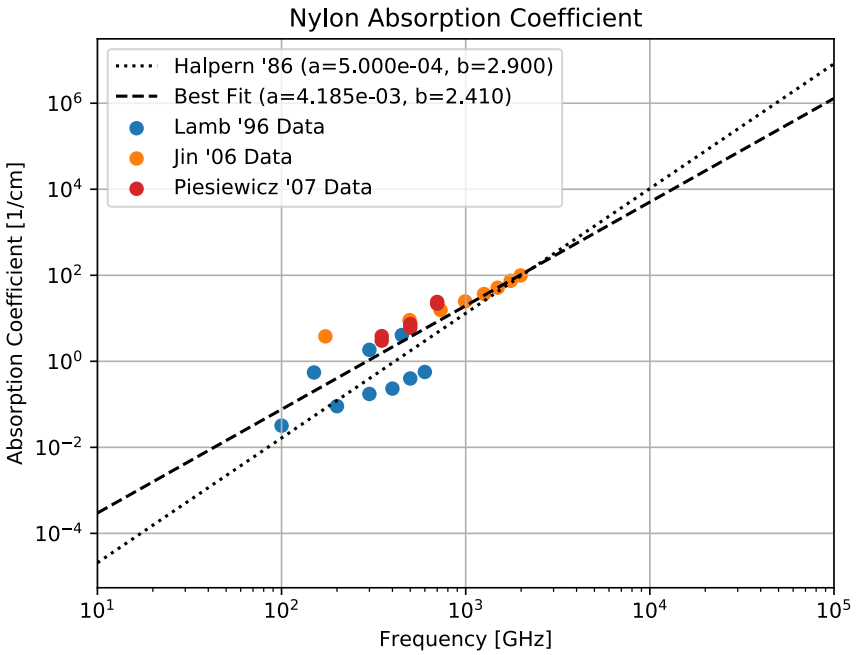

Figure 2.33: Measurements of the absorption coefficient for nylon from the literature [52, 61, 78] are presented, along with a best fit using the parameterization presented in Halpern 1986 [45]. For consistency with previous TIME calculations, the parameter results provided in Halpern are used directly instead of this new fit.

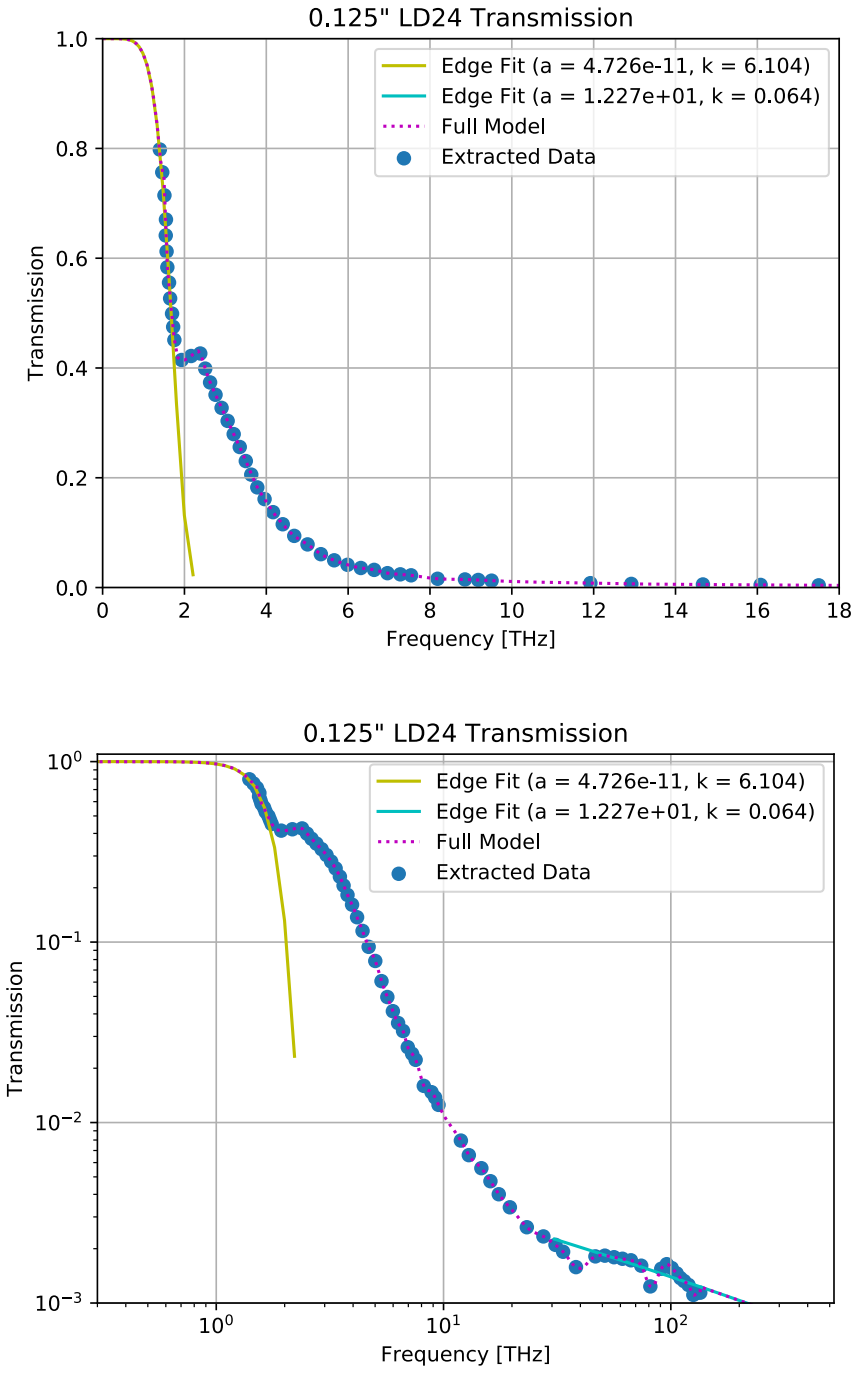

Figure 2.34: Transmission in LD24 foam is extracted from data presented by the BICEP team [103]; I extrapolate by fitting a separate power law to the absorption coefficient near each end (in the formalism of Halpern 1986 [45]).

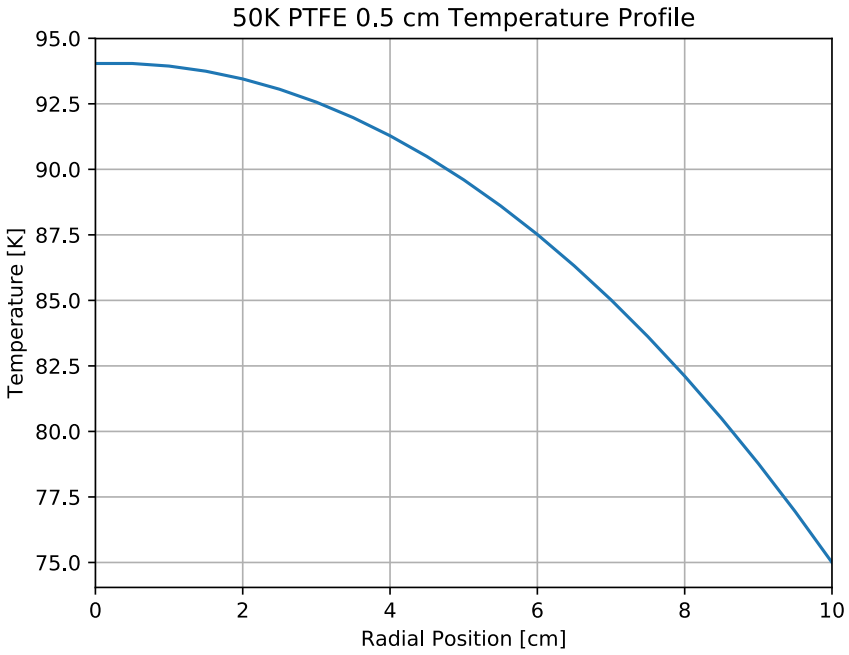

Figure 2.35: A sample temperature profile computed for a PTFE filter from a given conducted power and a temperature-dependent thermal conductivity.

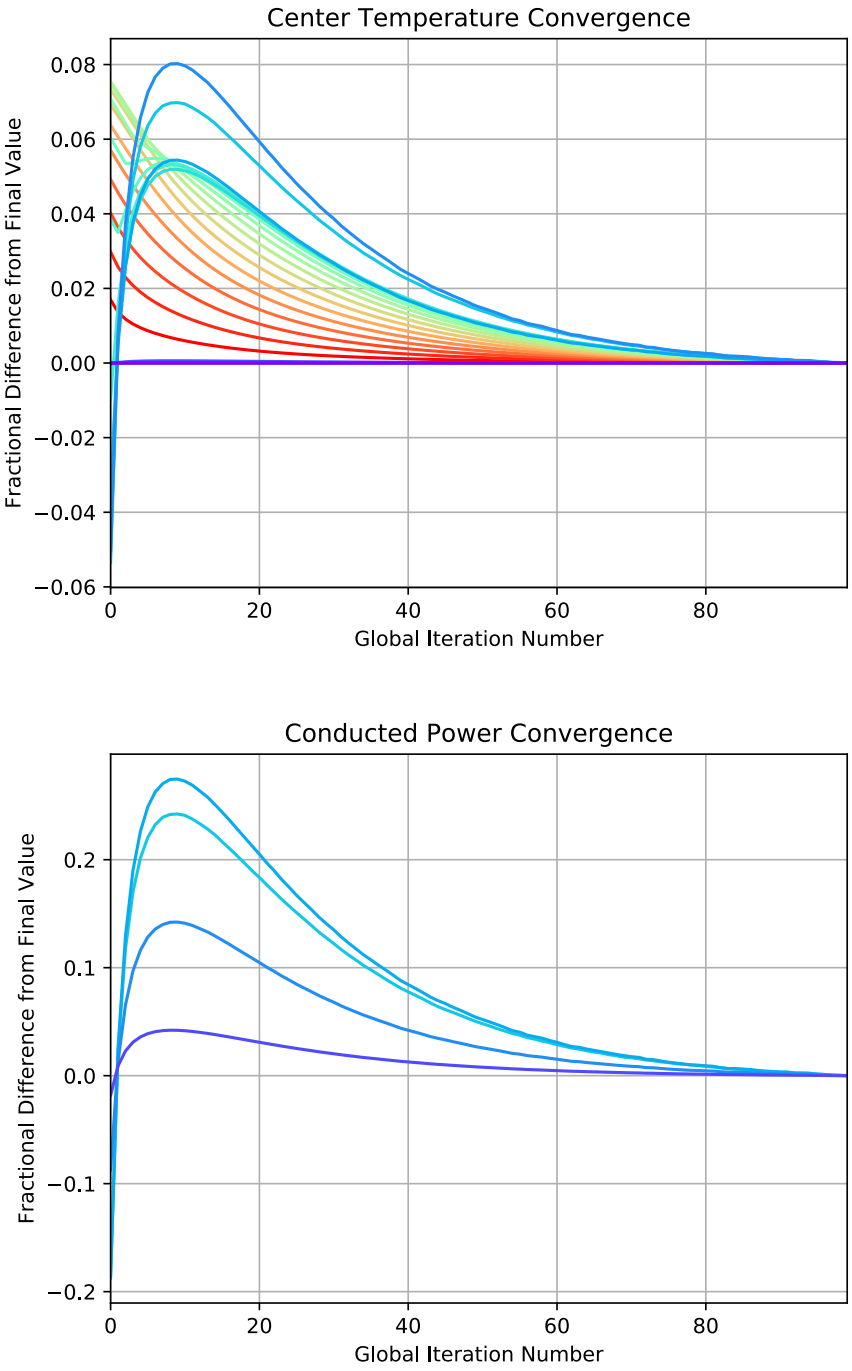

Figure 2.36: Sample convergence metrics for one instance of the filter stack model. Each line represents the fractional deviation in temperature or conducted (absorbed) power for a single optical element from its final value.

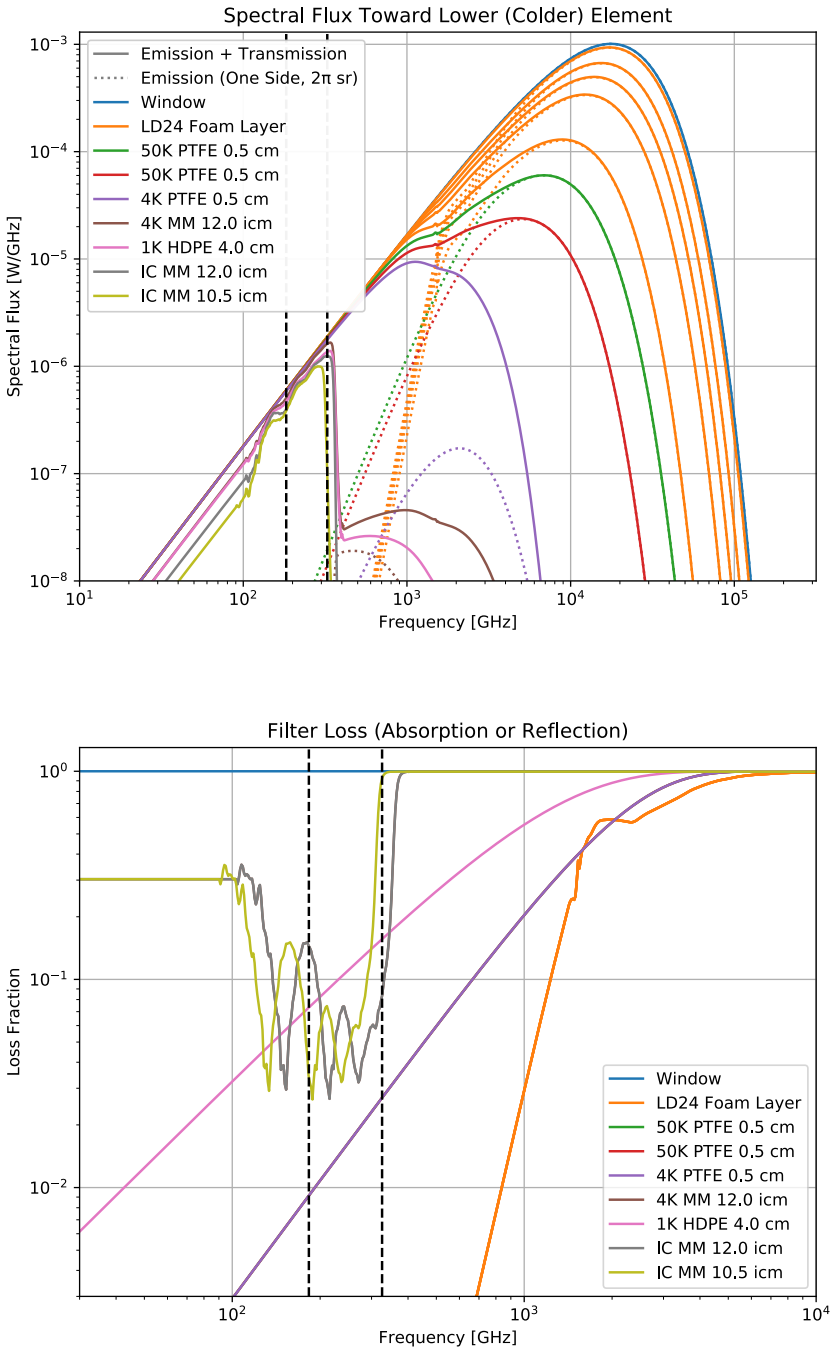

Figure 2.37: Simulation results for the nominal TIME filter stack design.

Element Name	Center Temperature	Edge Temperature	Absorption (Warm Side)	Absorption (Cold Side)	Conducted Power	Transmitted Power	Emission (One Side)
Window	300.0 K	300.0 K	0.000 uW	25.78 W	0.000 uW	0.000 uW	28.86 W
LD24 #1	292.4 K	292.4 K	28.58 W	22.99 W	0.000 uW	281.2 mW	25.78 W
LD24 #5	261.5 K	261.5 K	18.55 W	14.36 W	0.000 uW	228.8 mW	16.46 W
LD24 #8	236.8 K	236.8 K	12.72 W	9.336 W	0.000 uW	191.2 mW	11.03 W
LD24 #11	208.7 K	208.7 K	8.007 W	5.232 W	0.000 uW	154.2 mW	6.620 W
LD24 #15	151.1 K	151.1 K	2.937 W	0.633 W	0.000 uW	99.27 mW	1.785 W
50K PTFE 0.5 cm	135.0 K	95.00 K	1.848 W	174.6 mW	0.689 W	36.78 mW	0.667 W
50K PTFE 0.5 cm	94.04 K	75.00 K	0.675 W	287.6 uW	312.0 mW	28.34 mW	181.7 mW
4K PTFE 0.5 cm	29.04 K	8.000 K	189.6 mW	1.508 uW	188.8 mW	20.40 mW	0.434 mW
4K MM 12.0 icm	8.000 K	8.000 K	20.50 mW	0.001 uW	0.000 uW	0.329 mW	11.73 uW
1K HDPE 4.0 cm	2.029 K	2.000 K	100.7 uW	0.000 uW	100.7 uW	239.6 uW	0.004 uW
IC MM 12.0 icm	0.400 K	0.400 K	51.95 uW	0.000 uW	0.000 uW	187.6 uW	0.000 uW
IC MM 10.5 icm	0.400 K	0.400 K	61.64 uW	0.000 uW	0.000 uW	126.0 uW	0.000 uW

Figure 2.38: Simulation results for the nominal TIME filter stack design.

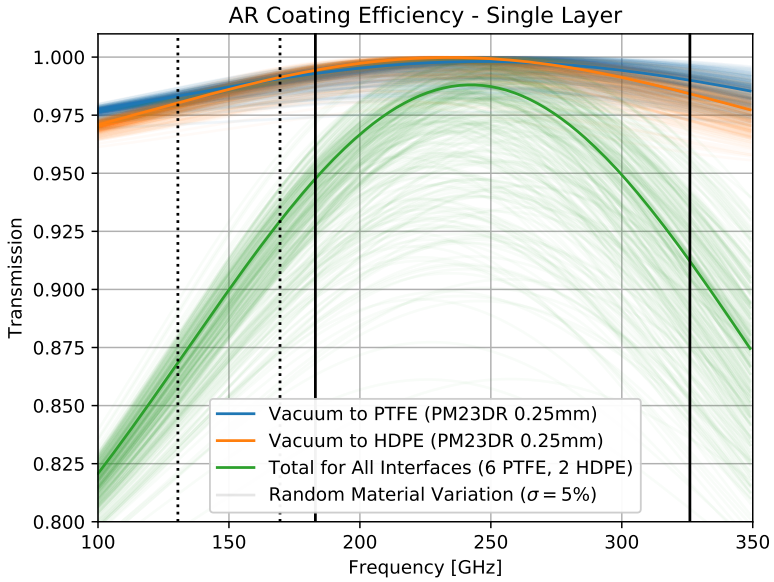

Figure 2.39: AR coating transmission using a single layer of 0.25 mm Porex PM23DR for both HDPE and PTFE interfaces. Dark solid lines show results for the nominal values of the refractive index and material thickness; faint solid lines show 300 realizations of Gaussian random perturbations in both material properties with a standard deviation $\sigma = 5\%$ of the nominal value.

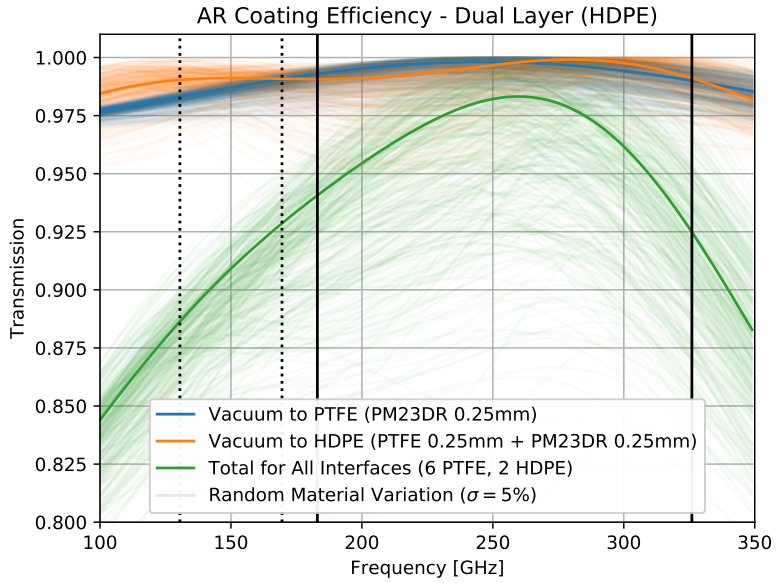

Figure 2.40: AR coating transmission using a single layer of 0.25 mm Porex PM23DR for PTFE interfaces and 0.25 mm Porex PM23DR plus 0.25 mm PTFE for HDPE interfaces.

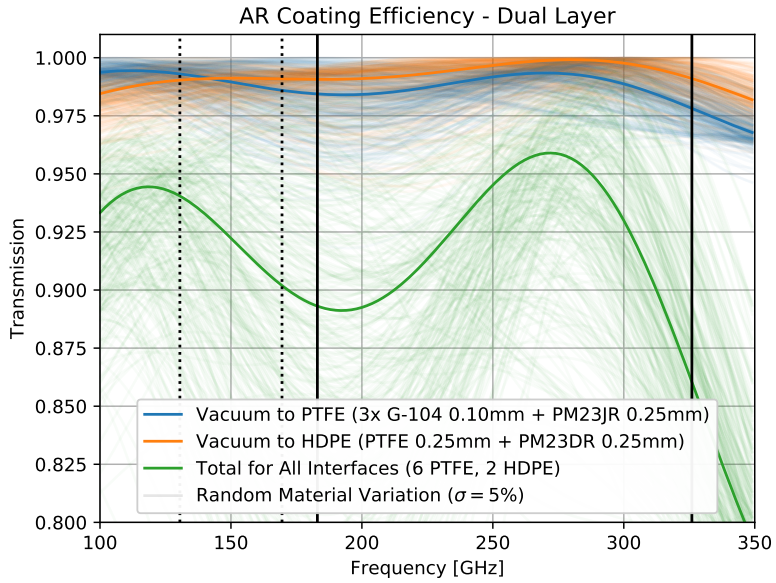

Figure 2.41: AR coating transmission using 0.25 mm Porex PM23DR plus 3 layers of 0.1 mm Zitex G-104 for PTFE interfaces and 0.25 mm Porex PM23DR plus 0.25 mm PTFE for HDPE interfaces.

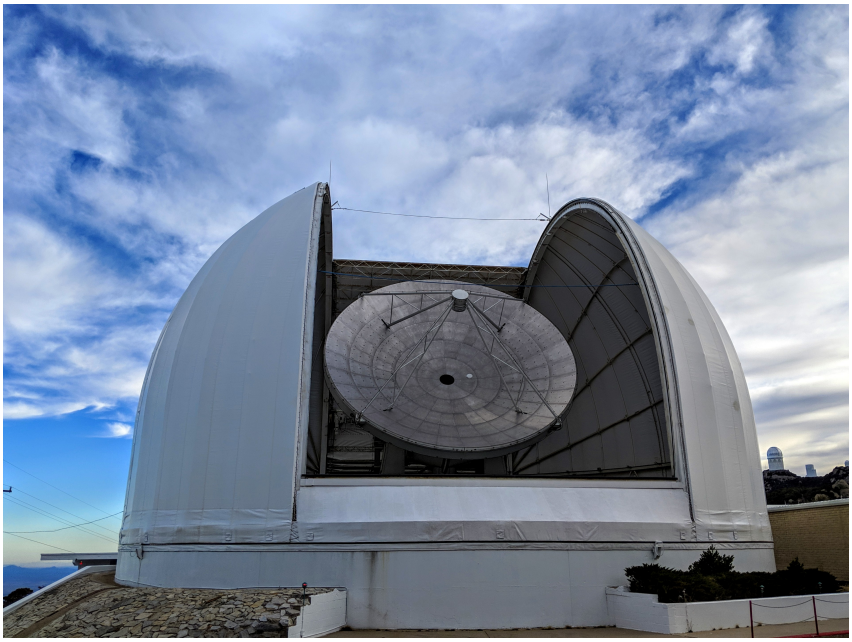

Figure 2.42: The Arizona Radio Observatory 12m ALMA Prototype Antenna (APA) at Kitt Peak in southern Arizona.

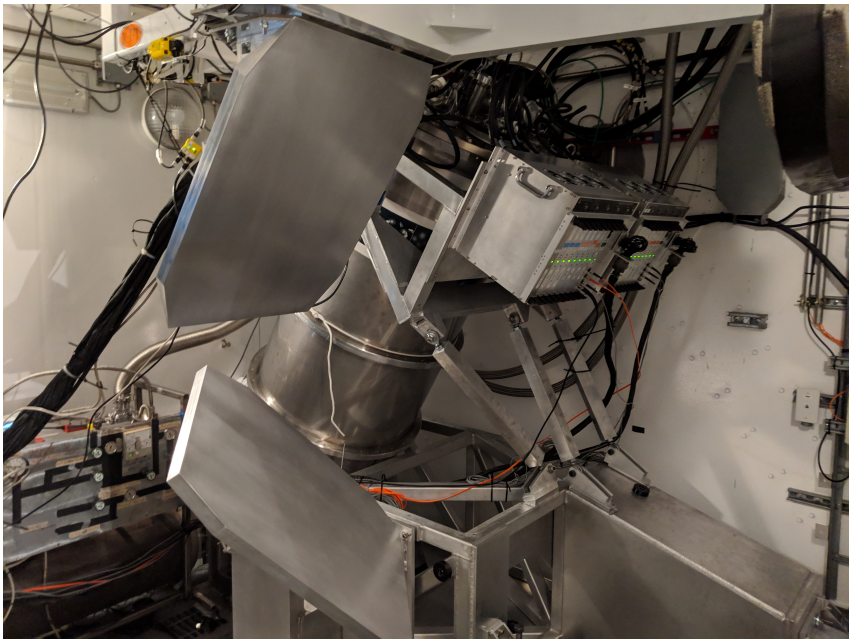

Figure 2.43: The TIME cryostat mounted in the receiver cabin of the ARO 12m at Kitt Peak. Six warm coupling mirrors (including a K-mirror for field rotation) are installed in the cabin.

2.6 Projected On-Sky Loading and Sensitivity

In this section I propagate an atmospheric model for Kitt Peak through the TIME optics chain to determine detector loading and on-sky sensitivity. The atmospheric model is produced by `am`, a radiative transfer tool developed by Scott Paine [76], and the assumed layer profile is the northern mid-latitude zonal average for Dec-Feb (derived from NASA MERRA-2 reanalysis and provided with `am`) truncated at the elevation of Kitt Peak. Water content has been scaled to match measured opacity values measured at the site by a 225 GHz tipper. As shown in Fig. 2.44 and 2.45, designing for a zenith τ of 0.13 allows us access to approximately 25% of the winter weather. Tracking the COSMOS field requires a zenith angle down to at least 50 degrees, so 50 degrees will be the assumed zenith angle for detector loading. A water scaling factor of 0.47 aligns the zenith opacity of the model at 225 GHz to $\tau = 0.13$. Comparable (25th percentile weather) models for Mauna Kea and the ALMA site profiles provided by `am` are presented in Fig. 2.46.

Each element in the simulated TIME optical chain allows different fractions of its incident power (representing absorption/scattering/spillover as a function of frequency) to terminate either on a blackbody or on the sky. The cumulative efficiency though each element is plotted in Fig. 2.47. Power in 10 MHz bins is computed from the spectral radiance and the etendue assuming diffraction limited beams. These 10 MHz bins are integrated and divided by two (accounting for polarization) to find the power in each spectral band. The thermal filter and optical stack assumed are as presented previously. Spectrometer grating illumination efficiency, blaze efficiency, and waveguide loss are interpolated from published values [65]. The primary mirror is assumed to have a 20 μm surface RMS (Ruze scattering to the sky), the secondary mirror 10 μm (to 300K), warm coupling mirrors K3/F1/P1 16 μm (to 300K), and warm coupling mirrors K1/K2/P2 10 μm (to 300K). Primary spillover is assumed to be 0.0002% to 300K, and secondary spillover 6.3% to the sky; all other mirrors are assumed to have 0.5% spillover to 300K. The 4K cold stop is assumed to have 22% spillover. A variable excess loss factor terminating at IC stage temperatures is included in the calculations; based on the measured optical efficiency shown in Fig. 5.23 for the alternate 2019 Kitt Peak optical stack, I chose an excess loss factor of 0.2 for the results presented here.

Fig. 2.49 shows the cumulative load seen at the detectors from each optical

element. Approximately a third of the load originates from the atmosphere, the largest single contributor. The sum of the room temperature mirrors accounts for slightly more than a third of the loading, indicating that mirror surface quality is particularly important for us. The largest source of loading within the cryostat is the Zotefoam window. Fig. 2.50 shows the Rayleigh-Jeans temperature of the atmosphere and warm mirrors normalized to a beam-filling black body in front of the cryostat; at the spectrometer mid-band we see a 50K load from the mirrors as simulated.

Fig. 2.51 shows the total channel loading expected from this model (0.5-1.5 pW). A TES saturation power target near 3 pW provides an adequate safety factor across the band while keeping phonon noise subdominant to photon noise. As shown in Fig. 2.52, higher saturation powers result in only modest increases in NEP while ensuring access to a variety of weather conditions and simplifying the constraints on device fabrication. Fig. 2.53 shows the expected TIME NEI and survey depth assuming 1000 hr at Kitt Peak. For comparison, I plot the projected performance for a similar instrument at the ALMA site with 3 (instead of 6) coupling mirrors in Fig. 2.54.

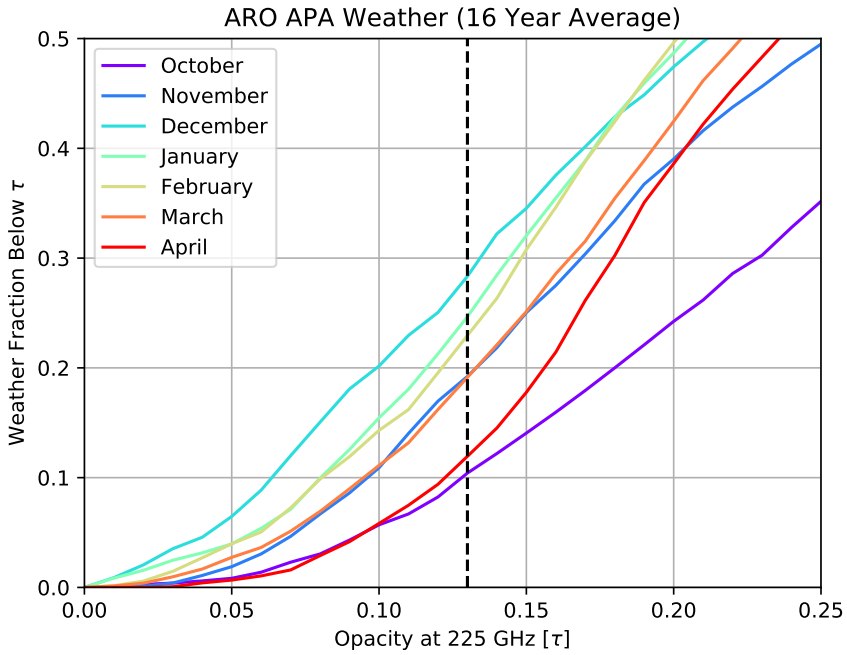

Figure 2.44: Weather statistics measured at the ARO 12m site at Kitt Peak with a 225 GHz tipper. TIME targets the best 25% of the winter weather.

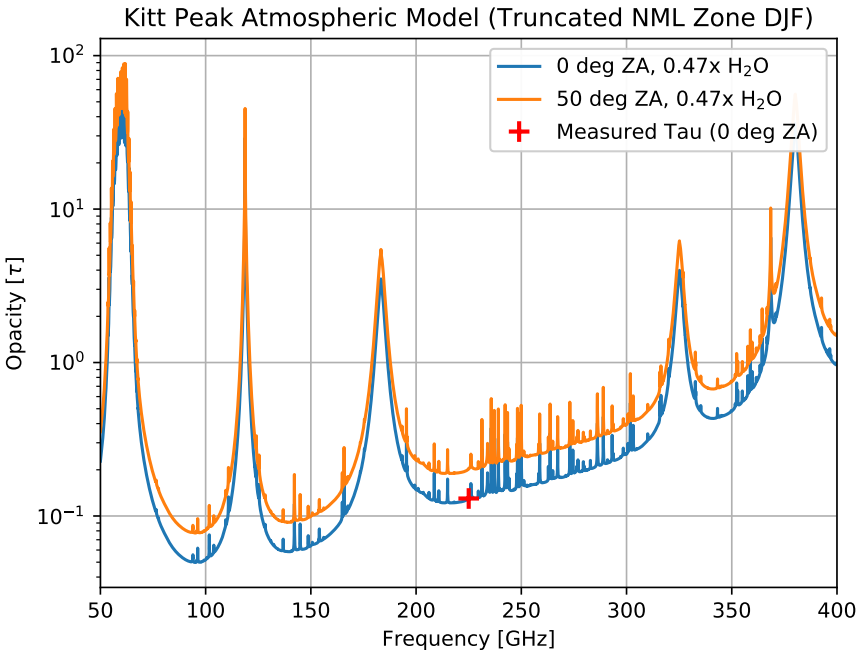

Figure 2.45: Atmospheric model for Kitt Peak with water vapor levels scaled to match the measured optical depth at 225 GHz.

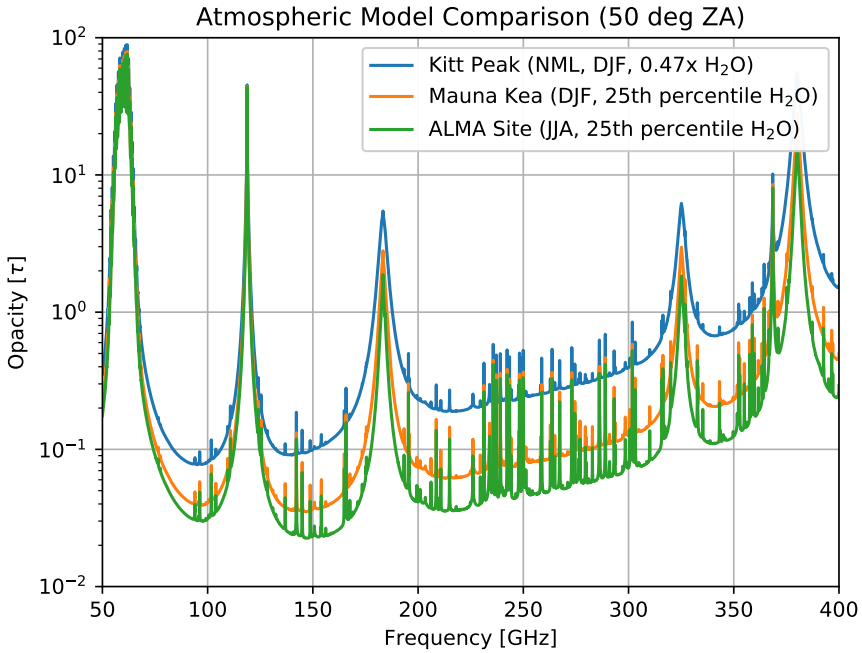

Figure 2.46: Fiducial atmospheric model comparisons for Kitt Peak, Mauna Kea, and the ALMA site.

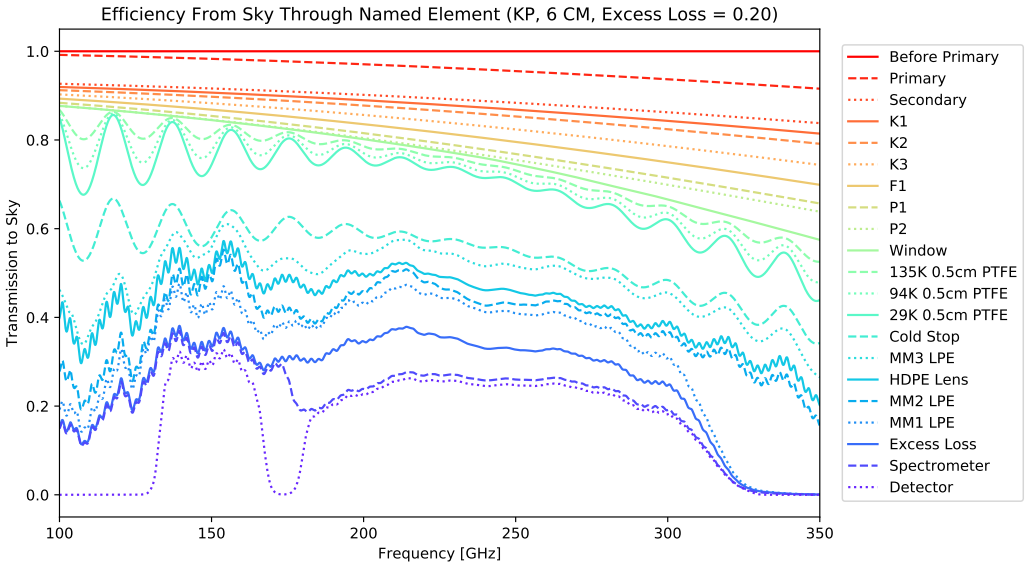

Figure 2.47: Cumulative efficiency at each element in the TIME optics model.

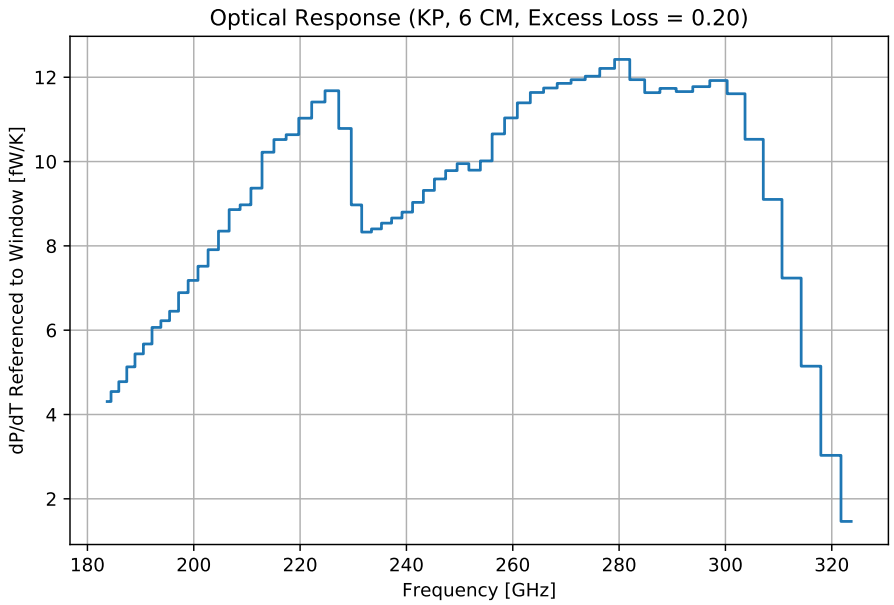

Figure 2.48: Expected detector optical response dP/dT referenced to front of the cryostat.

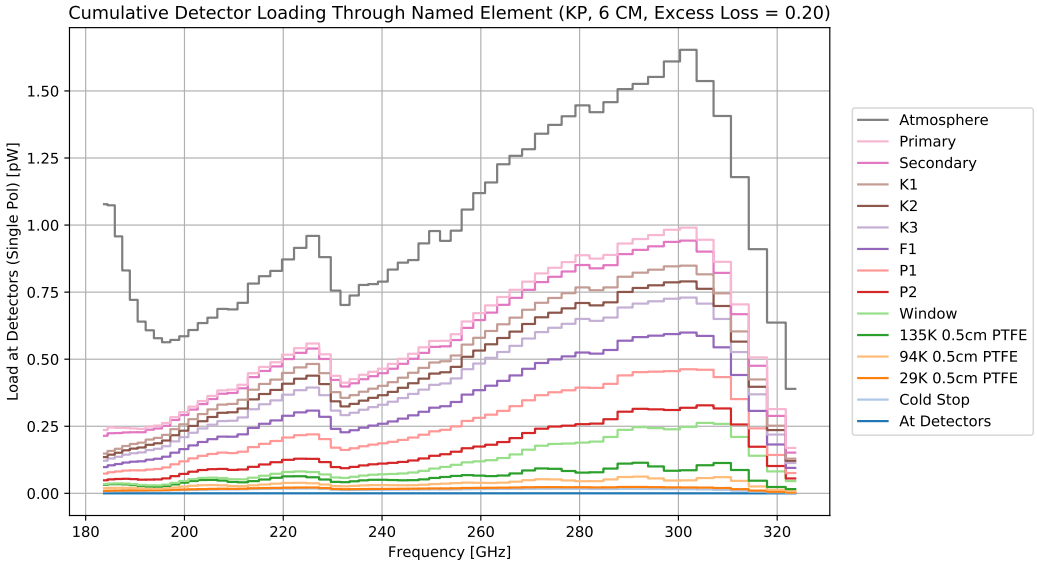

Figure 2.49: Cumulative detector loading from each element in the TIME optics model.

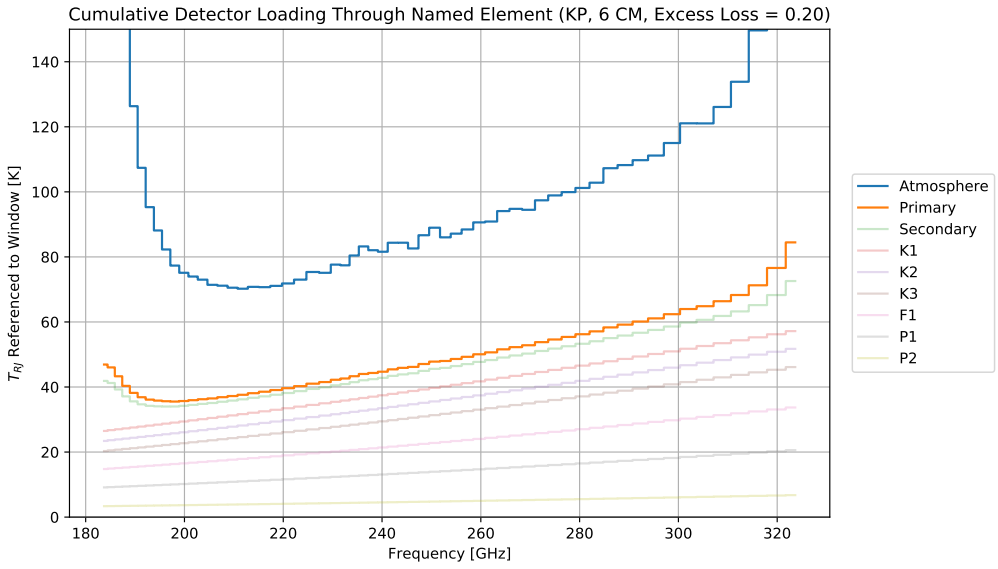

Figure 2.50: Cumulative detector loading temperature (referenced to a black body in front of the cryostat window) from each element in the TIME optics model.

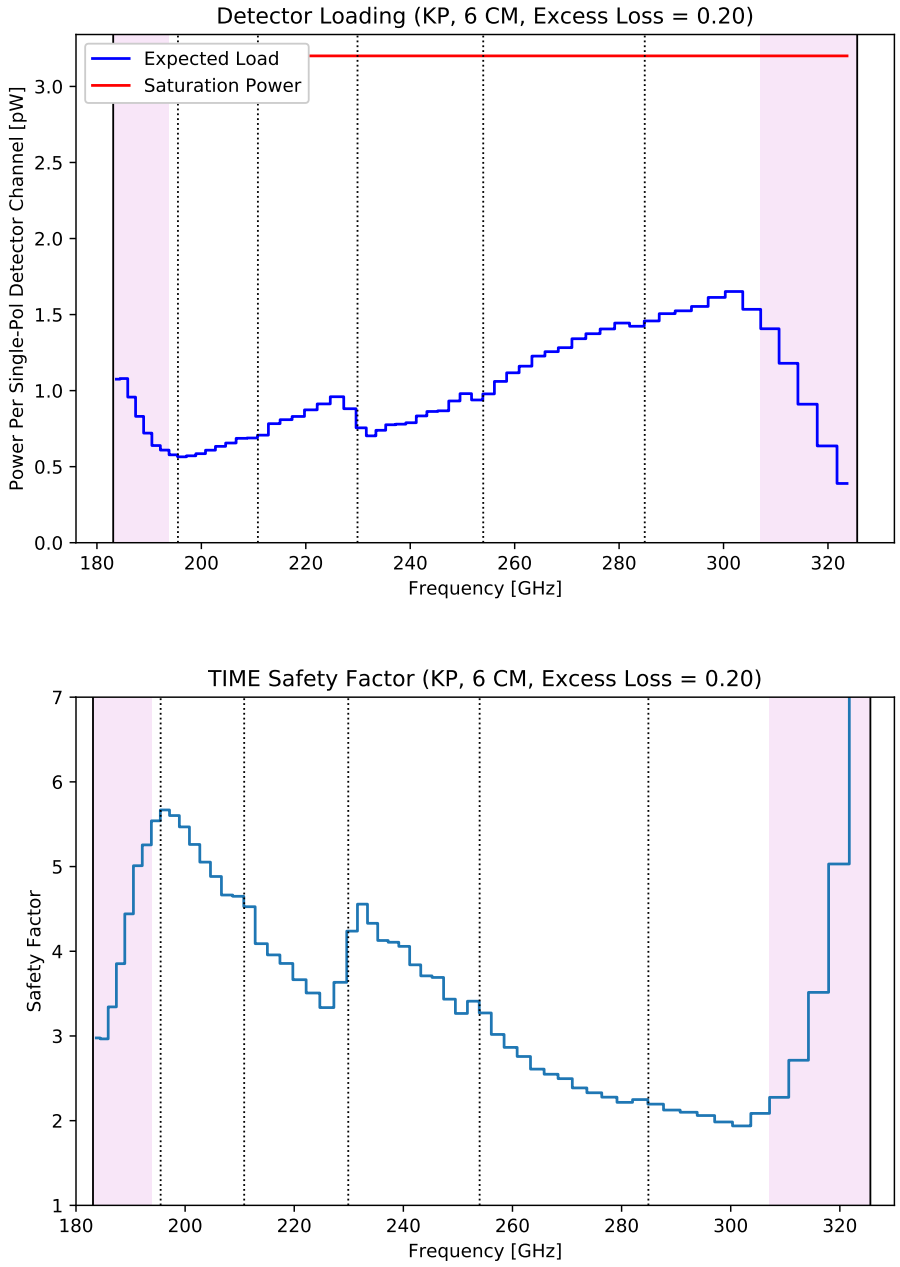

Figure 2.51: Projected total detector loading and safety factor for a fixed TES saturation power target. Natural scatter will occur between fabricated devices, so modules with higher saturation powers will be placed in the highest frequency position.

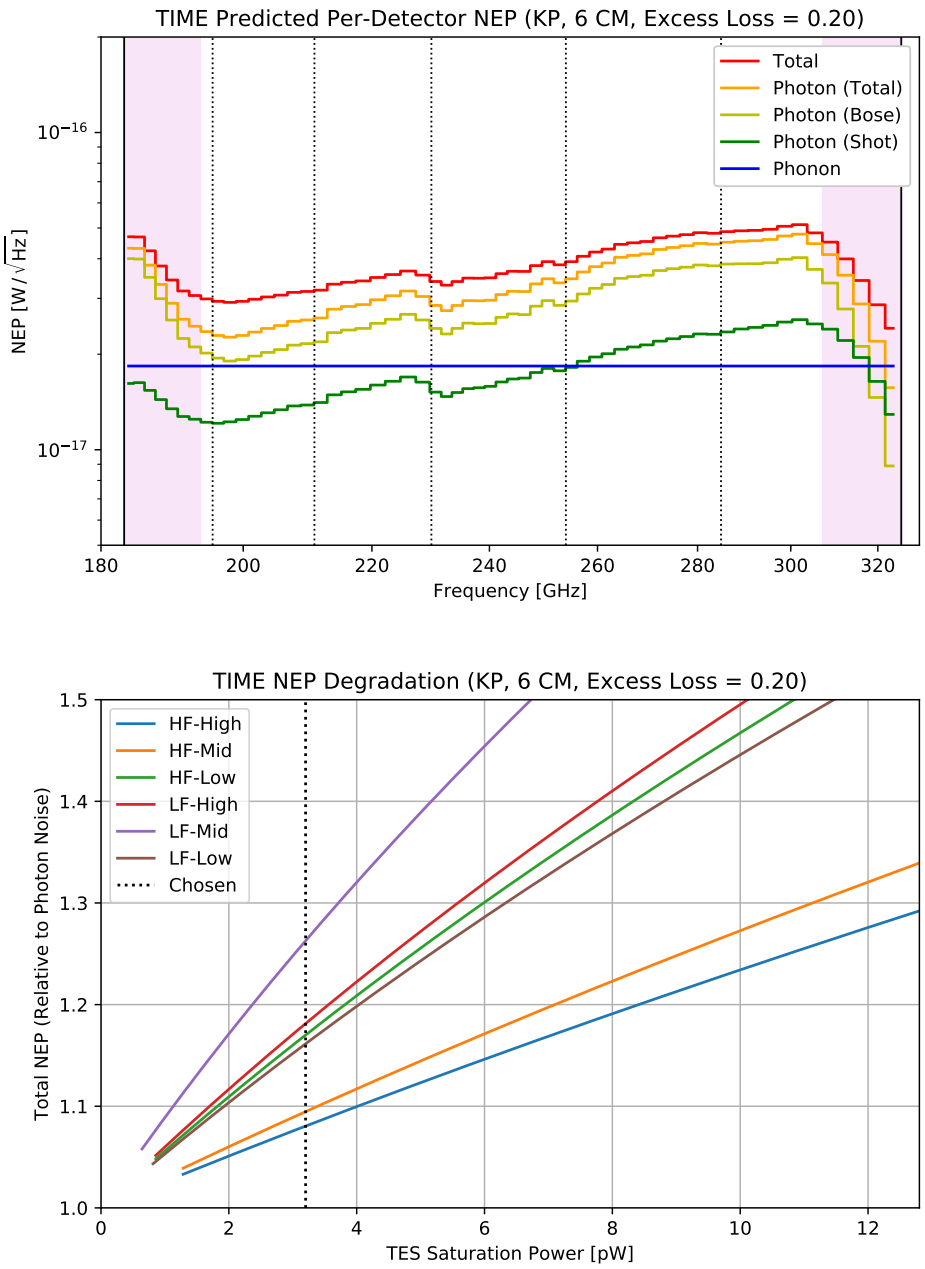

Figure 2.52: Projected total detector NEP and its degradation with increased TES saturation power.

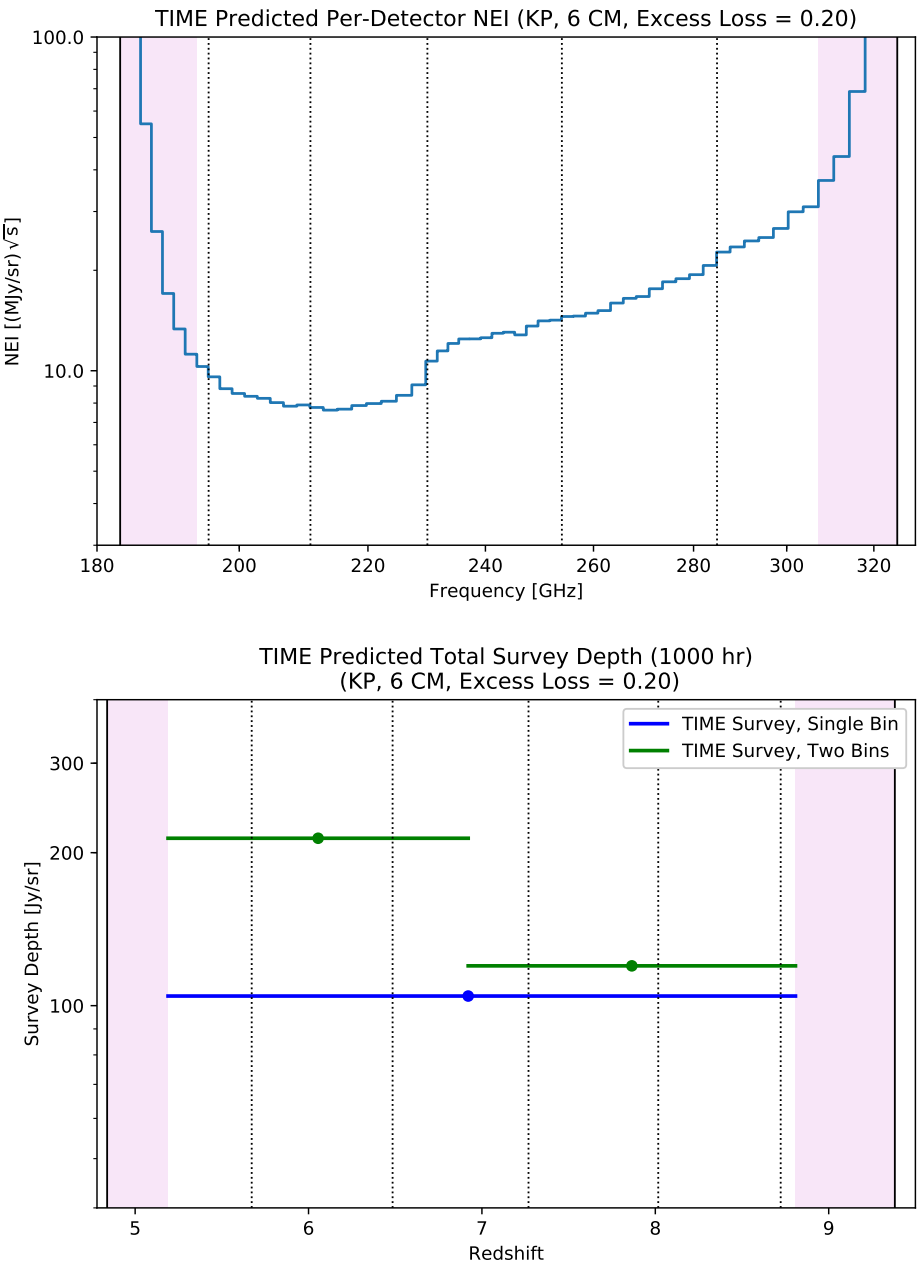

Figure 2.53: Total survey depth for 1000 hr at Kitt Peak using the optics model presented previously.

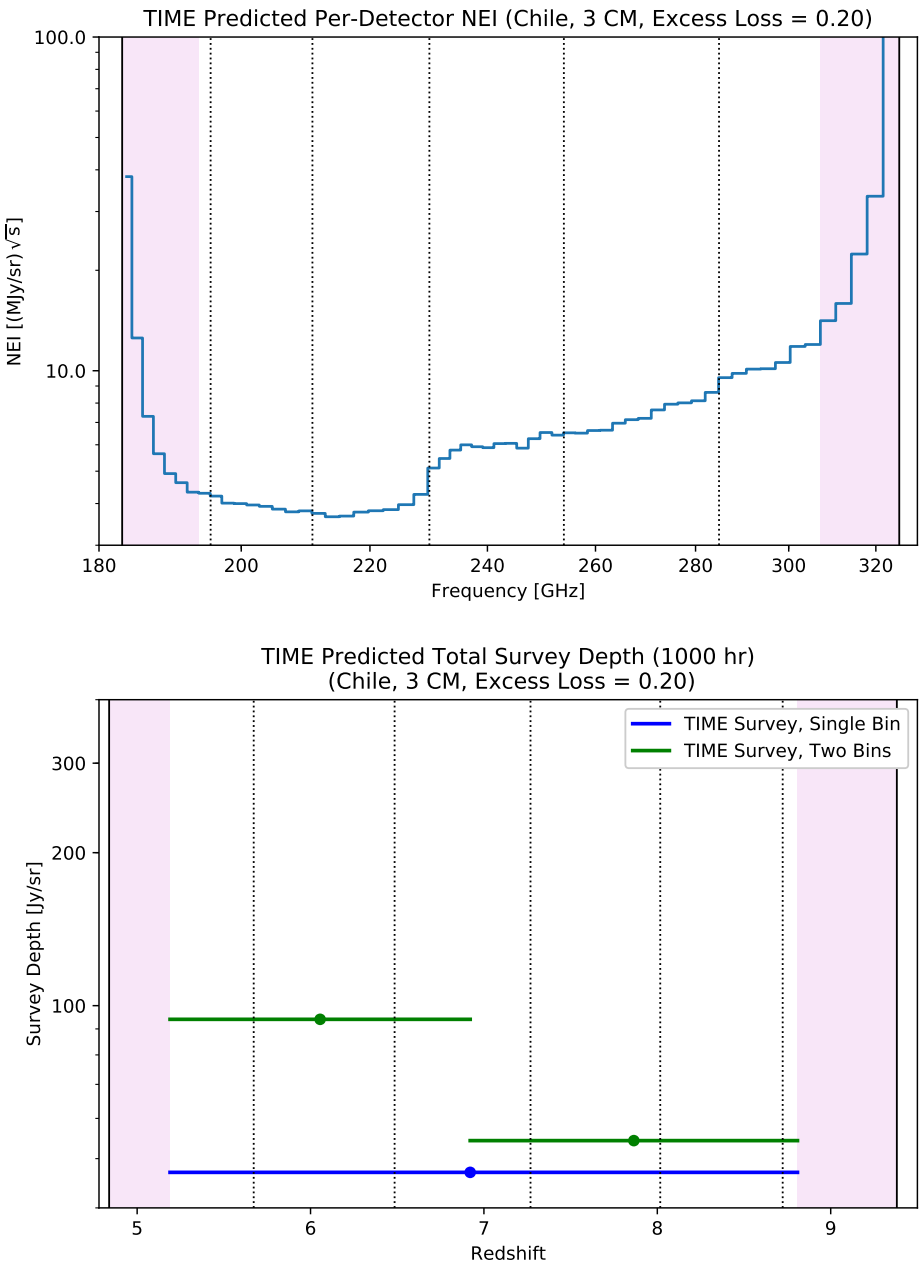

Figure 2.54: Total survey depth for 1000 hr at the ALMA site using a modified optics model with three fewer coupling mirrors.

Chapter 3

Detector Design and Modeling

3.1 Background

A bolometer measures the intensity of incident electromagnetic radiation by absorbing it as heat in a heat capacity C which is weakly thermally connected to a bath temperature T_{bath}. A measurable heat-dependent property change such as resistance or temperature is monitored as a proxy for the incident power. The simplified diagram in Fig. 3.1 shows a bolometer with temperature T absorbing incident radiation as heat ($P_{optical}$) as well as dissipating electrical power from a sensor bias line ($P_{electrical}$). In the steady state the sum of these two powers flows across the thermal link with thermal conductance G to the bath. TIME detectors use transition edge sensor (TES) bolometers [51], which use a film fixed at its superconducting transition temperature T_c by negative electrothermal feedback. Small changes in the incident optical power drive changes in the temperature and therefore in the sensor resistance, which for a fixed voltage bias results in an opposing change in bias power dissipated in the sensor without the need for active feedback. The changing current through the TES is monitored by the readout system and can be referred back to changes in the observed optical power.

As shown in Fig. 3.3 (left), our TES is placed in parallel with a small $3\,\mathrm{m}\Omega$ shunt resistor and fed with a constant bias current, approximating a purely voltage biased TES at the operating resistance ($R_{tes} \approx 30\,\mathrm{m}\Omega$). To simplify the calculations (without assuming the relative magnitudes of the relevant resistors), we can replace this bias circuit with its Thevenin equivalent: a bias voltage $V_{bias} \equiv I_{bias} R_{shunt}$ with a series resistor $R_{th} \equiv R_{shunt} + R_{series}$. Following the formalism used in Irwin and Hilton [51], I examine a TES model with current I, temperature T, and resistance R_{tes} described by the following differential equations:

$$\begin{aligned} P_{bias} + P_{optical} &= C\frac{\mathrm{d}T}{\mathrm{d}t} + P_{bath} \\ V_{bias} &= I\left(R_{th} + R_{tes}\right) + L\frac{\mathrm{d}I}{\mathrm{d}t} \end{aligned} \tag{3.1}$$

Note that in the Thevenin equivalent picture there is only one relevant current

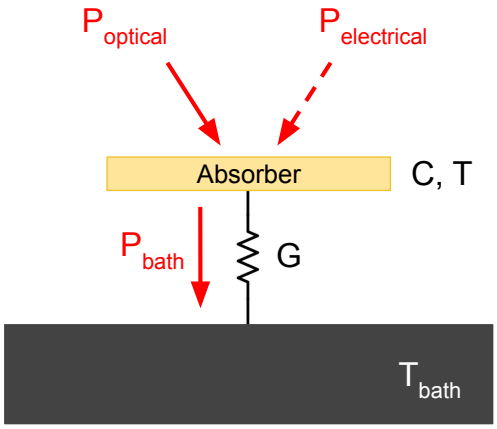

Figure 3.1: A diagram showing the basic configuration for a bolometer with heat capacity C, temperature T, and a thermal conductance to the bath G.

$I = I_{tes}$, we do not have a separate I_{bias}. In the small signal limit (again following Irwin and Hilton [51]) we assume the TES operates near steady state values for temperature $T_0 \approx T_c$, resistance $R_0 = R_{frac}R_n$, and current I_0:

$$\begin{aligned} I &\approx I_0 + \delta I \\ T &\approx T_0 + \delta T \\ R_{tes} &\approx R_0 + \delta R_{tes} \\ &= R_0 \left(1 + \alpha \frac{\delta T}{T_0} + \beta_I \frac{\delta I}{I_0}\right) \end{aligned} \tag{3.2}$$

The dimensionless temperature and current sensitivity parameters α and β_I describe the superconducting transition as follows. Note that β_I is distinct from the bolometer thermal conductance scaling exponent β.

$$\begin{aligned} \alpha &\equiv \frac{\partial \log R}{\partial \log T} = \frac{T_0}{R_0}\frac{\partial R}{\partial T} \\ \beta_I &\equiv \frac{\partial \log R}{\partial \log I} = \frac{I_0}{R_0}\frac{\partial R}{\partial I} \end{aligned} \tag{3.3}$$

The power flowing to the bath in the steady state is the sum of the bias and signal powers, allowing us to expand these as:

$$P_{optical} \approx P_{optical,0} + \delta P_{optical} \tag{3.4}$$

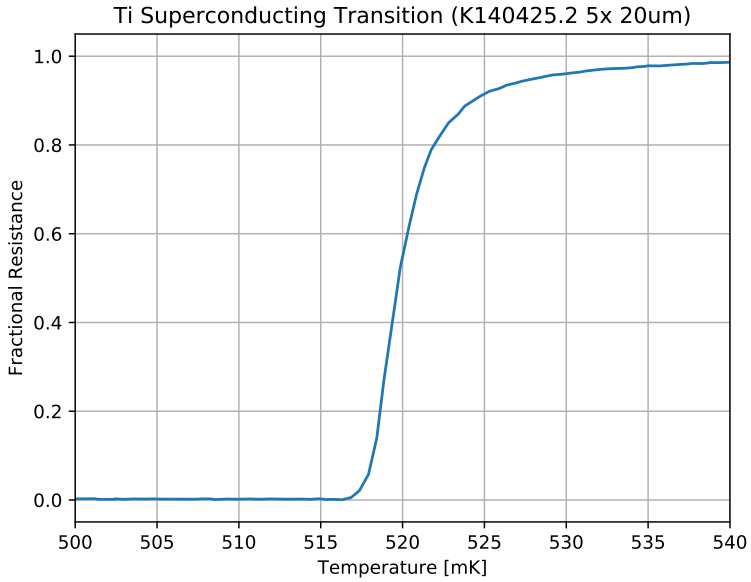

Figure 3.2: The measured superconducting transition of a bare Ti film comparable to that used for TIME transition edge sensors. *Device fabrication by Matthew Kenyon, JPL Microdevices Laboratory.*

$$\begin{aligned} P_{bath} &\approx P_{optical,0} + P_{bias,0} + \frac{\mathrm{d}P_{bath}}{\mathrm{d}T}\,\delta T \\ &= P_{optical,0} + I_0^2 R_0 + G_c\,\delta T \end{aligned} \tag{3.5}$$

The bias power dissipated in the TES is also expanded to first order in δI and δT.

$$\begin{aligned} P_{bias} = I^2 R_{tes} &= V_{bias}^2 \frac{R_{tes}}{(R_{th}+R_{tes})^2} \\ &\approx (I_0+\delta I)^2 \left(R_0 + \frac{R_0}{T_0}\alpha\,\delta T + \frac{R_0}{I_0}\beta_I\,\delta I\right) \\ &\approx \left(I_0^2 + 2I_0\,\delta I\right)\left(R_0 + \frac{R_0}{T_0}\alpha\,\delta T + \frac{R_0}{I_0}\beta_I\,\delta I\right) \\ &\approx I_0^2\left(R_0 + \frac{R_0}{T_0}\alpha\,\delta T + \frac{R_0}{I_0}\beta_I\,\delta I\right) + 2I_0R_0\,\delta I \\ &= I_0^2 R_0 + \frac{I_0^2 R_0}{T_0}\alpha\,\delta T + I_0 R_0\,(2+\beta_I)\;\delta I \end{aligned} \tag{3.6}$$

For very low frequencies the time derivatives in Eqn. 3.1 can be ignored. Substituting in the linearly expanded quantities leads to the following two equa-

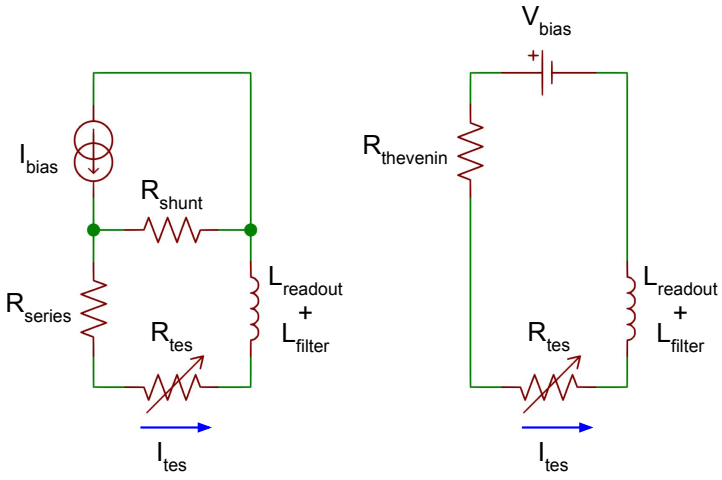

Figure 3.3: The TES bias circuit (*left*) and its Thevenin equivalent circuit (*right*), adapted from Irwin and Hilton [51]. A bias current is applied to a $3-4\,\mathrm{m}\Omega$ shunt resistor in parallel with the TES. An additional parasitic resistance R_{series} is included in the TES branch, which corresponds to the resistance of the polyimide readout cables in TIME. In the Thevenin equivalent circuit, a constant voltage $V_{bias} \equiv I_{bias} R_{shunt}$ is applied to the TES in series with a resistance $R_{th} \equiv R_{shunt} + R_{series}$. The TES is truly voltage biased only if $R_{th} \ll R_{TES}$ at the operating point, but the Thevenin circuit is an exact analog for any values of R_{th} or R_{TES}.

tions:

$$\frac{I_0^2 R_0}{T_0}\alpha\,\delta T + I_0 R_0\,(2+\beta_I)\;\delta I + \delta P_{optical} = G_c\,\delta T \tag{3.7}$$

$$\begin{aligned} V_{bias} &= (I_0+\delta I)\left(R_{th}+R_0+\frac{R_0}{T_0}\alpha\,\delta T+\frac{R_0}{I_0}\beta_I\,\delta I\right) \\ &\approx I_0\,(R_{th}+R_0)+\frac{I_0 R_0}{T_0}\alpha\,\delta T+R_0\left(1+\beta_I+\frac{R_{th}}{R_0}\right)\delta I \end{aligned} \tag{3.8}$$

In the Thevenin equivalent circuit in the steady state, $V_{bias} = I\,(R_{th}+R_{tes}) = I_0\,(R_{th}+R_0)$ is always constant (though V_{tes} need not be). Therefore, from Eqn. 3.8 it must be the case that:

$$\begin{aligned} 0 &= \frac{I_0 R_0}{T_0}\alpha\,\delta T + R_0\left(1+\beta_I+\frac{R_{th}}{R_0}\right)\delta I \\ \frac{\delta T}{\delta I} &= -\frac{T_0}{I_0\alpha}\left(1+\beta_I+\frac{R_{th}}{R_0}\right) \end{aligned} \tag{3.9}$$

Rearranging Eqn. 3.7 and substituting in this result gives:

$$\begin{aligned}
\frac{\delta P_{optical}}{\delta I} &= -I_0 R_0 \left(2+\beta_I\right) + \left(G_c - \frac{I_0^2 R_0}{T_0}\alpha\right)\frac{\delta T}{\delta I} \\
&= -I_0 R_0 \left(2+\beta_I\right) - \left(\frac{G_c T_0}{I_0 \alpha} - I_0 R_0\right)\left(1+\beta_I+\frac{R_{th}}{R_0}\right) \\
&= -I_0 R_0 \left(1 - \frac{R_{th}}{R_0} + \frac{G_c T_0}{I_0^2 R_0 \alpha}\left(1+\beta_I+\frac{R_{th}}{R_0}\right)\right) \\
&= -V_{bias}\left(\frac{R_0}{R_{th}+R_0}\right)\left(1 - \frac{R_{th}}{R_0} + \frac{G_c T_0}{I_0^2 R_0 \alpha}\left(1+\beta_I+\frac{R_{th}}{R_0}\right)\right) \\
&= -\sqrt{P_{bias,0}\, R_0}\left(1 - \frac{R_{th}}{R_0} + \frac{G_c T_0}{P_{bias,0}\,\alpha}\left(1+\beta_I+\frac{R_{th}}{R_0}\right)\right)
\end{aligned} \tag{3.10}$$

This quantity allows us to refer the TES current fluctuations we measure to the corresponding power fluctuations observed by the TES. For large values of α and small values of R_{th}, this is simply the bias voltage. However, as $R_{th} = R_{shunt} + R_{series}$ is increased at constant $P_{bias,0}$, the current responsivity to a fixed power signal decreases and the system is more susceptible to current noise in the readout chain.

The loop gain $\mathscr{L}$ is defined below, which characterizes the instantaneous change in bias power resulting from a small change in total input power $P_{bias} + P_{opt} = P_{input} = -P_{bath}$ at constant TES current (because of the inductance in the circuit, the TES current is instantaneously constant and the steady state relation $V_{bias} = I\left(R_{th}+R_{tes}\right)$ is not relevant, though $V_{bias} = I_0\left(R_0+R_{tes}\right)$ remains true). This gain is the driver behind electrothermal feedback in the sensor.

$$\begin{aligned}
\mathscr{L} &\equiv -\left.\frac{\partial P_{bias}}{\partial P_{input}}\right|_I = \left.\frac{\partial P_{bias}}{\partial P_{bath}}\right|_I = \left(\frac{dP_{bath}}{dT}\right)^{-1}\left.\frac{\partial P_{bias}}{\partial T}\right|_I \\
&= \frac{1}{G_c}\frac{I_0^2 R_0 \alpha}{T_0} = \frac{V_{bias}^2\, R_0\, \alpha}{\left(R_{th}+R_0\right)^2\, G_c\, T_0} \\
&= \frac{P_{bias,0}\,\alpha}{G_c\, T_0}
\end{aligned} \tag{3.11}$$

Note that at fixed V_{bias}, the TES series resistance ($R_{th} = R_{shunt} + R_{series}$) reduces the loop gain. However, for fixed optical loading it is the steady state bias power $P_{bias,0}$ that remains fixed by the saturation power of the device ($P_{optical,0} + P_{bias,0} = P_{sat}$) when biasing in the superconducting transition.

Therefore it is not the case in practice that the loop gain is affected by excess series resistance or by the TES resistance, they simply change the necessary bias voltage. Variation in loop gain through the transition arises from variation in α.

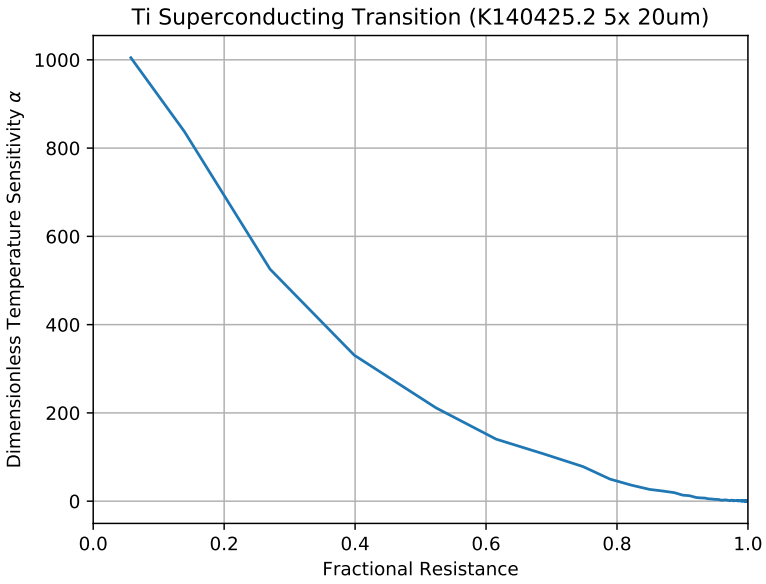

Figure 3.4: The dimensionless temperature sensitivity $\alpha \equiv \frac{\partial \log R}{\partial \log T}$ for the superconducting transition shown in Fig. 3.2. Note that the device measured is a bare Ti film of comparable thickness to the TIME TESs, so it does not use the TIME TES geometry or electrical contacts.

TIME operates in the over-damped regime, for which Irwin and Hilton derives the following TES stability criterion [51]:

$$1 > \frac{\mathscr{L} - 1}{\mathscr{L} + 1 + \beta_I} \frac{R_{th}}{R_0} \approx \frac{\mathscr{L} - 1}{\mathscr{L} + 1} \frac{R_{th}}{R_0} \tag{3.12}$$

Stability is impacted by excess series resistance. For large values of the loop gain $\mathscr{L}$, the device is unstable when $R_{th} = R_{shunt} + R_{series}$ exceeds the operating resistance of the TES, effectively limiting the region of the superconducting transition we can bias in. This can be thought of as the TES transitioning from being voltage biased ($P_{bias} \approx V_{bias}^2/R_{tes}$ for small R_{th}) to being current biased ($P_{bias} \approx (V_{bias}/R_{th})^2 R_{tes}$ for large R_{th}).

3.2 Detector Architecture

The output arc of each TIME spectrometer is populated with 60 transition-edge sensor (TES) bolometers coupled to broadband direct-absorber micromeshes. Detectors are organized into subarrays (Fig. 3.5) produced in two different varieties: high frequency (HF) containing 12 spectral by 4 spatial pixels, and low frequency (LF) containing 8 spectral by 4 spatial pixels. LF and HF subarrays occupy the same physical footprint, approximately 2.8 by 3.5 cm; the larger pixel size of the LF subarrays results in a more uniform spectral resolution ($R \sim 100$) across the full TIME band. In order to maintain continuous spectral coverage, the edge pixels from two subarrays must mount directly adjacent to each other. Therefore, the wire bond pads for the detector readout lines are recessed from the edge of the device, forming notches in the device perimeter; additionally, no support/protection frame can be incorporated at the upper and lower pixel edges, complicating fabrication and device handling.

Subarrays are mounted in groups of four (covering 16 spatial pixels) onto gold-plated aluminum detector module holders and attached to the output arc of the spectrometer, as described in Chapter 2. Replaceable spacers on the modules set the distance from the detector absorber surface to the edge of the spectrometer's parallel plate waveguide, which is on the order 1 mm (but can be made arbitrarily small). Note that because the parallel plate waveguide in the TIME spectrometers operates at frequencies far above the TE1 mode cutoff frequency (200-300 GHz operating frequency, 50 GHz cutoff frequency), the mode impedance is very close to that of free space ($Z/Z_0 \sim 1.02$) [81] and we do not need to embed the detector and its backshort within the parallel plate waveguide (an engineering challenge).

Individual detectors consist of a $0.5 - 1.0\,\mu$m thick low-stress silicon nitride mesh spanning approximately 3.2 mm by either 2.3 mm (HF) or 3.5 mm (LF). The detector is slightly oversized with respect to the 3.0 mm waveguide to relax alignment and mounting distance tolerances; tolerances are relaxed further by the fact that the electric field is zero at the waveguide walls. A thin layer of gold patterned on the silicon nitride forms a broadband absorber, dissipating incident radiation as heat. Rather than a continuous sheet of gold, the absorber is organized into $3\,\mu$m wide lines spaced $185\,\mu$m apart; this reduces the total silicon nitride volume of the device (affecting heat capacity) and allows for a thicker, more reproducible gold sheet impedance. The chosen line

spacing corresponds to $< \lambda/5$ across our band. A test strip with probe pads connected by a single $3\,\mu$m wide gold line is added on each device, allowing the fabrication team to monitor and adjust the gold thickness targets to achieve the desired absorber sheet impedance (as stated above, this is very close to the free space impedance). A series of gold bars perpendicular to the electric field direction conduct absorbed heat to the TES near the edge of the device. Early TIME devices (including those pictured in Fig. 3.7 and 3.8) used a symmetric absorber, where the vertical (as pictured) absorber lines and horizontal thermal sinking lines are of similar width, thickness, and spacing. Because the sheet resistance is only relevant in one direction for the TE1 mode, the thermal sinking lines (horizontal as pictured) have been moved to a separate, thicker gold layer for the v7 devices (Fig. 3.9 and 3.10); simulation results motivating this change are discussed in Sec. 3.4.

Near the edge of each web (as shown in Fig. 3.7) lies an elemental Ti TES with a normal resistance of $50-100\,\mathrm{m}\Omega$ and a superconducting transition temperature near 500 mK. This is the primary sensor used for science observations. In series with the Ti TES, we include an additional elemental Al TES with a higher transition temperature and saturation power; this TES is used when needed in high-loading laboratory testing and is fully superconducting during typical science operations. A pair of niobium bias lines connects to either end of the TES block; these lines run along the side of the mesh and across the silicon nitride support legs, where they terminate in wire bond pads near the edge of the device (Fig. 3.6). The bias lines operate at relatively low frequencies (hundreds of kHz) and are routed in adjacent feed/return pairs (there is no local ground plane). The area immediately surrounding the TESs contains a palladium-gold bilayer; this added heat capacity was added to limit the bandwidth of the TES, suppressing excess thermal noise at high frequencies arising from the distributed heat capacity of the mesh. However, as discussed in Sec. 3.4, our model for the high frequency noise behavior shows a peak well below our readout Nyquist frequency, indicating this added heat capacity is not necessary.

As shown in Fig. 3.8, the four corners of the TIME HF v6 detector mesh are held by a total of eight narrow silicon nitride legs, each approximately $500\,\mu$m long. Four of these legs (the outer, less-angled four) are $10\,\mu$m wide support legs added to improve device yield through the fabrication process, and

they are removed by a laser trimmer after devices are mounted into detector modules (hence the name "laser legs"). The remaining four legs are the 5 μm wide primary legs that define the thermal conductance from the bolometer to the surrounding bath temperature (and thus set the saturation power and phonon noise). Two of these legs carry the niobium bias lines from the TES to the wire bond pads near the perimeter of the device. In the v7 design (shown in Fig. 3.9 and 3.10), a increased number of narrower ($4-6\,\mu$m) laser legs are used to provide a more uniform constraint across the mesh during fabrication. This has the added benefit of increasing the precision for tuning the final thermal conductance to the bath (G) for the device; devices can be tested cryogenically with all laser legs intact, and then selectively trimmed to a desired G by removing some (but not necessarily all) laser legs.

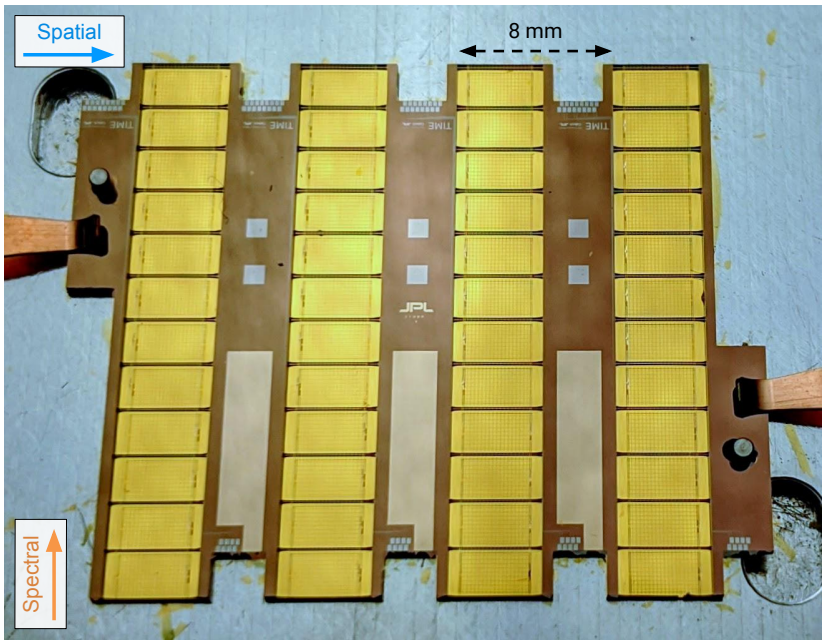

Figure 3.5: A single TIME high frequency subarray containing 4 spatial by 12 spectral pixels (48 detectors total). *Device fabrication by Clifford Frez and Anthony Turner, JPL Microdevices Laboratory.*

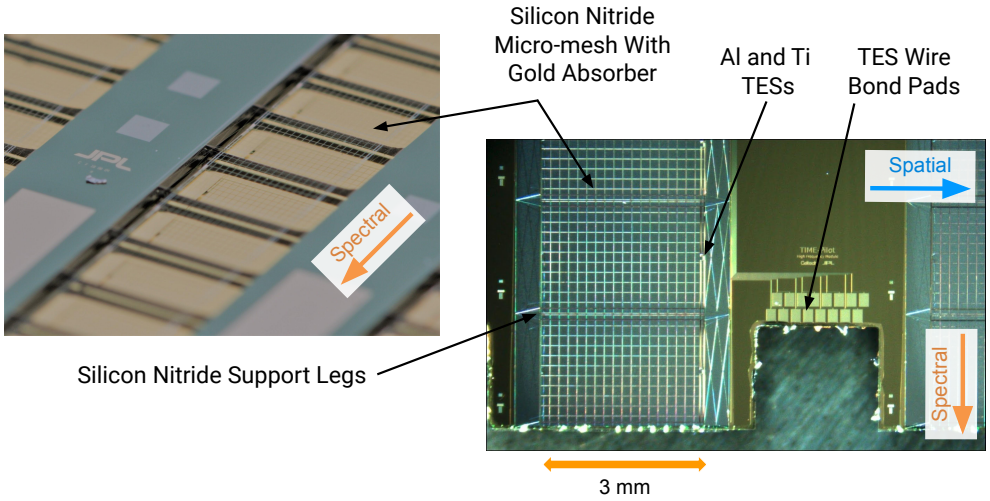

Figure 3.6: Absorber webs and wire bond pads on a TIME high frequency subarray. *Device fabrication by Clifford Frez and Anthony Turner, JPL Microdevices Laboratory.*

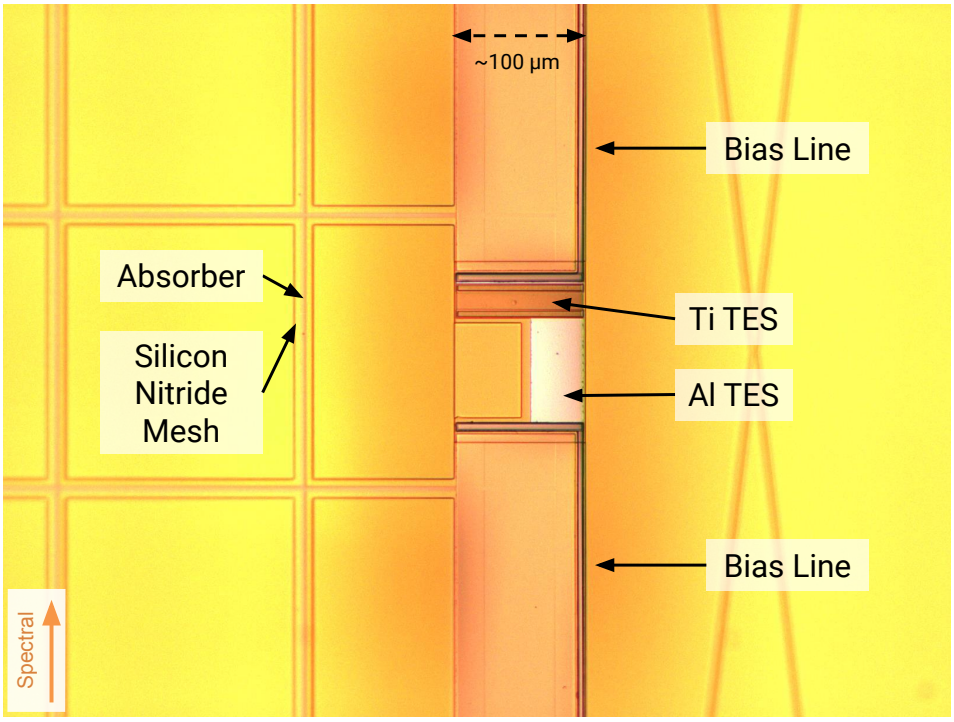

Figure 3.7: TESs and bias lines from a single TIME detector. *Device fabrication by Clifford Frez and Anthony Turner, JPL Microdevices Laboratory.*

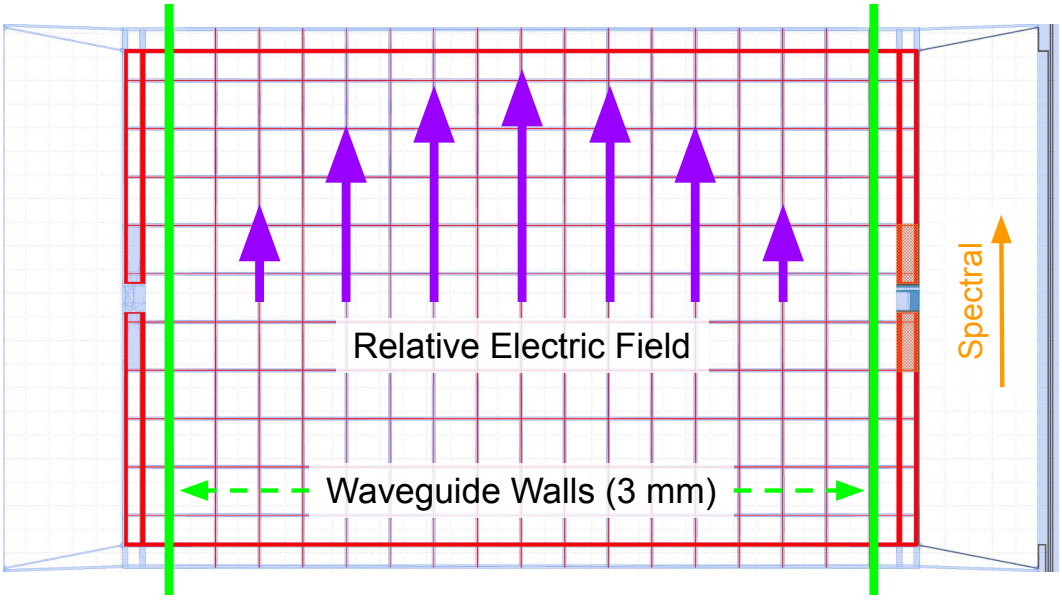

Figure 3.8: The spectrometer parallel plate waveguide wall positions (green) and TE1 mode electric field distribution (purple) overlaid on a TIME high frequency pixel (v6 design). The silicon nitride mesh is shown in light blue, and the thin absorber gold is shown in red.

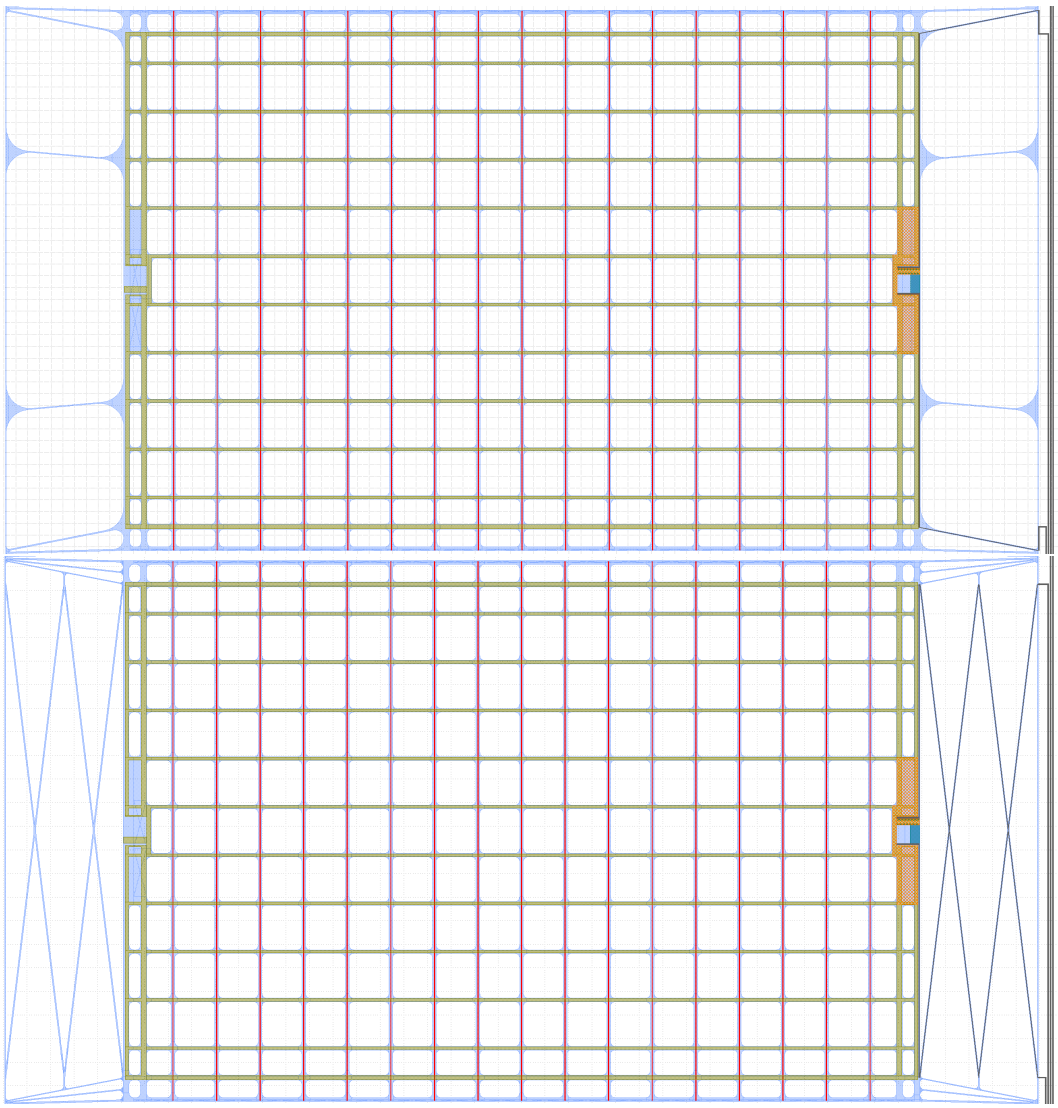

Figure 3.9: Two of the v7 TIME high frequency pixel designs. The upper design utilizes additional support legs that are removed with a laser trimmer after fabrication and initial testing. The lower design runs the TES bias lines over a meander (the cross pattern) to allow for thinner support legs and lower saturation power. The silicon nitride mesh is shown in light blue, and the thin absorber gold is shown in red. An additional thick layer of thermal-sinking gold running perpendicular to the electric field is shown in yellow.

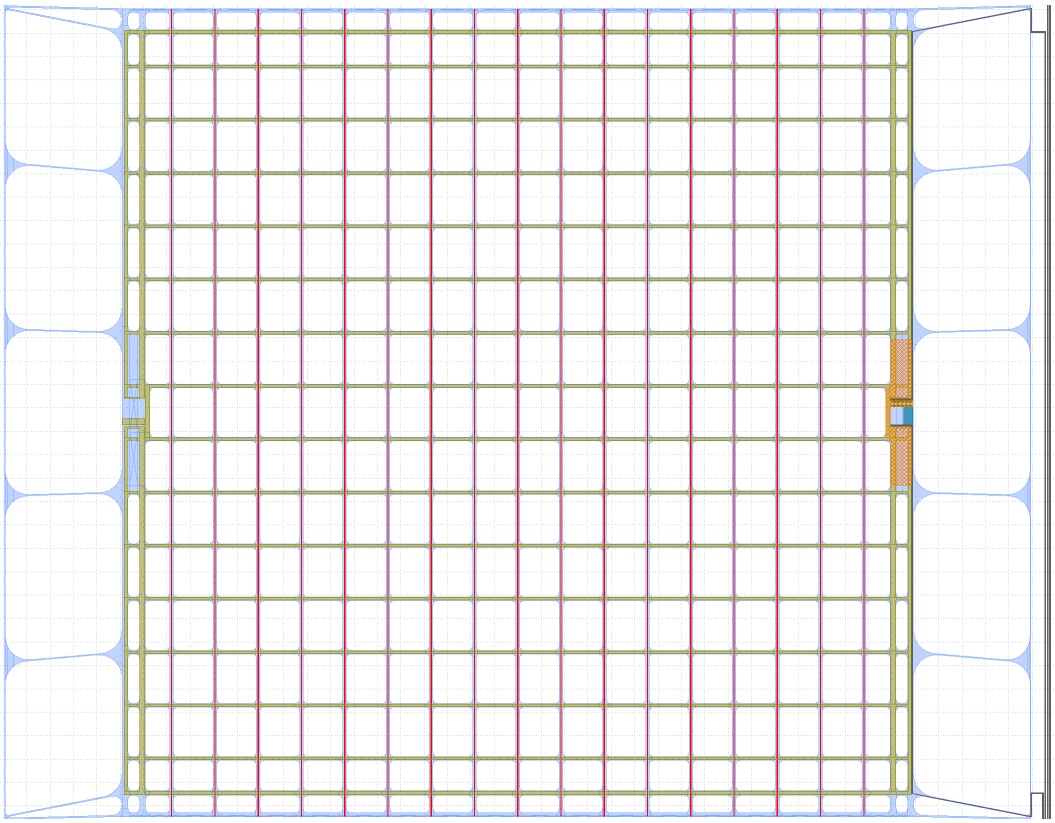

Figure 3.10: A v7 TIME low frequency pixel design. A 50% larger absorber results in 8 spectral pixels per subarray. Additional support legs are removed with a laser trimmer after fabrication and initial testing. The silicon nitride mesh is shown in light blue, and the thin absorber gold is shown in red. An additional thick layer of thermal-sinking gold running perpendicular to the electric field is shown in yellow.

3.3 Backshort

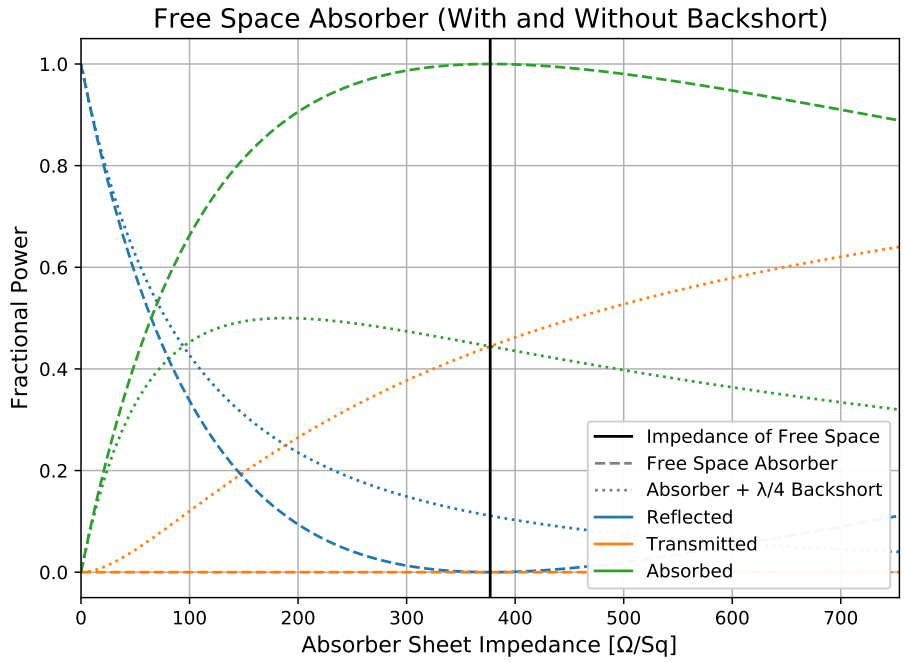

Figure 3.11: Power absorbed by a sheet impedance in free space, with and without a backshort. (Results for the backshort case are reported at the backshort design wavelength λ.)

As demonstrated in Fig. 3.11, a simple absorbing sheet in free space with the proper sheet resistance can absorb up to 50% of incident power [51, 81]; this arises from the fact that the absorber resistance acts in parallel with the free space impedance at the output side, forming a partially-reflective impedance boundary from the perspective of an incoming wave. Perfect absorption at a given wavelength λ can be achieved by introducing a perfect reflection boundary (a backshort) at a distance $(2n-1)*\lambda/4$ behind the absorber (for positive integer values of n); in this configuration, the wave transmitted through the absorber interferes destructively with the reflection off of the backshort.

I compute the expected absorption efficiency for TIME backshorts of varying complexity using a one-dimensional model [41] that analytically accounts for multiple (lossless) reflections at each of an arbitrary number of material interfaces. In Fig. 3.12 I verify this model against a series of HFSS simulation test cases with an absorbing sheet embedded in rectangular waveguide (exciting the TE01 mode, which matches the electric field of the distribution

of the TE1 parallel plate waveguide mode [81] while reducing the necessary simulation volume).

Two different backshort configurations and fabrication processes have been attempted for TIME. The current baseline process (developed by Clifford Frez and Anthony Turner, JPL Microdevices Laboratory) produces a fully-etched vacuum backshort cavity on the device wafer. A separate metalized wafer is later epoxied to the rear of the device wafer, forming the backshort reflector. A schematic cross section for the finished product is shown in Fig. 3.16. As discussed previously, the focal plane is divided into six segments in the spectral direction. In principle a different backshort distance could be chosen when fabricating detectors for each of these six segments; however, because the backshort is integrated into the subarray, it cannot be modified after fabrication. Producing fewer unique backshort options across the focal plane allows for detectors to be interchangeable. In this design, the backshort distance is directly set by the thickness of the silicon device wafer. As shown in Fig. 3.13, the optimal wafer thickness for the high frequency detectors approaches 230 μm at the band edge; handling of devices this thin during fabrication is a challenge, so we have elected to compromise with a fixed 320 μm backshort distance across the entire band. We expect a 10% efficiency hit at the very top of the band from this (the atmospheric monitor channels). A $3\lambda/4$ vacuum backshort was considered to allow for thicker device wafers; as shown in Fig. 3.14, the reduced bandwidth of the higher-order backshort would require at least three different backshort distances across the TIME band.

An earlier fabrication process (developed by Bruce Bumble and Matthew Kenyon, JPL Microdevices Laboratory) utilized a double silicon-on-insulator (SOI) wafer to produce an integrated mostly-silicon $\lambda/4$ backshort. The two inner oxide layers act as etch-stops, leaving a silicon layer with well-defined edges embedded in a thicker handle structure. Etching from the back allows access for metal deposition (forming the backshort reflector), and etching from the front releases the silicon nitride device layer (forming the thermally isolated bolometer membrane). The backshort is defined only by the top vacuum and inner silicon layers, allowing the total device wafers to be as thick as needed to survive the fabrication process. A schematic cross section for the finished product is shown in Fig. 3.17. As shown in Fig. 3.15, this is a relatively low-bandwidth backshort configuration which requires at least three different

backshort distances to cover the TIME band. This design was ultimately abandoned due to unrelated mechanical challenges with the prototypes.

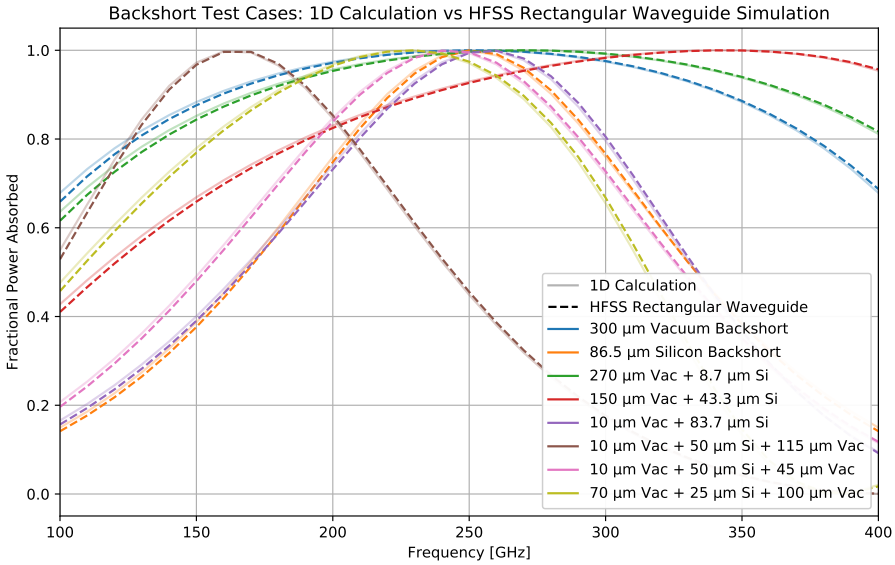

Figure 3.12: A series of test cases comparing 1D backshort efficiency calculations to HFSS simulations in rectangular waveguide (exciting the TE01 mode, which matches the electric field of the distribution of the TE1 parallel plate waveguide mode [81] while reducing the necessary simulation volume). Various combinations of vacuum and silicon are computed and show excellent agreement with simulation.

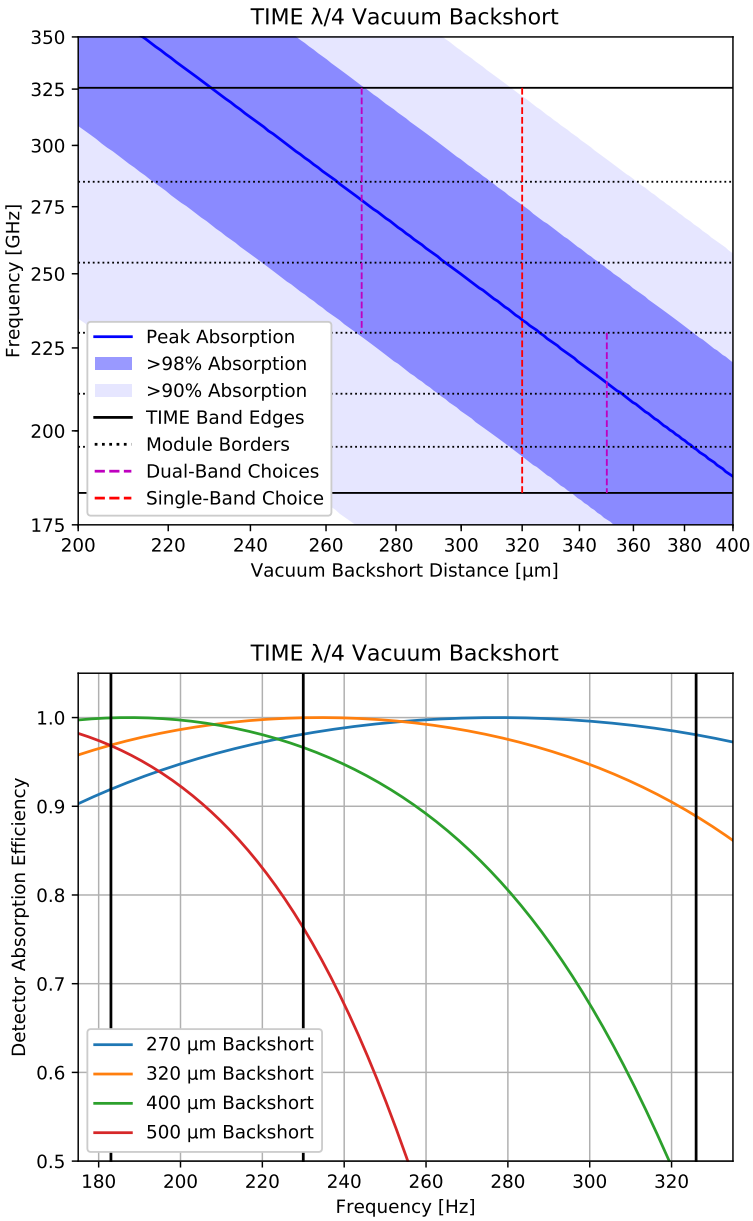

Figure 3.13: Computed efficiency for a vacuum $\lambda/4$ backshort. A single backshort distance provides adequate efficiency across the entire TIME band, simplifying fabrication.

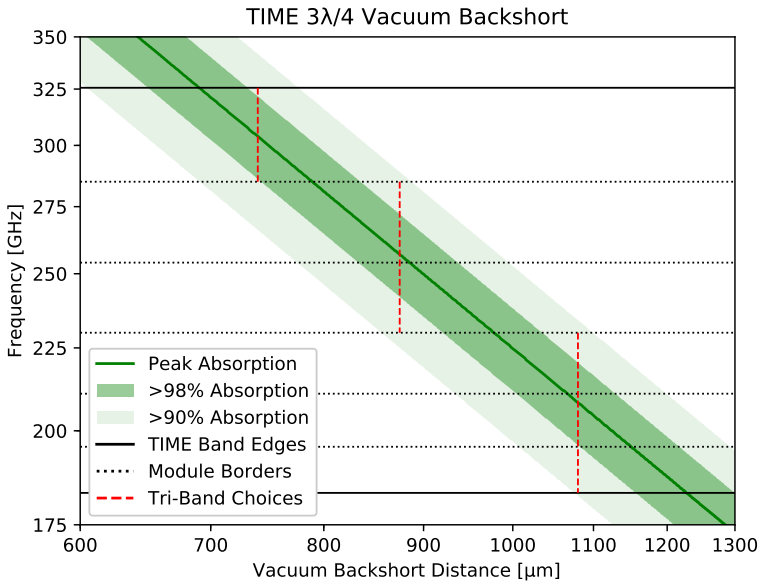

Figure 3.14: Computed efficiency for a vacuum $3\lambda/4$ backshort. Three different detector backshort distances are required to adequately cover the entire TIME band.

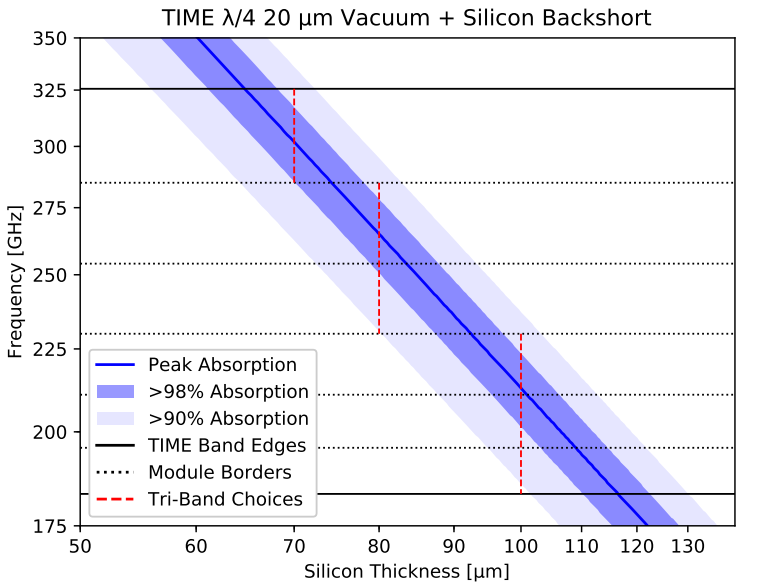

Figure 3.15: Computed efficiency for a mostly-silicon $\lambda/4$ backshort containing a 20 μm vacuum gap immediately behind the absorber (for thermal isolation). Three different detector backshort distances are required to adequately cover the entire TIME band.

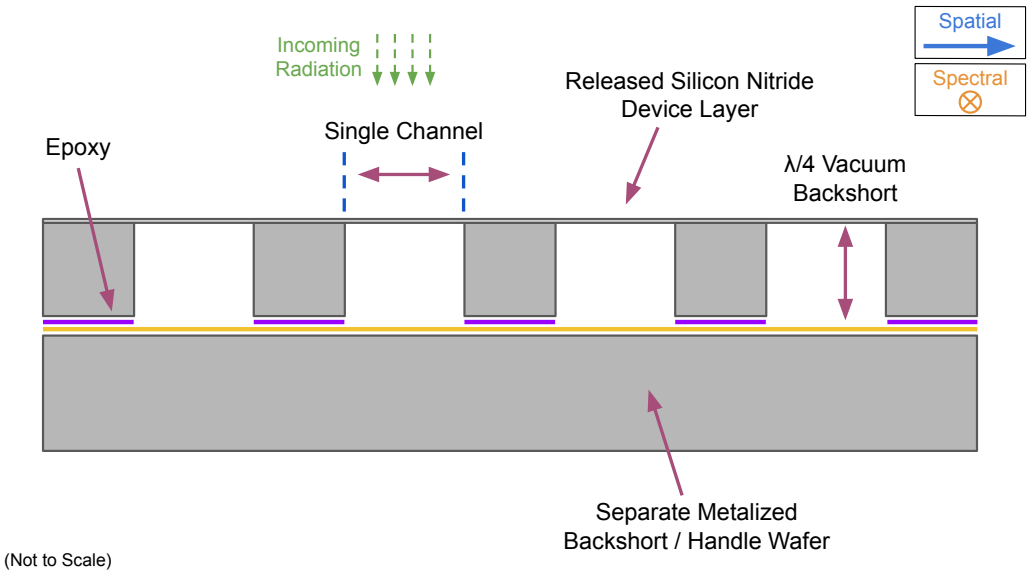

Figure 3.16: A schematic cross-section showing the current backshort design for TIME detectors, utilizing a separate wafer epoxied to the main wafer to form the backshort. *Fabrication process development by Clifford Frez and Anthony Turner, JPL Microdevices Laboratory.*

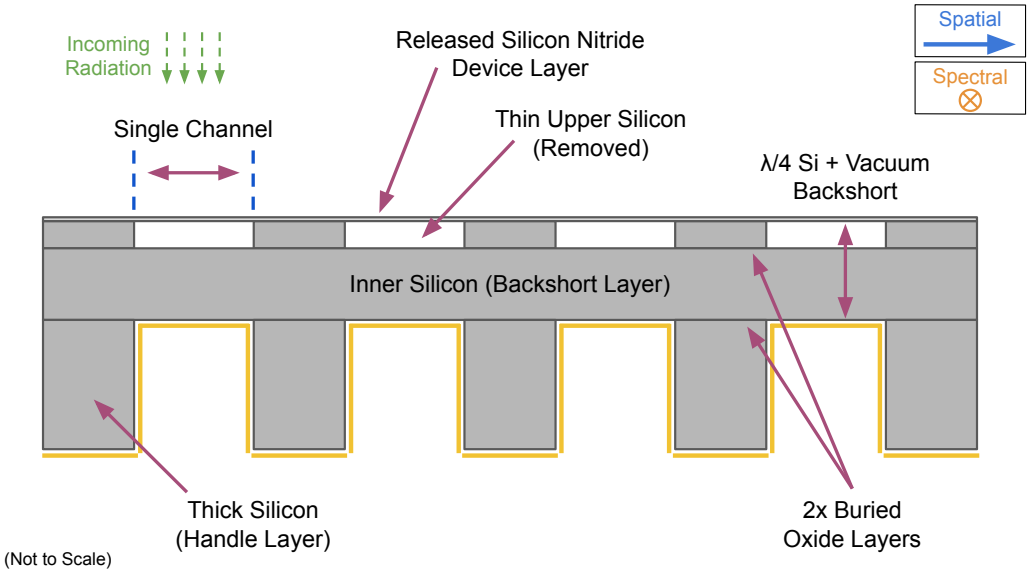

Figure 3.17: A schematic cross-section showing the original backshort design for TIME detectors, utilizing a double SOI wafer and producing an integrated backshort. *Fabrication process development by Bruce Bumble and Matthew Kenyon, JPL Microdevices Laboratory.*

3.4 Excess Phonon Noise

The results in this section were produced using a code base developed by Jeffrey Filippini [40], who also assisted in the initial model setup for TIME but who has not reviewed the final results. Plots generated using this code base are denoted as such in the figure captions.

A noise model for the TIME absorber mesh and TES is defined here by a network of lumped heat capacities (parameterized by values for temperature T and for the heat capacity C at that temperature) and thermal links (parameterized by values for the thermal conductance G and for β, which is used to scale G across temperature gradients). The phonon noise power in each of the various thermal links drives temperature fluctuations in the heat capacities which couple to the TES, and Johnson noise in the bias circuit drives TES current fluctuations directly. The code base developed by Jeffrey Filippini builds a system of coupled linear first order differential equations describing the time variation of the TES current and the temperatures of the heat capacities. This is solved in the Fourier domain, producing a TES noise current spectrum and the transfer functions dI/dP (the change in TES current from a change in optical power input into a specified heat capacity block) and dI/dV (the change in TES current from a change in the external TES bias voltage).

As shown in Fig. 3.18, I have broken the TIME high frequency detector (shown in the background) into a series of heat capacities (indicated by colored circles) and thermal links (indicated by colored bars). Each color corresponds to a different class of heat capacity C or thermal conductance G determined by the surrounding material geometries:

- **Green Circles:** Heat capacity of the surrounding silicon nitride, horizontal mesh-sinking Au/Pt, and vertical photon-absorbing Au/Pt (a thin Pt cap over the absorber gold is used as a protection layer)
- **Purple Circles:** Heat capacity of the surrounding (wide) horizontal silicon nitride and (wide) horizontal Au/Pt
- **Cyan Circles:** Heat capacity of the surrounding (wide) vertical silicon nitride and (wide) vertical Au/Pt
- **Red Circles:** Heat capacity of the cyan circles plus added Pd/Au near the TES

- **Black Circles:** Heat capacity of the TES itself
- **Blue Circles:** Heat capacity of the silicon nitride of the legs

- **Yellow Bars:** Thermal conductance of the vertical (photon absorbing) Au/Pt and silicon nitride
- **Orange Bars:** Thermal conductance of the horizontal (mesh thermal sinking) Au/Pt and silicon nitride
- **Red Bars:** Thermal conductance of the horizontal (wide) Au/Pt and (wide) silicon nitride
- **Magenta Bars:** Thermal conductance of the vertical (wide) Au/Pt and vertical (wide) silicon nitride
- **Purple Bars:** Thermal conductance of the magenta bars plus added Pd/Au near the TES
- **Blue Bars:** Thermal conductance of the silicon nitride of the legs
- **Dark Red Bars:** Thermal conductance arising from electron-phonon coupling in the Ti TES ($1.5 * 10^{21}\,\mathrm{pW/(m^3K^5)}$, agrees with [107] above 300 mK)

I take all points on the mesh to be at $T = T_c = 500\,\mathrm{mK}$; leg block temperatures are computed from a temperature profile ending at $T = T_{bath} = 300\,\mathrm{mK}$. The total heat capacity of a block is taken to be $C(T) = (\sum_i C_{v,i}(T_c) * V_i) * T/T_c$, where the sum is over the materials present in that block (each with a volume V_i). For a given material I assume $C_v(T_c) = C_{electron} * T_c + C_{phonon} * T_c^3$, with the values used for $C_{electron}$ and C_{phonon} used listed in Table 3.1.

Material	$\boldsymbol{C_{electron}}$ **[J/(cm^{3}K^2)]**	$\boldsymbol{C_{phonon}}$ **[J/(cm^{3}K^4)]**
Au	7.24E-05	4.23E-05
Pd	1.18E-03	1.07E-05
Pt	7.31E-04	1.54E-05
Ti	3.20E-04	2.43E-06
Si_3N_4	8.30E-08	5.09E-07

Table 3.1: Values from the literature [27, 106] used to characterize the electron and phonon components of the heat capacity for the materials modeled in Section 3.4.

The total thermal conductance G of a thermal link is taken to be $G(T) = (\sum_i G_i(T_c)) * (T/T_c)^\beta$, where the sum is over the materials present in that link (each with a G_i defined by the material and geometry). I take $\beta = 2.0$ for the blue links (silicon nitride dominated) and $\beta = 1.0$ for all other links (assuming they are metal-dominated). For metals, I use the Wiedemann-Franz law to compute G_i. The room temperature film resistance for gold is assumed to scale with thickness t as $t^{-1.63}$ [13] and is normalized to give $8\,\Omega$/sq at 10 nm (consistent with TIME measurements). The residual-resistance ratio (RRR) of gold is taken to be $(1 + t/(32.5\,\mathrm{nm}))$ [13]. Lacking better information, I use the same thickness scaling exponent and RRR for Pt and Pd films as I do for Au, but I normalize by the ratio of their respective room temperature bulk resistivities; Pt and Pd thermal conductivities are subdominant in this model, as the Pt is much thinner than Au over the same area and the Pd is over a relatively small area. For silicon nitride, I assume a thermal conductance $G(450\,\mathrm{mK}) = (519.7\ \mathrm{pW/(K\,\mu m)}) * A/l$ scaled to temperature T with $\beta = 2.0$ (which is consistent with previous TIME measurements).

The optical power input point for the purpose of computing the responsivity dI/dP was chosen to be the heat capacity node at the center of the mesh. Results show very little difference when instead averaging dI/dP uniformly across the mesh.

I assume a TES normal resistance of $70\,\mathrm{m\Omega}$ and an operation point $R_{frac} = R/R_n = 0.6$ with an added series resistance of $10\,\mathrm{m\Omega}$. I describe the linearized superconducting transition with a constant assumed value of $\beta_I \equiv (d\log R/d\log I) = 0.1$ and, unless otherwise noted in the figure header, $\alpha \equiv (d\log R/d\log T) = 100$.

Shown in Fig. 3.19 is the resulting current noise (NEI) for two specific model configurations, related to NEP by the optical responsivity dI/dP. The total output of the noise simulation (shown is solid black) is broken into several of its individual components, including an ideal phonon noise power (solid red) arising from the silicon nitride legs connecting the corners of the mesh to the thermal bath. The Nyquist sampling frequency for the TIME instrument is shown in dotted black; the results as presented are not aliased. Device parameters were chosen to approximate detectors fielded in the 2019 engineering run: 10 nm absorber and thermal sinking gold with a 4 nm Pt cap, a heat capacity near the TES arising from a bilayer of 100 nm Pd and 350 nm Au,

and 1 pW of optical power. Fig. 3.19 (upper) displays an optical time constant $f_{3\mathrm{dB}} = 35\,\mathrm{Hz}$ (as measured from the half-power point of the responsivity dI/dP, not pictured, and as demonstrated by its effect on the photon noise power in current space). To more accurately reflect measured devices, a total excess heat capacity of 3 pJ/K distributed across the silicon nitride is added to the model (Fig. 3.19, lower). This brings the time constant down to $f_{3\mathrm{dB}} = 12\,\mathrm{Hz}$, which will serve as the baseline model.

As discussed in Section 3.2, the TIME detector design includes a set of additional silicon nitride tethers ("laser legs") included to aid in fabrication and to allow for high-background configurations. The optical time constant is expected to scale as $\tau \sim (C/G)/\mathscr{L}$ for total heat capacity C, thermal conductance to the bath G, and loop gain $\mathscr{L}$. Fig. 3.20 shows the NEP for two laser leg configurations: all four laser legs present (upper plot), and all four laser legs removed (lower plot). The no leg configuration does indeed show slower response, by about a factor of two (as measured by the half-power point of dI/dP) for a 3x lower G. However, due to the lower phonon noise, the effective usable bandwidth (as defined by the frequency where the dark NEP is equal to the photon NEP) has actually increased.

Because the TIME grating spectrometer fundamentally supports a single polarization, the effective gold absorber sheet impedance need only match the waveguide mode impedance in one direction (vertical in Fig. 3.18). Fig. 3.21 demonstrates the effect on NEP when increasing the thickness of the gold lines in the opposite polarization, thus increasing the thermal conductance of the orange bars in Fig. 3.18 and increasing the thermal coupling between the TES and the absorber web. Fig. 3.21 (upper) differs from Fig. 3.20 (lower) by increasing this horizontal gold by a factor of 30, resulting in an improved thermal time constant; this indicates that the internal time constants are not negligible in the baseline TIME design. Increasing the gold volume beyond this point (such as Fig. 3.21, lower) brings small or negative gains as the heat capacity of the added gold begins to dominate the total heat capacity of the device.

Fig. 3.22 demonstrates one of the effects of added heat capacity (Pd and Au) surrounding the TES (red circles in Fig. 3.18). For low total heat capacities an excess phonon noise spike develops around the kHz range. The excess shown in Fig. 3.22 (upper) is well resolved by the sampling rate of TIME; however,

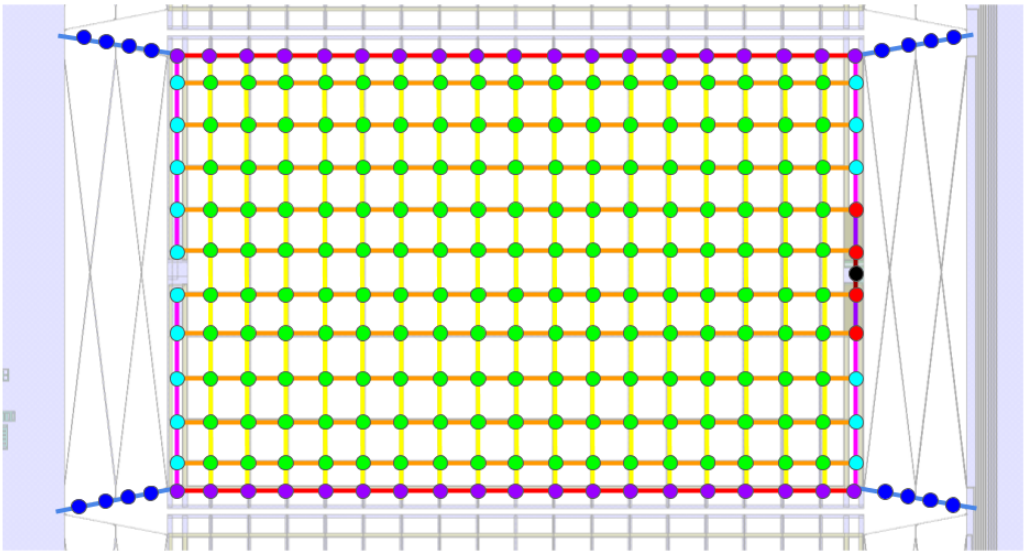

Figure 3.18: A diagram of the thermal model for the TIME high frequency detector superimposed on a rendering of the device layout. The device is divided into a series of heat capacities (indicated by colored circles) and thermal links (indicated by colored bars). Each color corresponds to a different class of heat capacity C or thermal conductance G determined by the surrounding material properties.

should this excess move to higher frequencies in physical devices, it could result in a significant aliased noise penalty in the science band. Added heat capacity softens this potential excess at the cost of slower time constants, but does not seem to help above the typical Nyquist frequency.

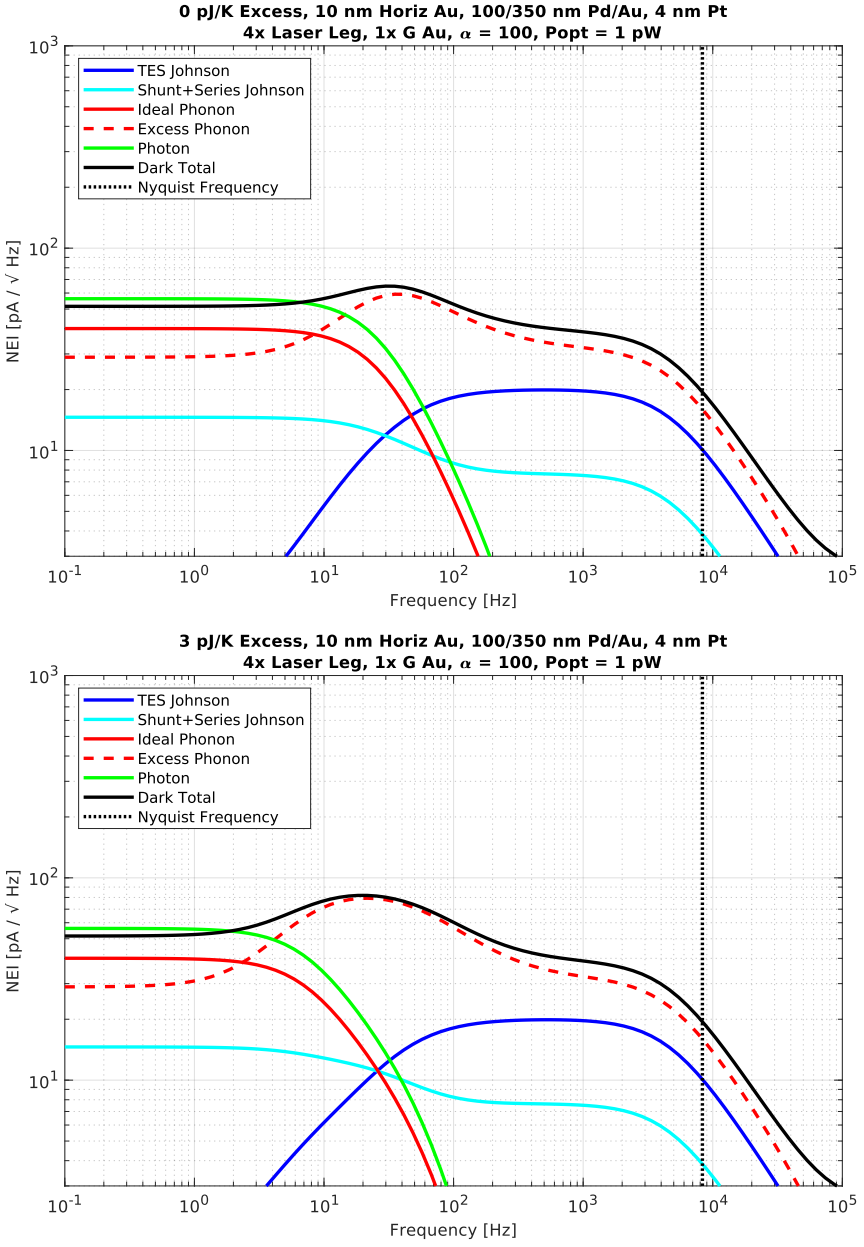

Figure 3.19: Expected NEI computed for the baseline TIME detector model with (*lower*) and without (*upper*) an excess distributed heat capacity of 3 pJ/K. The additional heat capacity brings the device time constants approximately in line with measured devices. The responsivity dI/dP is not shown here, but its effects can be seen through the projection of the white photon noise power into current space (*green*). *Results in this figure are generated with code developed by Jeffrey Filippini [40], who also assisted in the initial model setup for TIME.*

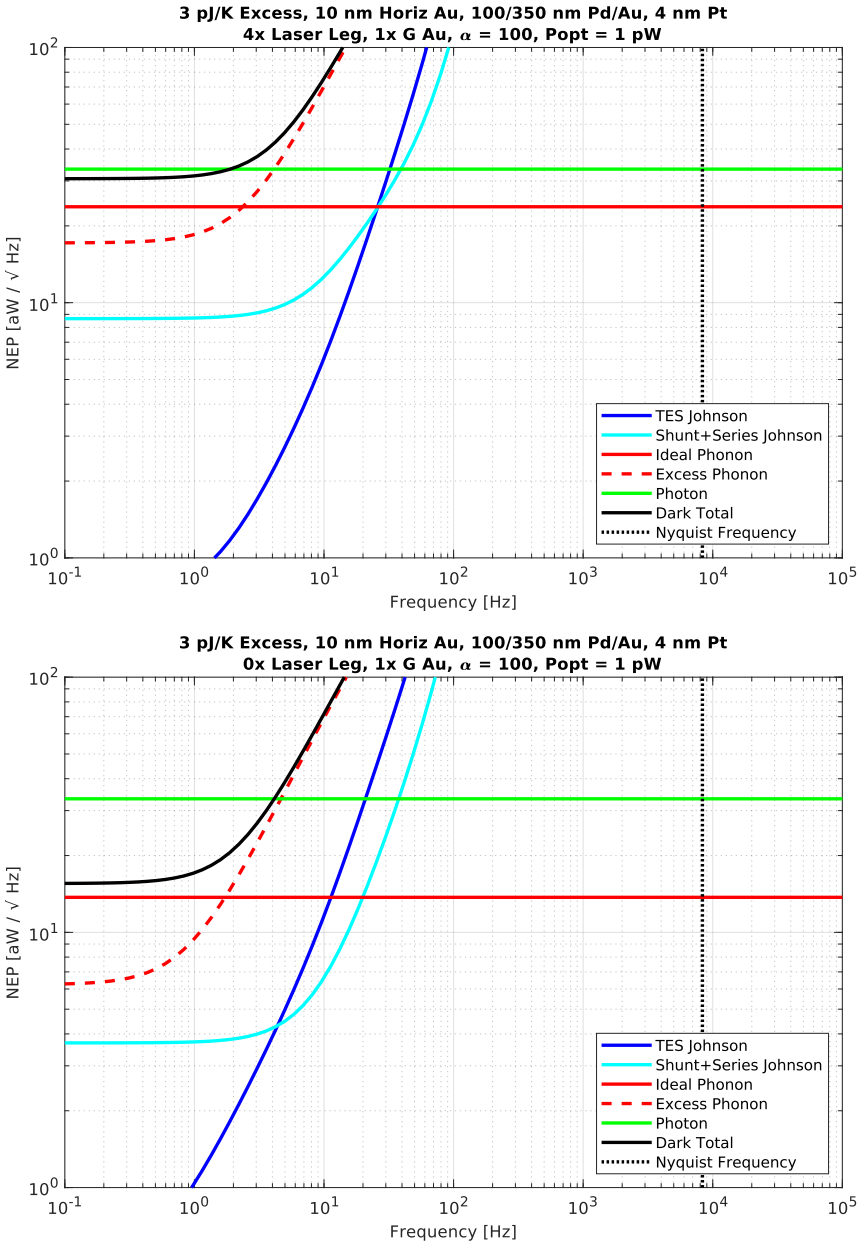

Figure 3.20: The expected NEP before (*upper*) and after (*lower*) trimming the detector's excess support tethers with a laser trimmer. The reduction in thermal conductance G from trimming reduces the speed off the detectors, but the overall usable NEP bandwidth improves slightly due to the reduced phonon noise. *Results in this figure are generated with code developed by Jeffrey Filippini [40], who also assisted in the initial model setup for TIME.*

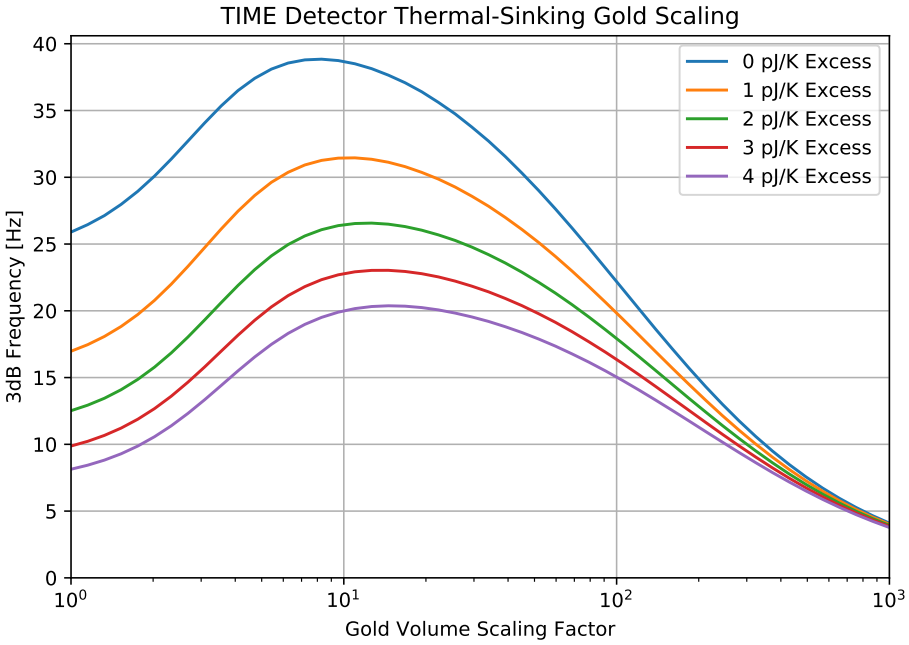

Figure 3.21: The expected detector time constants as the membrane thermal-sinking gold volume is increased for different membrane-distributed excess heat capacities. Gold scaling values up to 30x show an improved bandwidth, while values above 100x are bandwidth-limited by the heat capacity of the added gold. The results shown here assume $\alpha = 300$ with all laser tethers trimmed; variations in these assumptions affect the magnitude of the gains achieved, but the peak remains at ∼10x. *Results in this figure are generated with code developed by Jeffrey Filippini [40], who also assisted in the initial model setup for TIME.*

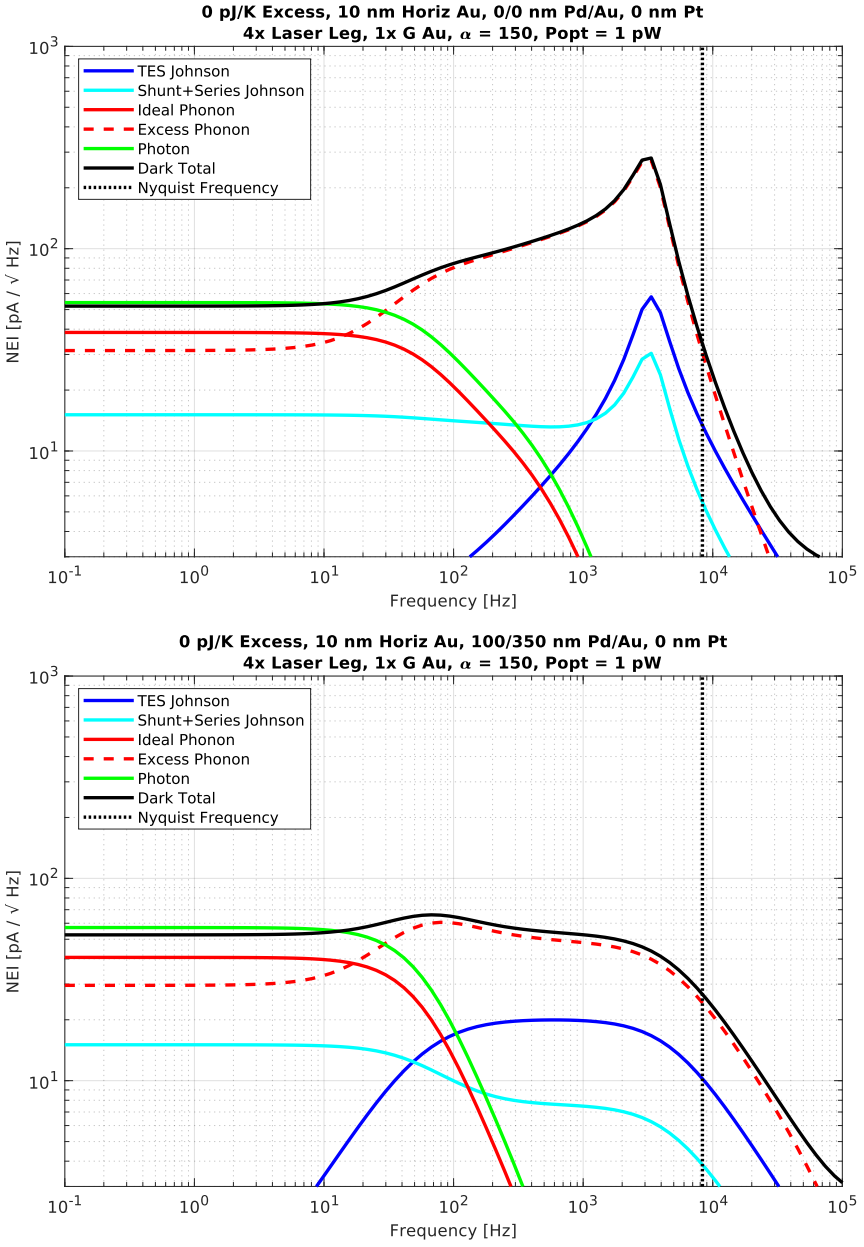

Figure 3.22: The expected NEI with (*lower*) and without (*upper*) the bandwidth-limiting palladium gold bilayer near the TES. The added heat capacity suppresses high frequency noise, but does not assist in reducing noise above the intended Nyquist frequency that would alias into the science band. *Results in this figure are generated with code developed by Jeffrey Filippini [40], who also assisted in the initial model setup for TIME.*

3.5 Transition Temperature

TIME uses an elemental Ti TES with a normal resistance of 50-100 mΩ and a transition temperature of 480-530 mK. The chosen saturation power (P_{sat}) of the device corresponds directly to a physical bolometer leg thermal conductance (G) target that depends on the bath temperature T_{bath} and the temperature of the bolometer (held at the transition temperature T_c by negative electrothermal feedback). Assuming the thermal conductivity scales as a power law with temperature, we can define a scaling constant G_{450} (the thermal conductance at an arbitrarily chosen 450 mK) that depends only on the effective silicon nitride thermal conductivity k_{450} and geometry (total leg cross-sectional area A and leg length l).

$$\begin{aligned} G(T) &= \frac{\mathrm{d}P}{\mathrm{d}T} = k(T)\,\frac{A}{l} \\ &= k_{450}\,\frac{A}{l}\,\left(\frac{T}{450\,\mathrm{mK}}\right)^{\beta} \\ P_{sat} &= \int_{T_{bath}}^{T_c} G(T)\,\mathrm{d}T \\ &= k_{450}\,\frac{A}{l}\,\frac{T_c^{\beta+1} - T_{bath}^{\beta+1}}{(\beta+1)(450\,\mathrm{mK})^{\beta}} \end{aligned} \tag{3.13}$$

We tune the detector saturation power primarily through the leg geometry, with low saturation powers corresponding to low phonon noise and long, narrow bolometer legs. However, as demonstrated in Fig. 3.23, reducing the transition temperature of the TES allows for heftier legs (and therefore more robust devices) with the same saturation power. Toward that end, elemental hafnium films were explored at JPL as an alternative to elemental titanium TESs for TIME; transition temperatures were found to be tunable from 250-450 mK by varying the argon gas pressure during deposition [50]. Fig. 3.24 shows the evolution with T_c of the phonon component of the NEP. For modest T_c reductions, the temperature reduction of the bolometer compensates for the increase in thermal conductance and NEP is nearly flat; as the T_c approaches the bath temperature (dT approaches 0), very large thermal conductances are required to support the power flow across the link and NEP rises rapidly.

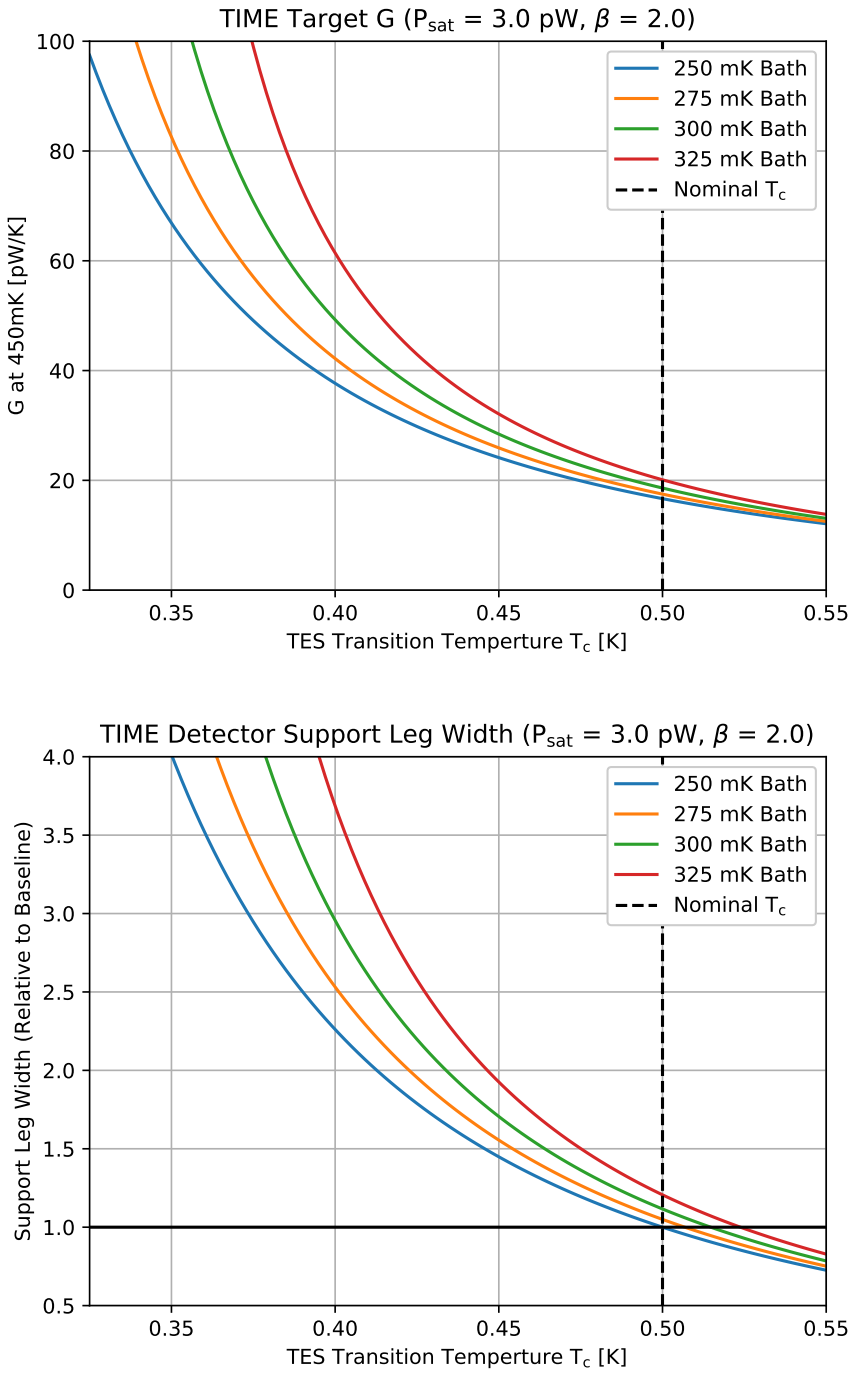

Figure 3.23: The bolometer leg geometry (or equivalently, the thermal conductance target at fixed temperature) required for a 3 pW saturation power as a function of TES transition temperature T_c.

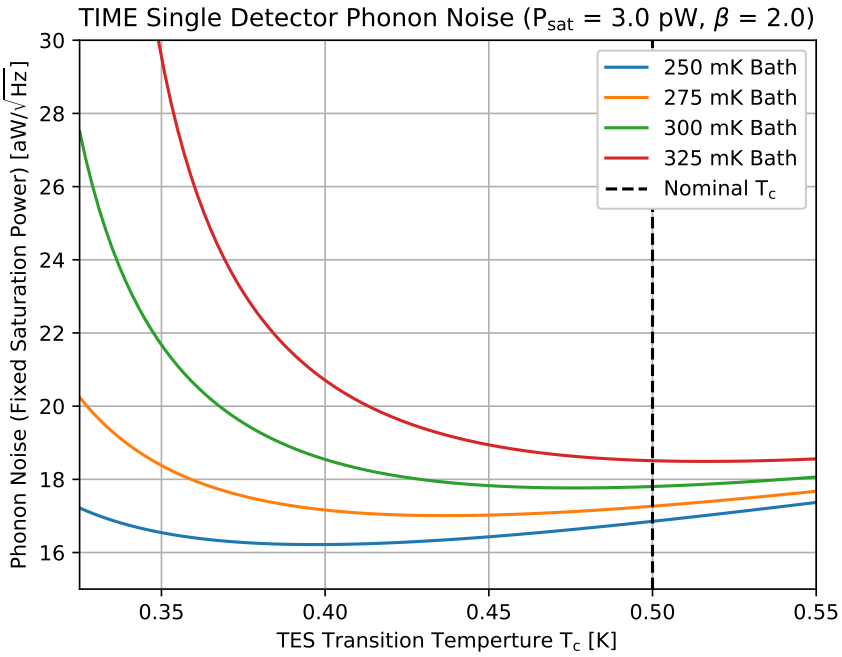

Figure 3.24: The NEP for a fixed saturation power detector as the transition temperature T_c is varied.

Chapter 4

Waveguide-Coupled Slot Antenna Arrays

The work presented in this section was done in collaboration with Roger O'Brient and Bryan Steinbach.

4.1 Motivation

As described previously, the baseline detector design for TIME consists of large 2.3 x 3.2 mm (high frequency) or 3.5 x 3.2 mm (low frequency) silicon nitride micro-meshes coated with gold absorber suspended near the corners by four 5 x 1 x 500 μm legs. Consistent yield of large device arrays (12 x 4 pixels) has proven to be a fabrication challenge. In this chapter I examine the possibility of using antenna-coupled TESs on the back of the TIME grating spectrometers. This is somewhat similar to the approach used in the BICEP/Keck family of experiments [75], except that the beam pattern and spectral profile are defined by a feedhorn and a diffraction grating respectively. Such devices would use a significantly smaller bolometer island ($\sim$ 150 x 300 μm) and leverage the existing processes and expertise developed at the JPL Microdevices Laboratory for the BICEP/Keck program. Suspected microstrip losses observed in high frequency Keck devices are mitigated in the TIME design by a significantly shorter total microstrip path length (6 mm for TIME LF vs 18 mm for Keck 270 GHz, Fig. 4.1) enabled by relatively smaller pixel sizes. Added complications for the TIME design include the need to couple efficiently to a single waveguide mode in multi-mode parallel plate waveguide and the need to steer the beam up to 25° from the detector plane normal axis to properly illuminate the grating.

In the sections below I build toward a TIME low frequency detector design, starting with a simple $1 \times \infty$ slot array centered in parallel plate waveguide and adding complications step-by-step. Simulations are done using the frequency solver in CST 2014 unless otherwise specified; sanity checks on the performance of CST for our use case can be found in the appendices. I conclude with a completed mask design for a TIME low frequency detector array. Fabrication of test devices from this mask began in 2018, but was halted prior to completion due to lack of funding.

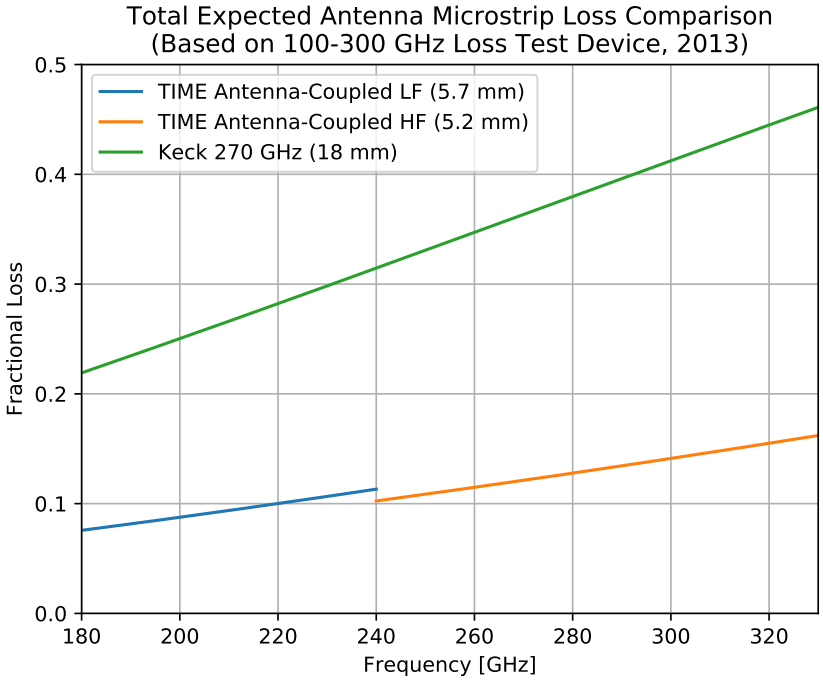

Figure 4.1: Based on the results of a 100-300 GHz BICEP/Keck-style microstrip loss test device which I assisted in testing in 2013, I show the projected loss across the TIME band for the expected microstrip lengths in an antenna-coupled TIME design. For reference, I compare the loss I would project with the same method for the noticeably larger Keck 270 GHz pixel design.

4.2 $1 \times \infty$ Slot Arrays

Impedance in Waveguide

I begin with a simple $1 \times \infty$ slot antenna array geometry centered in the 3 mm parallel plate waveguide used for TIME. A $\lambda_0/4$ ($f = 220\,\mathrm{GHz}$) backshort sits behind the antenna ground plane. The slots have a length $l = 0.5\lambda_0$, width $w = l/50$, and spacing $d = 0.5\lambda_0$. A single slot is simulated, with periodic boundary conditions creating the effective infinite array. $2\lambda_0$ of parallel plate waveguide is included, with the end capped with a perfect absorber (also known as perfectly matched layer, PML, or "Open" boundary condition in CST). Metallic surfaces (the waveguide walls and backshort) are defined as perfect electrical conductor (PEC) surfaces. The slot antenna impedance at the first resonance is shown in Fig. 4.2; the resonance appears well-behaved in the presence of the waveguide.

The silicon substrate, not included in the previous simulation, must be placed either in front of or behind the antenna ground plane in a real device. Keck-

style detectors place the silicon on the sky-side of the device and keep a vacuum backshort [75]. For drop-in compatibility with existing TIME wiring, I chose to place the silicon in the backshort; this may or may not be the optimal choice if the requirement for drop-in compatibility were to be relaxed. The slot length and spacing was adjusted empirically to $l = 0.195\lambda_0$ to compensate for the presence of the dielectric. Impedance results, shown in Fig. 4.3, show a greatly reduced bandwidth compared to the vacuum case. This bandwidth is recovered with the addition of a $\lambda_{quartz}/4$ quartz anti-reflection coating, as shown in Fig. 4.4. The slot length and spacing was further adjusted to $l = 0.175\lambda_0$ to compensate for the presence of the added quartz. Fig. 4.5 compares this antenna configuration to the same configuration in free space (no waveguide walls, same dielectric stack and backshort). The presence of the waveguide has little effect on the antenna impedance except near the TE5 cut-on frequency, indicating that we are well coupled to some combination of waveguide modes.

Mode Coupling

The lowest-order modes of a 3 mm parallel plate waveguide are shown in Table 4.1. Both TE and TM modes are supported, including a TEM mode that is equivalent to TM0. The TIME spectrometers use only the TE1 mode, but we operate far above the 50 GHz cutoff to reduce loss. Thus, higher order modes can propagate and must be suppressed by the antenna element design to prevent efficiency loss (the antenna array supports a single mode, so it must be well matched to TE1). TM modes (including the TEM mode) are suppressed by the polarization of the slot antenna when oriented as shown in Fig. 4.2. The electric field distribution of the TE modes is shown in Fig. 4.6. From this, the single centered slot used in the previous section can be expected to share power between all propagating odd TE modes, with no power in the even TE modes. This can be tested in CST by capping the end of the waveguide with a multi-mode waveguide port instead of the perfect absorber used previously. Due to limitations in CST, waveguide ports cannot be used with 1D period structures; thus, the periodic boundaries used to simulate the infinite array have been replaced with perfect electrical conductor. These boundary conditions are equivalent for parallel plate waveguide in which only TE modes are allowed to propagate, since the rectangular waveguide TE0n modes are identical to the parallel plate waveguide TEn modes. The aspect

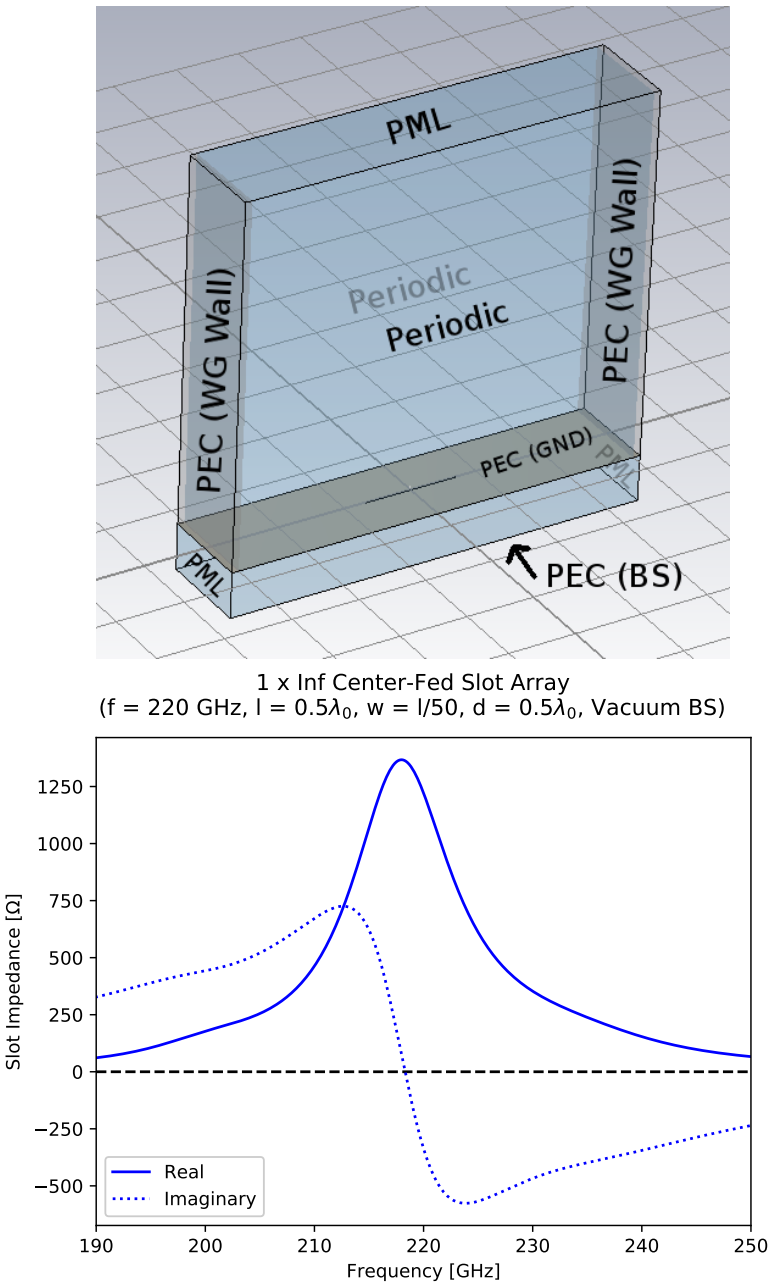

Figure 4.2: Simulation volume and impedance results for a $1 \times \infty$ center-fed slot array with a vacuum backshort coupled to parallel plate waveguide.

ratio of the simulation ensures that the TE0n modes of interest (8 are included here) are the lowest order modes; this is verified by inspecting the electric fields and mode classifications produced by CST.

The slot impedance for the silicon backshort with quartz AR coating case can be seen in Fig. 4.7. This was computed by terminating each of the waveguide

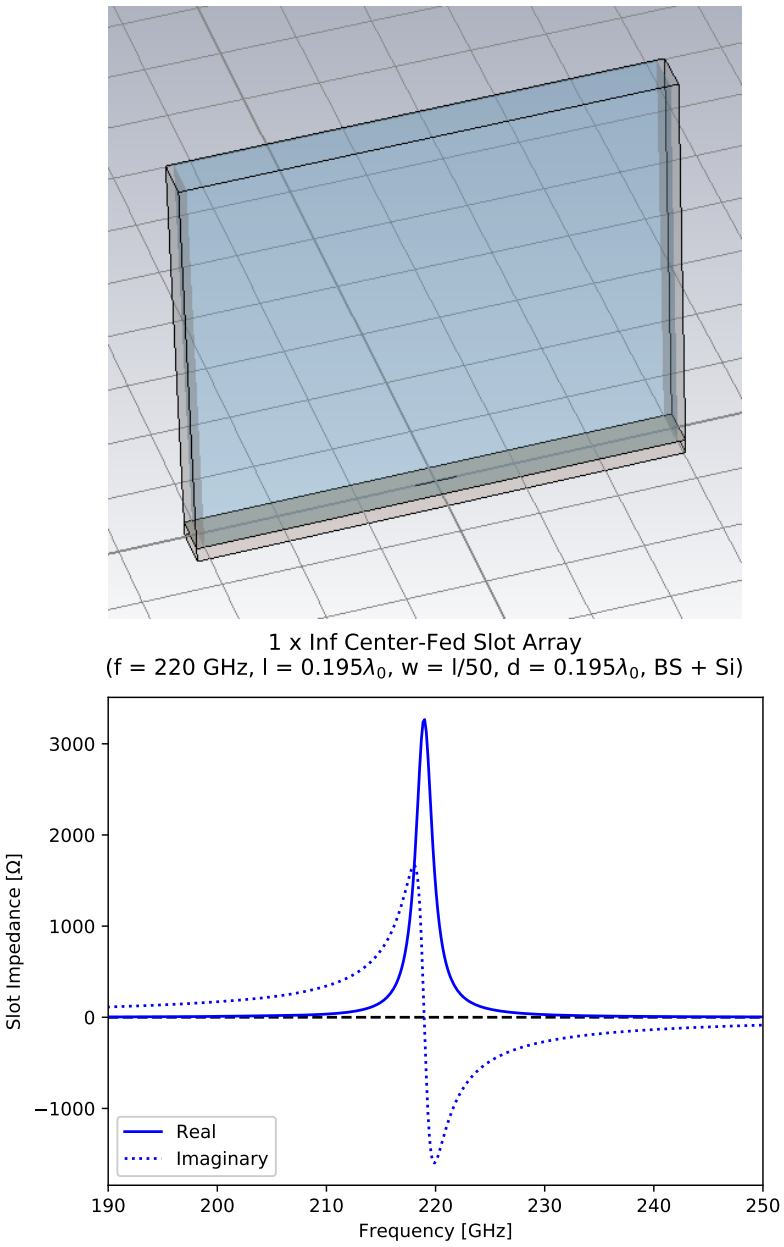

Figure 4.3: Simulation volume and impedance results for a $1 \times \infty$ center-fed slot array with a silicon backshort coupled to parallel plate waveguide.

modes with their textbook frequency-dependent impedance in post processing. The scattering parameters at a chosen feed impedance from the slot to each of the waveguide TE modes is shown in Fig. 4.8. As expected, at resonance the radiated power is shared approximately evenly between all propagating odd-numbered TE modes (TE1 and TE3 this frequency). Even TE modes are suppressed to below -60 dB. Above the 250 GHz cutoff frequency, power also

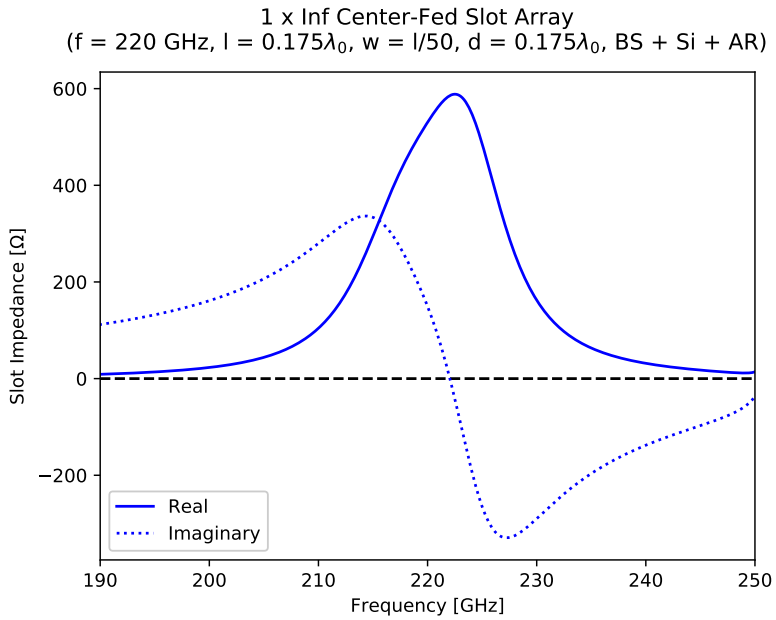

Figure 4.4: Impedance results for a $1 \times \infty$ center-fed slot array with a silicon backshort and quartz AR coating coupled to parallel plate waveguide.

couples to TE5.

Mode	Cutoff [GHz]	Attenuation Length [mm]
TM0 (TEM)	-	-
TE1, TM1	50	-
TE2, TM2	100	-
TE3, TM3	150	-
TE4, TM4	200	-
TE5, TM5	250	0.69
TE6, TM6	300	0.27

Table 4.1: Mode cutoff frequencies and the attenuation length at 240 GHz for 3 mm parallel plate waveguide.

Bandwidth

The bandwidth presented in the previous section (Fig. 4.8) is sufficient only for small segments of the R $\sim$ 100 TIME spectrometer focal arc. While in principle each spectral pixel can be tuned to the narrow bandwidth required required at each location, using the same broadband detectors for large portions of the spectrometer simplifies the fabrication and screening process. TIME is naturally divided into low and high frequency channels (183-230 GHz and 230-326 GHz respectively), each using different spectral pixel sizes and thus

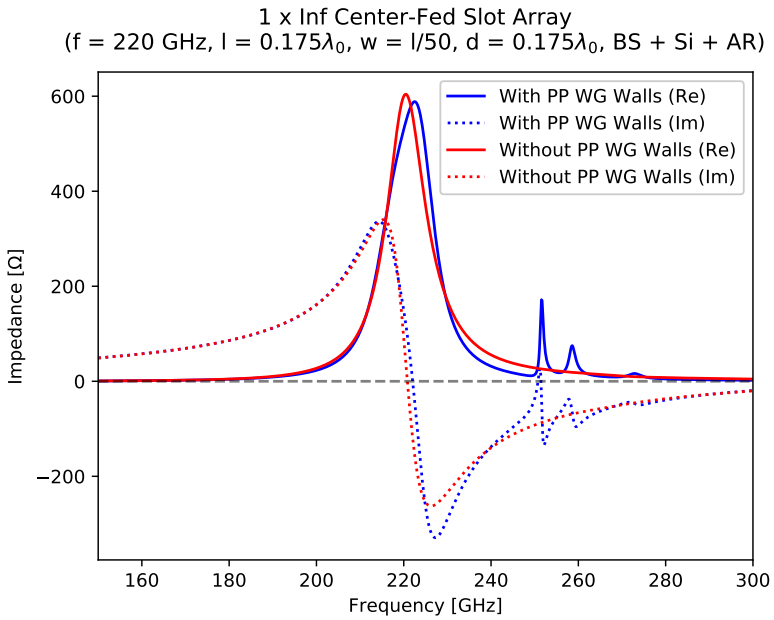

Figure 4.5: Impedance results for a $1 \times \infty$ center-fed slot array with a silicon backshort and quartz AR coating coupled to parallel plate waveguide compared to the same configuration without a waveguide. Note that 250 GHz is the cut-off frequency of the TE5 waveguide mode.

requiring separate detector designs regardless of other constraints. Therefore, I now present the results of slot parameter variation in an attempt to develop a design which covers the entire low frequency band. It should be noted that typical 3 dB or integrated-power bandwidth definitions are not particularly useful metrics for broadband TIME detectors. Each individual spectral pixel will only be receiving a small R $\sim$ 100 input frequency band; while sensitivity at the -3 dB level adds useful signal in broadband photometry instruments, this results in an unacceptable 50% efficiency hit for the TIME spectral channel in question. In short, a somewhat narrower top-hat band is more valuable here than a broad Gaussian band. I target an antenna bandwidth providing $\geq$ 90% (-0.5 dB) efficiency for the low frequency science band (195-230 GHz) and $\geq$ 80% (-1 dB) efficiency for the atmospheric monitor band (183-195 GHz)

In Fig. 4.9 I explore the effect on the slot impedance of changing the width of a slot of length and spacing $l = d = 0.175\lambda_0$ ($f = 220\,\mathrm{GHz}$). The slot is center-fed and uses periodic boundaries to simulate a $1 \times \infty$ array. The same $\lambda_{si}/4$ silicon backshort and $\lambda_{quartz}/4$ quart AR coating are used, but the waveguide walls and waveguide port are omitted (in the time-reverse sense, this

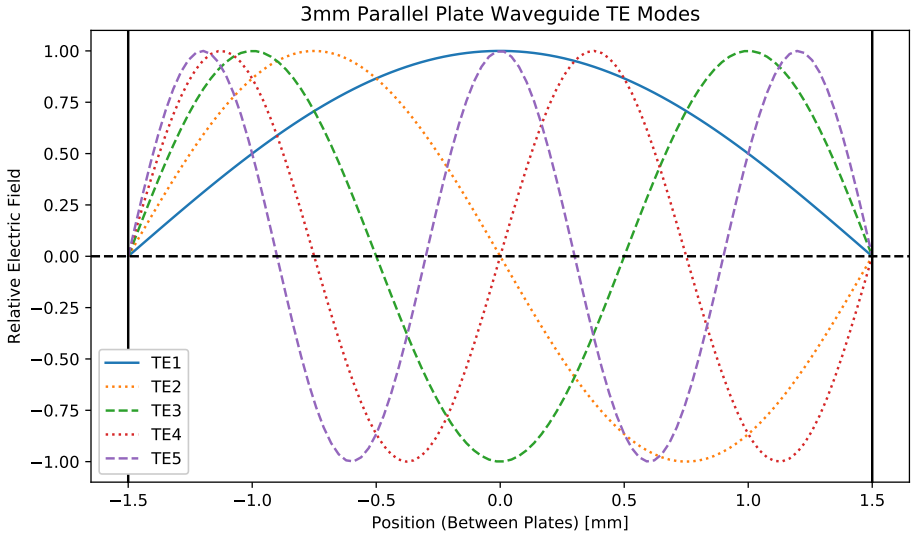

Figure 4.6: Electric field distributions for the TE modes in parallel plate waveguide.

antenna projects power into free space and not into a waveguide). Increasing the slot width increases the bandwidth of the first resonance, but increases the reactance significantly.

In Fig. 4.10 I explore the effect of varying the slot spacing d of the previous simulation at fixed slot width $w = 0.0035\lambda_0$. Dense slot packing dramatically increases the bandwidth of the first resonance while simultaneously reducing the real impedance to manageable levels for microstrip-fed designs (eliminating the need to use dual edge feeds instead of a center feed). Note that such extreme packing density is possible in TIME due to our single-polarization spectrometer design; experiments using interleaved dual-polarization slot arrays cannot achieve this density without antenna intersection.

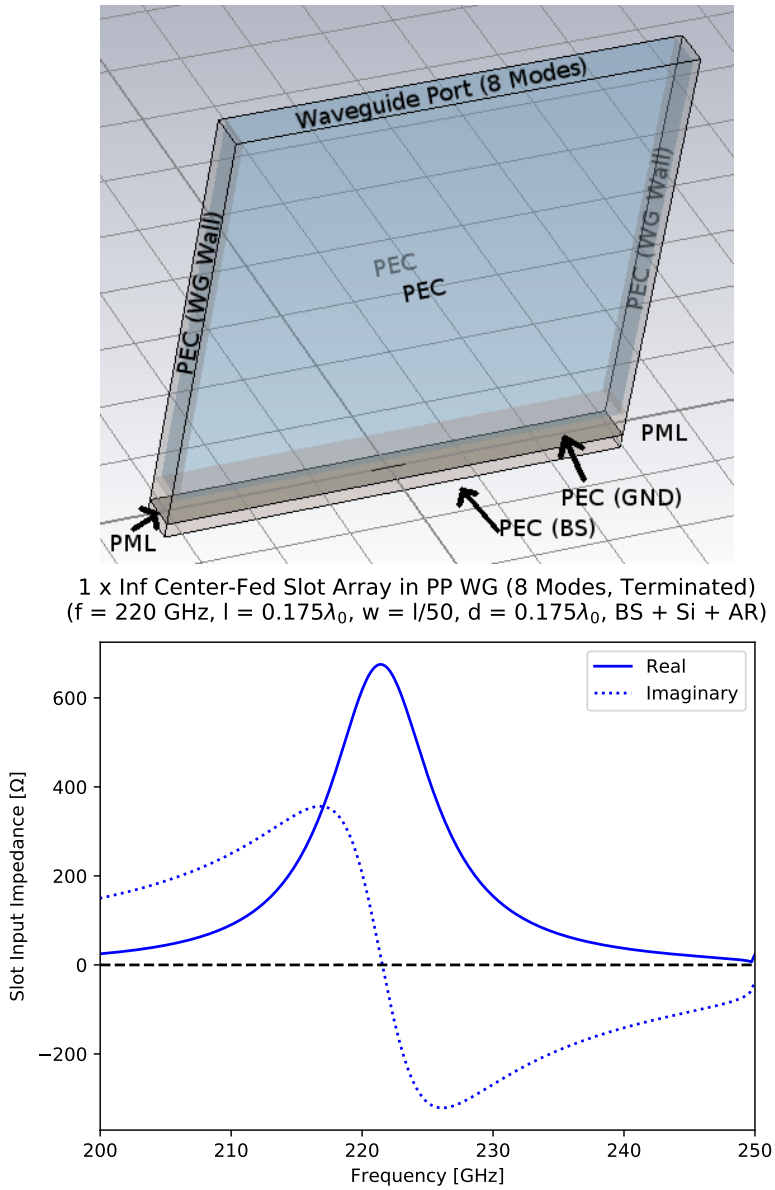

Figure 4.7: Simulation volume and impedance results for a $1 \times \infty$ center-fed slot array with a silicon backshort and quartz AR coating coupled to parallel plate waveguide.

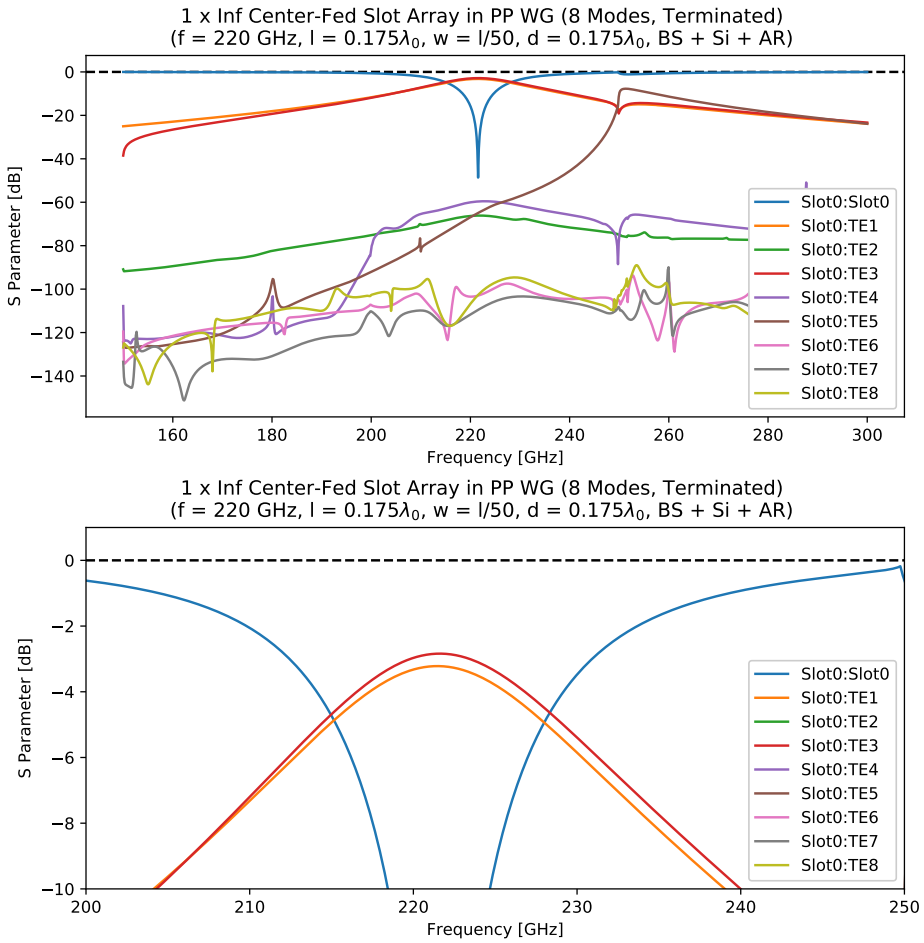

Figure 4.8: Parallel plate waveguide mode coupling for a $1 \times \infty$ center-fed slot array with a silicon backshort and quartz AR coating coupled to parallel plate waveguide.

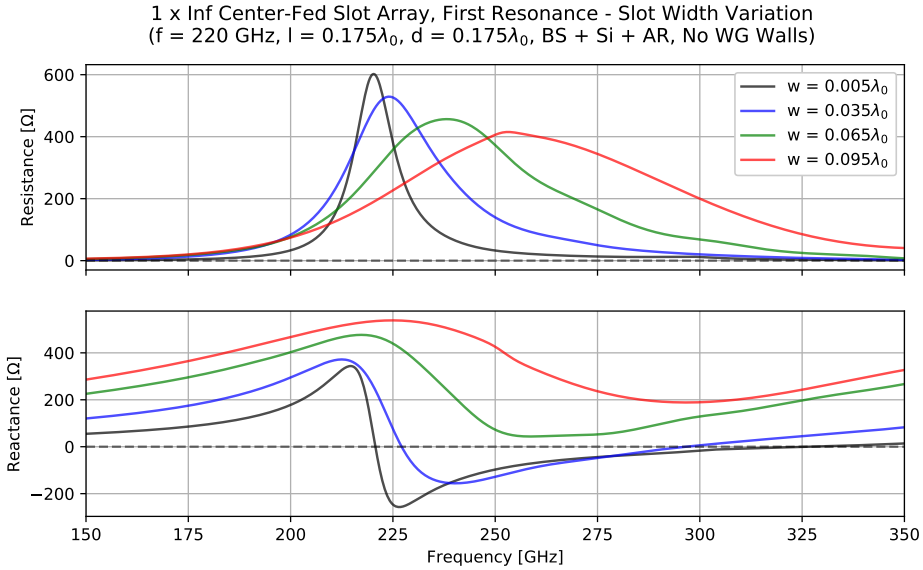

Figure 4.9: Slot width variation for a $1 \times \infty$ array without the parallel plate waveguide (in free space).

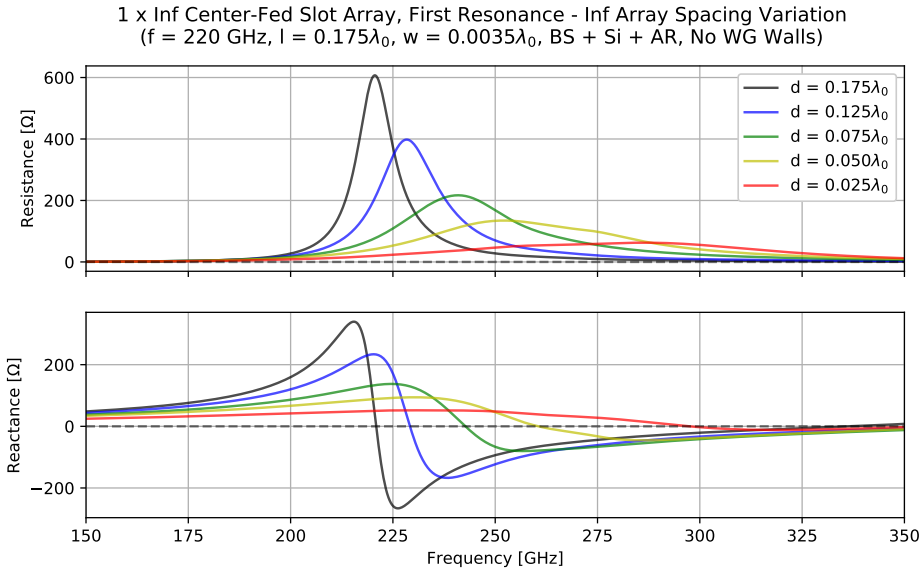

Figure 4.10: Slot spacing variation for a $1 \times \infty$ array without the parallel plate waveguide (in free space).

4.3 $3 \times \infty$ Slot Arrays

Mode Coupling

Adding additional slots to each antenna element (fed in phase, potentially with different feed impedances) can be used to restrict mode coupling of the final antenna array. As discussed previously, coupling to TM modes is suppressed by the polarization of the slot antenna, and thus only TE modes need be considered here. Even-numbered TE modes are asymmetric about the center of the waveguide, so symmetric designs naturally reject them. Therefore, over the full 183-326 GHz TIME spectrometer bandwidth, we need only discriminate against TE3 and TE5 in favor of TE1. TE1 has a single peak in the electric field, at the center of the waveguide, providing a natural position to place a slot antenna. As shown in Fig. 4.11, at positions $x = \pm 0.75\,\text{mm}$ relative to the center of the waveguide the TE3 and TE5 modes have an equal field magnitude that is opposite in sign to the peak at $x = 0$. Thus, by choosing feed impedances here such that the three slots summed produces no signal for TE3, we should simultaneously discriminate against TE5.

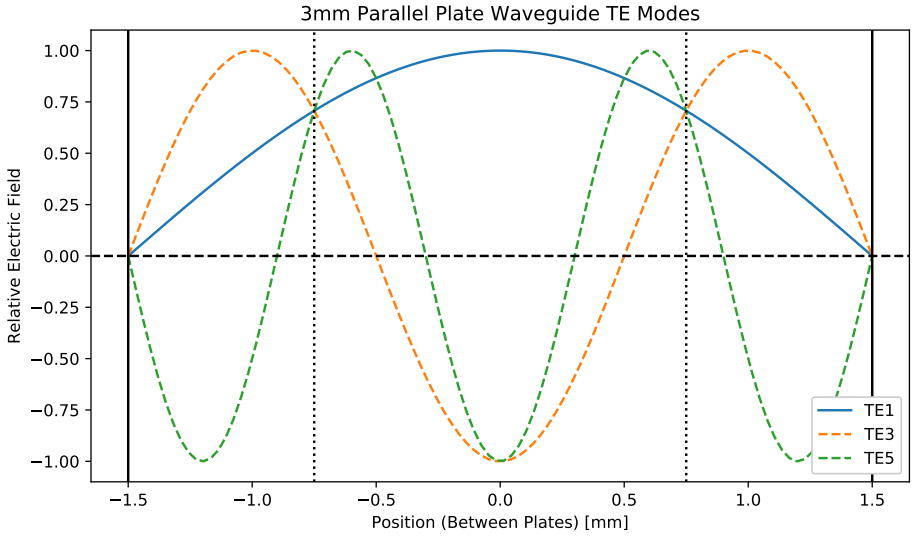

Figure 4.11: The odd TE modes supported in the 3 mm TIME parallel plate waveguide.

First Resonance, Tightly Packed

Here I examine a $3 \times \infty$ slot antenna array geometry centered in the 3 mm TIME parallel plate waveguide. Slots in each element are positioned at $x =$

0, ±0.75 mm within the waveguide. A $\lambda_0/4$ ($f = 220\,\text{GHz}$) silicon backshort sits behind the antenna ground plane. The slots have a length $l = 0.268\lambda_0$ (using the first resonance), width $w = 0.005\lambda_0$, and a tightly-packed spacing $d = 0.025\lambda_0$. A single three-slot element is simulated, with PEC boundary conditions creating the effective infinite array. $2\lambda_0$ of parallel plate waveguide is included, with the end capped with an 8-mode waveguide port. Metallic surfaces (the waveguide walls and backshort) are defined as perfect electrical conductor (PEC) surfaces. The simulation geometry and slot impedances are shown in Fig. 4.12. Slot input impedances are computed by terminating the waveguide modes with their textbook frequency-dependent characteristic impedances and by combining slot mutual impedance terms using the demand that the electric field E_n near slot n follows some chosen distribution.

$$\begin{aligned} V_n &= I_n Z_n = Z_{n1} I_1 + Z_{n2} I_2 + Z_{n3} I_3 \\ Z_n &= Z_{n1} I_1/I_n + Z_{n2} I_2/I_n + Z_{n3} I_3/I_n \\ &= Z_{n1} E_1/E_n + Z_{n2} E_2/E_n + Z_{n3} E_3/E_n \end{aligned} \tag{4.1}$$

When E_n is chosen to follow the electric field of the TE1 mode, the input impedances Z_n are then the impedances one would need to match to produce only TE1 radiation. I find that a uniform feed for all three slots provides the best performance, which I speculate could be due to intrinsic slot impedance variations due to proximity to the waveguide wall and to the other two slots in a three-slot element. Fig. 4.13 shows the mode coupling for a chosen feed impedance (a constant real impedance from a microstrip plus frequency-dependent reactance from a series capacitor, both shown in Fig. 4.12). This antenna is well coupled to TE1; efficiency over the band of interest (183-230 GHz) exceeds 90%. Bandwidth degradation with reduced slot packing density is shown in Fig. 4.14 (feed impedance and slot length is optimized at each density separately).

Second Resonance, Tightly Packed

In Fig. 4.15 I examine using the second resonance of a $3 \times \infty$ slot antenna array. Slots in each element are positioned at $x = 0, \pm 0.75\,\text{mm}$ within the waveguide. A $\lambda_0/4$ ($f = 220\,\text{GHz}$) silicon backshort sits behind the antenna ground plane. The slots have a length $l = 0.460\lambda_0$, width $w = 0.005\lambda_0$, and a tightly-packed spacing $d = 0.025\lambda_0$. An extraordinarily large bandwidth is observed, potentially covering the entire TIME band, though the low feed

resistance may pose a challenge. Further study is needed to determine if this result is physical.

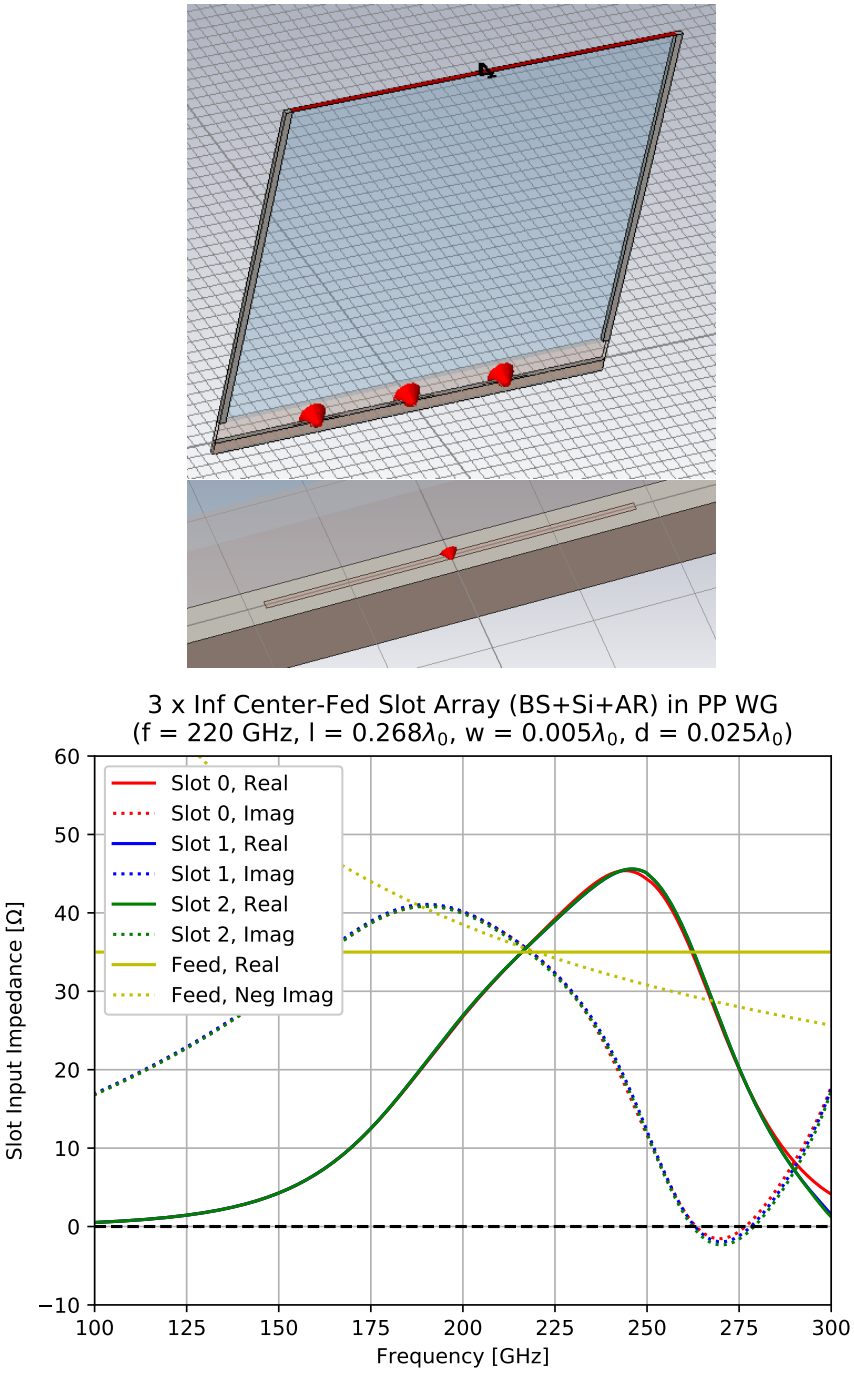

Figure 4.12: Simulation volume and impedance results for the first resonance of a tightly packed $3 \times \infty$ slot antenna array with silicon backshort and quartz AR coating in parallel plate waveguide.

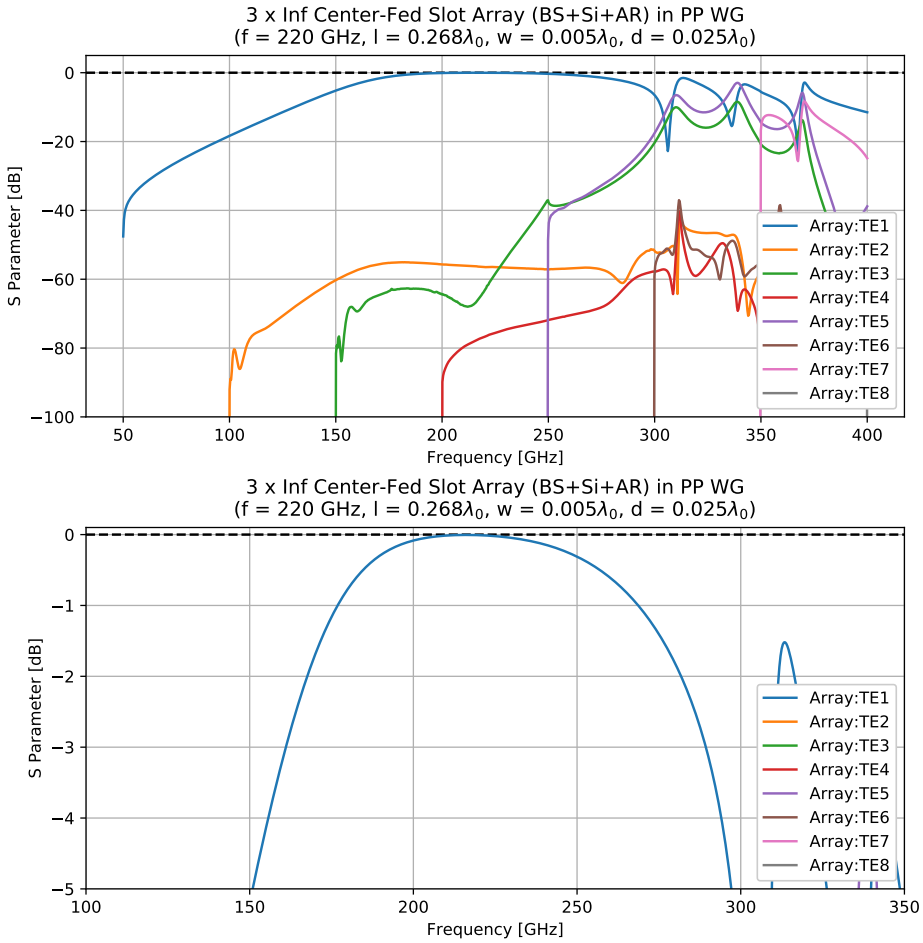

Figure 4.13: S parameters for the first resonance of a tightly packed $3 \times \infty$ slot antenna array with silicon backshort and quartz AR coating in parallel plate waveguide.

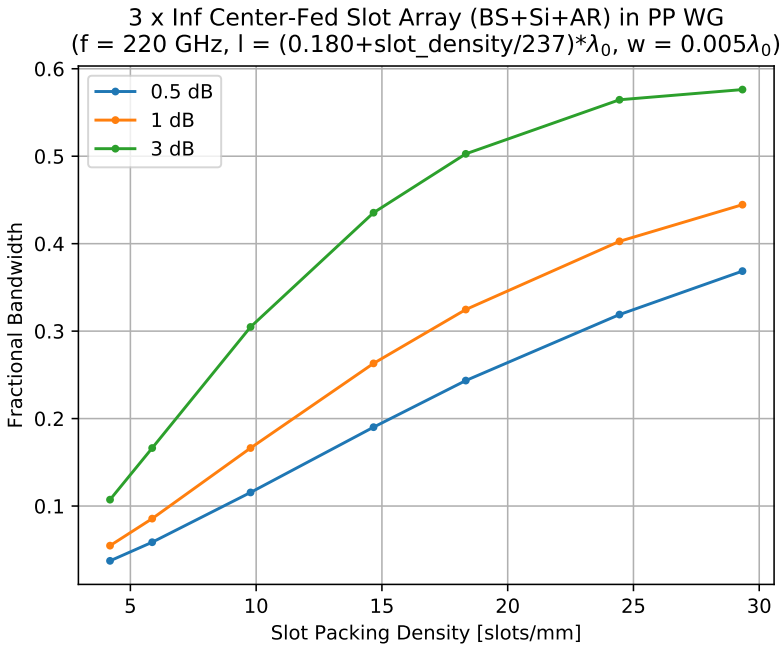

Figure 4.14: Bandwidth contours for a $3 \times \infty$ slot antenna array with silicon backshort and quartz AR coating in parallel plate waveguide.

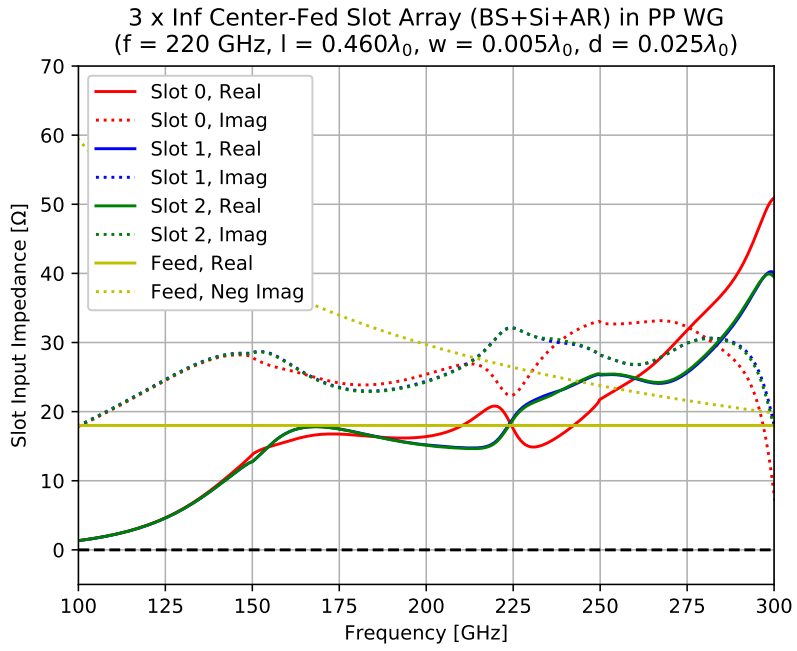

Figure 4.15: Impedance results for the second resonance of a tightly packed $3 \times \infty$ slot antenna array with silicon backshort and quartz AR coating in parallel plate waveguide.

4.4 Antenna Coupled Low Frequency Design for TIME

I now present the baseline TIME LF-AC (antenna coupled) design based on the results present in Sec. 4.3. At the cost of bandwidth, I remove the quartz AR coating to simplify fabrication and assembly. I retain the $3 \times \infty$ slot antenna array geometry centered in the 3 mm TIME parallel plate waveguide. A $\lambda_0/4$ ($f = 220\,\mathrm{GHz}$) silicon backshort sits behind the antenna ground plane. The slots have a length $l = 0.460\lambda_0$, width $w = 0.005\lambda_0$, and a tightly-packed spacing $d = 35.9\,\mu\mathrm{m}$; note the larger slot lengths required by the removal of the quartz immediately above the antenna.

The impedance for the three slots in the baseline design can be found in Fig. 4.17, repeated with both the Frequency and Transient solvers of CST as a check of robustness. I choose to feed with a 40Ω microstrip terminated with a 24.7 fF capacitor to ground. Alignment tolerancing studies were done by introducing a mounting gap between the antenna and the waveguide and by decentering the slots within the waveguide. I find negligible impact on the antenna performance with a 1 mm mounting gap and a 0.1 mm decentering, both of which should be achievable in TIME.

The density of the slots places 96 of the 3×1 antenna sub-elements spanning the spectral direction of one low frequency pixel. Terminating 96 separate antennas on one bolometer island is not feasible, so we must coherently sum multiple elements in a microstrip tree. Fig. 4.18 demonstrates the reduction in the antenna beam width due to destructive interference when adding multiple elements coherently. I choose a compromise by using three 3×32 antenna elements per pixel, which requires three terminations on the bolometer island and provides adequate illumination across the entire spectrometer grating. The central of the three low frequency modules is mounted 19° off-axis from the center of the grating, so we must introduce a beam steer to illuminate it properly. This is accomplished with a running microstrip path length difference between adjacent 3×1 antenna sub-elements, which introduces a time delay that can be thought of as tilting the plane of the antenna. All time delays for beam steering are done in 1.45 um microstrip, for which Sonnet simulations reports a wavelength of 585 um at 210 GHz. We need $\sim 2°$ relative phase shift per sub-element at 210 GHz to illuminate the grating center, which corresponds to an additional path length of 3.25 um per element. The resulting beam patterns computed in CST are shown in Fig. 4.19.

A completed device layout can be seen in Figures 4.20-4.23. This design is fully drop-in compatible with existing TIME LF modules and can coexist with micro-mesh based detectors on the focal plane. The feed capacitor and three-to-one microstrip coupler used were simulated in Sonnet and found to perform as expected. Adjacent microstrip crosstalk for the spacing used was found in simulation to be below -35 dB. I use Dolph-Chebyshev microstrip tapers [72] after the summing tree to reduce the microstrip width to keep the bolometer legs sufficiently thin; simpler taper designs were found to be inadequate for the magnitude of change required (see Fig. 4.24).

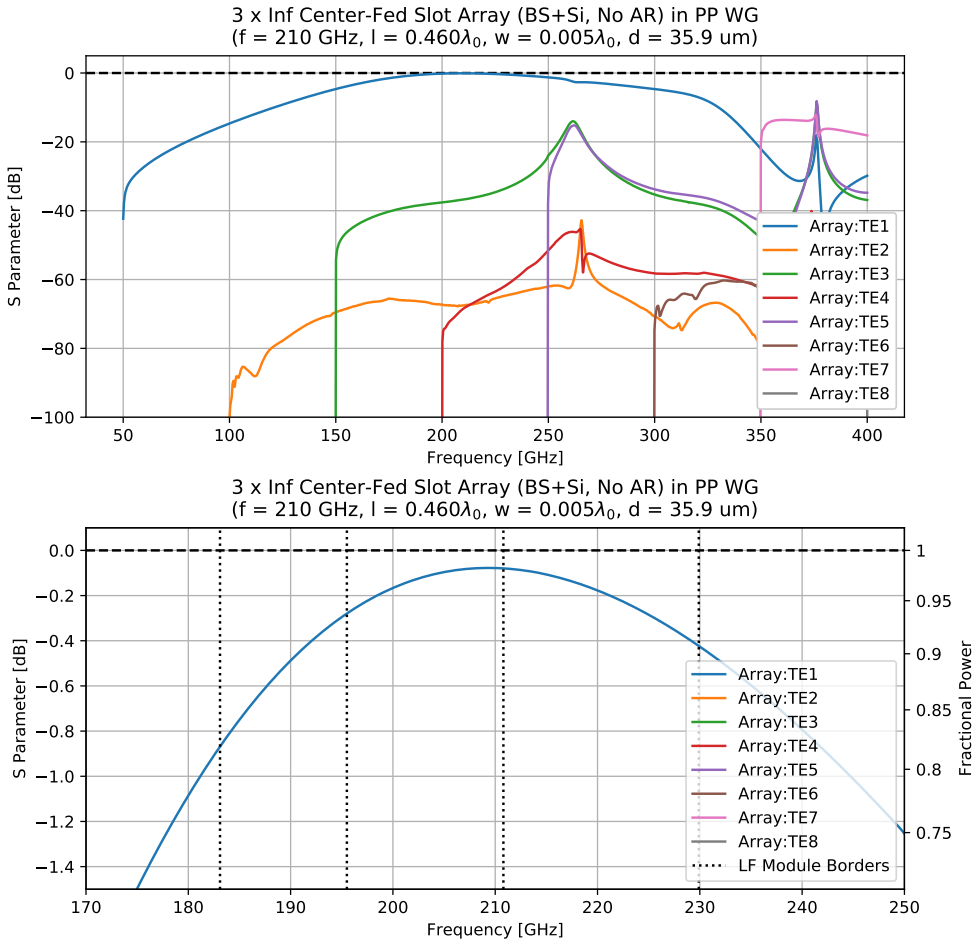

Figure 4.16: The S parameters for the baseline TIME LF-AC design, showing sufficient bandwidth in the band of interest (186-230 GHz, with the lowest frequencies devoted to atmospheric monitoring).

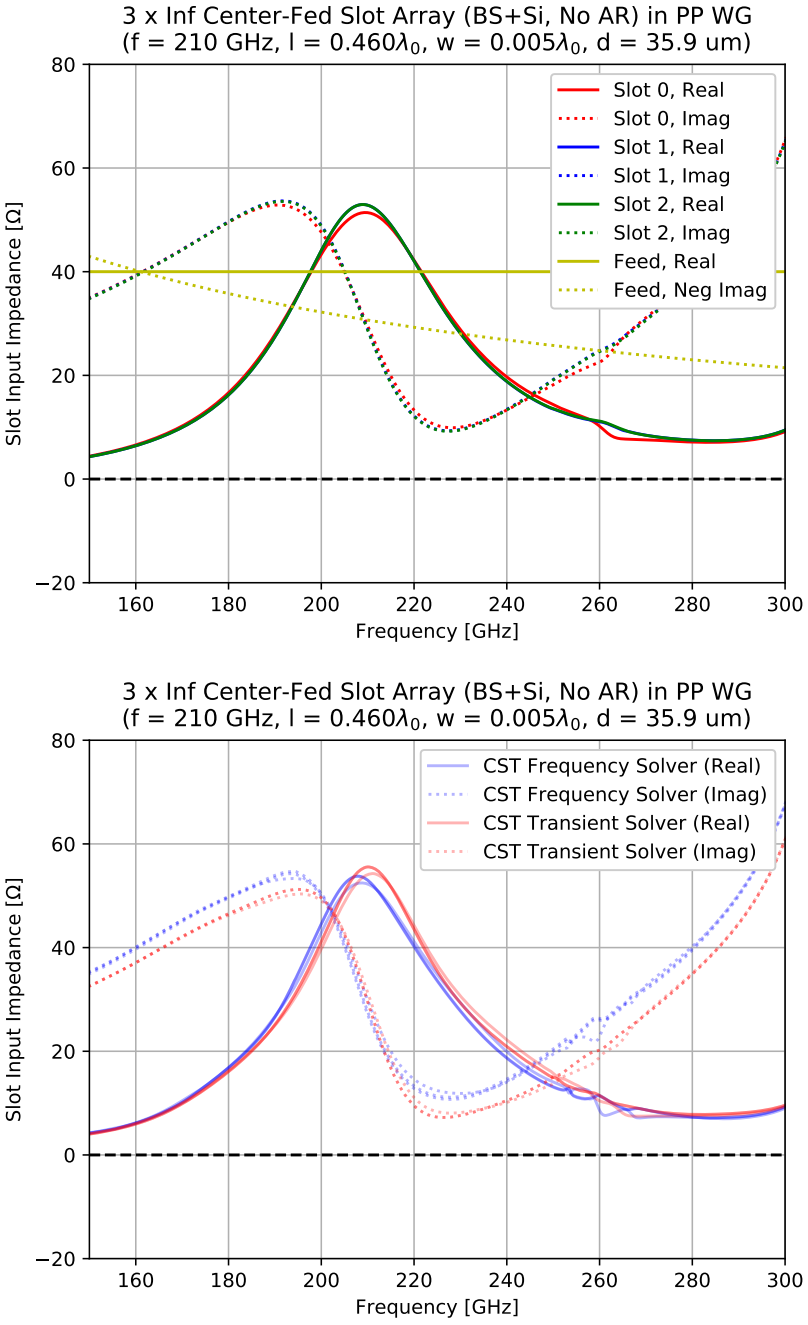

Figure 4.17: The slot impedances for the baseline TIME LF-AC design, repeated with both the Frequency and Transient solvers of CST.

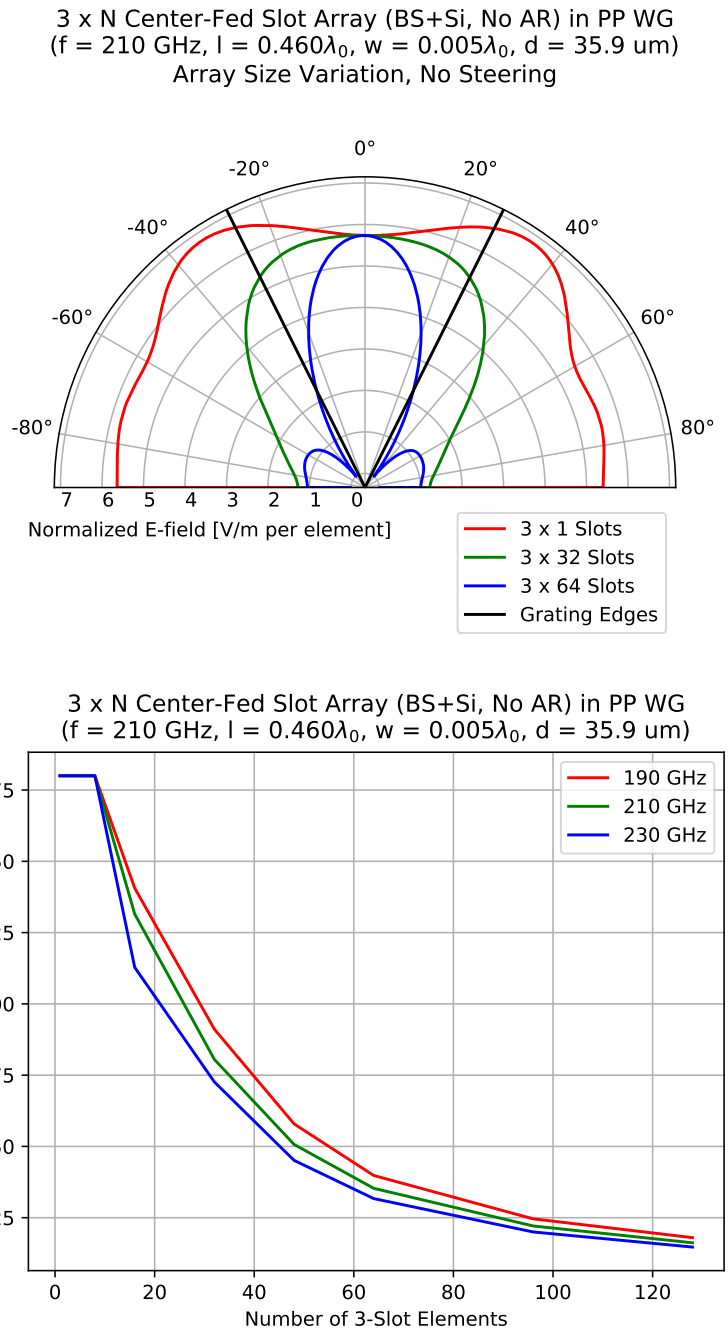

Figure 4.18: Expected beam size for 3×1, 3×32, and 3×64 element slot antenna arrays with the TIME LF-AC design.

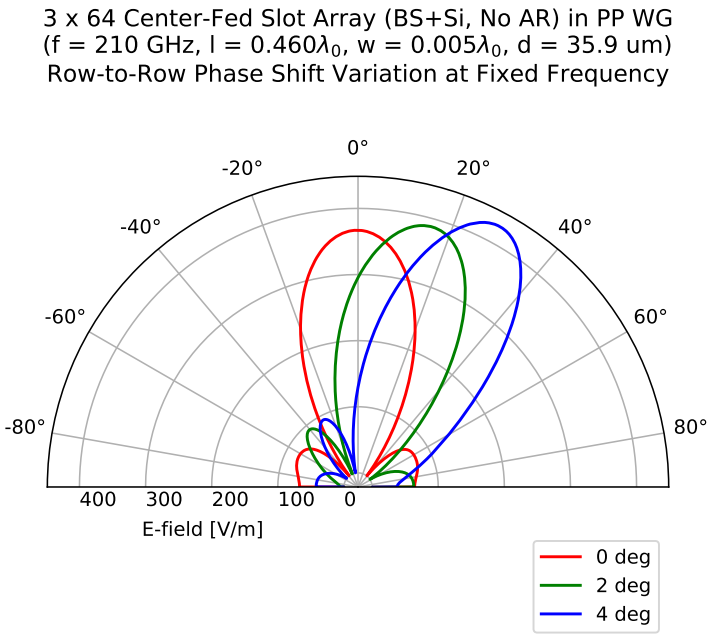

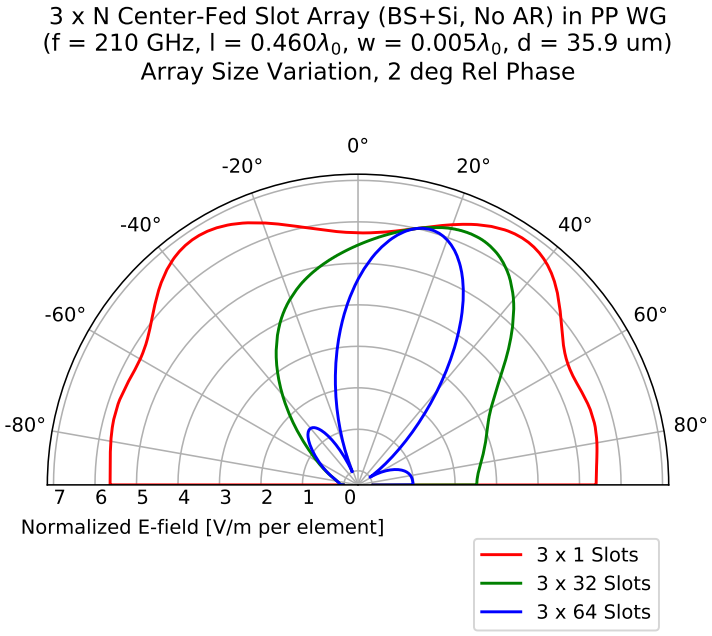

Figure 4.19: *Upper:* Expected beam steer for different subelement phasings in a 3×64 element slot antenna array with the TIME LF-AC design. *Lower:* Expected beam steer for different element sizes at a fixed 2° per sub-element relative phase.

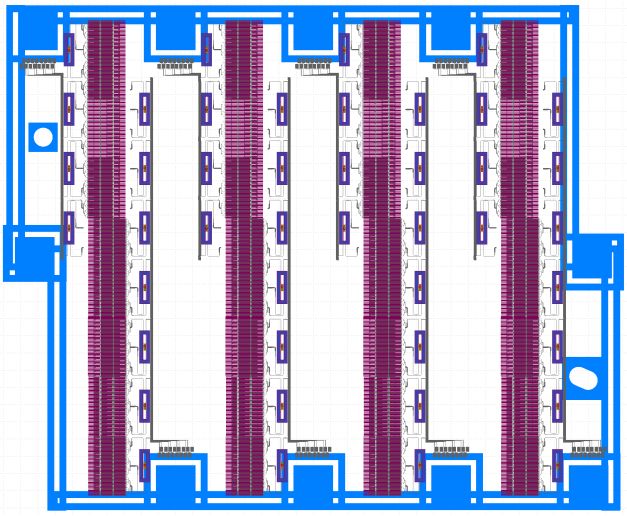

Figure 4.20: Overall subarray layout for the TIME LF-AC device, showing four spatial by eight spectral pixels. The completed design is drop-in compatible with traditional TIME LF modules, and can coexist with micro-mesh based subarrays.

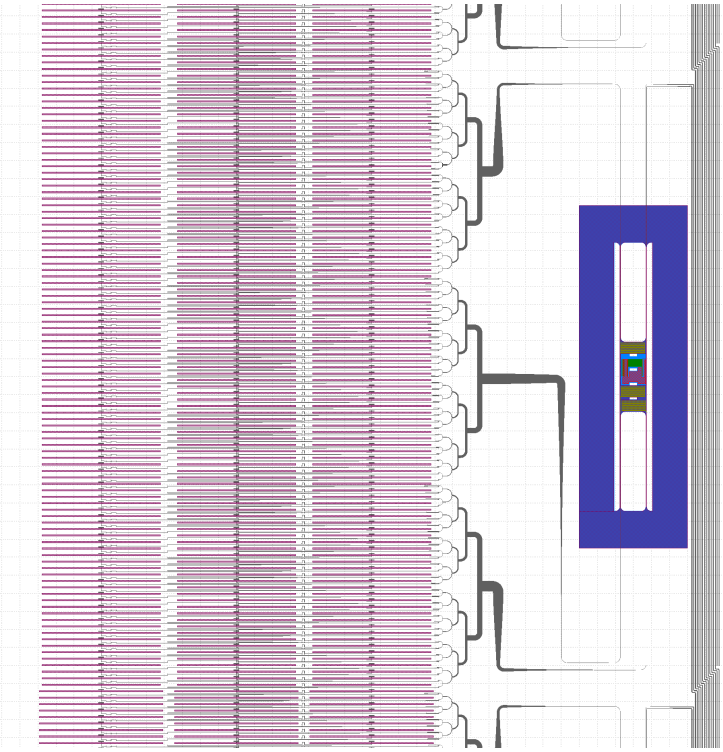

Figure 4.21: A single pixel (and the edges of the adjacent pixels) in the TIME LF-AC design. Three phased arrays of 3×32 slot antennas (pink) terminate on a single TES bolometer island, visible at the right.

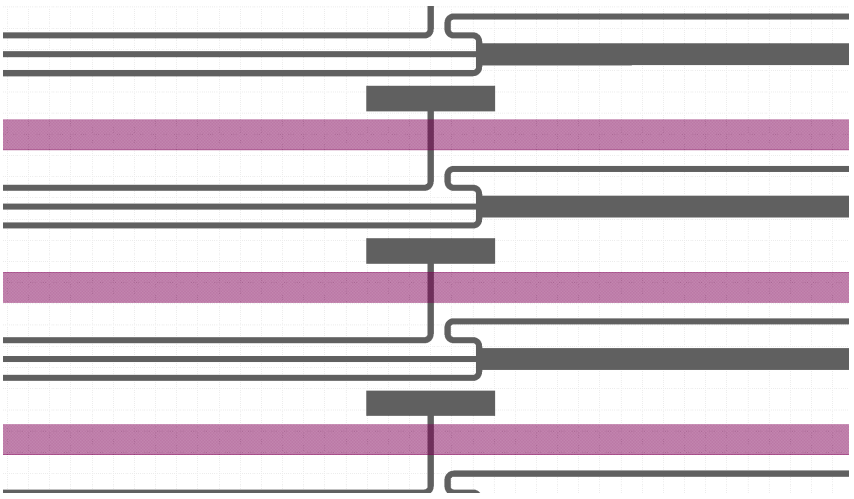

Figure 4.22: The feed capacitor and three-to-one microstrip coupler found near the middle of the central slot (part of which is shown in pink) in the TIME LF-AC design.

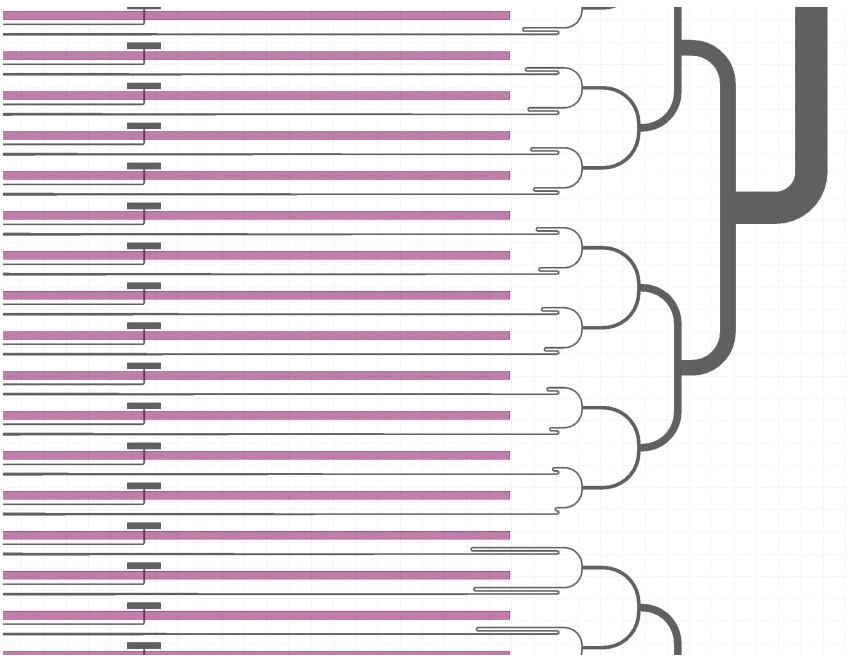

Figure 4.23: A portion of the TIME LF-AC microstrip summing tree, showing the relative path length difference between sub-elements to steer the beam.

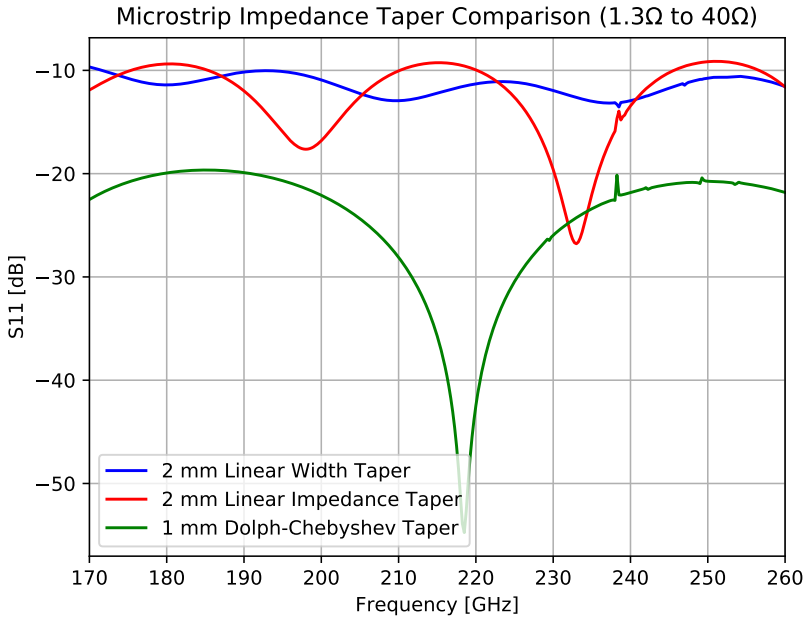

Figure 4.24: Expected performance of microstrip tapers from 1.3Ω to 40Ω over a specified length (1 mm or 2 mm), simulated in Sonnet. Simple tapers that linearly vary the microstrip width or impedance are insufficient for the TIME LF-AC design.

Chapter 5

Laboratory Instrument Characterization

In this chapter I describe efforts to characterize properties of the TIME instrument using the detectors described in Ch. 3. Characterization of the instrument while coupled to the telescope is covered in Ch. 6.

5.1 Saturation Power and Phonon Noise

Analogous to Johnson noise in an electrical resistor, a bolometer's weak thermal conductance G to the surrounding bath temperature results in a white phonon noise whose power spectral density is of the form $S = 4k_B T^2 G$ [51]. The proper form for this noise power should account for the temperature gradient driven across the thermal link (from the Ti TES superconducting transition temperature T_c on the bolometer to T_{bath} at the bath); as a conservative estimate, we take the temperature to be T_c and the thermal conductance to be $G_c = G(T_c)$. For background limited detectors, this phonon noise must be subdominant to the white photon noise level under the expected sky loading conditions (Sec. 2.6); this drives design targets to low temperature (Sec. 3.5) and low thermal conductance G. The temperature gradient across the thermal conductance is fixed by T_{bath} and T_c for a TES bolometer; as shown in Eqn. 5.1, this requires a constant power flow across the link that is proportional to G_c. This is referred to as the saturation power (P_{sat}) of the device, which is the optical power limit for the channel ($P_{sat} = P_{optical} + P_{bias}$). At powers exceeding P_{sat}, the detectors are driven normal and cease to operate, limiting the weather conditions in which the detector can operate and driving design targets toward high values of G_c. The optimal value for G_c is thus one that provides a sufficient saturation power safety factor, while remaining low enough to be photon noise dominated. As presented in Sec. 2.6, TIME targets a saturation power of 3-4 pW for an expected load of 0.5-1.5 pW across the band. For $T_c = 500\,\mathrm{mK}$ and $T_{bath} = 300\,\mathrm{mK}$ with a thermal conductance scaling exponent $\beta = 2$, this corresponds to a target $G_c = 23 - 31\,\mathrm{pW/K}$ or $G_{450} = 18 - 25\,\mathrm{pW/K}$ ($G_{450} = G(450\,\mathrm{mK})$ is reported because it is a property of the geometry of the legs, which can be compared directly for devices with moderate variation in T_c). Modeling $G(T)$ as a power law, the detector

saturation power can be written in terms of G_{450} as follows.

$$\begin{aligned} G(T) &= \frac{\mathrm{d}P}{\mathrm{d}T} = G_c \left(\frac{T}{T_c}\right)^{\beta} = G_{450} \left(\frac{T}{450\,\mathrm{mK}}\right)^{\beta} \\ P_{sat} &= \int_{T_{bath}}^{T_c} G(T)\,\mathrm{d}T \\ &= \frac{G_c T_c}{(\beta+1)} \left(1 - \left(\frac{T_{bath}}{T_c}\right)^{\beta+1}\right) \\ &= G_{450}\,\frac{T_c^{\beta+1} - T_{bath}^{\beta+1}}{(\beta+1)(450\,\mathrm{mK})^{\beta}} \end{aligned} \tag{5.1}$$

We measure the saturation power of a TES bolometer from a load curve, during which the TES bias current (though the shunt resistor, see Fig. 3.3) is swept while monitoring the TES branch current. Load curves for a single detector at multiple bath temperatures are shown in Fig. 5.1 (upper). At high bias currents ($\gtrsim 300\,\mu$A as shown), the TES bias power exceeds its saturation power and the TES acts as a normal resistor in a current divider configuration with the shunt resistor. At low bias current ($\lesssim 100\,\mu$A as shown), the TES is fully superconducting, and its series resistance acts in a current divider configuration with the shunt resistor. Using the known resistance of the shunt in parallel with the TES ($R_{shunt} \approx 4\,\mathrm{m}\Omega$), the slopes in the normal and superconducting state provide measurements of the TES normal resistance R_n and TES series resistance R_{series} respectively.

At intermediate bias points (the region of negative slope) the TES is locked at some point in its superconducting transition. The TES current as measured by the readout chain includes an unknown offset that is corrected by forcing the Ti normal slope to intercept zero. (Note that near the low-bias edge of the superconducting transition, the SQUIDs can momentarily lose lock, resulting in a change in this offset that presents as a discontinuity. Because load curves are taken from high to low bias, the offset inferred from the Ti normal slope is accurate in the transition. We therefore only require the slope of the superconducting region, its offset need not be corrected.) Using the measured series and shunt resistance, one can transform the TES current and bias current into the TES dissipated power and TES resistance (Fig. 5.1, lower). In this space, the TES transition presents itself as a region of constant dissipated power (the saturation power) over a range of TES resistances (lock points).

At the TES normal resistance the dissipated power begins to rise rapidly at effectively constant resistance.

With the TES saturation power measured at various bath temperatures (achieved with a focal plane heater), one can fit Eqn. 5.1 and extract values for the thermal conductance G_{450}, the transition temperature T_c, and the scaling factor β. One such fit is shown in Fig. 5.2. Results across the focal plane in Run 2019-10 are shown in Fig. 5.3 and 5.4. Note the extraordinarily high values for G_{450} presented (up to 140 pW/K); nearly all devices shown are untrimmed, meaning the extra silicon nitride bolometer legs used to improve fabrication yield have not yet been removed with a laser trimmer. Initial G measurements are performed on untrimmed devices, allowing the results to inform the trimming process (potentially leaving some number of extra legs to tune the G to its desired value). To measure the impact of leaving various numbers of laser legs intact, the detectors installed in coordinates $23 < f < 36$ have been partially trimmed to leave a sample set of detectors of each of five configurations (mostly accounting for the variation seen in the results). Final G_{450} values for a trimmed device would be 3x lower than for an untrimmed device, which still places much of the array above the target value. As a result, future TIME bolometers will be using thinner silicon nitride, reducing the cross-sectional area of the suspension legs.

Measurements for G_{450} across years of TIME device production and testing are presented in Fig. 5.6, showing significant variation between subarrays. Some of this scatter is believed to arise from uncertainty in the silicon nitride thickness, which is not measured on a per-wafer basis.

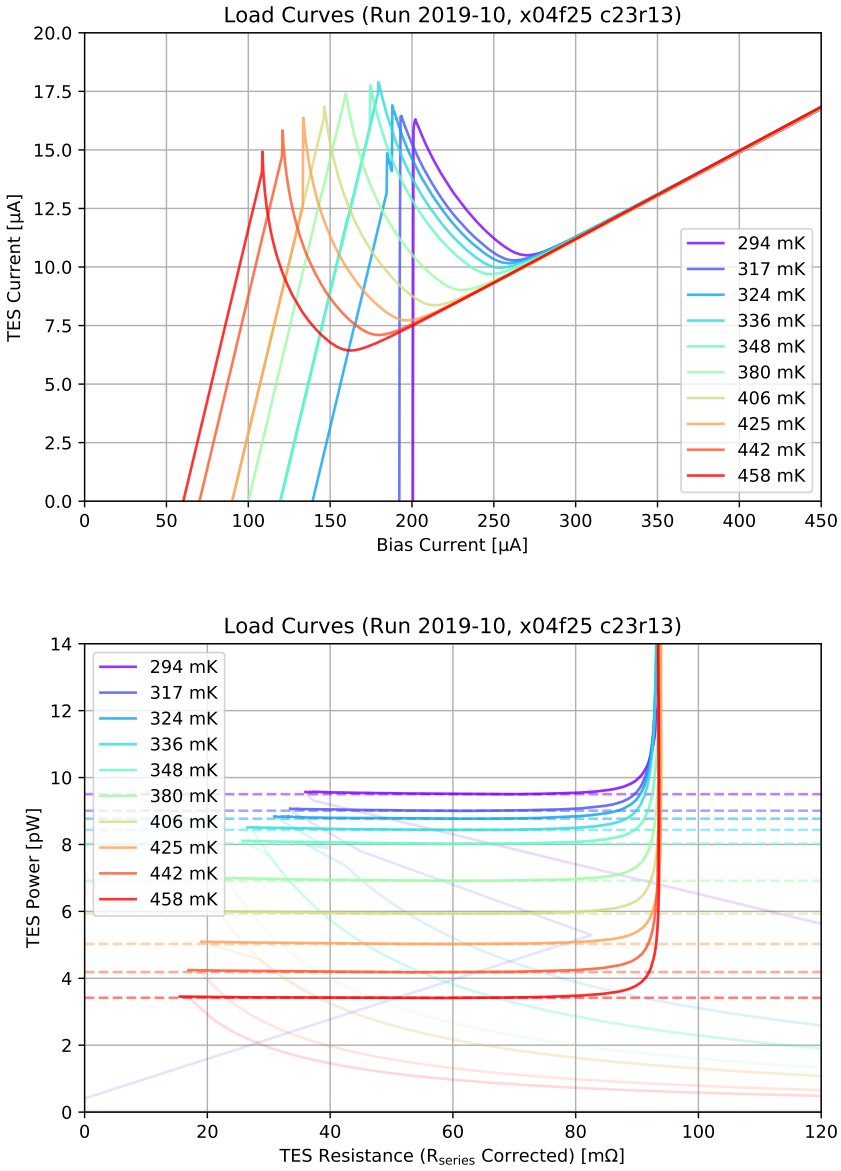

Figure 5.1: TES load curves for a single detector taken at various bath temperatures.

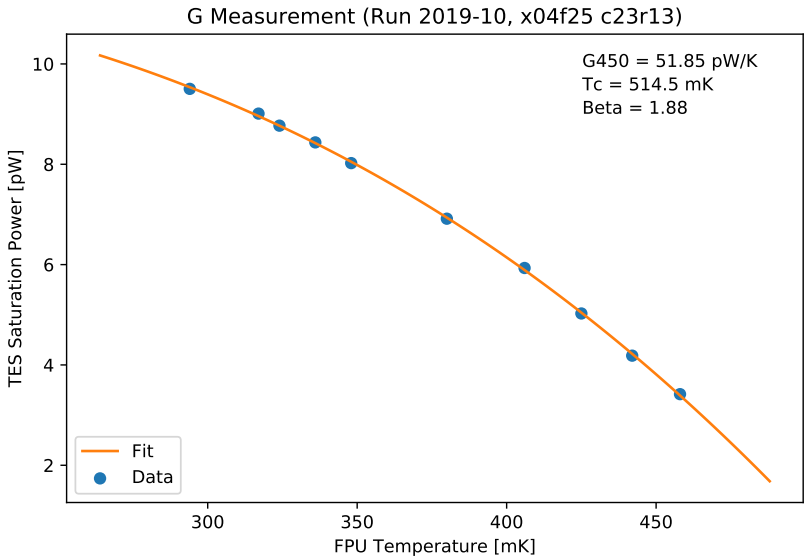

Figure 5.2: Model fitting results for the TES saturation powers extracted from Fig. 5.1.

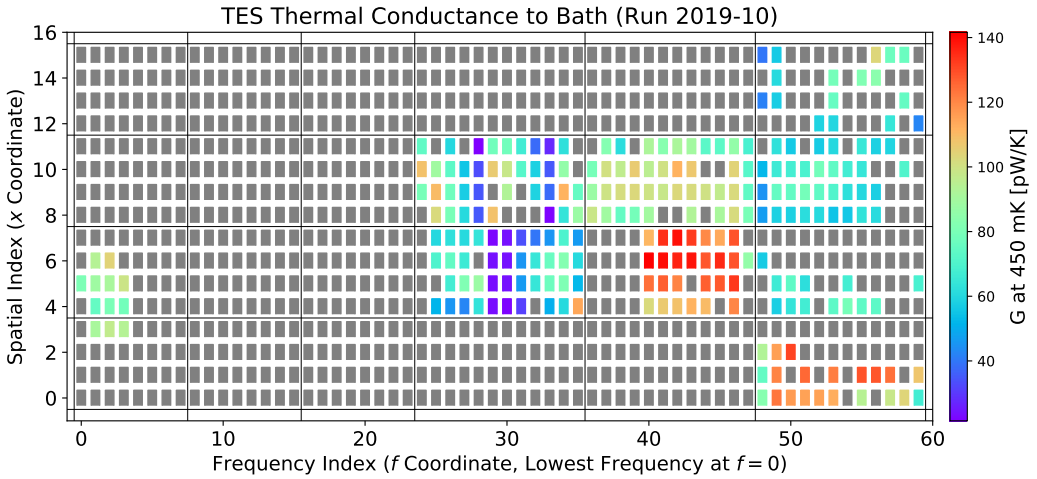

Figure 5.3: A focal plane map showing the observed variation in G_{450}. Black lines indicate subarray borders, the fundamental fabrication unit. Note that, with the exception of the subarrays installed at coordinates $23 < f < 36$, all detectors shown are tested before laser leg trimming; the final G_{450} after trimming is expected to be 3x lower. The detectors in coordinates $23 < f < 36$ are trimmed to varying degrees, forming five distinct G_{450} clusters and explaining much of the scatter observed.

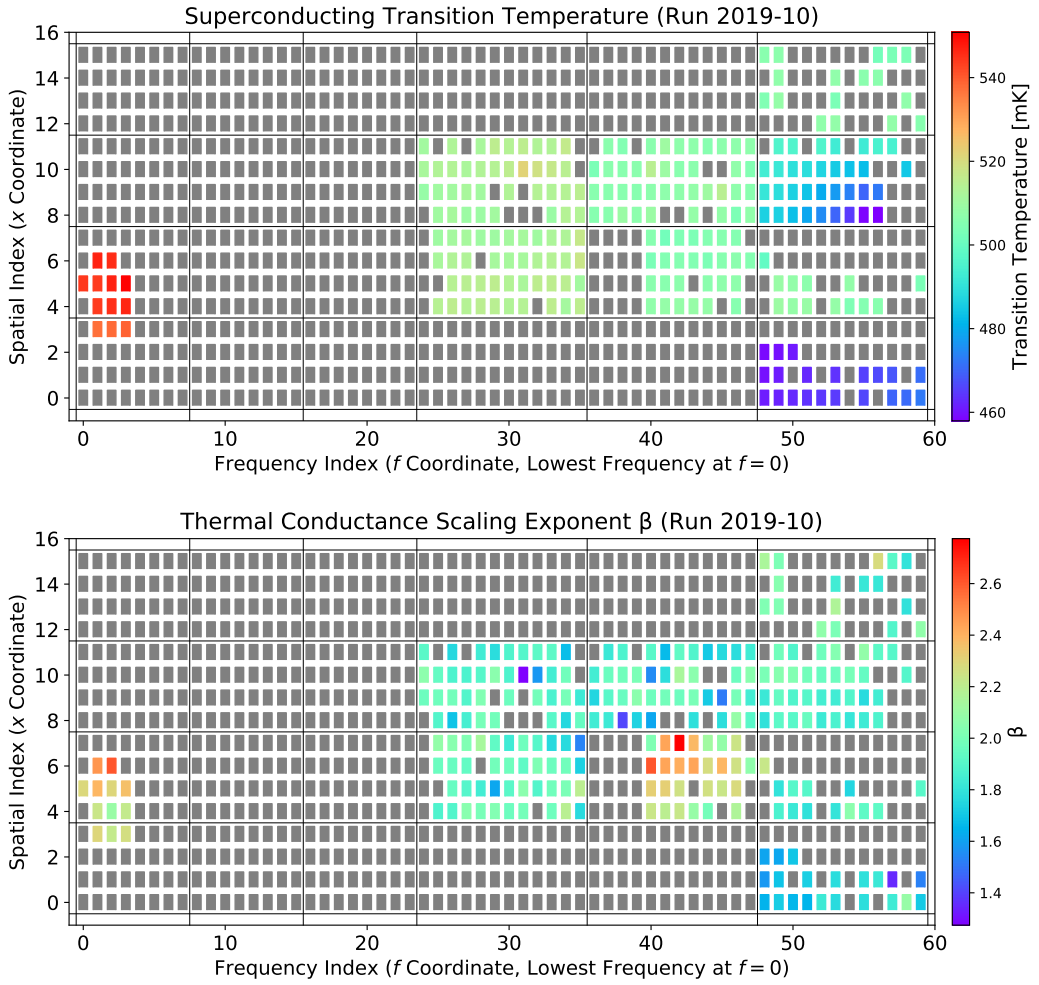

Figure 5.4: A focal plane map showing the observed variation in T_c and β. Black lines indicate subarray borders, the fundamental fabrication unit.

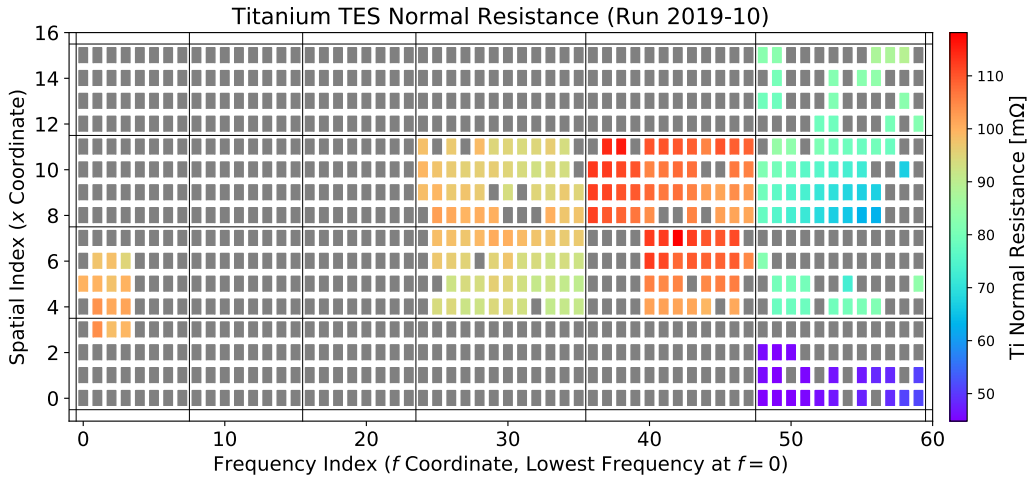

Figure 5.5: A focal plane map showing the observed variation in the Ti normal resistance. Black lines indicate subarray borders, the fundamental fabrication unit.

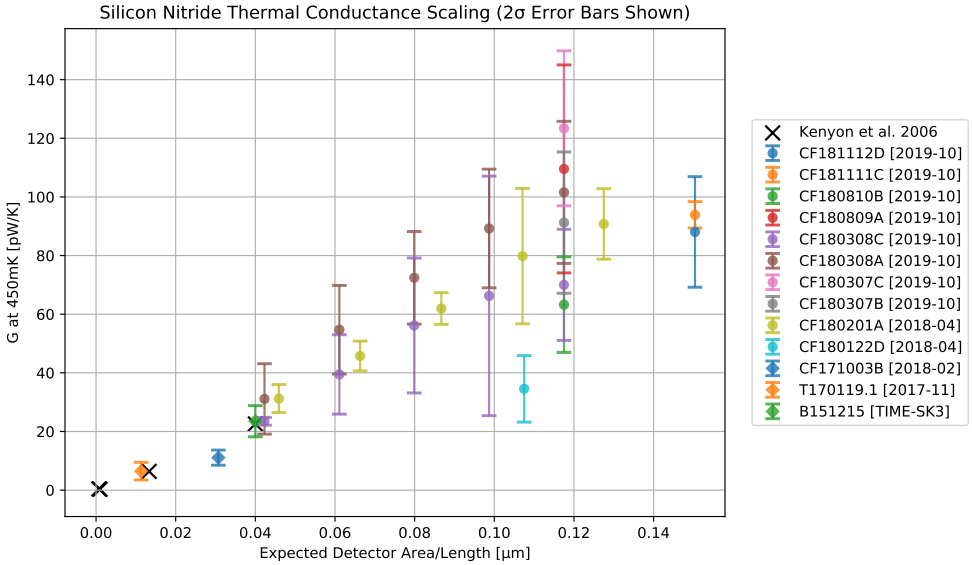

Figure 5.6: A compilation of measurements of G_{450} in TIME detectors (over several years of fabrication and testing) plotted against the geometric scaling factor of the silicon nitride support legs. Median values and 2σ error bars are shown for each tested subarray. Note that precise silicon nitride thickness measurements are not available for most subarrays, so their respective target thicknesses are assumed.

5.2 Time Constants

Detector optical response time constants have been measured both with the cryostat in its nominal optical configuration and with the cryostat in a dark configuration (with metal plates replacing each of the thermal filters). In the optical configuration we use a 900C thermal source with a 1 inch aperture that is modulated by either a trigger-controlled shutter or a rotating chopper wheel; the modulation frequency is swept, and a chopper state reference single is recorded by the readout electronics. In the dark configuration, a room temperature 1650 nm IR LED (MTE5016-525-IR) driven by a frequency-swept function generator is coupled to a low-OH 600 um 0.22 NA 400-2200 nm fiber (Thor Labs MV64L1), which runs (via a vacuum fiber feedthrough and thermal breaks at each temperature stage) to a module enclosure at the FPU (depicted in Fig. 5.8). A single module is mounted in the enclosure. An optically-white inner cavity acts as a crude integrating sphere to distribute the light across the module, and a series of 0.8 mm holes centered above each channel's absorber reduces coupling to the silicon wafer. The reverse side of this wafer guard is painted optically black to absorb light reflected by the detectors, which are not expected to be well-coupled to infrared light (the detector absorber grid spacing is too large at these wavelengths). 1650 nm is chosen to be above the silicon band-gap of 1130 nm, further reducing wafer coupling. Despite the added complexity, the fiber excitation allows for time constants to be measured for detectors that would saturate on a room temperature load (which is not the case for the detectors presented).

Data is recorded and processed for both configurations similarly. I step through a range of detector biases values and square wave frequencies (0.5-150 Hz for the LED, 0.5-15 Hz for the shutter), recording between 5 and 60 seconds of data at each. The reference signal from the function generator or chopper wheel is recorded as a single bit by the readout electronics, so a bandpass filter (centered at the excitation frequency) is applied to both the detector signal Y and the reference I_{ref} to remove higher order harmonics of the square wave. I then construct a 90° phase shifted version of the reference signal from the Hilbert transform ($Q_{ref} = -\operatorname{Im}(\hat{I}_{ref})$, where $\hat{I}_{ref}$ is the Hilbert transform of I_{ref}). At each excitation frequency, the in-phase (I) and quadrature (Q) demodulation terms are found by multiplying these two references against a copy of the signal timestream and filtering down to DC. At each frequency f I multiply the complex quantity $I + iQ$ by $\exp(2\pi i\, f\, t(f))$, where $t(f)$ is the

frequency-dependent group delay of the MCE digital low pass filter (shown in Fig. 5.7, Type 1 was used); I' and Q' refer to the real and imaginary components of this new complex quantity, which has the known filter time shift removed (the digital filter is not applied to the single-bit auxiliary input channel). I fit a single-pole low-pass transfer function to the measured I and Q points simultaneously with three free parameters: a cutoff frequency at which half of power is lost (f_{3dB}), an overall amplitude or DC gain (A_0), and a time shift (linear phase difference) between the signal and reference (Δt). The Δt term accounts for any time offset (beyond that already accounted for from the MCE filter) between the chopper reference and the physical change in the signal, which is negligible for the LED but significant for the shutter; in principle Δt can be assumed constant across all detectors, but that has not been done here. Note that I define the half-power point f_{3dB} to be the point where the amplitude of the transfer function is 1/2 instead of $1/\sqrt{2}$, as observed power is proportional to the measured TES current (not the current squared, see Sec. 3.1).

$$\begin{aligned} H(\omega) = I(\omega) + i\,Q(\omega) &= \frac{A_0}{1+i\omega\alpha}\, e^{i\omega\,\Delta t} \\ |H(2\pi f_{3dB})| \equiv \frac{A_0}{2} &= \frac{A_0}{\sqrt{1+(2\pi f_{3dB}\alpha)^2}} \\ \alpha &= \frac{\sqrt{3}}{2\pi f_{3dB}} \end{aligned} \tag{5.2}$$

I weight each point in the least-squares fitting of the model to I and Q by the inverse of the magnitude $\sqrt{I^2+Q^2}$ to ensure that points with a higher signal-to-noise ratio are well-captured by the fit. Finally, I convert I and Q to a magnitude and a phase; I divide out the DC gain when plotting magnitude, but I do not remove the linear phase offset introduced by Δt from the plotted phase to simplify visual inspection of fit quality.

Sample results from the thermal source and the IR LED (from different detectors) are shown in Figures 5.9-5.12. To demonstrate the validity of the IR fiber time constant measurements, sample detectors measured with both methods in different cryogenic runs are shown in Fig. 5.13.

Overall, detector time constants are found to be slower than desired (a 3dB cut-off frequency in the range 10-30 Hz at optimal bias) and highly variable from subarray to subarray. Assuming we cover a 1° field with 0.4 arcmin

beams, we have 150 spatial bins in the scan direction. We scan continuously, but as an approximation I assume we need 5τ settling for each bin to avoid bleed from any bright point sources in the field. $f_{3dB} = 10\,\mathrm{Hz}$ corresponds to $\tau \approx 16\,\mathrm{ms}$, which leads to crossing our field every 12 seconds. At these speeds, atmospheric and instrumental $1/f$ noise contribution is not negligible, affecting sensitivity on large spatial scales.

Results from two subarrays are shown in Fig. 5.14, which are of particular interest due to their large range in detector thermal conductance G achieved by selectively trimming varying numbers of laser legs. To first order, one expects the time constant of the detectors to scale as the heat capacity over the thermal conductance ($\tau_{eff} \sim (C/G)/\mathscr{L}$, where $\mathscr{L}$ is the detector loop gain) [51]. Subarray m3s1 in Fig. 5.14 displays only a factor of two reduction in its 3dB cut-off frequency over a fourfold reduction in its measured G, indicating time constants are being limited by a separate factor. Model results presented in Sec. 3.4 suggest that the internal time constant between the absorber and the TES may be responsible for this observation. Improved thermal sinking across the mesh is expected in upcoming TIME devices based on the v7 design presented in Chapter 3. With the goal of testing whether or not internal time constants were the limiting factor for TIME devices, I purposely severed all metallic connections between the main absorber web and the TES bridge for three detectors in subarray m3s1 using a laser trimmer; the resulting mesh is coupled to the TES only by narrow silicon nitride bars at the top and bottom of the structure, as shown in Fig.5.15. Time constant results for these channels are shown in black in Fig. 5.14; these channels are significantly slower than their otherwise-equivalent neighbors.

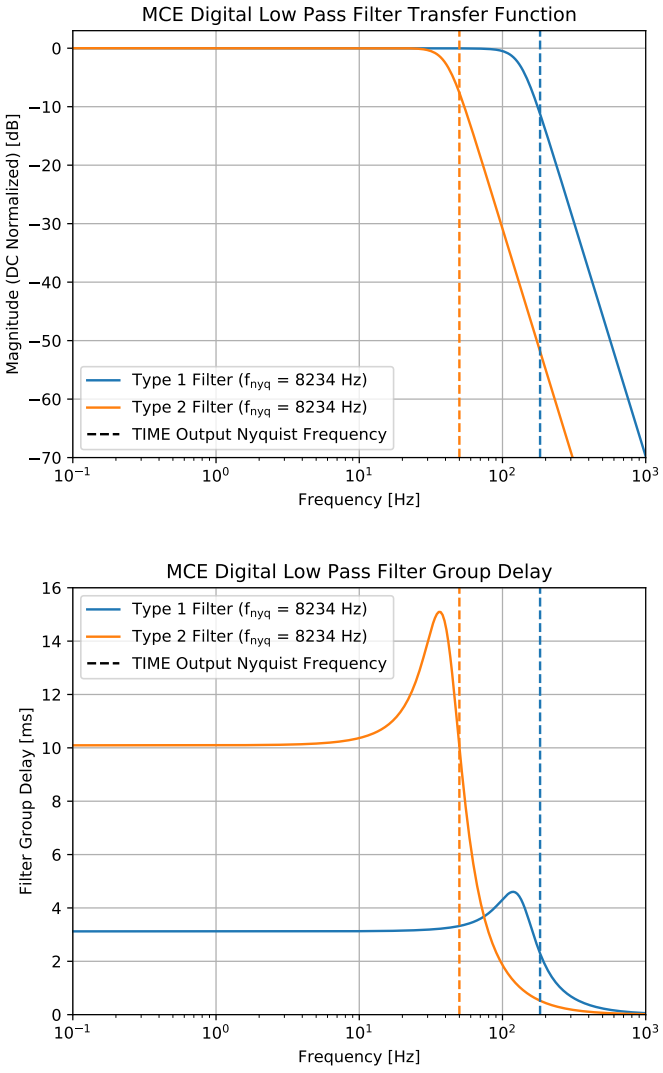

Figure 5.7: The transfer function and group delay for two of the digital low pass filters designed by UBC for the MCE readout electronics. This group delay is not applied to recorded reference signals and must be accounted for separately.

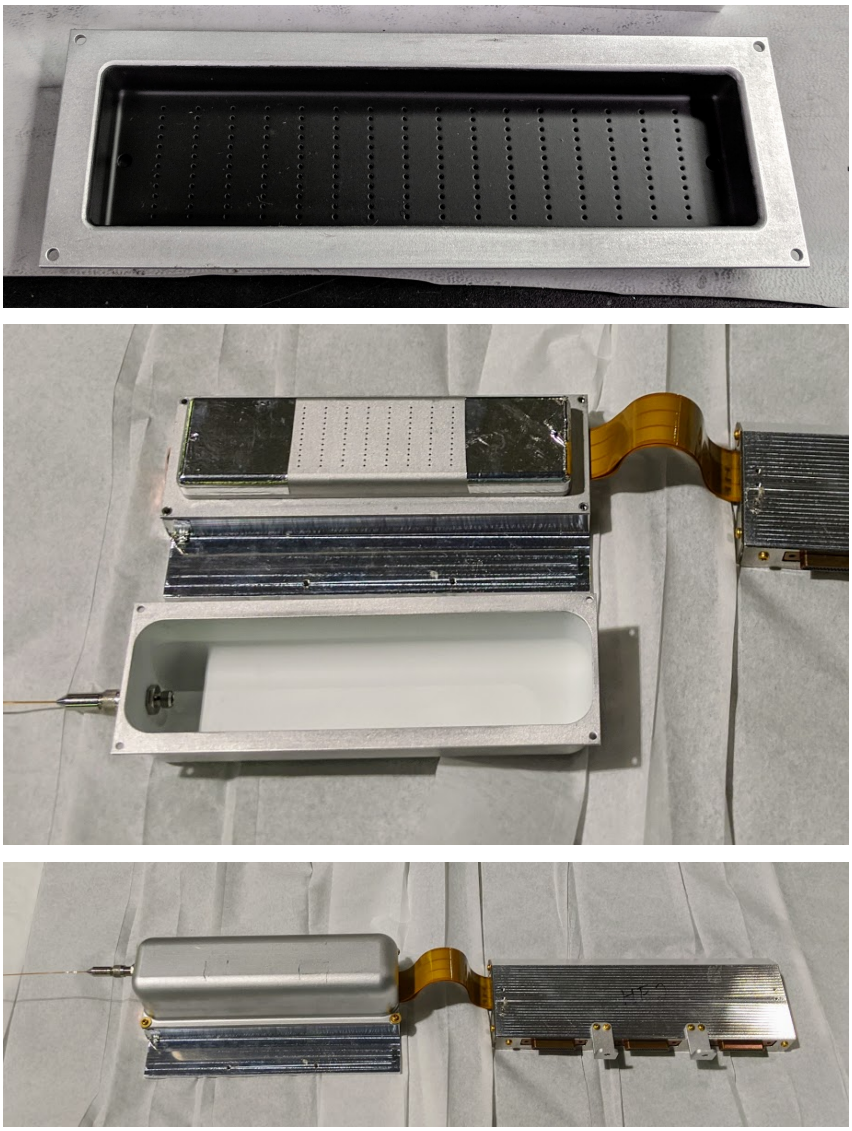

Figure 5.8: The fiber-coupled module holder used for when measuring detector time constants. An optically-white inner cavity acts as a crude integrating sphere to distribute the light across the detector module, and a series of holes centered above each channel's absorber reduces coupling to the silicon wafer. The reverse side of this wafer guard is painted optically black to absorb light reflected by the detectors.

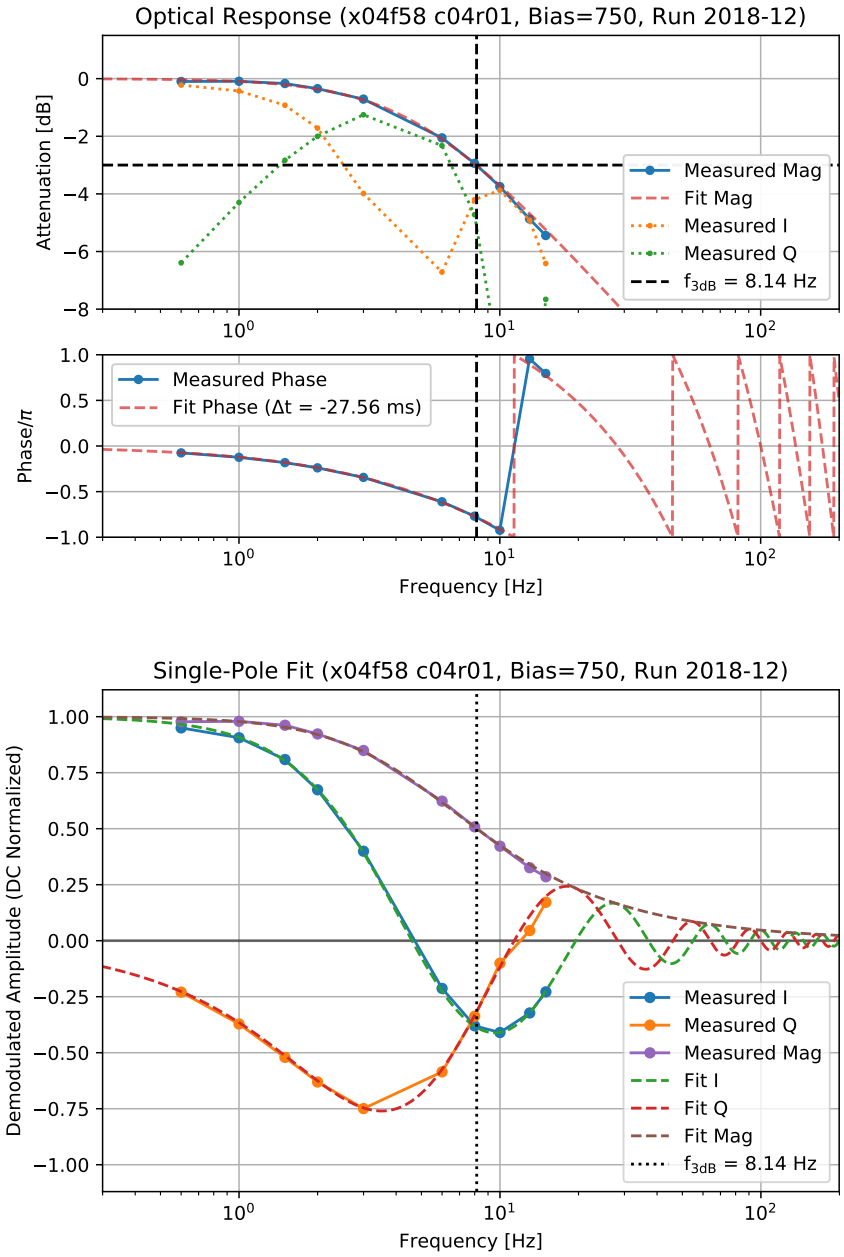

Figure 5.9: Optical transfer function and fit results measured with a thermal source and a trigger-controlled shutter for a single channel at one detector bias level.

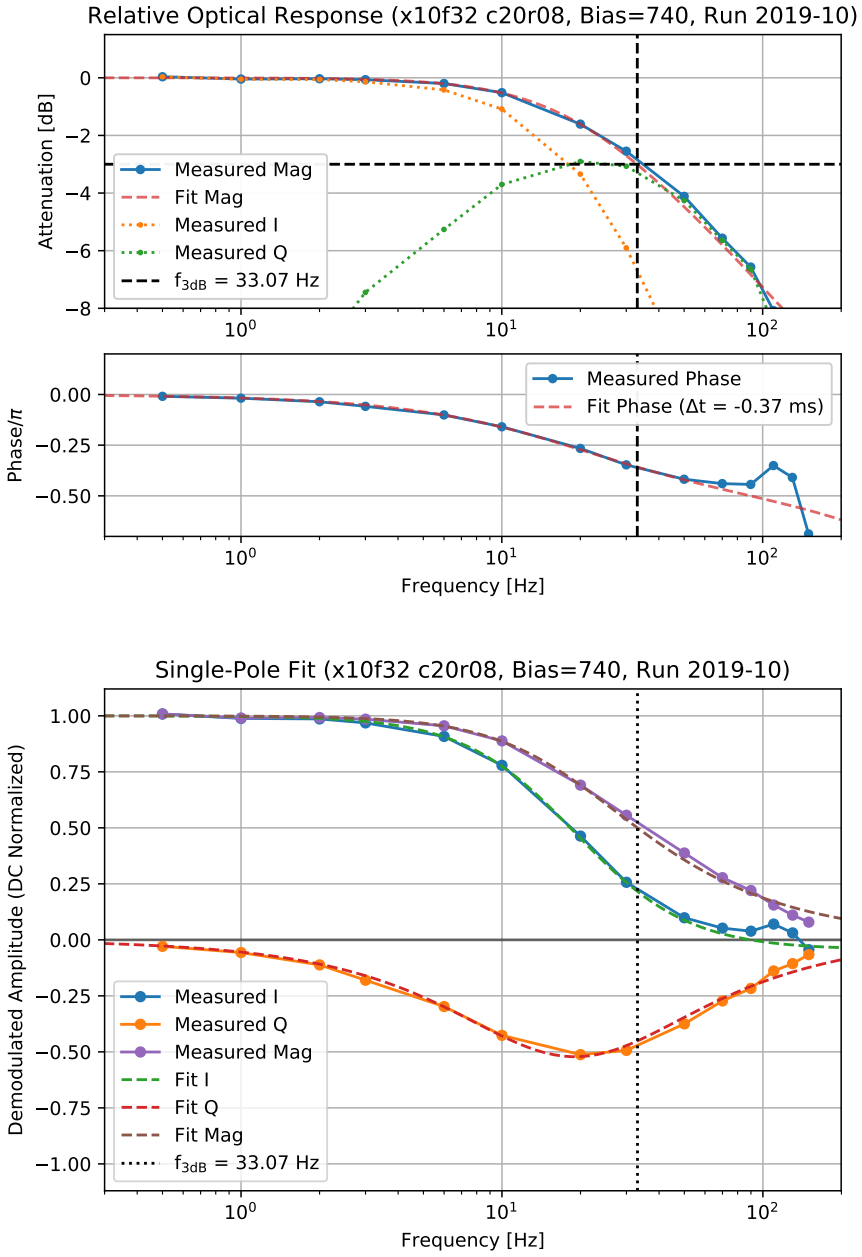

Figure 5.10: Optical transfer function and fit results measured with a fiber-coupled IR LED for a single channel at one detector bias level.

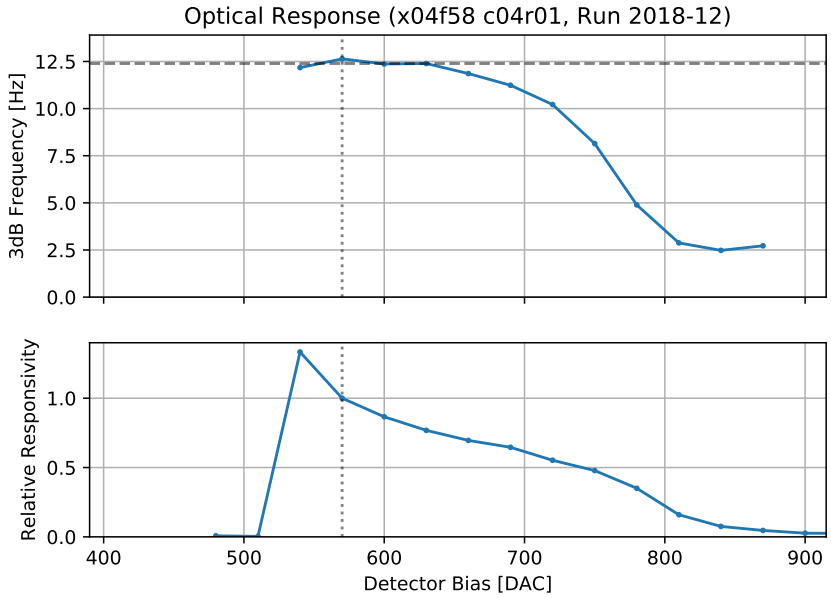

Figure 5.11: Cut-off frequency and relative responsivity measured with a thermal source and a trigger-controlled shutter for a single channel across a range of bias levels.

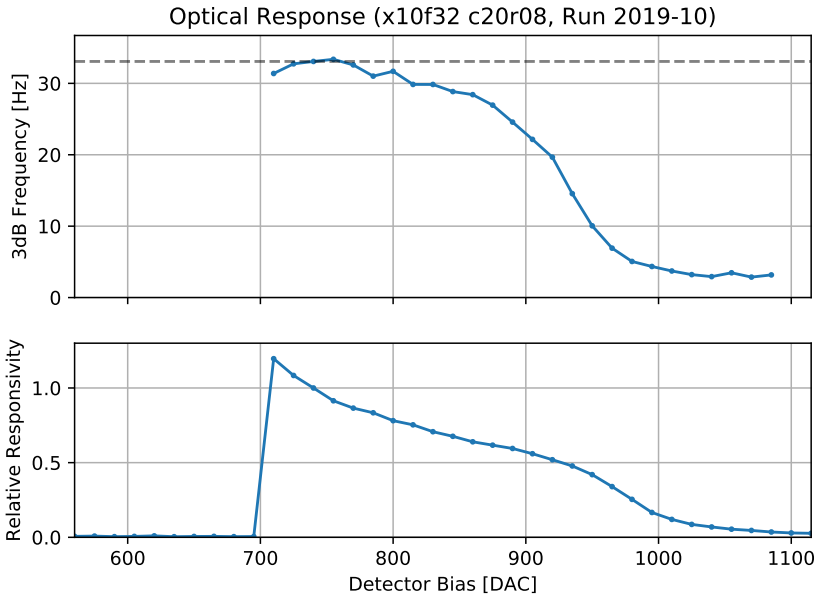

Figure 5.12: Cut-off frequency and relative responsivity measured with a fiber-coupled IR LED for a single channel across a range of bias levels.

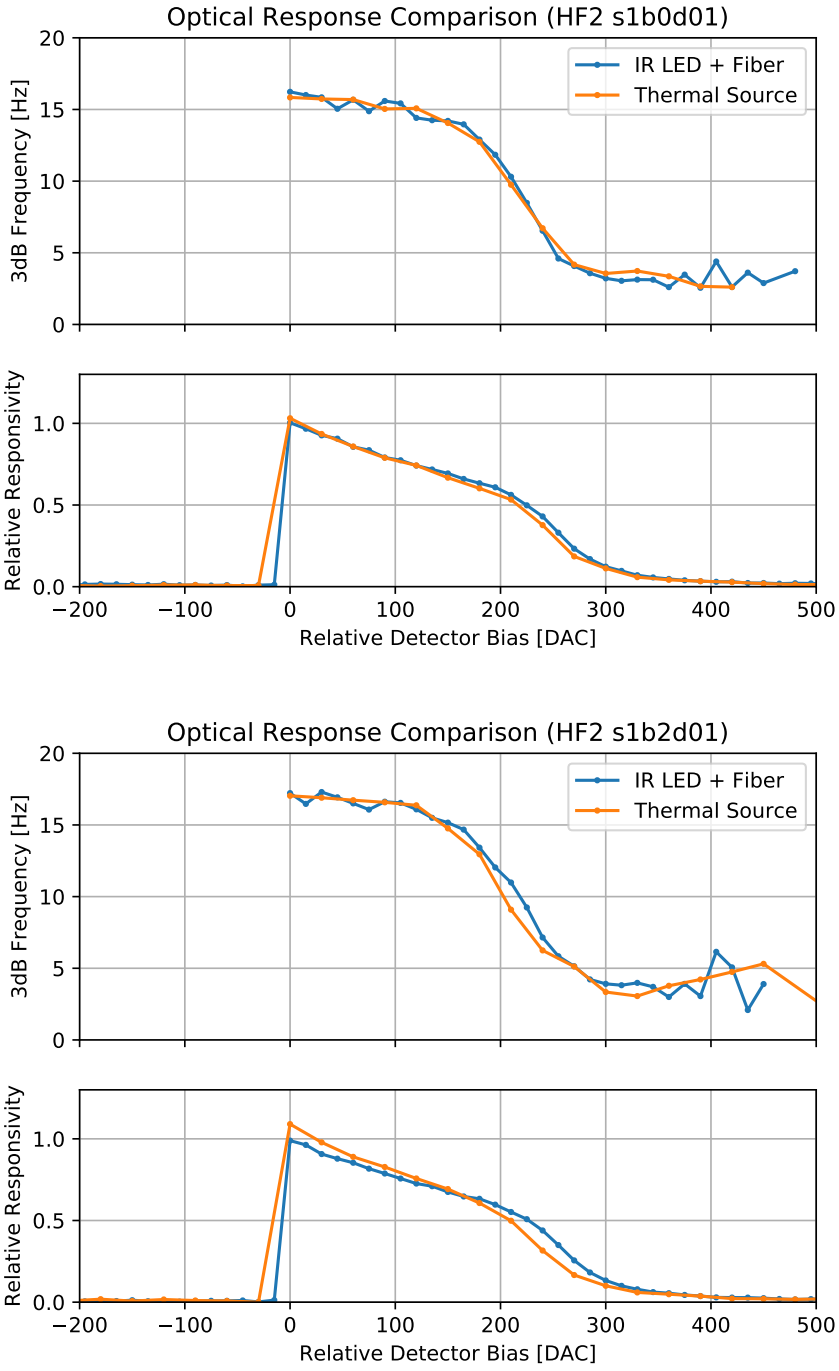

Figure 5.13: A comparison of time constants measured for two sample detector with both a chopped thermal source and a fiber-coupled infrared LED.

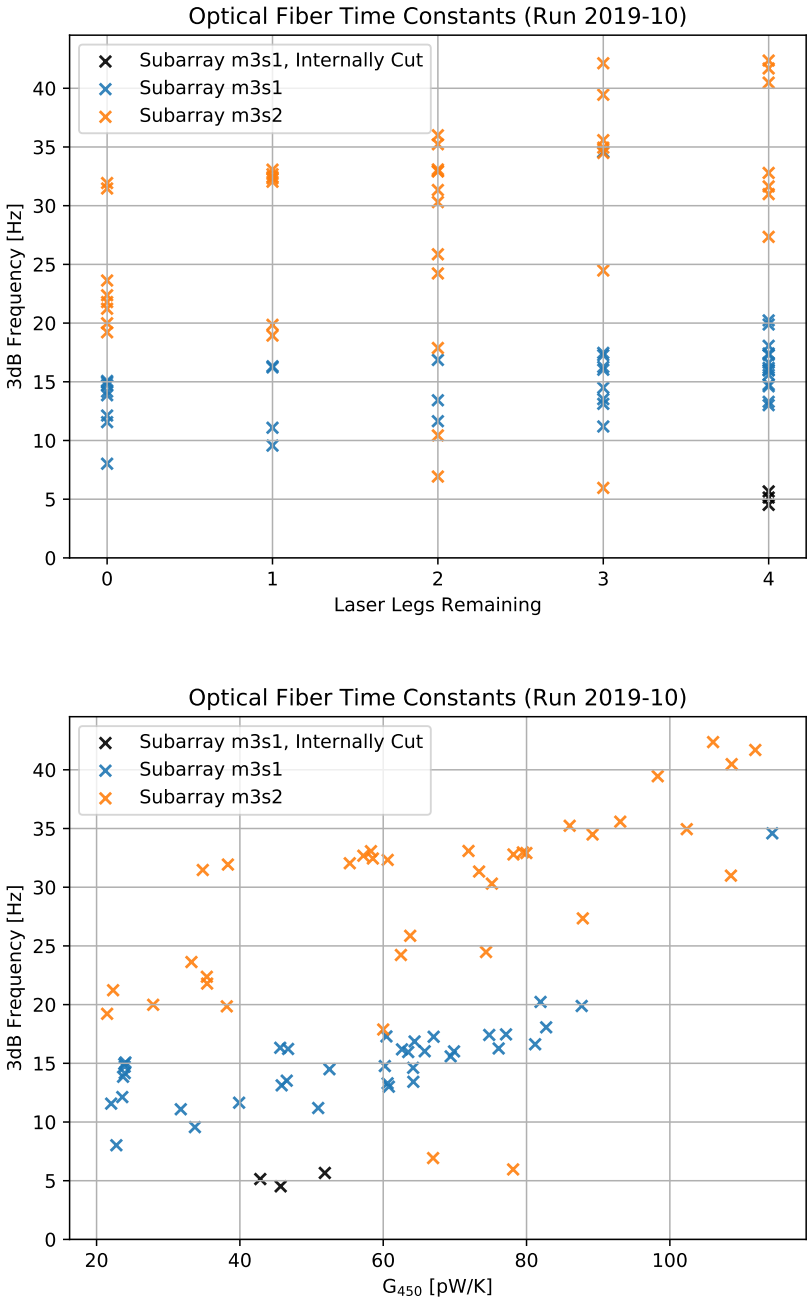

Figure 5.14: Measured time constants plotted against the number of remaining laser legs (*upper*) or the measured detector thermal conductance to the bath G (*lower*). Time constants appear to be limited by factors beyond a simple scaling the G.

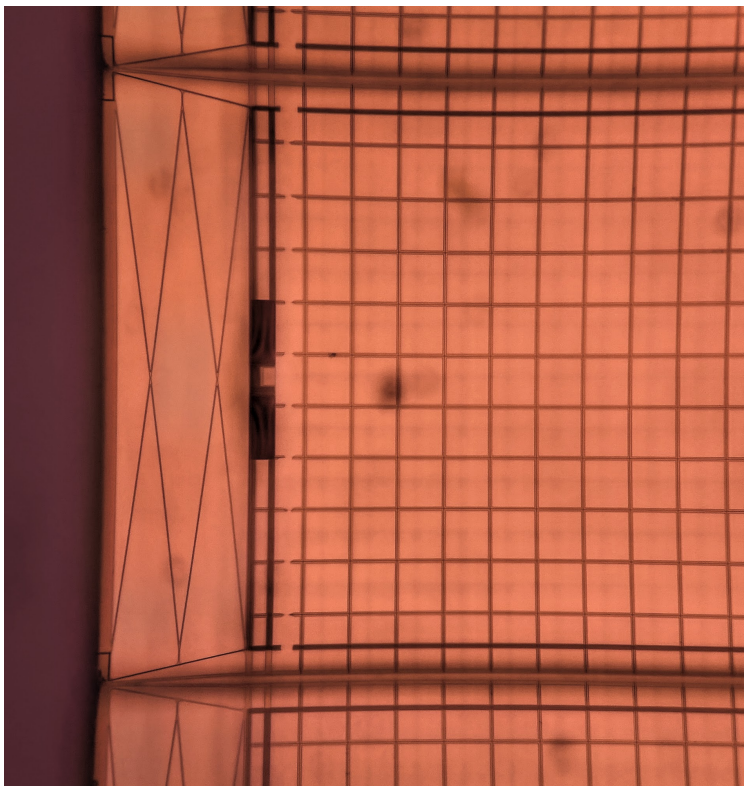

Figure 5.15: For three tested detectors the internal thermal sinking gold lines connecting the absorber mesh to the TES bridge were cut with a laser trimmer to exacerbate the effects of the internal device time constant. Results for these detectors are shown as black points in Fig. 5.14.

5.3 TES Series Resistance

TIME uses a series of 12 by 1 inch polyimide flex circuits to connect the detector modules to the SQUID readout boards. These "cables" use 1/4 oz thick copper traces with 5 mil traces and spacing. Because these cables are in series with the TES, their total resistance should ideally be kept much lower than the operating resistance of the TES ($20 - 50$ mΩ). Toward this end, the copper traces are coated with approximately $3\,\mu$m of tin, a superconductor with $T_c = 3.7\,$K. We use superconducting aluminum wire bonds to connect to either end of the cable due to the relatively large resistance of a connectorized interface. The presence of tin complicates the wire bonding process, necessitating the inclusion of gold plated tin-free bond pads at both ends of the cable.

A measurement of the resistance per detector wiring pair versus temperature is shown in Fig. 5.16, illustrating their key deficiency. At the operating temperature ($\sim$ 300 mK) each line pair shows a residual resistance of 6.5 mΩ, corresponding to the non-tinned wire bond pads. In reality, the series resistance is larger than this measured value due to the configuration of the test as shown (lines were intercepted further up on the pad than is normally the case for detector readout). A better estimate can be computed from the 0.4 Ω per pair measured above the superconducting transition; using the known geometry of the cables, we expect 10 mΩ per pair of series resistance, which is a non-negligible fraction of our TES operating resistance. Effects of TES series resistance are discussed in Sec. 3.1. To reduce this resistance I have electroplated additional tin onto edges of the cables, masking a small bond pad area that remains uncoated; the coverlay is removed on one side coat the underlying traces, but is left in place on the opposing side to avoid removing the stiffener. Results are depicted in Fig. 5.17, with series resistance measurements extracted from TES load curves shown in Fig. 5.18. The extended tinning procedure reduces the measured median channel series resistance from 11.9 mΩ to 6.6 mΩ.

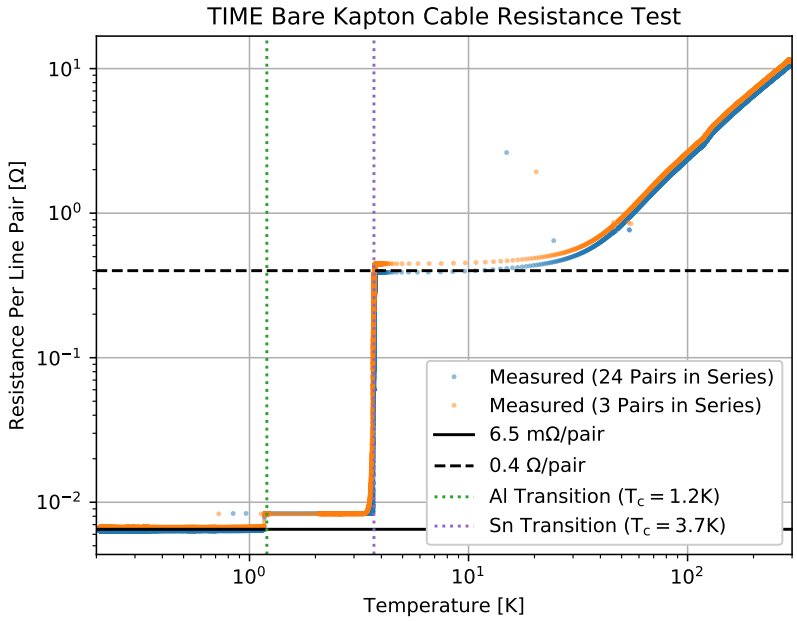

Figure 5.16: Resistance measurement for two sets of (unmodified) polyimide cable traces wired in series. Measurement was done in the TIME cryostat in four-wire configuration with a Lakeshore 370. The wire bond positioning for this test bypassed one-half to two-thirds of the bare copper, since this test was intended to screen for bulk trace resistance caused by improper tin plating.

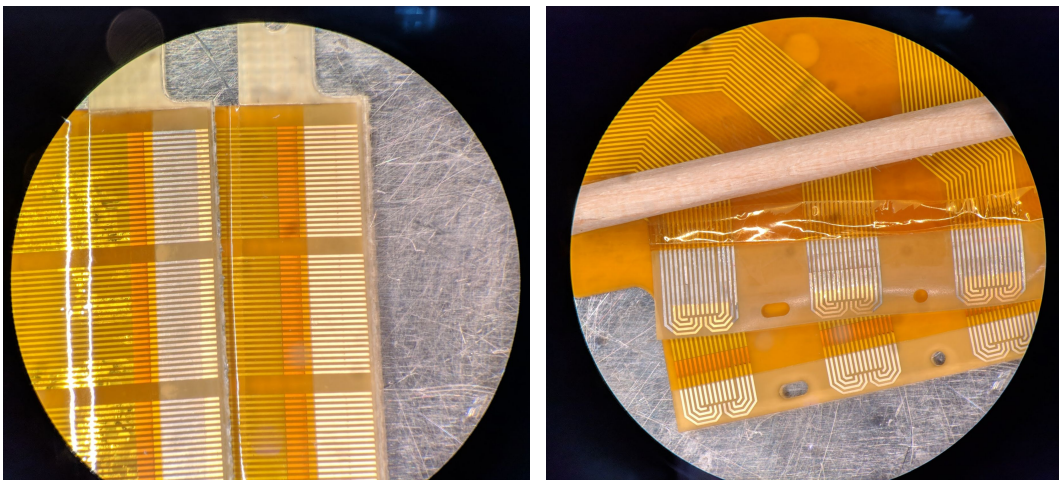

Figure 5.17: The two ends of a TIME polyimide readout cable, before and after the the tin extension procedure. The gray coating present on the upper cable is the added tin. On the detector side, the polyimide coverlay is lifted before electroplating.

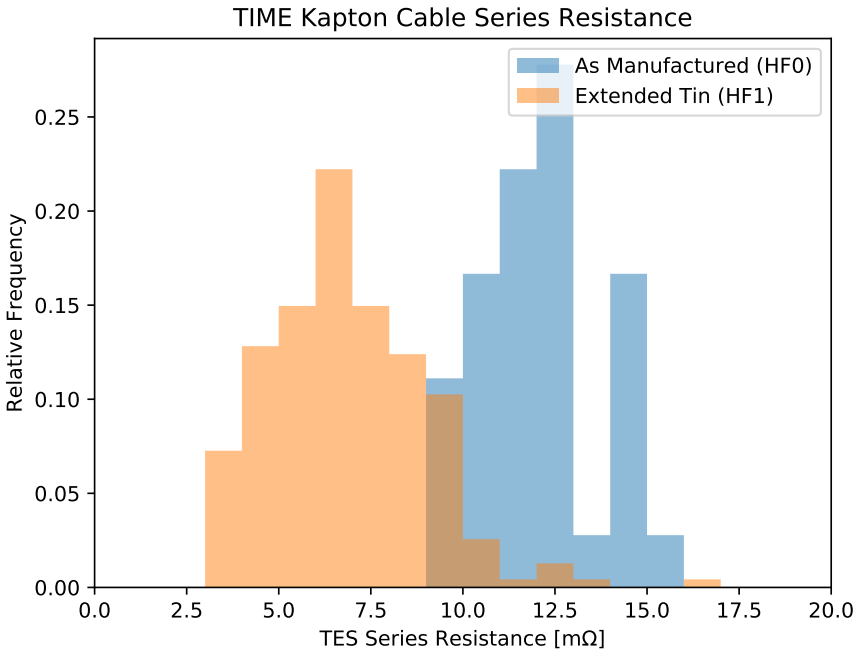

Figure 5.18: Measured TES series resistance distribution for a TIME detector module with and without the extended tin polyimide cable procedure.

5.4 Absorber Surface Deflection

Early TIME devices used a primarily silicon backshort (see Fig. 3.17), with only 20 μm of vacuum behind the silicon nitride detector mesh. This raises the concern of unwanted physical contact between the mesh and the bulk silicon, a potential explanation for anomalously high values for the bath thermal conductance (G) observed in some early devices. Using a metrology microscope, I mapped the surface deflection for sample detectors on several subarrays; two such maps are shown in Fig. 5.19. Deflections with a magnitude comparable to the vacuum gap were observed, with the polarity varying between subarrays. A 20 μm deflection corresponds to 2% of a wavelength at 300 GHz, which should not result in any noticeable optical effects. However, the potential impacts on G were one of several reasons why we switched to a vacuum backshort.

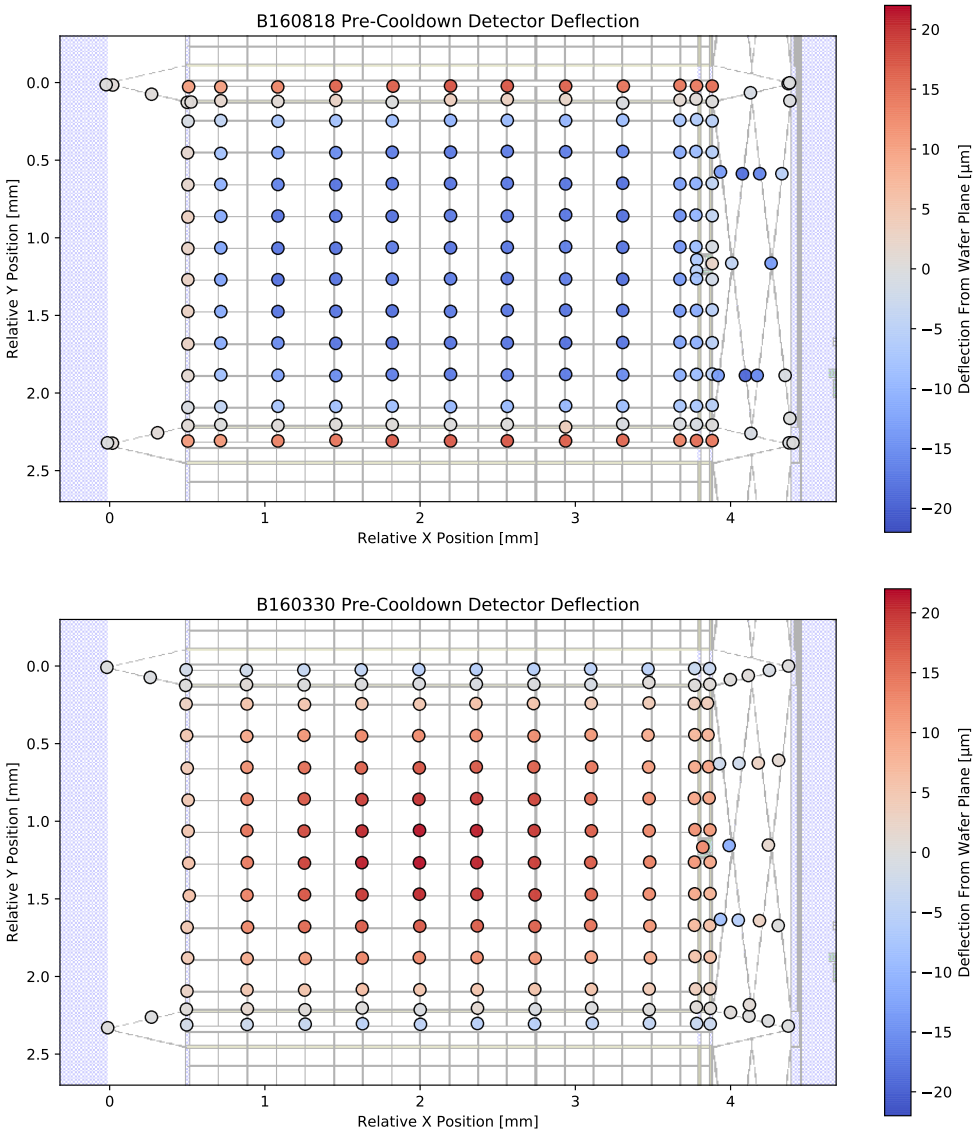

Figure 5.19: Measured detector mesh surface deflection relative to the surrounding silicon for two sample TIME detectors (one with positive deflection, one with negative).

5.5 High-Frequency Noise

The detector readout electronics for TIME (two MCE crates produced by a team at UBC) have a dedicated ADC for each multiplexing column. The 50 MHz ADC sampling is time-domain multiplexed across 33 channels (the multiplexing rows); the row-revisit frequency depends on this row count and on the number of samples discarded while waiting for the row switch transients to settle. TIME typically chooses to discard 82 samples and coadd 10, resulting in a channel sampling frequency of $50\,\mathrm{MHz} \,/\, (33 \times 92) = 16.47\,\mathrm{kHz}$. This rate is downsampled to 100 Hz output per channel via a digital filter in the MCE. Increasing the sampling frequency reduces the penalty of aliased noise, but can increase crosstalk between adjacent rows. In laboratory testing we can bypass the digital filter and record a limited subset of detectors at their full sampling rate. Further more, by reducing the number of multiplexing rows addressed from 33 to 2, we can increase the sampling rate of those channels without changing the transient settling period between rows. In Fig. 5.20 I show the noise in one representative TIME detector taken at different TES bias levels (one superconducting point, several points in the transition, and one Ti normal point). For reference, I plot the expected Johnson white noise level and L/R 3dB frequency in the normal and superconducting state based on the measured channel series and normal resistances. The Nyquist frequency for the typical TIME sampling rate is shown in black, and the expected total noise after aliasing assuming this sampling rate is shown for each bias point. Similar to predictions by the simulations in Sec. 3.4 (Fig. 3.22 in particular), we see a broad excess noise feature above 100 Hz with a sharp peak near 6 kHz deeper in the transition when the logarithmic temperature sensitivity α is high. The low frequency tail below 100 Hz in the measured data contributes to excess noise at 10 Hz, and the noise above 10 kHz results in a significant aliased noise penalty below 10 Hz. Simulation results indicate that increases in device heat capacity push the lower bound of the excess noise feature to lower frequencies and reduce the intensity of the sharp 6 kHz peak without noticeably affecting the noise slope above 10 kHz. Therefore, v7 TIME devices will reduce the total heat capacity by reducing the bandwidth-limiting gold deposited near the TES island; we expect a sharper noise peak at 6 kHz from this, but no major effects on aliased noise. TIME is exploring options for pushing to faster multiplexing rates to reduce aliased noise.

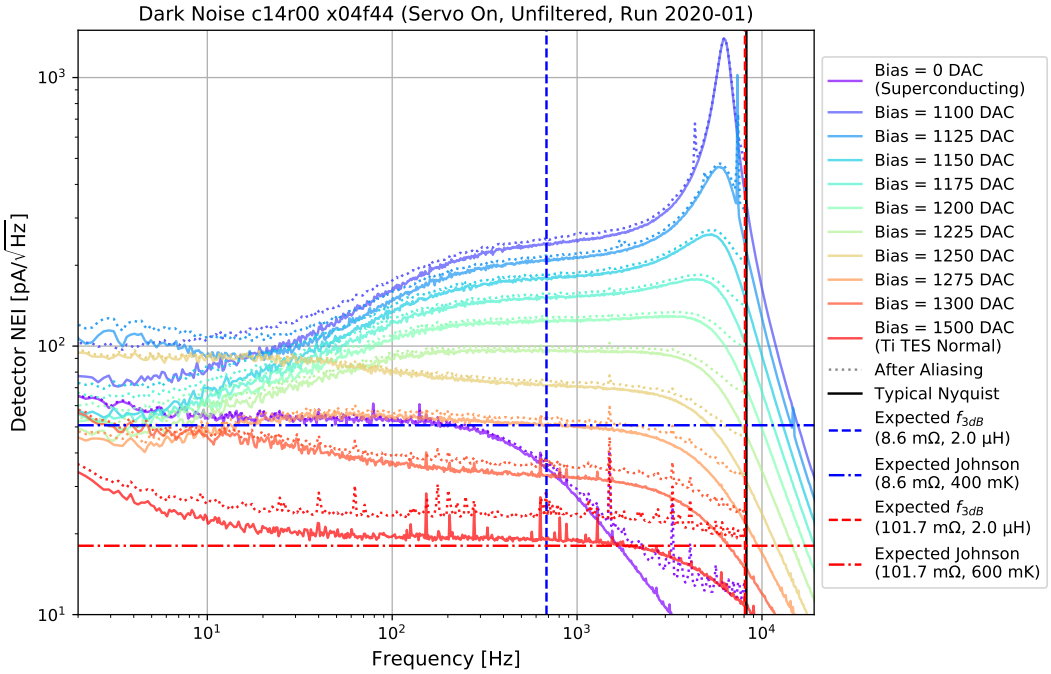

Figure 5.20: Noise current for a single channel taken at high data rates; the number of rows addressed is reduced to two, but the time spent at each row has not changed from typical TIME parameters. Data is shown at several bias points in the transition as well as in the superconducting and normal states. For the superconducting and normal states I plot the expected Johnson noise and L/R 3dB frequency for the channel in question. Expected noise with aliasing given the typical sampling rate used for TIME is shown in dotted lines for each bias.

5.6 Optical Efficiency

At each frequency ν the TIME feedhorn couples a single mode (defined by the diffraction limit $A\,\Omega = \lambda^2 = c^2/\nu^2$ for cross-sectional area A and solid angle Ω [32]) to the TE1 parallel plate waveguide mode via a stretch of rectangular waveguide. The power incident on the detector is given as follows, where $\Delta\nu$ is the bandwidth (defined for TIME as the channel spacing) and $B(\lambda, T)$ is the spectral radiance:

$$P = B(\nu, T)\,\Delta\nu\,A\,\Omega = B(\nu, T)\,\Delta\nu\,c^2/\nu^2 \tag{5.3}$$

In the Rayleigh-Jeans limit, the spectral radiance for a single polarization is given by $B(\nu, T) = k_B T\,(\nu^2/c^2)$, allowing us to express the derivative of power

with respect to temperature simply in terms of the channel bandwidth.

$$\begin{aligned} P &= k_B T\, \Delta\nu \\ \frac{\mathrm{d}P}{\mathrm{d}T} &= k_B\, \Delta\nu \end{aligned} \tag{5.4}$$

We can therefore define optical efficiency as the measured $\frac{\mathrm{d}P}{\mathrm{d}T}$ divided by the theoretical maximum value $k_B\, \Delta\nu$.

The instrument optical response $\frac{\mathrm{d}P}{\mathrm{d}T}$ is measured by observing the detector response to a pair of reference temperature loads. Detector load curves (see Sec. 5.1 for a description of load curves) are taken with a beam-filling absorber in front of the cryostat window both at room temperature and immersed in liquid nitrogen. The difference in the detector saturation power is equivalent in magnitude (and opposite in sign) to the difference in the observed optical power. Sample load curves for a single detector are found in Fig. 5.21. Focal plane maps of the optical response $\frac{\mathrm{d}P}{\mathrm{d}T}$ and the resulting optical efficiency from detectors used in the 2019 engineering run can be found in Fig. 5.22. Note that spatial pixels 11, 12, and 13 were dark spectrometers in this run (the feedhorns were covered with aluminum tape) to check for loading from reflections inside the cryostat. Optical efficiency from a subset of adjacent feedhorns (three light, one dark) is shown in Fig. 5.23; at each frequency, the four plotted detectors are located on the same subarray and therefore have similar absorber impedances and backshort distances. For reference, I have plotted the expected transmission from the detectors through the cryostat window for this instrument configuration using a modified version of the model presented in Sec. 2.6 (thicker/lossier thermal filters matching the deployed configuration were used at the 4K and 5K stage, and the excess loss term was removed). Note that significant loss at the highest frequencies is observed as predicted by the model; part of this loss arises from the sub-optimal cutoff frequency of one of the three metal mesh low pass filters in the optical path.

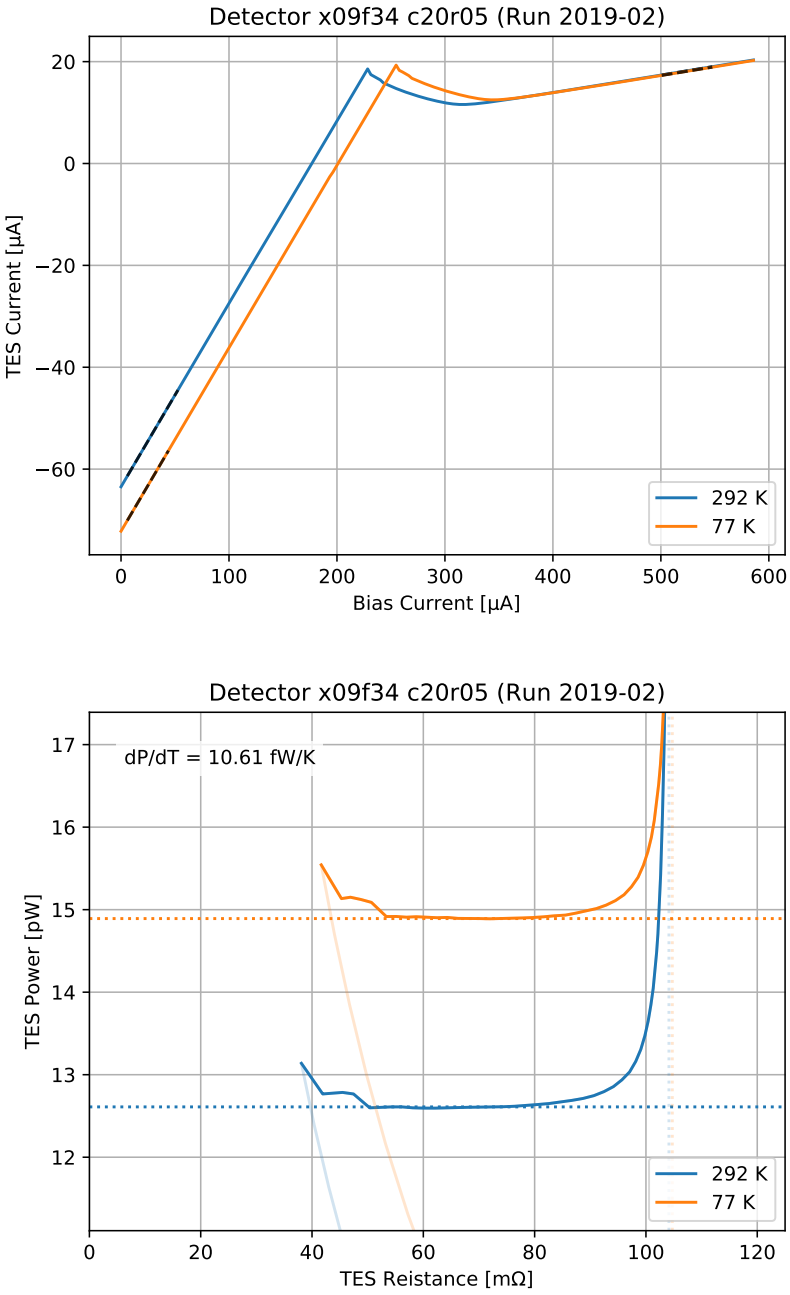

Figure 5.21: Sample TES load curves for a single channel demonstrating the measured saturation power difference with beam-filling temperature loads in front of the cryostat window.

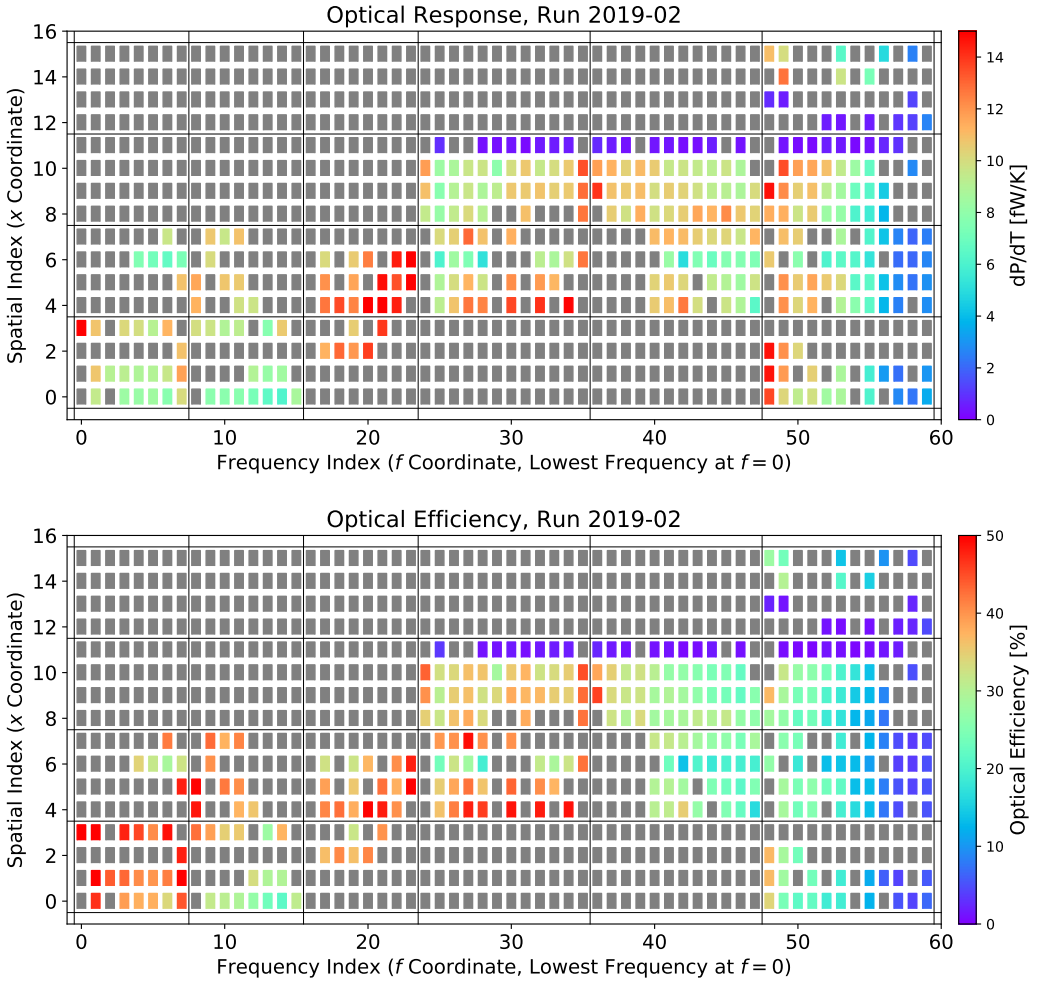

Figure 5.22: Focal plane maps of the optical response $\frac{\mathrm{d}P}{\mathrm{d}T}$ and the resulting optical efficiency for the 2019 TIME engineering run. Note that spatial pixels 11, 12, and 13 correspond to dark feedhorns (blocked with aluminum tape).

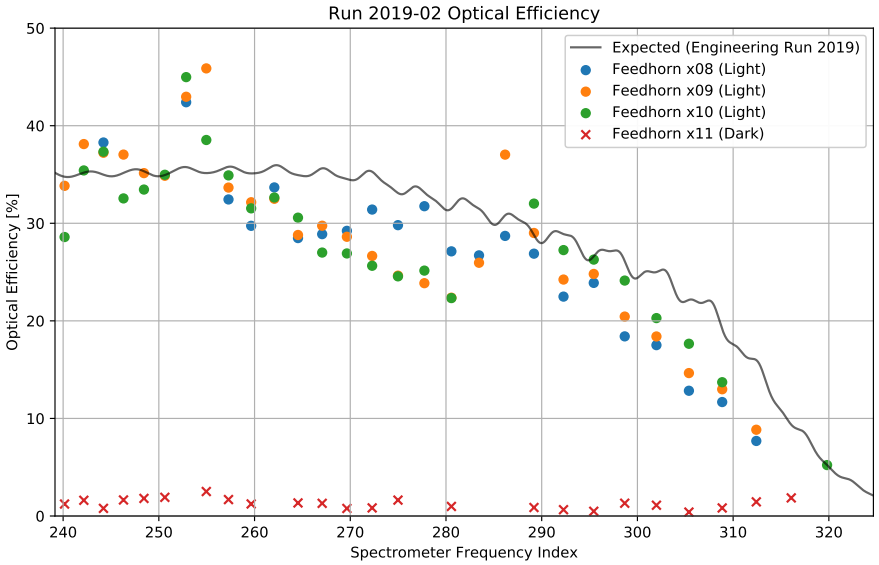

Figure 5.23: Measured optical efficiency for four feedhorns, three light and one dark. At each frequency, all four displayed channels reside on the same subarray and therefore share similar absorber impedance and backshort distances. The expected value based on the filter stack used is included for comparison.

5.7 Channel Passbands

Channel passbands in TIME are measured with a Martin–Puplett Fourier-transform spectrometer (FTS), a type of interferometer [70]. A linearly polarized aperture-defined liquid nitrogen cold source is collimated by an off-axis reflector (the orthogonal linear polarization seen by this reflector couples to the room temperature absorptive wall of the FTS). The resulting beam is split by a central wire-grid polarizer rotated 45° with respect to the input beam, passing one linear polarization (consisting of both 77K and 300K signal) through the fixed (short) interferometer arm, and passing the orthogonal polarization through the variable-length (long) interferometer arm. V-shaped mirrors at the arm ends (one fixed, one mounted on a moving linear stage) rotate the polarization by 90° and (acting as a two-dimensional retroreflector) reflect the beam back toward the central wire grid, where they couple to the output port. At each frequency ν a relative phase lag in the two orthogonal components of the resulting electric field arising from the path difference between the two arms forms an elliptically polarized output, which varies between the two linear polarizations for 0° and 180° difference and the two circular polarizations for 90° and 270°. An output linear polarizer (or, alternatively, a polarized detector) results in a path-difference dependent amplitude whose contrast depends on the temperature of the source load and the room temperature reference load.

The observed detector signal depends on both the source spectrum (a broadband black body here, scaling as ν^2 in the Rayleigh-Jean limit) and the detector passband. For a perfectly monochromatic detector, scanning the FTS mirror at constant velocity produces a sinusoidal timestream whose frequency depends on the mirror speed and the frequency of the observed radiation. For channels with a finite bandwidth multiple such sine waves are superimposed, producing a wave packet with its peak at the point of zero path difference (an "interferogram") whose Fourier transform is the channel passband. Resolution of the resulting passband is thus dependent on the maximum observed path difference (with the high frequency passband measurement limit set by the sampling rate). In principle a single-sided interferogram starting at the point of zero-path difference contains all of the desired spectral information; however, systematic errors and misalignment within the FTS result in an asymmetric interferogram. The imaginary component of the Fourier transform, which is zero for a perfectly symmetric interferogram, can be monitored or corrected

when two-sided data is available. TIME uses an asymmetric FTS, producing a two-sided interferogram with 90 cm available path difference behind the zero-path point but only 15 cm in front. This allows for slowly-varying phase errors to be corrected while still achieving the higher resolution required for TIME.

A sample interferogram for a single detector can be seen in Fig. 5.24, recorded with the FTS mirror moving at 2 mm/s. Because TIME uses relatively narrow band channels ($\nu/\Delta\nu \sim 100$), it is difficult to infer the zero path position from a single channel. To assist in this process, interferograms from multiple spectral channels on the same feedhorn are coadded to produce a broad-band interferogram with a clear zero-path point, as shown in Fig. 5.25. As shown in Fig. 5.26, a linear ramp window [80] is applied to the data over the region sampled symmetrically to avoid double-counting points, and a Blackman window is applied to the entire interferogram. The real and imaginary components of the Fourier transform are shown in Fig. 5.27. Over the high signal region a linear phase error (equivalent to a time delay) is fit and removed from the data, and the resulting corrected spectrum is co-plotted. A residual oscillation in the phase remains uncorrected; forcing the phase to be identically zero at all points would be equivalent to using the magnitude of the complex passband, which is a noise-biased estimate of the true passband. In addition to the corrected spectrum, I co-plot the result obtained from performing a Discrete Cosine Transform (DCT) on the long-ended portion of the interferogram (ignoring the short-ended portion entirely); results are very similar.

Passbands from several adjacent channels within a single TIME spectrometer can be seen in Fig. 5.28. Channel band centers determined by a per-channel Gaussian fit for a few different spectrometers are shown in Fig 5.29, demonstrating relatively good agreement with expected values. Similarly, channel bandwidths are shown in Fig. 5.30.

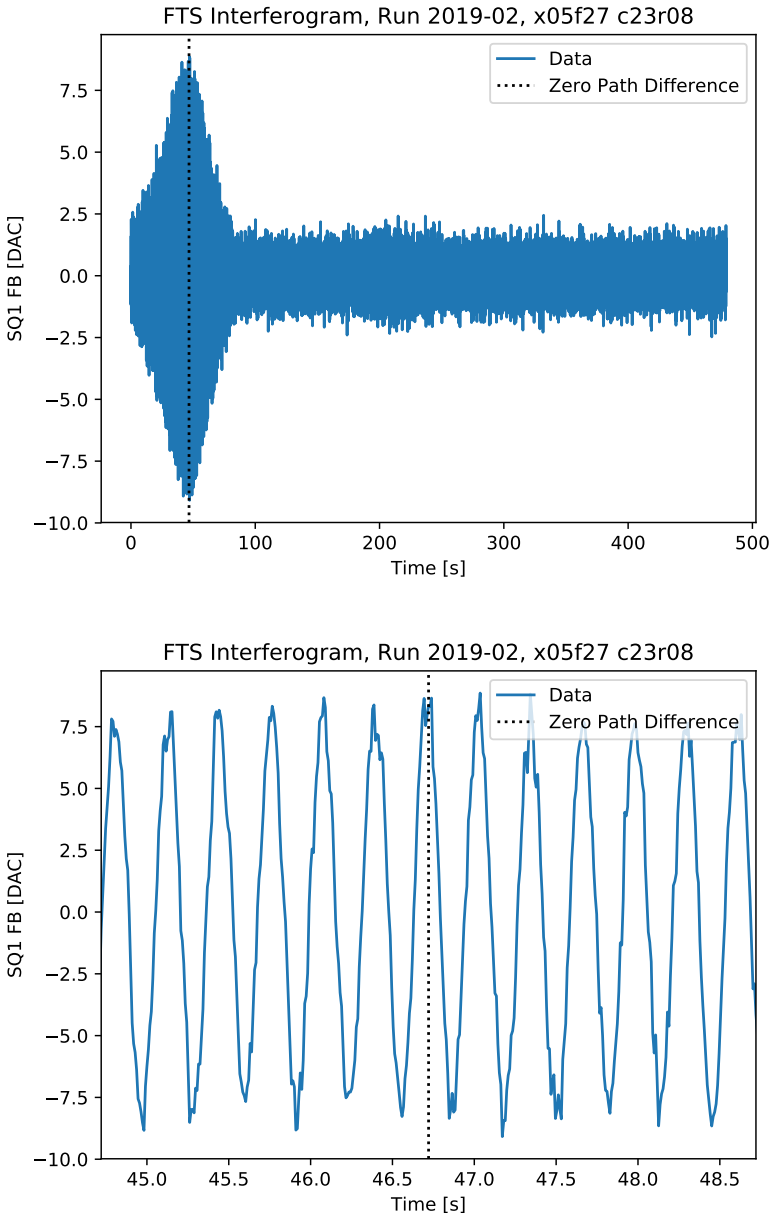

Figure 5.24: A sample asymmetric FTS interferogram for a single TIME channel.

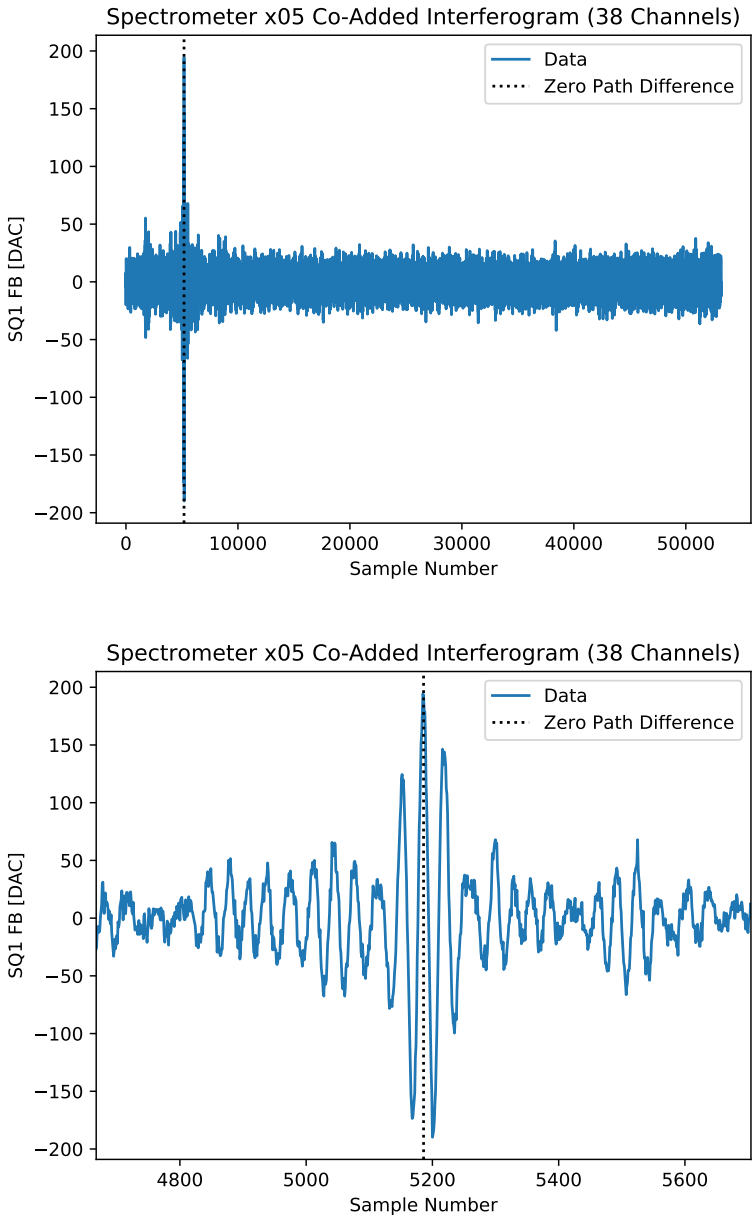

Figure 5.25: A sample asymmetric FTS interferogram produced by coadding multiple spectral channels on the same feedhorn, improving our ability to infer the zero-path position from the data.

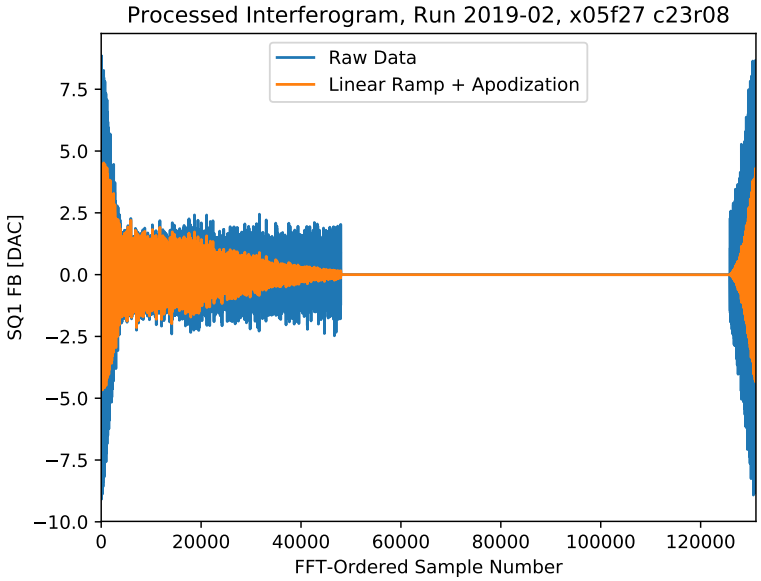

Figure 5.26: A sample asymmetric FTS interferogram for a single TIME channel in FFT order, both before and after application of the linear ramp window [80] and apodization.

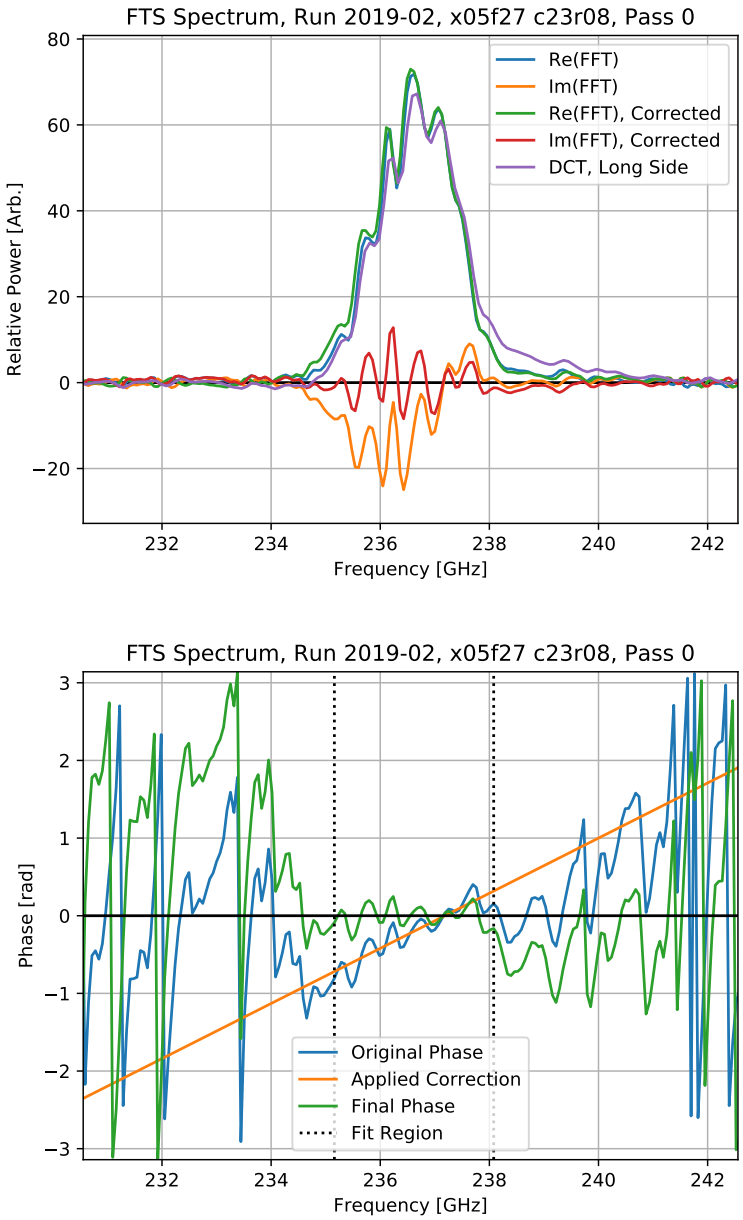

Figure 5.27: Sample passband results for a single TIME channel, before and after correcting for a linear phase error.

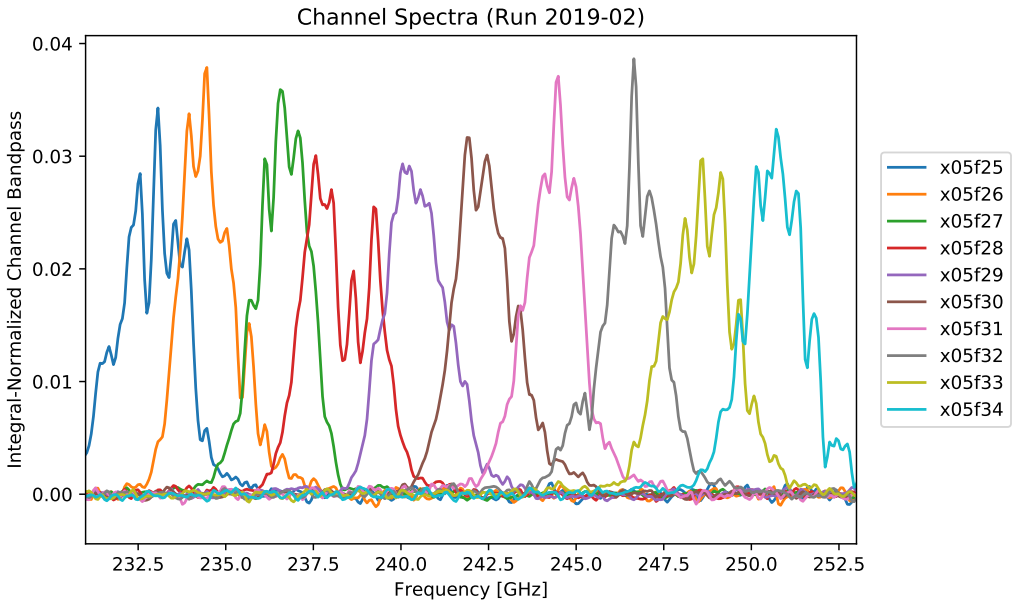

Figure 5.28: A series of passbands from adjacent channels in a single TIME spectrometer.

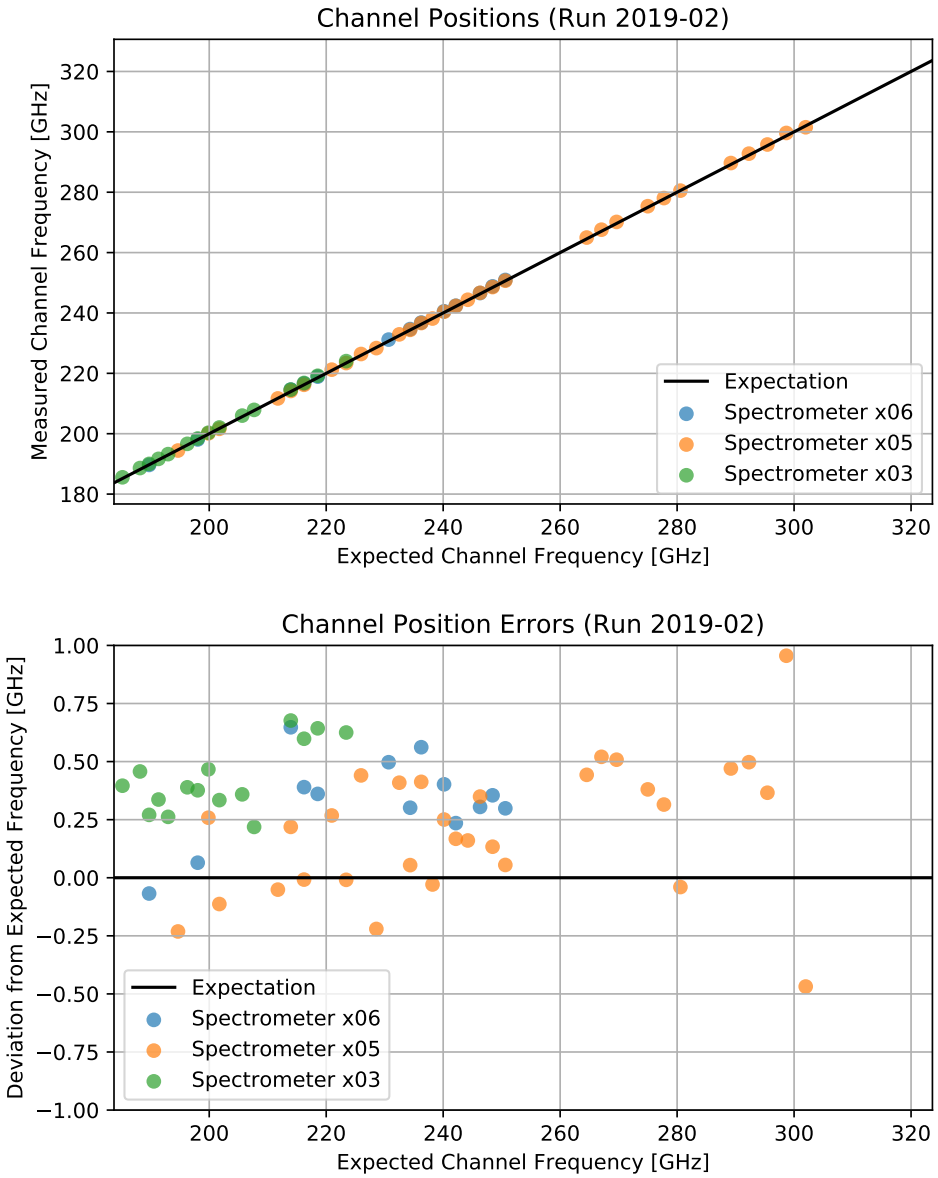

Figure 5.29: Measured TIME channel positions compared to expected values.

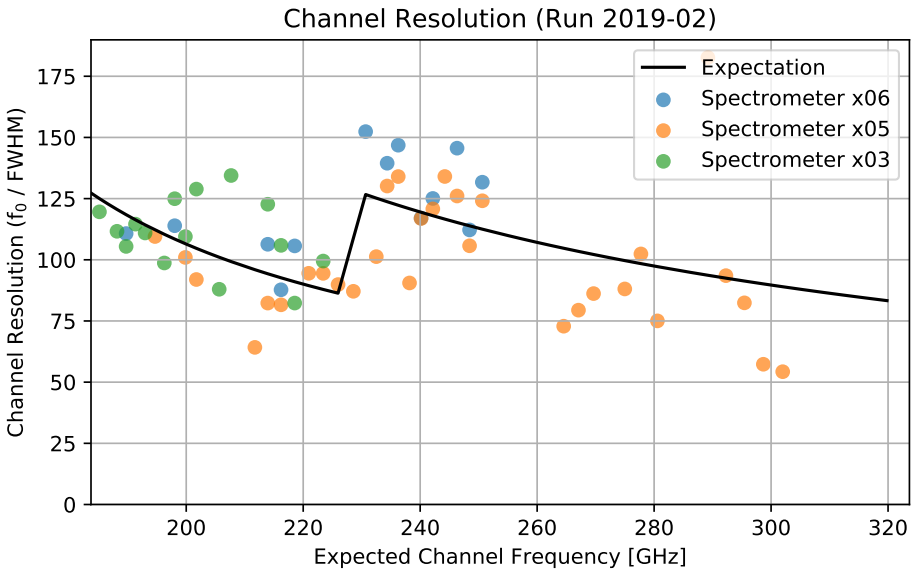

Figure 5.30: Measured TIME channel bandwidths compared to expected values. The discontinuity in the expectation corresponds to the change from the larger low frequency pixels to the smaller high frequency pixels.

Chapter 6

On-Sky Performance

In January 2019 we shipped the TIME receiver to the site of the Arizona Radio Observatory's 12 meter ALMA prototype antenna at Kitt Peak in southern Arizona. This was intended to be an early engineering run, as we shipped with known cryogenic issues and with only a quarter of our designed detector count (most of which had never been cryogenically tested before). After reassembling the cryostat and working though some additional unexpected cryogenic issues we began characterizing these new detectors in a building adjacent to the telescope. In mid-February the cold receiver was lifted into the telescope dome (Fig. 6.1) and installed in the Cassegrain cabin. As a result of power failures caused by inclement weather, our "first light" (in a sense) came from a scan over the moon with the canvas telescope dome closed (Fig. 6.2); our first light with a clear line of sight occurred several days later. In this chapter I describe some of the instrument performance measurements done at Kitt Peak. Despite failing to acquire any science-quality data, we left having worked through countless mechanical, electrical, and digital bugs and with a clearer understanding of what improvements are required for the next deployment.

Figure 6.1: Photos from the installation of the TIME receiver on the 12 meter ALMA prototype antenna at Kitt Peak in southern Arizona.

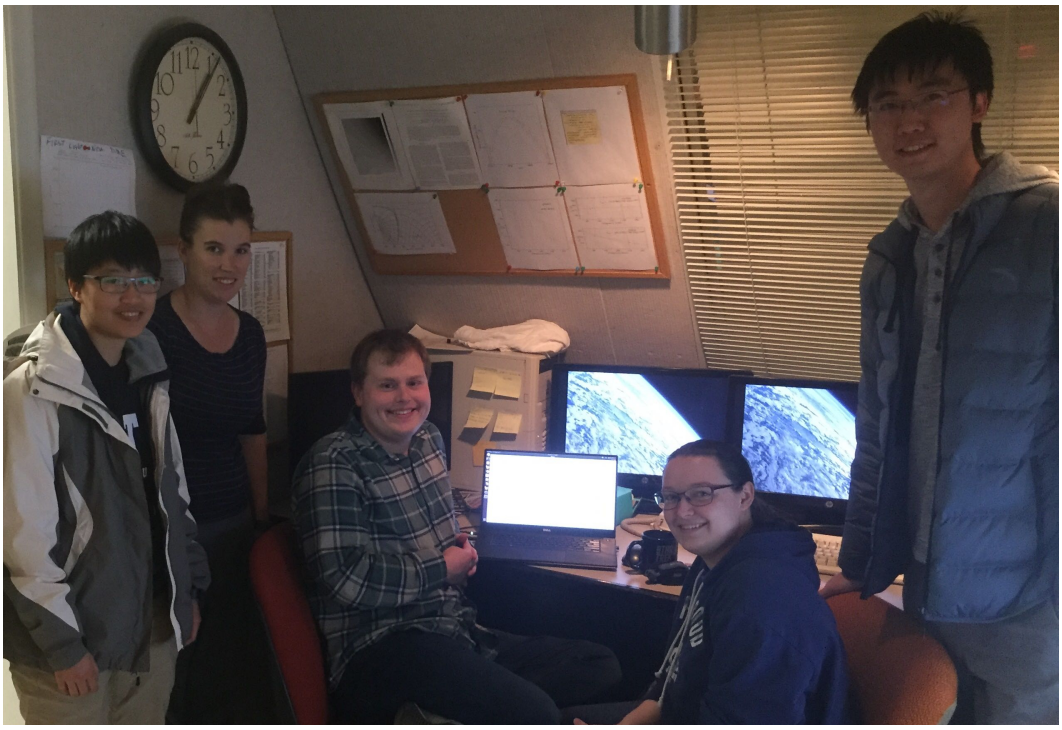

Figure 6.2: The TIME site team following TIME's "first light" in March of 2019. The moon was observed through the canvas telescope dome, which was closed due to a power failure; first light with a clear line-of-sight occurred several days later. *Pictured, left to right: Yun-Ting Cheng, Abigail Crites, Jonathon Hunacek, Victoria Butler, Guochao (Jason) Sun. Photo by Jamie Bock.*

6.1 Cold Detector Yield

An accounting of the detector yield in the 2019 engineering run can be found in Fig. 6.3. One of the two spectrometer banks was installed, providing 16 spatial pixels in a single polarization. Of the 24 total subarrays (12 HF, 12 LF) present in a complete (single-polarization) focal plane, 14 were installed (8 HF, 6 LF). Considering only the channels where subarrays were installed and the readout was functioning, 323 of a possible 534 channels (60%) show valid TES load curves, with the best single subarray showing 88% cold yield. Multiplexing columns of 32 detectors must share a common TES bias line, meaning poorly matched detectors within the same column cannot be biased simultaneously. This was a significant hit for TIME, where only 68% of working detectors were able to be biased simultaneously for uniform fixed loading (Fig. 6.4); finer per-detector tuning of G enabled by the new laser leg configuration of upcoming

TIME devices may improve detector matching.

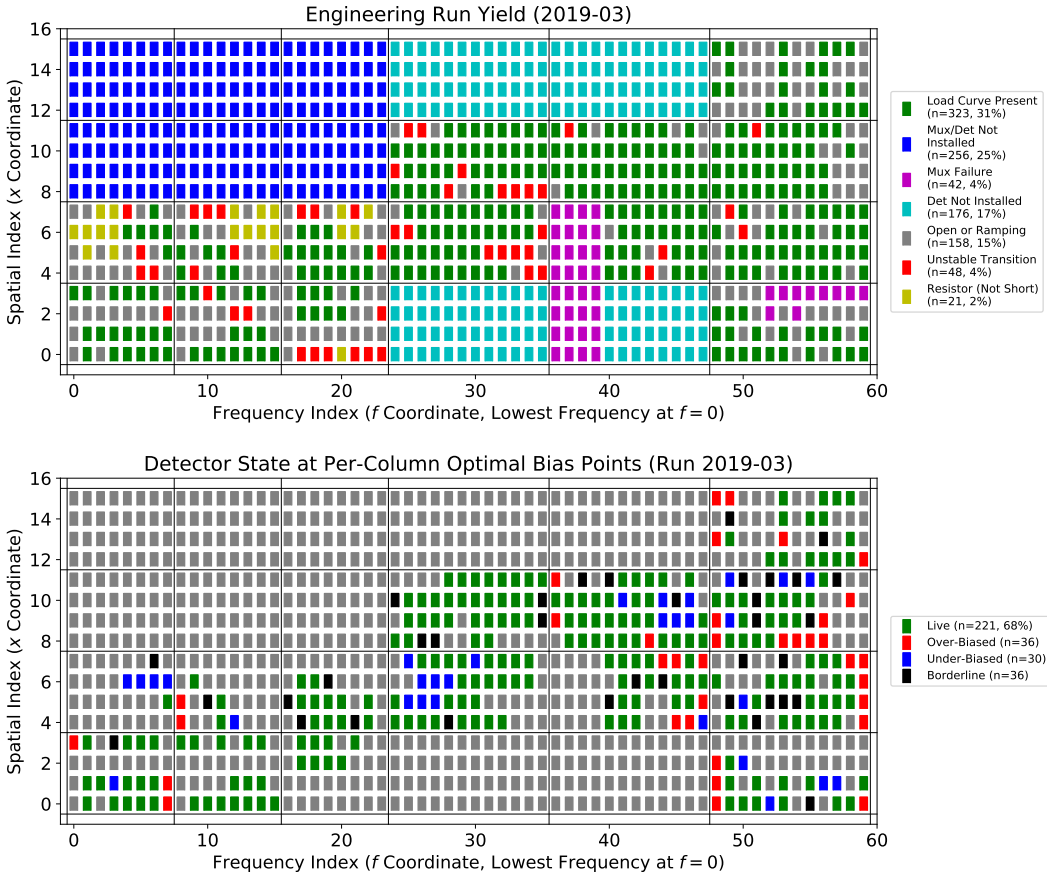

Figure 6.3: An accounting of the detector yield in the 2019 TIME engineering run.

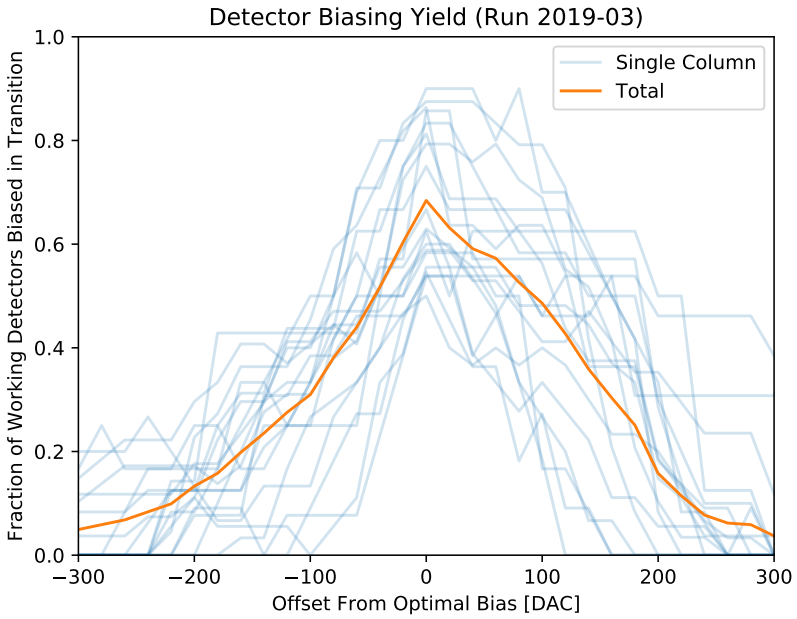

Figure 6.4: Degradation of the detector yield as the bias DAC code deviates from the per-column optimal value (on the order of 1000 DAC units).

6.2 Loading

The on-sky loading seen by the instrument scales with atmospheric air mass, which can be assumed to scale as $\sec(z)$ for modest zenith angles z ($\sim 1\%$ error at $z = 70°$ [109]). Alternatively, this can be written in terms of elevation from the horizon θ as $\csc(\theta)$. The total Rayleigh-Jeans temperature for each narrow band channel is thus:

$$T = T_{atm}\left(1 - e^{-\tau \csc(\theta)}\right) + T_0 \tag{6.1}$$

where T_{atm} is the effective atmospheric temperature, τ is the optical depth, and T_0 is the constant loading term from the telescope and coupling optics. This model was fit to a set of TES saturation powers measured at elevations from 30° to 70° in different weather conditions. As measured by a 225 GHz tipper mounted near the telescope, the datasets from 2019-03-10, 2019-03-14, and 2019-03-15 had mean values of τ_{225} at 0.38, 0.09, and 0.27 respectively. Sample TES load curves (see Sec. 5.1) from one dataset are shown in Fig. 6.5. Note the scatter between measurements taken at slightly different times, believed to be due to weather variations on the timescale of the measurements. Each of the three datasets was taken over the course of 10-30 min. Full TES load curves

down to zero bias leave the detectors in the superconducting state, requiring focal plane heating and significant recovery time between each load curve (tens of minutes). We therefore measured partial load curves, stopping at a bias high enough to prevent the detector of interest from latching in the superconducting state. In practice, this severely limited the number of active detectors during this measurement; heaters integrated onto the subarrays themselves have been added to newer detector designs with the hope of improving the unlatching recovery time.

For this analysis I assume T_{atm} is fixed at all temperatures, with $\tau(f)$ absorbing all frequency dependence. I also assume T_0 is independent of weather. τ is taken as constant in time within each of the three datasets, but is allowed to vary with frequency in an unconstrained way; that is, I do not assume a τ scaling model for the atmosphere, and I do not use the measured value τ_{225} at all. Therefore, for each channel I fit four parameters (T_0, τ_a, τ_b, τ_c) across a range of globally assumed values for T_{atm}. The reduced χ^2 is computed across all channels and plotted in Fig. 6.6. Note that the effective atmospheric temperature as shown does not include a model for the telescope efficiency, which acts to reduce T_{atm} from a more physically meaningful value; assuming this T_{atm} is constant in frequency implicitly assumes the transmission of the telescope optics are constant in frequency as well. $T_{atm} = 220$K provides the best global fit. Sample fitting results for a single channel channel can be seen in Fig. 6.7 both for the best fit value and for a value of T_{atm} far from the best fit. The total Rayleigh-Jeans temperature and the fit values for the atmospheric opacity for all measured channels are shown in Fig. 6.8. For reference, I plot expectations from the atmospheric model presented in Ch. 2 pinned at 225 GHz to the measured τ_{225}. We observe reasonable agreement with the model mid-band, though there is significant noise in the data. The extracted values for T_0 under the best fit conditions are shown in Fig. 6.10, and unfortunately are too noisy to be useful diagnostics. To attempt to better constrain the results, I repeat the analysis assuming the model values for $\tau(f)$ that were presented in Fig. 6.8. The three datasets for each channel are now fit with a single free parameter (T_0) instead of the four parameters used previously. Results, shown in Fig. 6.11, do not improve.

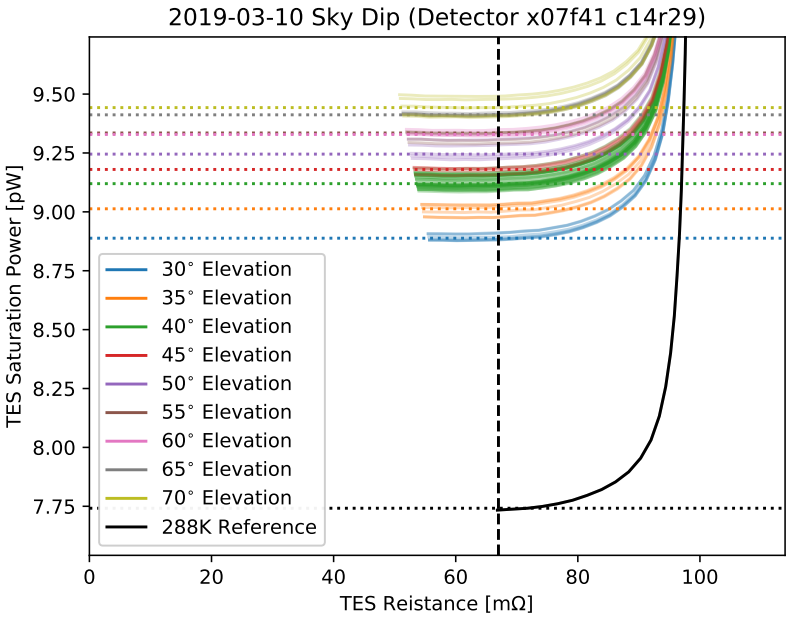

Figure 6.5: Sample TES load curves at different elevations for a single channel.

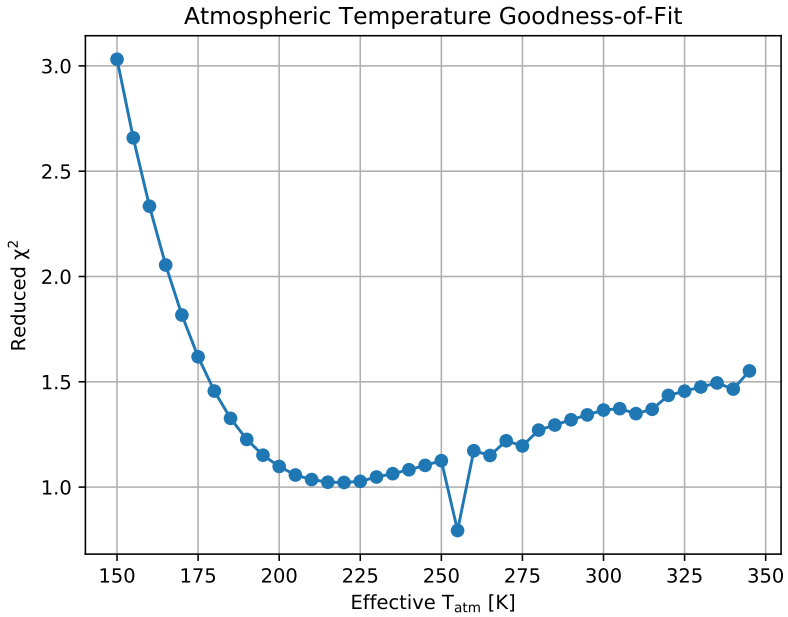

Figure 6.6: Goodness-of-fit metric for the globally-assumed effective atmospheric temperature. The resulting temperature is not corrected for telescope efficiency, which acts to reduce T_{atm} from a more physically meaningful value.

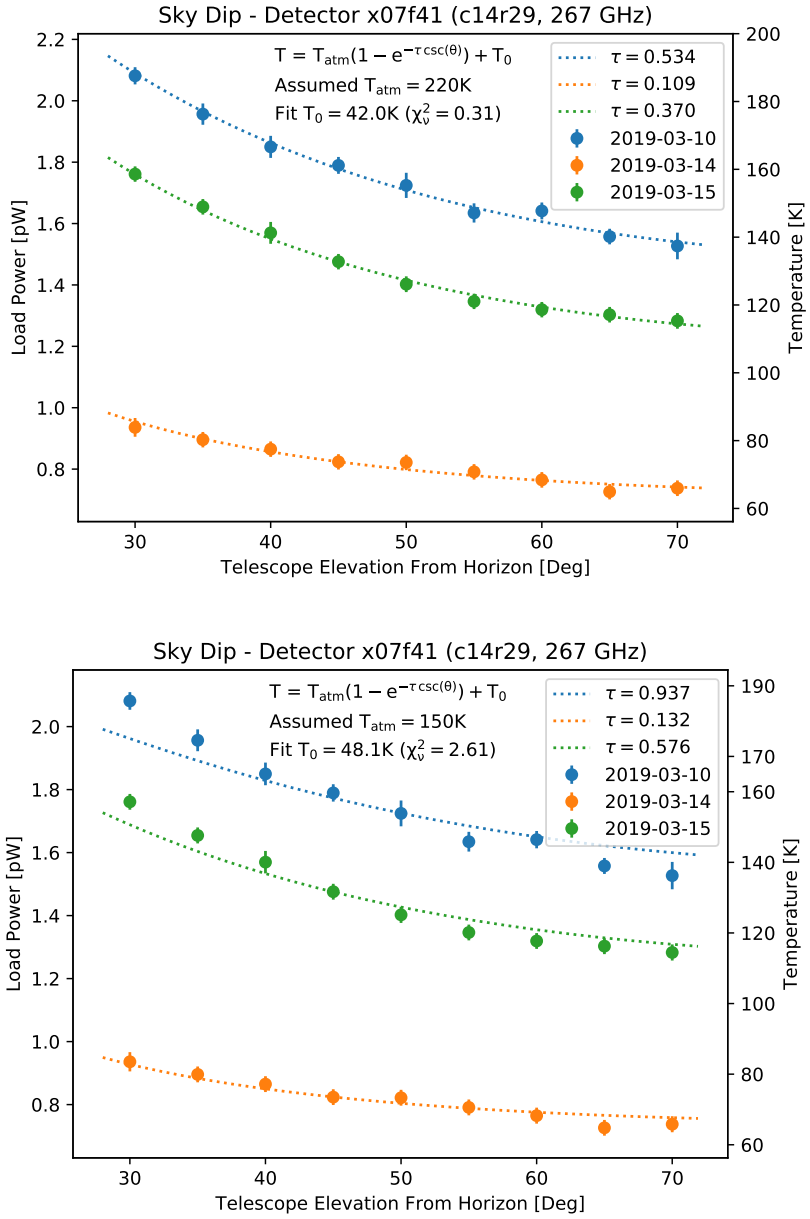

Figure 6.7: A sample fit to the three available datasets for a single channel assuming (*upper*) the best fit value of T_{atm} or (*lower*) something far from the best fit value of T_{atm}. Four independent parameters are fit to the data shown: T_0 and three values for τ.

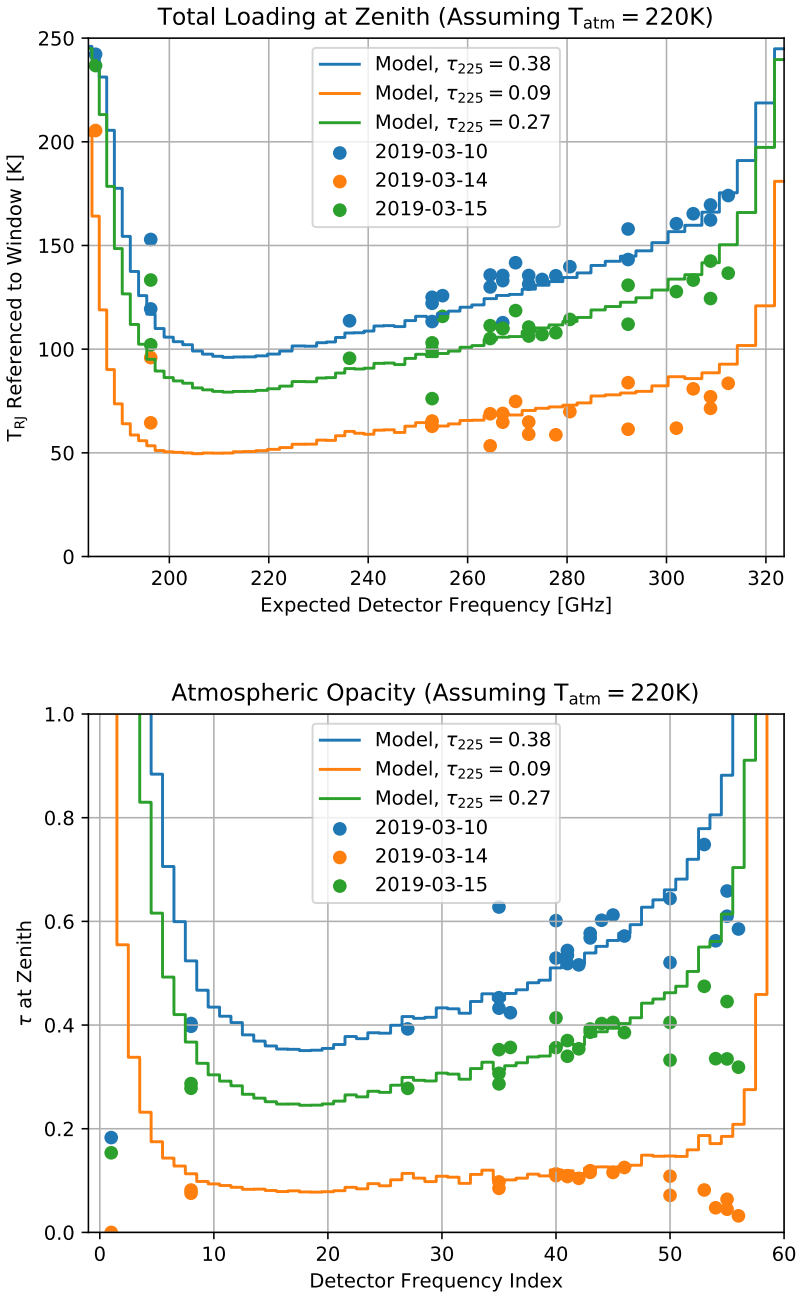

Figure 6.8: The total Rayleigh-Jeans temperature and atmospheric opacity at the best fit value of T_{atm}. A predicted atmospheric model pinned to the measured value for τ_{225} (measured separately and not used in the fitting) is included for comparison.

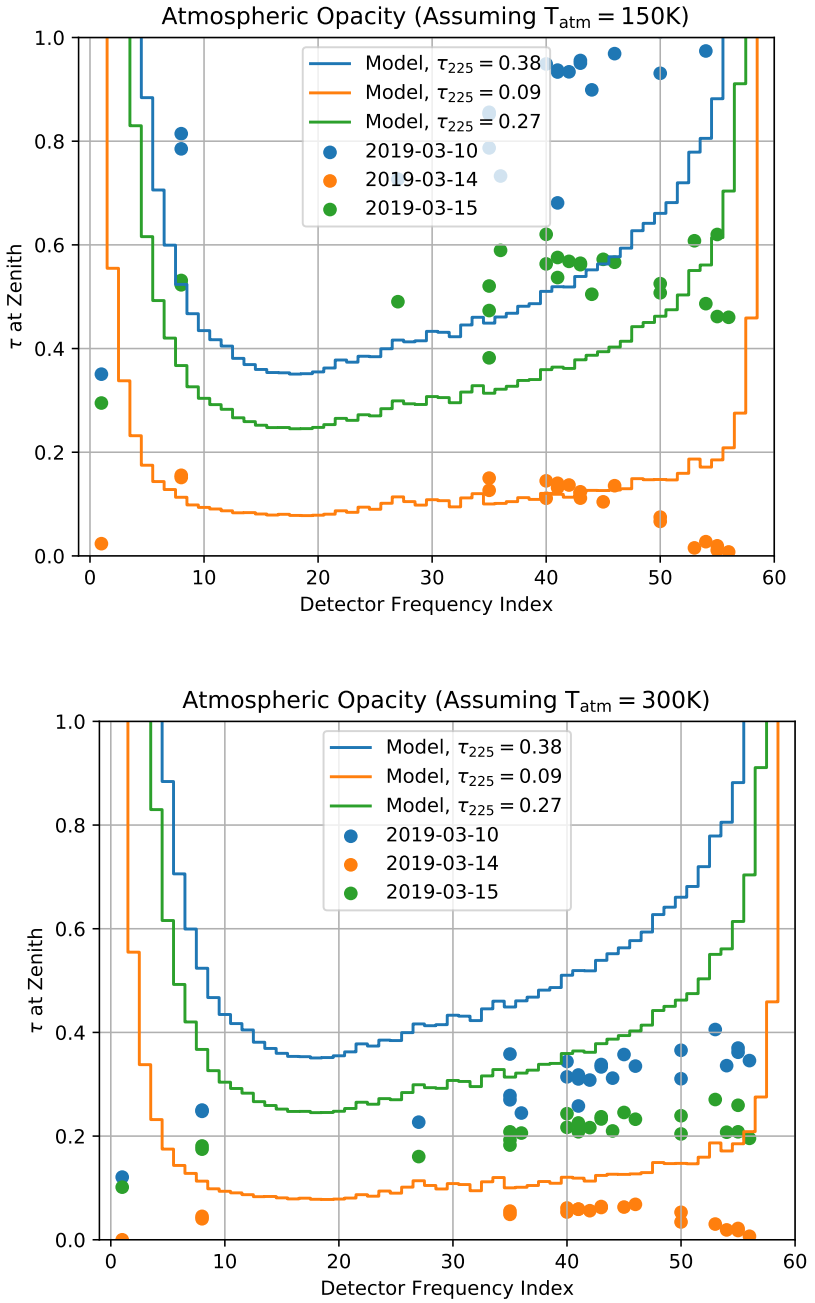

//

Figure 6.9: The atmospheric opacity at values of T_{atm} away from the best fit. A predicted atmospheric model pinned to the measured value for τ_{225} (measured separately and not used in the fitting) is included for comparison.

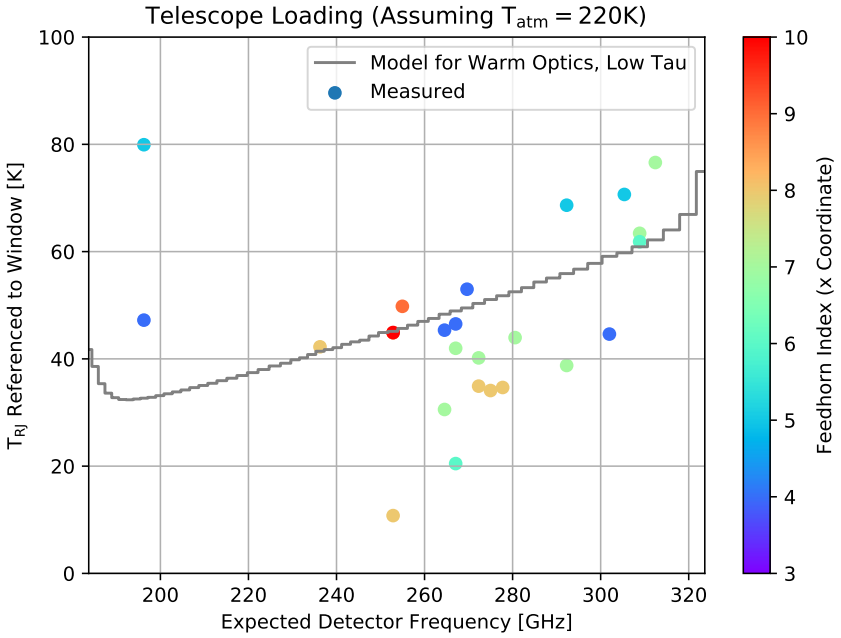

Figure 6.10: Extracted values for the constant loading term T_0 for each measured channel. The results are inconclusive.

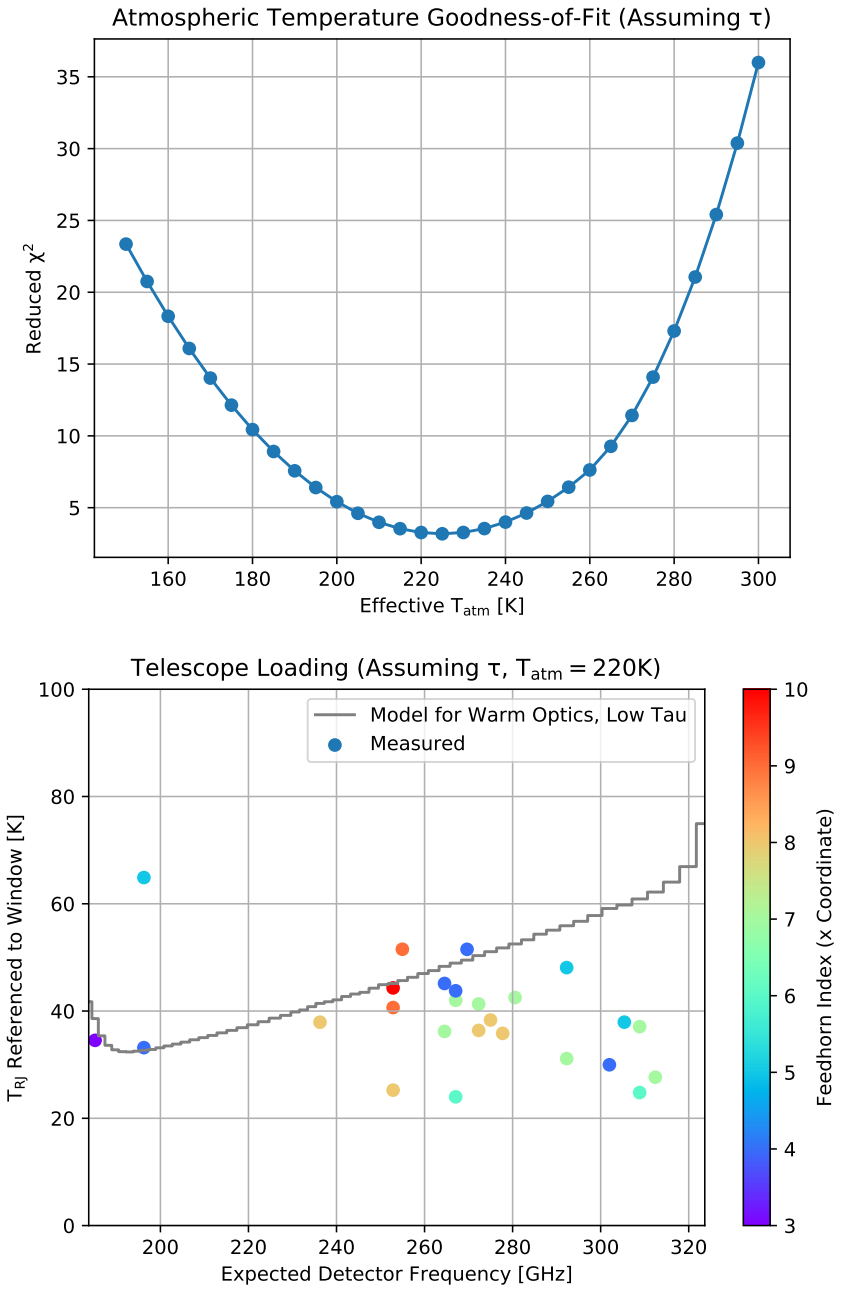

Figure 6.11: Goodness of fit and the resulting values of T_0 for an alternate analysis of the same data assuming the τ model presented in Fig. 6.8. The three datasets for each channel are therefore fit with a single free parameter (T_0) instead of four (T_0 plus three independent values of τ). The results are inconclusive.

6.3 Beam Maps

TIME completed its first successful on-sky map of a planetary source near the very end of the 2019 engineering run at Kitt Peak. Observations with a limited number of detectors of Jupiter, Venus, and Mars were made in $\sim 0.5^\circ$ square maps take over the course of about 30 min each. A segment of the scan timestream for one observation of Venus can be seen in Fig. 6.12, where the right ascension and declination are as reported by the telescope's pointing model (correction terms for the instrument have not been applied). Note that the unnecessary motion between declination steps arises from a telescope control interface limitation that has since been addressed. Threshold cuts on the first derivative of the telescope position are used to remove the turn-around regions, leaving a set of scans at nearly constant declination (18 arcsec steps) with a nearly constant velocity in right ascension. As shown in Fig. 6.13, I bin these scans into extremely narrow (1.8 arcsec) pixels, resulting in a sparse map. The map is then convolved with a two dimensional Gaussian with $\sigma = 9''$ (using `convolve_fft` from Astropy [7, 82]); missing data is ignored by the convolution and the resulting map is divided by a convolution kernel hit-count map, effectively interpolating the data. The resulting maps can then be downsampled to a more reasonable pixel spacing.

As seen in the Jupiter and Mars maps in Fig. 6.14, the TIME beams observed were much larger than expected. On our last on-sky day we began telescope focus observations on Venus; results for three positions of the secondary mirror are shown in Fig. 6.15. Observation C shows the best focus, though the beam is still several times larger than predicted. Beam maps with a Hawkeye IR flasher at the Cassegrain focus and in front of the cryostat window also show beams several times larger than predicted, indicating a potential positioning error of the lens or feedhorns within the cryostat. Work to resolve this is ongoing.

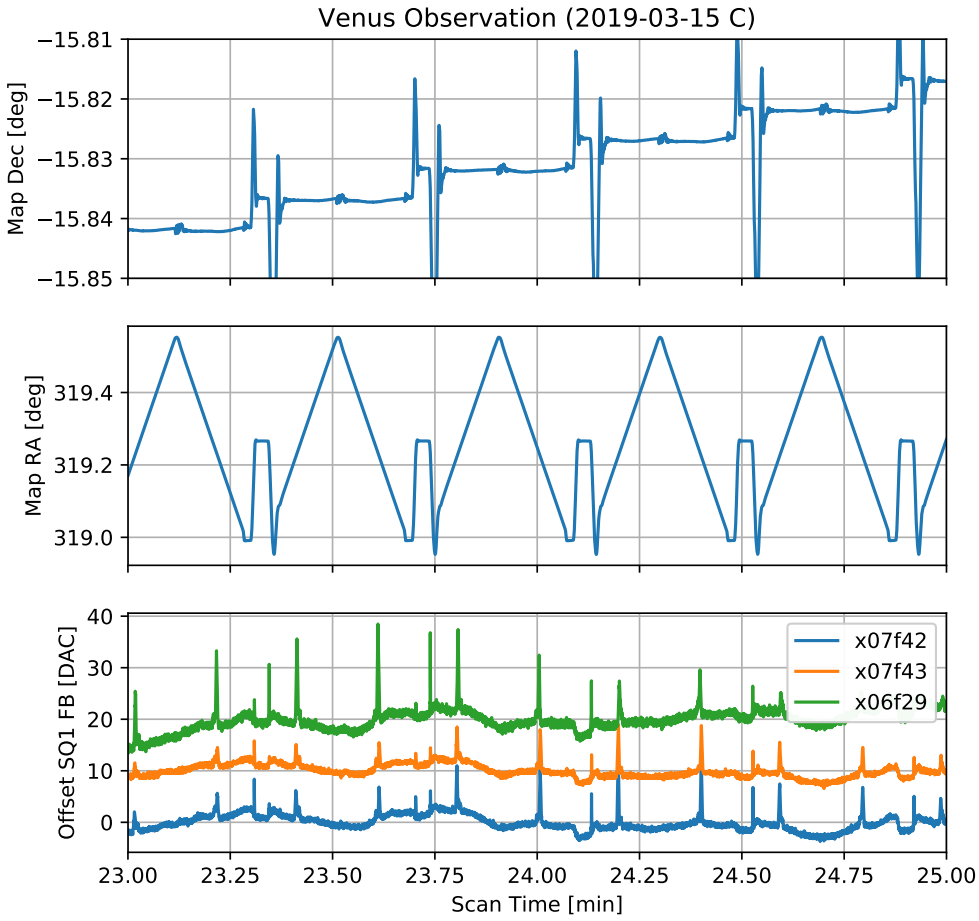

Figure 6.12: A portion of the time streams from a 2D scan of Venus. Continuous scans are made in right ascension for discrete declinations. The reported telescope position as well as the response of three detector channels are shown. The unnecessary motion between declination steps arises from a telescope control interface limitation that has since been addressed.

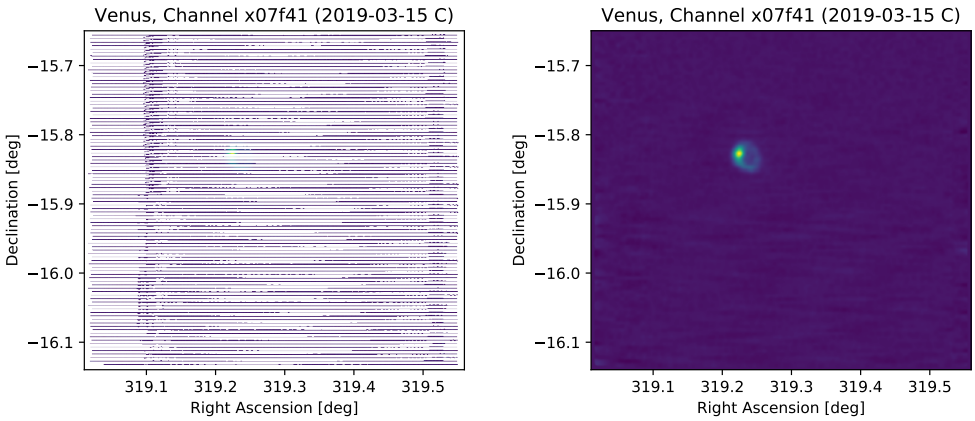

Figure 6.13: *Left:* A raw planet map from a single channel using finely spaced bins. Bins that were not sampled by the scan pattern are indicated in white. *Right:* A planet map produced by the convolution of the sparse raw map with a two-dimensional Gaussian.

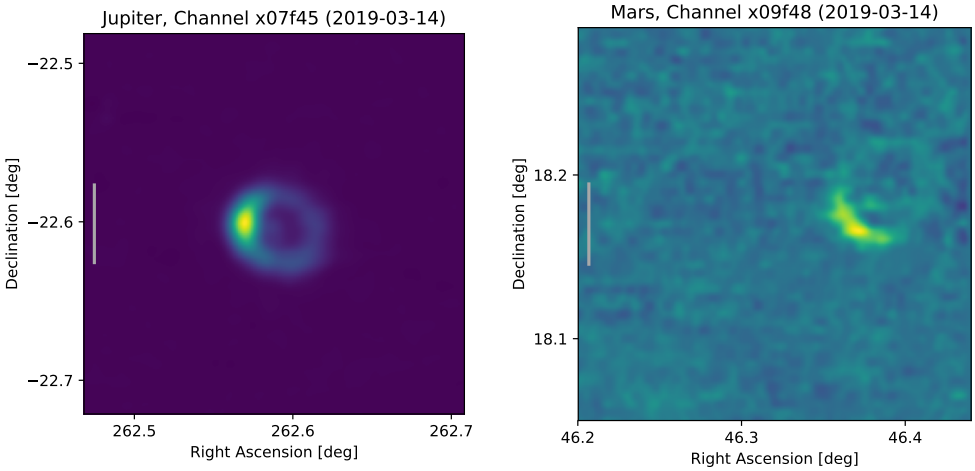

Figure 6.14: Sky beam maps taken at a non-optimal secondary mirror focus position. Jupiter and Mars are expected to have angular sizes of 37.8 and 5.0 arcsec respectively on the date in question [24]. The gray bar on the left is a 0.05° scale to visually indicate relative zoom on the plots.

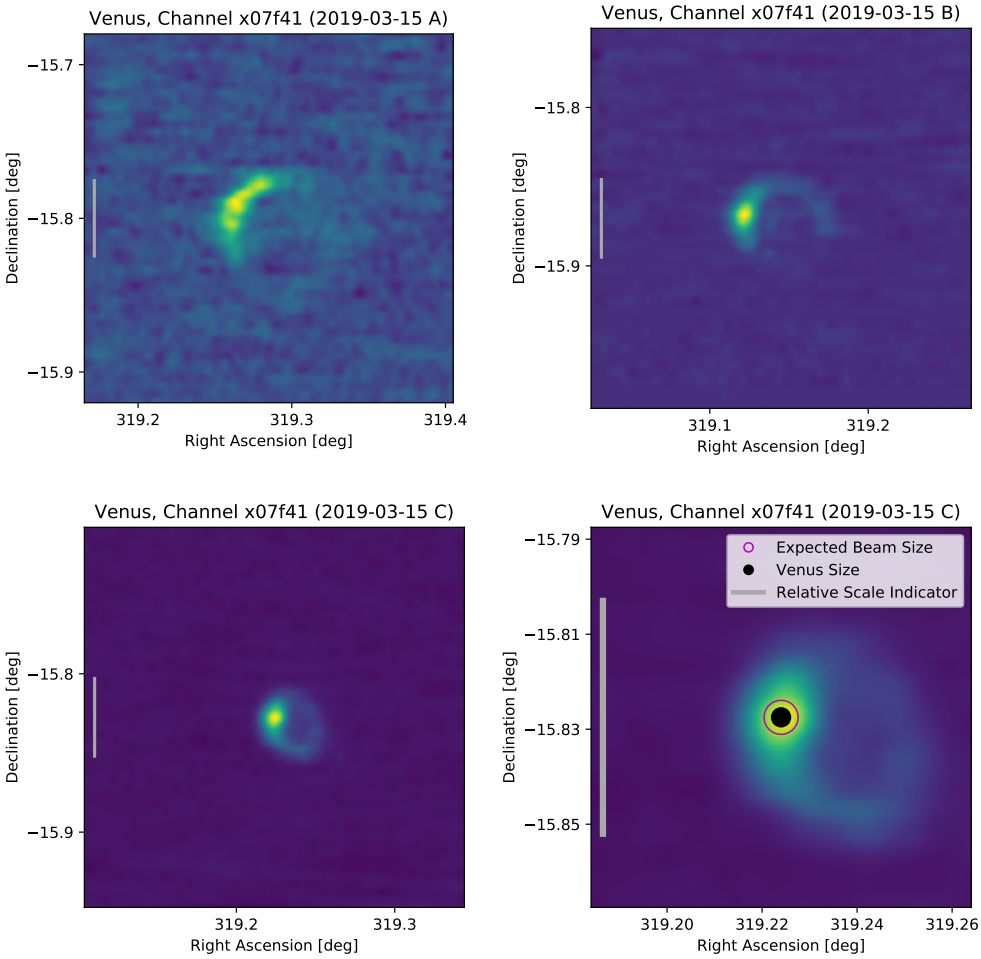

Figure 6.15: Initial focus observations taken with three different positions of the secondary mirror. Venus is expected to have an angular size of 14.3 arcsec on the date in question [24]. At the best achieved focus (expanded for visibility in the lower right panel), the beam is noticeably larger than expectations, indicating a remaining focus error. The gray bar on the left is a 0.05° scale to visually indicate relative zoom on the plots.

6.4 Noise

Low frequency noise performance at Kitt Peak during the 2019 engineering run was, generally, quite poor. A slate of cryogenic failures and a largely untested detector complement left little time for detailed noise diagnostics prior to or during deployment. In laboratory testing at Caltech following the engineering run we identified and addressed significant radio frequency interference leaks (particularly in the 50-200 MHz region) that appear to have contributed to both common mode and per-channel 1/f noise. Vibrational coupling is also a significant issue that is being addressed with changes to the focal plane support structure. The state of the noise performance at Kitt Peak prior to these improvements is demonstrated in Fig. 6.16, which shows the excess low frequency noise power relative to the white noise floor even after the removal of the two dominant common modes. This is observed even in dark feedhorns, which were blocked with aluminum tape. Furthermore, data acquired with a moving telescope suffered from readout configuration issues, severely limitings the number of active detectors for sky map data and thus limiting our ability to subtract a common mode component that doesn't also remove the bulk of the sky signal.

Despite the known issues with noise performance, I have attempted to quantify the on-sky noise through analysis of the background of the planet maps presented previously. I begin by converting a planet map in a single channel from the measured units (pA) to units of spectral radiance on the sky (MJy/sr), which I assume is a linear scaling in the small signal limit (see Sec. 3.1). Lacking more complete and rigorous calibration data, I perform this conversion by setting the integrated flux in the observed planet to an assumed value. Our TES current measurement includes an unknown per-detector offset, so the measured mean sky flux is physically meaningless and subtracted from the data; therefore, the observed flux in the planet is determined by $T_{eff} = T_{venus} - T_{sky}$. I take $T_{venus} \approx 275$K in our band [49] and $T_{sky} \approx 50$K, giving $T_{eff} \approx 225$K; the final intensity is linearly proportional to T_{eff} in the Rayleigh-Jeans limit, so the end result can be scaled by corrections to this factor. I assume Venus is a disk of uniform temperature T_{eff} with an angular diameter of 14.3 arcsec on the date in question [24], and I match the integrated flux for that disk to the integrated flux in our out-of-focus measurement. Results are shown in Fig. 6.17. The window I have chosen to apply uses a flat-top disk ($r = 0.15°$) with a smaller disk subtracted at the position

of the planet and a Gaussian taper at all edges ($\sigma = 0.05^\circ$); alternate windows are compared in Fig. 6.18, and for the purposes here any of them would be acceptable. The resulting noise map and its two dimensional power spectral density (PSD) are shown in Fig. 6.19. Significant streaking is present in the scan direction, which is represented in the PSD as a bright band for low RA spatial frequencies. Additionally, our relatively broad beam impacts spatial scales present on this plots; to quantify this, I plot the beam correction factor inferred from the squared magnitude of the FFT of the planet map (removed from the noise map) in Fig. 6.20. Note that instrumental noise is amplified by this correction, as it is not affected by the beam on the sky. The circularly-averaged 2D power spectral density is plotted in Fig. 6.21 both before or after this correction, and with or without masking RA spatial scales $k < 12\,\mathrm{deg}^{-1}$. I compare this to the expected values derived from the expected white noise NEP and the total map integration time. Results with masking and beam correction are approximately an order of magnitude above expectations. Assuming only instrumental noise is present, a more focused beam will allow us to approach the curve without beam correction, which is closer to (but still exceeding) expectations; this observed noise level can plausibly be explained by the excess 1/f noise observed at the time.

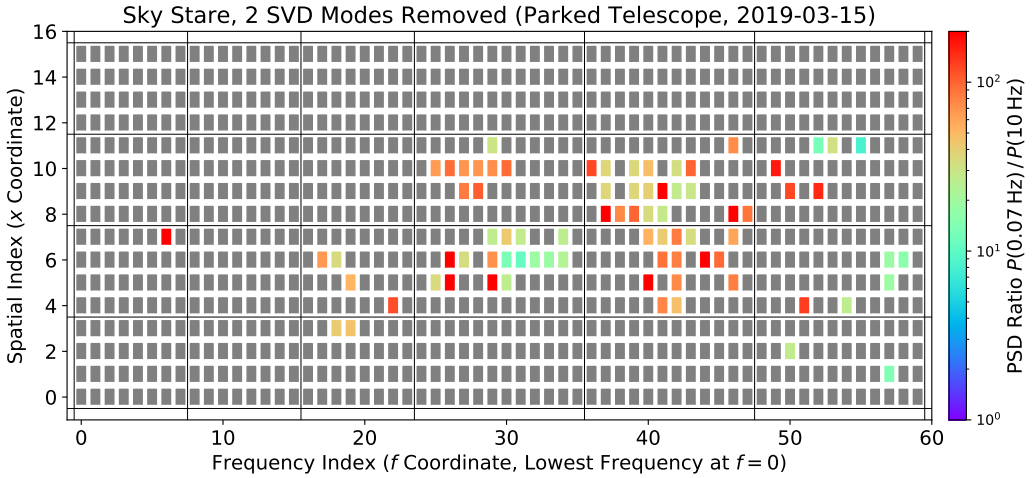

Figure 6.16: A demonstration of the poor 1/f noise performance during the 2019 TIME engineering run. The ratio of the noise power spectral density at 0.07 Hz to the power spectral density at 10 Hz (a proxy for the white noise floor) is shown for only the best live (in-transition) channels. The excess noise seen is the residual despite removing the two dominant SVD modes across the array; without this common mode subtraction, the noise excess is $\sim 100\times$ higher. The data shown was taken with the telescope parked. Feedhorns x11-x13 are dark feeds (covered at the focal plane) and still show excess noise. Significant improvements to the RF shielding have been implemented in the following months.

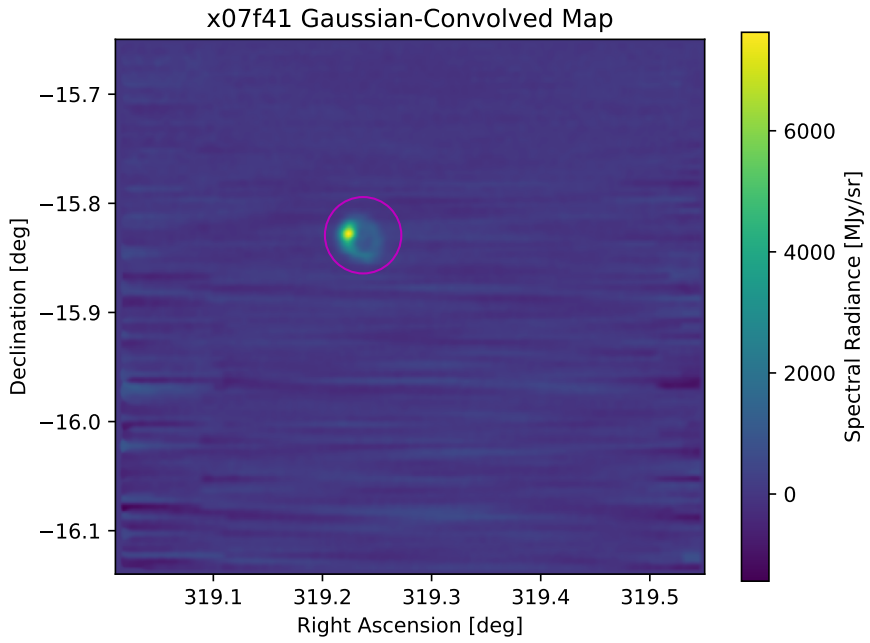

Figure 6.17: The Venus map presented in Fig. 6.13 linearly rescaled to spectral radiance on the sky by assuming the integrated flux from Venus relative to the mean-subtracted sky background.

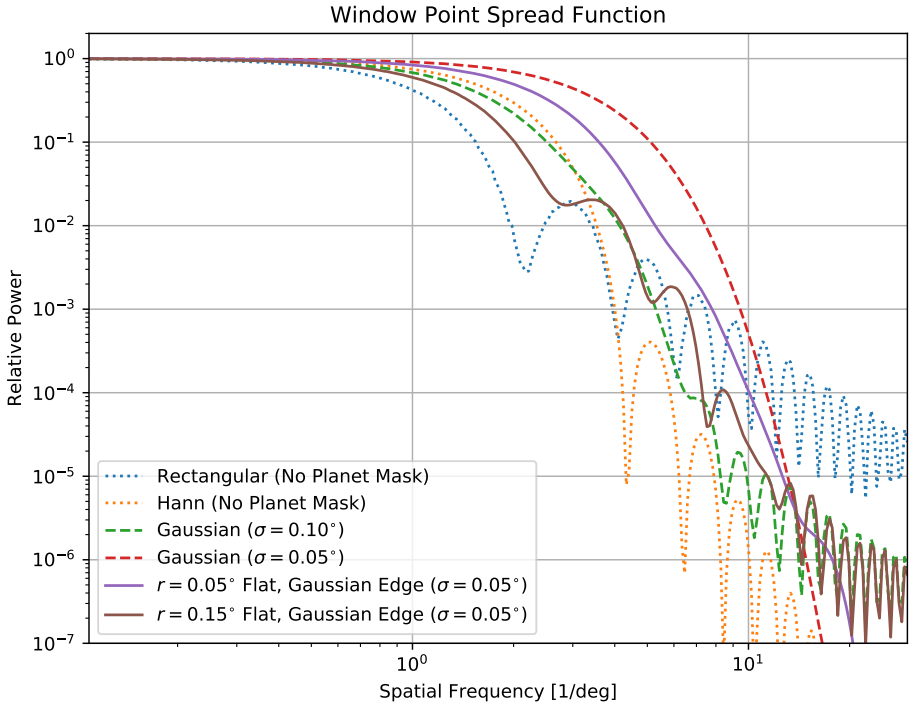

Figure 6.18: A comparison of possible data windows.

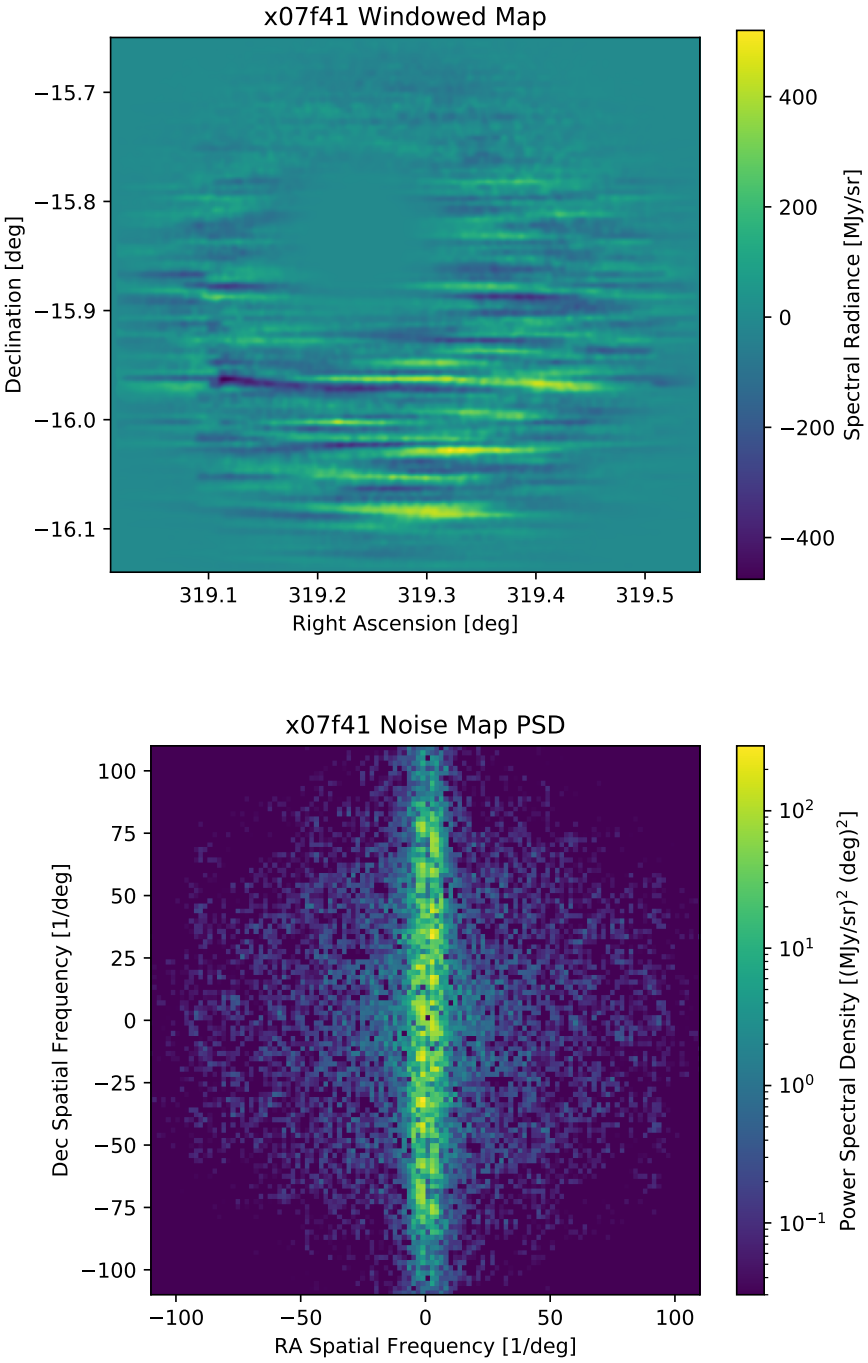

Figure 6.19: The data from Fig. 6.17 with a planet mask and a window applied, and its two dimensional power spectral density. Excess power is observed on low RA spatial scales, corresponding to instrument noise/drift in the time domain (the scan direction).

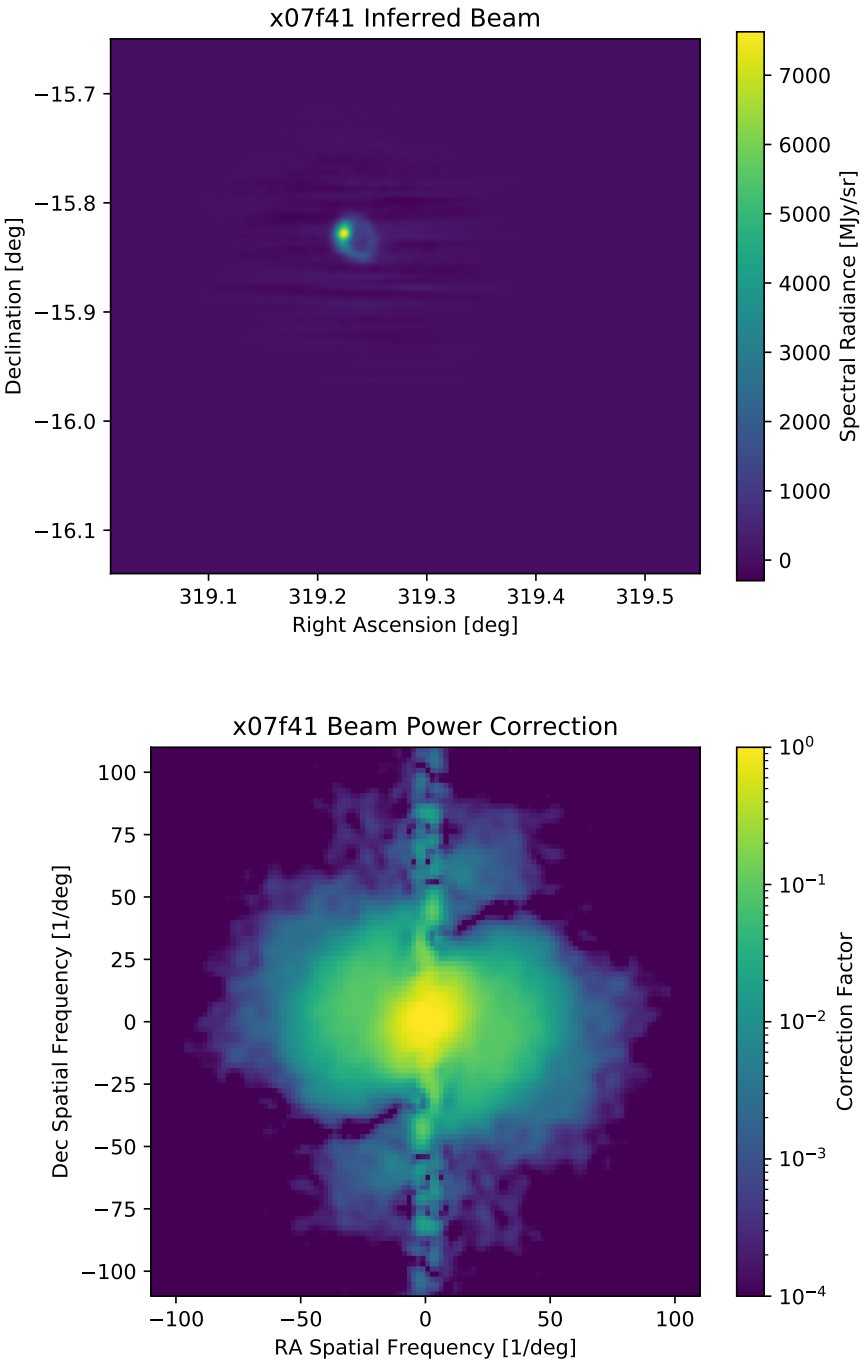

Figure 6.20: The correction factor to the 2D PSD arising from the poorly-focused wide beam on the sky.

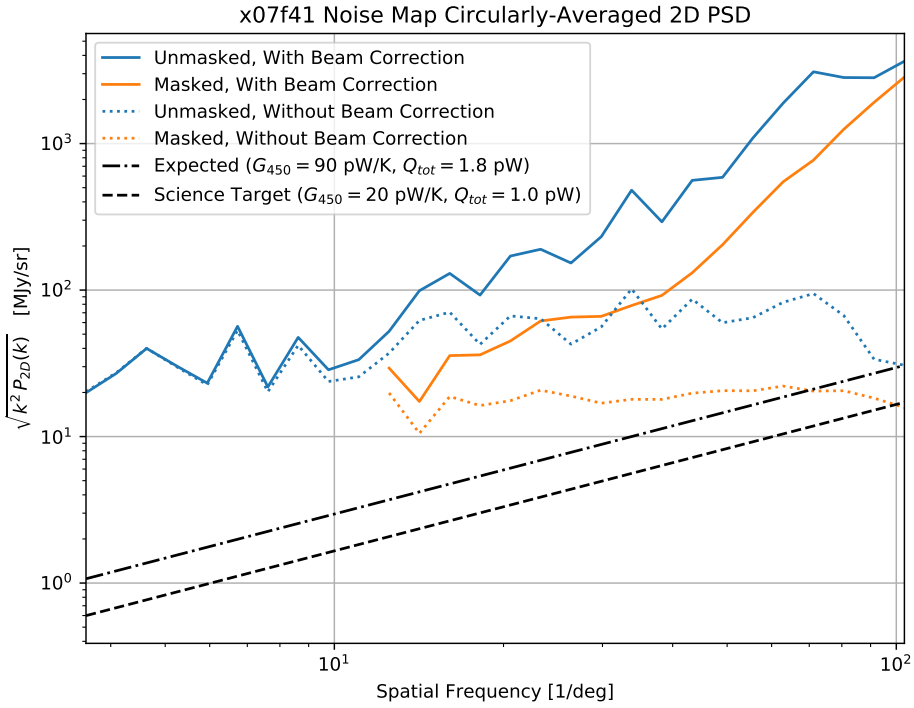

Figure 6.21: The circularly-averaged 2D power spectral density both before or after the beam correction presented in Fig. 6.20, and with or without masking RA spatial scales $k < 12\,\mathrm{deg}^{-1}$. I compare this to the expected values derived from the expected white noise NEP and the total map integration time. The observed noise level can plausibly be explained by the excess 1/f noise observed at the time.

6.5 Future Plans

The TIME instrument is being prepared for redeployment in late 2020. Significant improvements in low frequency noise performance have been made (see Fig. 6.22), though additional work remains on that front. Reductions in radiative loading on the 50K and 4K shields have enabled more robust 1K fridge performance and thinner, more transmissive thermal filters. In the coming months we intend to measure the lens and feedhorn positions with a FARO arm, apply any necessary positioning corrections, and remeasure the beam profile at the output of the cryostat window to address the focus issue observed in the engineering run. Finally, prototypes for the v7 detector design are in fabrication, which we believe will show faster time constants and improved noise performance at and above 10 Hz. The sum of all of these changes should enable initial science-quality on-sky data acquisition.

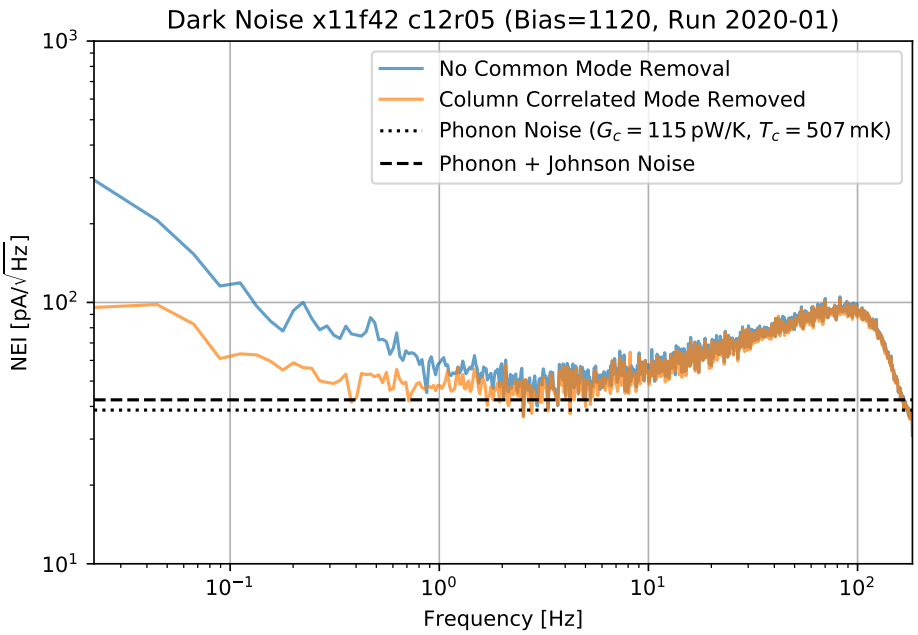

Figure 6.22: Dark noise for a single channel after improving the cryostat and readout RF shielding, both with and without a multiplexing column correlated noise signal removed. The rise above 10 Hz corresponds to the slope seen in Fig. 5.20, which is being addressed in the v7 detector design with reduced heat capacity. Residual low frequency noise is under investigation.

Bibliography

[1] Typical engineering properties of high density polyethylene. Technical report, INEOS Olefins and Polymers.

[2] Appendix I: Cryogenic Reference Tables. Technical report, Lake Shore Cryotronics, 2015. URL https://www.lakeshore.com/docs/default-source/product-downloads/literature/lstc_appendixi_l.pdf.

[3] T M C Abbott, F B Abdalla, A Alarcon, S Allam, F Andrade-Oliveira, J Annis, S Avila, M Banerji, N Banik, K Bechtol, R A Bernstein, G M Bernstein, E Bertin, D Brooks, E Buckley-Geer, D L Burke, H Camacho, A Carnero Rosell, M Carrasco Kind, J Carretero, F J Castander, R Cawthon, K C Chan, M Crocce, C E Cunha, C B D'Andrea, L N da Costa, C Davis, J De Vicente, D L DePoy, S Desai, H T Diehl, P Doel, A Drlica-Wagner, T F Eifler, J Elvin-Poole, J Estrada, A E Evrard, B Flaugher, P Fosalba, J Frieman, J García-Bellido, E Gaztanaga, D W Gerdes, T Giannantonio, D Gruen, R A Gruendl, J Gschwend, G Gutierrez, W G Hartley, D Hollowood, K Honscheid, B Hoyle, B Jain, D J James, T Jeltema, M D Johnson, S Kent, N Kokron, E Krause, K Kuehn, S Kuhlmann, N Kuropatkin, F Lacasa, O Lahav, M Lima, H Lin, M A G Maia, M Manera, J Marriner, J L Marshall, P Martini, P Melchior, F Menanteau, C J Miller, R Miquel, J J Mohr, E Neilsen, W J Percival, A A Plazas, A Porredon, A K Romer, A Roodman, R Rosenfeld, A J Ross, E Rozo, E S Rykoff, M Sako, E Sanchez, B Santiago, V Scarpine, R Schindler, M Schubnell, S Serrano, I Sevilla-Noarbe, E Sheldon, R C Smith, M Smith, F Sobreira, E Suchyta, M E C Swanson, G Tarle, D Thomas, M A Troxel, D L Tucker, V Vikram, A R Walker, R H Wechsler, J Weller, B Yanny, Y Zhang, and (The Dark Energy Survey Collaboration). Dark Energy Survey Year 1 results: measurement of the baryon acoustic oscillation scale in the distribution of galaxies to redshift 1. *Monthly Notices of the Royal Astronomical Society*, 483(4): 4866–4883, 12 2018. ISSN 0035-8711. doi: 10.1093/mnras/sty3351. URL https://doi.org/10.1093/mnras/sty3351.

[4] Peter A. Ade, Zeeshan Ahmed, Randol Aikin, Kate D. Alexander, Denis Barkats, Steve J. Benton, Colin A. Bischoff, James J. Bock, Hans Boenish, Rachel Bowens-Rubin, and et al. 2017 upgrade and performance of bicep3: a 95ghz refracting telescope for degree-scale cmb polarization. *Millimeter, Submillimeter, and Far-Infrared Detectors and Instrumentation for Astronomy IX*, Jul 2018. doi: 10.1117/12.2313854. URL http://dx.doi.org/10.1117/12.2313854.

[5] Randol W. Aikin, P. A. Ade, S. Benton, J. J. Bock, J. A. Bonetti, J. A. Brevik, C. D. Dowell, L. Duband , J. P. Filippini, S. R. Golwala,

M. Halpern, V. V. Hristov, K. Irwin, J. P. Kaufman, B. G. Keating, J. M. Kovac, C. L. Kuo, A. E. Lange, C. B. Netterfield, H. T. Nguyen, IV Ogburn, R. W., A. Orlando, C. Pryke, S. Richter, J. E. Ruhl, M. C. Runyan, C. Sheehy, S. A. Stokes, R. Sudiwala, G. P. Teply, J. E. Tolan, A. D. Turner, P. Wilson, and C. L. Wong. *Optical performance of the BICEP2 Telescope at the South Pole*, volume 7741 of *Society of Photo-Optical Instrumentation Engineers (SPIE) Conference Series*, page 77410V. 2010. doi: 10.1117/12.857868.

[6] Amuneal. Magnetic shielding materials. URL `http://www.amuneal.com/magnetic-shielding/magnetic-shielding-materials`.

[7] Astropy Collaboration, T. P. Robitaille, E. J. Tollerud, P. Greenfield, M. Droettboom, E. Bray, T. Aldcroft, M. Davis, A. Ginsburg, A. M. Price-Whelan, W. E. Kerzendorf, A. Conley, N. Crighton, K. Barbary, D. Muna, H. Ferguson, F. Grollier, M. M. Parikh, P. H. Nair, H. M. Unther, C. Deil, J. Woillez, S. Conseil, R. Kramer, J. E. H. Turner, L. Singer, R. Fox, B. A. Weaver, V. Zabalza, Z. I. Edwards, K. Azalee Bostroem, D. J. Burke, A. R. Casey, S. M. Crawford, N. Dencheva, J. Ely, T. Jenness, K. Labrie, P. L. Lim, F. Pierfederici, A. Pontzen, A. Ptak, B. Refsdal, M. Servillat, and O. Streicher. Astropy: A community Python package for astronomy. *A&A*, 558:A33, October 2013. doi: 10.1051/0004-6361/201322068.

[8] Hakim Atek, Johan Richard, Mathilde Jauzac, Jean-Paul Kneib, Priyamvada Natarajan, Marceau Limousin, Daniel Schaerer, Eric Jullo, Harald Ebeling, Eiichi Egami, and Benjamin Clement. Are Ultra-faint Galaxies at z = 6-8 Responsible for Cosmic Reionization? Combined Constraints from the Hubble Frontier Fields Clusters and Parallels. *ApJ*, 814(1):69, November 2015. doi: 10.1088/0004-637X/814/1/69.

[9] E. S. Battistelli, M. Amiri, B. Burger, M. Halpern, S. Knotek, M. Ellis, X. Gao, D. Kelly, M. MacIntosh, K. Irwin, and C. Reintsema. Functional description of read-out electronics for time-domain multiplexed bolometers for millimeter and sub-millimeter astronomy. *Journal of Low Temperature Physics*, 151(3):908–914, 2008. ISSN 1573-7357. doi: 10.1007/s10909-008-9772-z. URL `http://dx.doi.org/10.1007/s10909-008-9772-z`.

[10] George D. Becker, James S. Bolton, and Adam Lidz. Reionisation and High-Redshift Galaxies: The View from Quasar Absorption Lines. *PASA*, 32:e045, Dec 2015. doi: 10.1017/pasa.2015.45.

[11] M. Bethermin, Y. Fudamoto, M. Ginolfi, F. Loiacono, Y. Khusanova, P. L. Capak, P. Cassata, A. Faisst, O. Le Fevre, D. Schaerer, J. D. Silverman, L. Yan, R. Amorin, S. Bardelli, M. Boquien, A. Cimatti, I. Davidzon, M. Dessauges-Zavadsky, S. Fujimoto, C. Gruppioni, N. P. Hathi,

E. Ibar, G. C. Jones, A. M. Koekemoer, G. Lagache, B. C. Lemaux, P. A. Oesch, F. Pozzi, D. A. Riechers, M. Talia, S. Toft, L. Vallini, D. Vergani, G. Zamorani, and E. Zucca. The ALPINE-ALMA [CII] Survey: data processing, catalogs, and statistical source properties. *arXiv e-prints*, art. arXiv:2002.00962, February 2020.

[12] BICEP2 Collaboration, Keck Array Collaboration, P. A. R. Ade, Z. Ahmed, R. W. Aikin, K. D. Alexand er, D. Barkats, S. J. Benton, C. A. Bischoff, J. J. Bock, R. Bowens-Rubin, J. A. Brevik, I. Buder, E. Bullock, V. Buza, J. Connors, J. Cornelison, B. P. Crill, M. Crumrine, M. Dierickx, L. Duband, C. Dvorkin, J. P. Filippini, S. Fliescher, J. Grayson, G. Hall, M. Halpern, S. Harrison, S. R. Hildebrand t, G. C. Hilton, H. Hui, K. D. Irwin, J. Kang, K. S. Karkare, E. Karpel, J. P. Kaufman, B. G. Keating, S. Kefeli, S. A. Kernasovskiy, J. M. Kovac, C. L. Kuo, N. A. Larsen, K. Lau, E. M. Leitch, M. Lueker, K. G. Megerian, L. Moncelsi, T. Namikawa, C. B. Netterfield, H. T. Nguyen, R. O'Brient, R. W. Ogburn, S. Palladino, C. Pryke, B. Racine, S. Richter, A. Schillaci, R. Schwarz, C. D. Sheehy, A. Soliman, T. St. Germaine, Z. K. Staniszewski, B. Steinbach, R. V. Sudiwala, G. P. Teply, K. L. Thompson, J. E. Tolan, C. Tucker, A. D. Turner, C. Umiltà, A. G. Vieregg, A. Wand ui, A. C. Weber, D. V. Wiebe, J. Willmert, C. L. Wong, W. L. K. Wu, H. Yang, K. W. Yoon, and C. Zhang. Constraints on Primordial Gravitational Waves Using Planck, WMAP, and New BICEP2/Keck Observations through the 2015 Season. *Phys. Rev. Lett.*, 121(22):221301, November 2018. doi: 10.1103/PhysRevLett.121.221301.

[13] James Bock. Private Communication, May 2015. Tabulated measurements of gold thin film resistance.

[14] A. Boselli, G. Gavazzi, J. Lequeux, and D. Pierini. [CII] at 158 mu m as a star formation tracer in late-type galaxies. *A&A*, 385:454–463, Apr 2002. doi: 10.1051/0004-6361:20020156.

[15] R. J. Bouwens, G. D. Illingworth, P. A. Oesch, M. Trenti, I. Labbé, L. Bradley, M. Carollo, P. G. van Dokkum, V. Gonzalez, B. Holwerda, and et al. Uv luminosity functions at redshifts z=4 to z=10: 10,000 galaxies from hst legacy fields. *The Astrophysical Journal*, 803(1):34, Apr 2015. ISSN 1538-4357. doi: 10.1088/0004-637x/803/1/34. URL `http://dx.doi.org/10.1088/0004-637X/803/1/34`.

[16] Rychard Bouwens. *High-Redshift Galaxy Surveys and the Reionization of the Universe*, volume 423 of *Astrophysics and Space Science Library*, page 111. 2016. doi: 10.1007/978-3-319-21957-8_4.

[17] C. M. Bradford, B. J. Naylor, J. Zmuidzinas, J. J. Bock, J. Gromke, H. Nguyen, M. Dragovan, M. Yun, L. Earle, J. Glenn, H. Matsuhara, P. A. R. Ade, and L. Duband. WaFIRS: a waveguide far-IR spectrometer:

enabling spectroscopy of high-z galaxies in the far-IR and submillimeter. In J. C. Mather, editor, *IR Space Telescopes and Instruments*, volume 4850 of *Proc. SPIE*, pages 1137–1148, March 2003.

[18] C. M. Bradford, A. Beyer, M. Kenyon, M. C. Runyan, B. Bumble, P. Echternach, T. Prouvé, W. A. Holmes, J. J. Bock, and K. Irwin. *Progress toward BLISS, the background-limited infrared-submillimeter spectrograph for SPICA*, volume 8442 of *Society of Photo-Optical Instrumentation Engineers (SPIE) Conference Series*, page 84420P. 2012. doi: 10.1117/12.926843.

[19] C. Matt Bradford, Peter A. R. Ade, James E. Aguirre, James J. Bock, Mark Dragovan, Lionel Duband, Lieko Earle, Jason Glenn, Hideo Matsuhara, Bret J. Naylor, Hien T. Nguyen, Minhee Yun, and Jonas Zmuidzinas. *Z-Spec: a broadband millimeter-wave grating spectrometer: design, construction, and first cryogenic measurements*, volume 5498 of *Society of Photo-Optical Instrumentation Engineers (SPIE) Conference Series*, page 257. 2004. doi: 10.1117/12.552182.

[20] S Burgess and D Greig. The low-temperature thermal conductivity of polyethylene. *Journal of Physics C: Solid State Physics*, 8(11):1637–1648, jun 1975. doi: 10.1088/0022-3719/8/11/015. URL `https://doi.org/10.1088%2F0022-3719%2F8%2F11%2F015`.

[21] Y. A. Cengel and A. J. Ghajar. *Heat and Mass Transfer: Fundamentals and Applications 4th ed.* McGraw-Hill Education, 2009. ISBN 9780073398129.

[22] Tzu-Ching Chang, Ue-Li Pen, Kevin Bandura, and Jeffrey B. Peterson. Hydrogen 21-cm Intensity Mapping at redshift 0.8. *arXiv e-prints*, art. arXiv:1007.3709, July 2010.

[23] Yun-Ting Cheng, Tzu-Ching Chang, James Bock, C. Matt Bradford, and Asantha Cooray. Spectral Line De-confusion in an Intensity Mapping Survey. *ApJ*, 832(2):165, Dec 2016. doi: 10.3847/0004-637X/832/2/165.

[24] Fabien Chereau. Stellarium. URL `http://stellarium.org`.

[25] J. Choi, H. Ishitsuka, S. Mima, S. Oguri, K. Takahashi, and O. Tajima. Radio-transparent multi-layer insulation for radiowave receivers. *Review of Scientific Instruments*, 84(11):114502, Nov 2013. ISSN 1089-7623. doi: 10.1063/1.4827081. URL `http://dx.doi.org/10.1063/1.4827081`.

[26] A. L. Cooksy, G. A. Blake, and R. J. Saykally. Direct Measurement of the Fine-Structure Interval and G J Factors of Singly Ionized Atomic Carbon by Laser Magnetic Resonance. *ApJ*, 305:L89, Jun 1986. doi: 10.1086/184691.

[27] R.J. Corruccini and J.J. Gniewek. Specific heats and enthalpies of technical solids at low temperatures. a compilation from the literature. Technical report, 10 1960.

[28] A. T. Crites, J. J. Bock, C. M. Bradford, T. C. Chang, A. R. Cooray, L. Duband, Y. Gong, S. Hailey-Dunsheath, J. Hunacek, P. M. Koch, C. T. Li, R. C. O'Brient, T. Prouve, E. Shirokoff, M. B. Silva, Z. Staniszewski, B. Uzgil, and M. Zemcov. The TIME-Pilot intensity mapping experiment. In *Millimeter, Submillimeter, and Far-Infrared Detectors and Instrumentation for Astronomy VII*, volume 9153 of *Proc. SPIE*, page 91531W, August 2014. doi: 10.1117/12.2057207.

[29] Cryomech. Pt415 cryocoolers. URL `https://www.cryomech.com/products/pt415/`.

[30] Lake Shore Cryotronics. Dt-670 silicon diodes. URL `https://www.lakeshore.com/products/categories/overview/temperature-products/cryogenic-temperature-sensors/dt-670-silicon-diodes`.

[31] Paul Cunningham, Nestor Valdes, Felipe Vallejo, L. Hayden, Brent Polishak, Xing-Hua Zhou, Jingdong Luo, Alex Jen, Jarrod Williams, and Robert Twieg. Broadband terahertz characterization of the refractive index and absorption of some important polymeric and organic electro-optic materials. *Journal of Applied Physics*, 109:043505 – 043505, 05 2011. doi: 10.1063/1.3549120.

[32] Rene Dandliker. Concept of modes in optics and photonics. In *PROCEEDINGS-SPIE THE INTERNATIONAL SOCIETY FOR OPTICAL ENGINEERING*, pages 193–199. International Society for Optical Engineering; 1999, 1999.

[33] Kyle S. Dawson, David J. Schlegel, Christopher P. Ahn, Scott F. Anderson, Éric Aubourg, Stephen Bailey, Robert H. Barkhouser, Julian E. Bautista, Alessand ra Beifiori, Andreas A. Berlind, Vaishali Bhardwaj, Dmitry Bizyaev, Cullen H. Blake, Michael R. Blanton, Michael Blomqvist, Adam S. Bolton, Arnaud Borde, Jo Bovy, W. N. Brandt, Howard Brewington, Jon Brinkmann, Peter J. Brown, Joel R. Brownstein, Kevin Bundy, N. G. Busca, William Carithers, Aurelio R. Carnero, Michael A. Carr, Yanmei Chen, Johan Comparat, Natalia Connolly, Frances Cope, Rupert A. C. Croft, Antonio J. Cuesta, Luiz N. da Costa, James R. A. Davenport, Timothée Delubac, Roland de Putter, Saurav Dhital, Anne Ealet, Garrett L. Ebelke, Daniel J. Eisenstein, S. Escoffier, Xiaohui Fan, N. Filiz Ak, Hayley Finley, Andreu Font-Ribera, R. Génova-Santos, James E. Gunn, Hong Guo, Daryl Haggard, Patrick B. Hall, Jean-Christophe Hamilton, Ben Harris, David W. Harris, Shirley Ho, David W. Hogg, Diana Holder, Klaus Honscheid,

Joe Huehnerhoff, Beatrice Jordan, Wendell P. Jordan, Guinevere Kauffmann, Eyal A. Kazin, David Kirkby, Mark A. Klaene, Jean-Paul Kneib, Jean-Marc Le Goff, Khee-Gan Lee, Daniel C. Long, Craig P. Loomis, Britt Lundgren, Robert H. Lupton, Marcio A. G. Maia, Martin Makler, Elena Malanushenko, Viktor Malanushenko, Rachel Mandelbaum, Marc Manera, Claudia Maraston, Daniel Margala, Karen L. Masters, Cameron K. McBride, Patrick McDonald, Ian D. McGreer, Richard G. McMahon, Olga Mena, Jordi Miralda-Escudé, Antonio D. Montero-Dorta, Francesco Montesano, Demitri Muna, Adam D. Myers, Tracy Naugle, Robert C. Nichol, Pasquier Noterdaeme, Sebastián E. Nuza, Matthew D. Olmstead, Audrey Oravetz, Daniel J. Oravetz, Russell Owen, Nikhil Padmanabhan, Nathalie Palanque-Delabrouille, Kaike Pan, John K. Parejko, Isabelle Pâris, Will J. Percival, Ismael Pérez-Fournon, Ignasi Pérez-Ràfols, Patrick Petitjean, Robert Pfaffenberger, Janine Pforr, Matthew M. Pieri, Francisco Prada, Adrian M. Price-Whelan, M. Jordan Raddick, Rafael Rebolo, James Rich, Gordon T. Richards, Constance M. Rockosi, Natalie A. Roe, Ashley J. Ross, Nicholas P. Ross, Graziano Rossi, J. A. Rubiño-Martin, Lado Samushia, Ariel G. Sánchez, Conor Sayres, Sarah J. Schmidt, Donald P. Schneider, C. G. Scóccola, Hee-Jong Seo, Alaina Shelden, Erin Sheldon, Yue Shen, Yiping Shu, Anže Slosar, Stephen A. Smee, Stephanie A. Snedden, Fritz Stauffer, Oliver Steele, Michael A. Strauss, Alina Streblyanska, Nao Suzuki, Molly E. C. Swanson, Tomer Tal, Masayuki Tanaka, Daniel Thomas, Jeremy L. Tinker, Rita Tojeiro, Christy A. Tremonti, M. Vargas Magaña, Licia Verde, Matteo Viel, David A. Wake, Mike Watson, Benjamin A. Weaver, David H. Weinberg, Benjamin J. Weiner, Andrew A. West, Martin White, W. M. Wood-Vasey, Christophe Yeche, Idit Zehavi, Gong-Bo Zhao, and Zheng Zheng. The Baryon Oscillation Spectroscopic Survey of SDSS-III. *AJ*, 145(1):10, January 2013. doi: 10.1088/0004-6256/145/1/10.

[34] S. De Barros, L. Pentericci, E. Vanzella, M. Castellano, A. Fontana, A. Grazian, C. J. Conselice, H. Yan, A. Koekemoer, S. Cristiani, M. Dickinson, S. L. Finkelstein, and R. Maiolino. VLT/FORS2 view at z 6: Lyman-α emitter fraction and galaxy physical properties at the edge of the epoch of cosmic reionization. *A&A*, 608:A123, December 2017. doi: 10.1051/0004-6361/201731476.

[35] Piet A. J. de Korte, Joern Beyer, Steve Deiker, Gene C. Hilton, Kent D. Irwin, Mike MacIntosh, Sae Woo Nam, Carl D. Reintsema, Leila R. Vale, and Martin E. Huber. Time-division superconducting quantum interference device multiplexer for transition-edge sensors. *Review of Scientific Instruments*, 74(8):3807–3815, August 2003. doi: 10.1063/1.1593809.

[36] Ilse De Looze, Maarten Baes, George J. Bendo, Luca Cortese, and Ja-

copo Fritz. The reliability of [C II] as an indicator of the star formation rate. *MNRAS*, 416(4):2712–2724, Oct 2011. doi: 10.1111/j.1365-2966.2011.19223.x.

[37] Ilse De Looze, Diane Cormier, Vianney Lebouteiller, Suzanne Madden, Maarten Baes, George J. Bendo, Médéric Boquien, Alessandro Boselli, David L. Clements, Luca Cortese, Asantha Cooray, Maud Galametz, Frédéric Galliano, Javier Graciá-Carpio, Kate Isaak, Oskar Ł. Karczewski, Tara J. Parkin, Eric W. Pellegrini, Aurélie Rémy-Ruyer, Luigi Spinoglio, Matthew W. L. Smith, and Eckhard Sturm. The applicability of far-infrared fine-structure lines as star formation rate tracers over wide ranges of metallicities and galaxy types. *A&A*, 568:A62, August 2014. doi: 10.1051/0004-6361/201322489.

[38] Mark Dickinson, Mauro Giavalisco, and GOODS Team. The Great Observatories Origins Deep Survey. In Ralf Bender and Alvio Renzini, editors, *The Mass of Galaxies at Low and High Redshift*, page 324, January 2003. doi: 10.1007/10899892_78.

[39] L. Earle, P. Ade, J. Aguirre, R. Aikin, J. Battle, J. Bock, C. M. Bradford, M. Dragovan, L. Duband, J. Glenn, G. Griffin, V. Hristov, P. Maloney, H. Matsuhara, B. Naylor, H. Nguyen, M. Yun, and J. Zmuidzinas. *Z-Spec: a broadband direct-detection millimeter-wave spectrometer – instrument status and first results*, volume 6275 of *Society of Photo-Optical Instrumentation Engineers (SPIE) Conference Series*, page 627510. 2006. doi: 10.1117/12.672309.

[40] J. Filippini. Spider internal note. Jul 2010.

[41] Jan Mathias Gildemeister. PhD thesis, 2000.

[42] Y. Gong, A. Cooray, M. Silva, M. G. Santos, J. Bock, C. M. Bradford, and M. Zemcov. Intensity Mapping of the [C II] Fine Structure Line during the Epoch of Reionization. *ApJ*, 745:49, January 2012. doi: 10.1088/0004-637X/745/1/49.

[43] Rebecca Grinham and Andrew Chew. Gas correction factors for vacuum pressure gauges. *Vakuum in Forschung und Praxis*, 29(2):25–30, 2017. doi: 10.1002/vipr.201700640. URL `https://onlinelibrary.wiley.com/doi/abs/10.1002/vipr.201700640`.

[44] J. E. Gunn and B. A. Peterson. On the Density of Neutral Hydrogen in Intergalactic Space. *ApJ*, 142:1633–1641, November 1965. doi: 10.1086/148444.

[45] M. Halpern, H. P. Gush, E. Wishnow, and V. de Cosmo. Far infrared transmission of dielectrics at cryogenic and room temperatures: glass, Fluorogold, Eccosorb, Stycast, and various plastics. *Appl. Opt.*, 25(4):565–570, Feb 1986. doi: 10.1364/AO.25.000565.

[46] Yuichi Harikane, Masami Ouchi, Akio K. Inoue, Yoshiki Matsuoka, Yoichi Tamura, Tom Bakx, Seiji Fujimoto, Kana Moriwaki, Yoshiaki Ono, Tohru Nagao, Ken-ichi Tadaki, Takashi Kojima, Takatoshi Shibuya, Eiichi Egami, Andrea Ferrara, Simona Gallerani, Takuya Hashimoto, Kotaro Kohno, Yuichi Matsuda, Hiroshi Matsuo, Andrea Pallottini, Yuma Sugahara, and Livia Vallini. Large Population of ALMA Galaxies at z>6 with Very High [OIII]88um to [CII]158um Flux Ratios: Evidence of Extremely High Ionization Parameter or PDR Deficit? *arXiv e-prints*, art. arXiv:1910.10927, October 2019.

[47] Shawn W. Henderson, Jason R. Stevens, Mandana Amiri, Jason Austermann, James A. Beall, Saptarshi Chaudhuri, Hsiao-Mei Cho, Steve K. Choi, Nicholas F. Cothard, Kevin T. Crowley, Shannon M. Duff, Colin P. Fitzgerald, Patricio A. Gallardo, Mark Halpern, Matthew Hasselfield, Gene Hilton, Shuay-Pwu Patty Ho, Johannes Hubmayr, Kent D. Irwin, Brian J. Koopman, Dale Li, Yaqiong Li, Jeff McMahon, Federico Nati, Michael Niemack, Carl D. Reintsema, Maria Salatino, Alessandro Schillaci, Benjamin L. Schmitt, Sara M. Simon, Suzanne T. Staggs, Eve M. Vavagiakis, and Jonathan T. Ward. *Readout of two-kilopixel transition-edge sensor arrays for Advanced ACTPol*, volume 9914 of *Society of Photo-Optical Instrumentation Engineers (SPIE) Conference Series*, page 99141G. 2016. doi: 10.1117/12.2233895.

[48] G. Hinshaw, D. Larson, E. Komatsu, D. N. Spergel, C. L. Bennett, J. Dunkley, M. R. Nolta, M. Halpern, R. S. Hill, N. Odegard, L. Page, K. M. Smith, J. L. Weiland, B. Gold, N. Jarosik, A. Kogut, M. Limon, S. S. Meyer, G. S. Tucker, E. Wollack, and E. L. Wright. Nine-year Wilkinson Microwave Anisotropy Probe (WMAP) Observations: Cosmological Parameter Results. *ApJS*, 208(2):19, October 2013. doi: 10.1088/0067-0049/208/2/19.

[49] H. S. Hudson, C. A. Lindsey, and B. T. Soifer. Submillimeter Observations of Planets. *Icarus*, 23(3):374–379, November 1974. doi: 10.1016/0019-1035(74)90055-4.

[50] J. Hunacek, J. Bock, C. M. Bradford, V. Butler, T. C. Chang, Y. T. Cheng, A. Cooray, A. Crites, C. Frez, S. Hailey-Dunsheath, B. Hoscheit, D. W. Kim, C. T. Li, D. Marrone, L. Moncelsi, E. Shirokoff, B. Steinbach, G. Sun, I. Trumper, A. Turner, B. Uzgil, A. Weber, and M. Zemcov. Hafnium Films and Magnetic Shielding for TIME, A mm-Wavelength Spectrometer Array. *Journal of Low Temperature Physics*, 193(5-6):893–900, Dec 2018. doi: 10.1007/s10909-018-1906-3.

[51] K. D. Irwin and G. C. Hilton. *Transition-Edge Sensors*, volume 99, page 63. 2005. doi: 10.1007/10933596_3.

[52] Y.-S Jin, G.-J Kim, and S.-G Jeon. Terahertz dielectric properties of polymers. *Journal of the Korean Physical Society*, 49:513–517, 08 2006.

[53] Alexander A. Kaurov, Dan Hooper, and Nickolay Y. Gnedin. The Effects of Dark Matter Annihilation on Cosmic Reionization. *ApJ*, 833(2):162, December 2016. doi: 10.3847/1538-4357/833/2/162.

[54] Garrett K. Keating, Geoffrey C. Bower, Daniel P. Marrone, David R. DeBoer, Carl Heiles, Tzu-Ching Chang, John E. Carlstrom, Christopher H. Greer, David Hawkins, James W. Lamb, Erik Leitch, Amber D. Miller, Stephen Muchovej, and David P. Woody. First Results from COPSS: The CO Power Spectrum Survey. *ApJ*, 814(2):140, December 2015. doi: 10.1088/0004-637X/814/2/140.

[55] Garrett K. Keating, Daniel P. Marrone, Geoffrey C. Bower, Erik Leitch, John E. Carlstrom, and David R. DeBoer. COPSS II: The Molecular Gas Content of Ten Million Cubic Megaparsecs at Redshift z$\sim$3. *ApJ*, 830(1):34, October 2016. doi: 10.3847/0004-637X/830/1/34.

[56] Piyanat Kittiwisit, Judd D. Bowman, Daniel C. Jacobs, Adam P. Beardsley, and Nithyanandan Thyagarajan. Sensitivity of the Hydrogen Epoch of Reionization Array and its build-out stages to one-point statistics from redshifted 21 cm observations. *MNRAS*, 474(4):4487–4499, Mar 2018. doi: 10.1093/mnras/stx3099.

[57] Saul A. Kohn, James E. Aguirre, Paul La Plante, Tashalee S. Billings, Paul M. Chichura, Austin F. Fortino, Amy S. Igarashi, Roshan K. Benefo, Samavarti Gallardo, Zachary E. Martinot, Chuneeta D. Nunhokee, Nicholas S. Kern, Philip Bull, Adrian Liu, Paul Alexander, Zaki S. Ali, Adam P. Beardsley, Gianni Bernardi, Judd D. Bowman, Richard F. Bradley, Chris L. Carilli, Carina Cheng, David R. DeBoer, Eloy de Lera Acedo, Joshua S. Dillon, Aaron Ewall-Wice, Gcobisa Fadana, Nicolas Fagnoni, Randall Fritz, Steven R. Furlanetto, Brian Glendenning, Bradley Greig, Jasper Grobbelaar, Bryna J. Hazelton, Jacqueline N. Hewitt, Jack Hickish, Daniel C. Jacobs, Austin Julius, MacCalvin Kariseb, Matthew Kolopanis, Telalo Lekalake, Anita Loots, David MacMahon, Lourence Malan, Cresshim Malgas, Matthys Maree, Nathan Mathison, Eunice Matsetela, Andrei Mesinger, Miguel F. Morales, Abraham R. Neben, Bojan Nikolic, Aaron R. Parsons, Nipanjana Patra, Samantha Pieterse, Jonathan C. Pober, Nima Razavi-Ghods, Jon Ringuette, James Robnett, Kathryn Rosie, Raddwine Sell, Craig Smith, Angelo Syce, Max Tegmark, Nithyanandan Thyagarajan, Peter K. G. Williams, and Haoxuan Zheng. The HERA-19 Commissioning Array: Direction-dependent Effects. *ApJ*, 882(1):58, Sep 2019. doi: 10.3847/1538-4357/ab2f72.

[58] Matthew Kolopanis, Daniel C. Jacobs, Carina Cheng, Aaron R. Parsons, Saul A. Kohn, Jonathan C. Pober, James E. Aguirre, Zaki S. Ali, Gi-

anni Bernardi, Richard F. Bradley, Chris L. Carilli, David R. DeBoer, Matthew R. Dexter, Joshua S. Dillon, Joshua Kerrigan, Pat Klima, Adrian Liu, David H. E. MacMahon, David F. Moore, Nithyanandan Thyagarajan, Chuneeta D. Nunhokee, William P. Walbrugh, and Andre Walker. A Simplified, Lossless Reanalysis of PAPER-64. *ApJ*, 883(2): 133, Oct 2019. doi: 10.3847/1538-4357/ab3e3a.

[59] M. Kominami, D. Pozar, and D. Schaubert. Dipole and slot elements and arrays on semi-infinite substrates. *IEEE Transactions on Antennas and Propagation*, 33(6):600–607, Jun 1985. ISSN 0018-926X. doi: 10.1109/TAP.1985.1143638.

[60] Ely D. Kovetz, Marco P. Viero, Adam Lidz, Laura Newburgh, Mubdi Rahman, Eric Switzer, Marc Kamionkowski, James Aguirre, Marcelo Alvarez, James Bock, J. Richard Bond, Goeffry Bower, C. Matt Bradford, Patrick C. Breysse, Philip Bull, Tzu-Ching Chang, Yun-Ting Cheng, Dongwoo Chung, Kieran Cleary, Asantha Corray, Abigail Crites, Rupert Croft, Olivier Doré, Michael Eastwood, Andrea Ferrara, José Fonseca, Daniel Jacobs, Garrett K. Keating, Guilaine Lagache, Gunjan Lakhlani, Adrian Liu, Kavilan Moodley, Norm Murray, Aurélie Pénin, Gergö Popping, Anthony Pullen, Dominik Reichers, Shun Saito, Ben Saliwanchik, Mario Santos, Rachel Somerville, Gordon Stacey, George Stein, Francesco Villaescusa-Navarro, Eli Visbal, Amand a Weltman, Laura Wolz, and Micheal Zemcov. Line-Intensity Mapping: 2017 Status Report. *arXiv e-prints*, art. arXiv:1709.09066, September 2017.

[61] James W. Lamb. Miscellaneous data on materials for millimetre and submillimetre optics. *International Journal of Infrared and Millimeter Waves*, 17(12):1997–2034, Dec 1996. doi: 10.1007/BF02069487.

[62] N. Lehner, B. P. Wakker, and B. D. Savage. C II Radiative Cooling of the Diffuse Gas in the Milky Way. *ApJ*, 615(2):767–793, Nov 2004. doi: 10.1086/424730.

[63] A. Lewis and A. Challinor. Code for anisotropies in the microwave background (camb). URL `http://camb.info`.

[64] C.-T. Li, T. Wei, J.-C. Cheng, C. Shiu, A. T. Crites, and C. M. Bradford. Development of a millimeter wave grating spectrometer for TIME Pilot. The 27th International Symposium on Space Terahertz Technology, 2016.

[65] Chao-Te Li, C. M. Bradford, Abigail Crites, Jonathon Hunacek, Tashun Wei, Jen-Chieh Cheng, Tzu-Ching Chang, and James Bock. TIME millimeter wave grating spectrometer. In Jonas Zmuidzinas and Jian-Rong Gao, editors, *Millimeter, Submillimeter, and Far-Infrared Detectors and Instrumentation for Astronomy IX*, volume 10708, pages 540 –

547. International Society for Optics and Photonics, SPIE, 2018. doi: 10.1117/12.2311415. URL https://doi.org/10.1117/12.2311415.

[66] R.G. Lyons. *Understanding Digital Signal Processing 2nd ed.* Prentice Hall Professional Technical Reference. Prentice Hall/PTR, 2004. ISBN 9780131089891.

[67] Gabriel M. Rebeiz and G.V. Eleftheriades. Self and mutual admittance of slot antennas on a dielectric half-space. 14, 10 1993.

[68] Piero Madau and Francesco Haardt. Cosmic Reionization after Planck: Could Quasars Do It All? *ApJ*, 813(1):L8, Nov 2015. doi: 10.1088/2041-8205/813/1/L8.

[69] Eric Marquardt, J. Le, and Ray Radebaugh. *Cryogenic Material Properties Database*, pages 681–687. 01 2002. doi: 10.1007/0-306-47112-4_84.

[70] D.H. Martin and E. Puplett. Polarised interferometric spectrometry for the millimetre and submillimetre spectrum. *Infrared Physics*, 10(2):105 – 109, 1970. ISSN 0020-0891. doi: https://doi.org/10.1016/0020-0891(70)90006-0. URL http://www.sciencedirect.com/science/article/pii/0020089170900060.

[71] K. W. Masui, E. R. Switzer, N. Banavar, K. Bandura, C. Blake, L. M. Calin, T. C. Chang, X. Chen, Y. C. Li, Y. W. Liao, A. Natarajan, U. L. Pen, J. B. Peterson, J. R. Shaw, and T. C. Voytek. Measurement of 21 cm Brightness Fluctuations at z $\sim$0.8 in Cross-correlation. *ApJ*, 763(1): L20, January 2013. doi: 10.1088/2041-8205/763/1/L20.

[72] D. P. McGinnis and J. B. Beyer. A broad-band microwave superconducting thin-film transformer. *IEEE Transactions on Microwave Theory and Techniques*, 36(11):1521–1525, Nov 1988. ISSN 1557-9670. doi: 10.1109/22.8916.

[73] Steven Murray. powerbox: A python package for creating structured fields with isotropic power spectra. *Journal of Open Source Software*, 3 (28):850, 2018. doi: 10.21105/joss.00850. URL https://doi.org/10.21105/joss.00850.

[74] Hien Trong Nguyen, John Kovac, Peter Ade, Rand ol Aikin, Steve Benton, James Bock, Justus Brevik, John Carlstrom, Darren Dowell, Lionel Duband, Sunil Golwala, Mark Halpern, Matthew Hasslefield, Kent Irwin, William Jones, Jonathan Kaufman, Brian Keating, Chao-Lin Kuo, Andrew Lange, Tomotake Matsumura, Barth Netterfield, Clem Pryke, John Ruhl, Chris Sheehy, and Rashmi Sudiwala. *BICEP2/SPUD: searching for inflation with degree scale polarimetry from the South Pole*, volume 7020 of *Society of Photo-Optical Instrumentation Engineers (SPIE) Conference Series*, page 70201F. 2008. doi: 10.1117/12.787997.

[75] R. O'Brient, P. A. R. Ade, Z. Ahmed, R. W. Aikin, M. Amiri, S. Benton, C. Bischoff, J. J. Bock, J. A. Bonetti, J. A. Brevik, B. Burger, G. Davis, P. Day, C. D. Dowell, L. Duband, J. P. Filippini, S. Fliescher, S. R. Golwala, J. Grayson, M. Halpern, M. Hasselfield, G. Hilton, V. V. Hristov, H. Hui, K. Irwin, S. Kernasovskiy, J. M. Kovac, C. L. Kuo, E. Leitch, M. Lueker, K. Megerian, L. Moncelsi, C. B. Netterfield, H. T. Nguyen, R. W. Ogburn, C. L. Pryke, C. Reintsema, J. E. Ruhl, M. C. Runyan, R. Schwarz, C. D. Sheehy, Z. Staniszewski, R. Sudiwala, G. Teply, J. E. Tolan, A. D. Turner, R. S. Tucker, A. Vieregg, D. V. Wiebe, P. Wilson, C. L. Wong, W. L. K. Wu, and K. W. Yoon. Antenna-coupled TES bolometers for the Keck array, Spider, and Polar-1. In *Millimeter, Submillimeter, and Far-Infrared Detectors and Instrumentation for Astronomy VI*, volume 8452 of *Proc. SPIE*, page 84521G, September 2012. doi: 10.1117/12.927214.

[76] Scott Paine. The am atmospheric model. Sep 2019. doi: 10.5281/zenodo.3406496.

[77] David Parkinson, Signe Riemer-Sørensen, Chris Blake, Gregory B. Poole, Tamara M. Davis, Sarah Brough, Matthew Colless, Carlos Contreras, Warrick Couch, Scott Croom, Darren Croton, Michael J. Drinkwater, Karl Forster, David Gilbank, Mike Gladders, Karl Glazebrook, Ben Jelliffe, Russell J. Jurek, I. hui Li, Barry Madore, D. Christopher Martin, Kevin Pimbblet, Michael Pracy, Rob Sharp, Emily Wisnioski, David Woods, Ted K. Wyder, and H. K. C. Yee. The WiggleZ Dark Energy Survey: Final data release and cosmological results. *Phys. Rev. D*, 86 (10):103518, November 2012. doi: 10.1103/PhysRevD.86.103518.

[78] R. Piesiewicz, C. Jansen, S. Wietzke, D. Mittleman, M. Koch, and T. Kürner. Properties of Building and Plastic Materials in the THz Range. *International Journal of Infrared and Millimeter Waves*, 28(5): 363–371, Mar 2007. doi: 10.1007/s10762-007-9217-9.

[79] Planck Collaboration, N. Aghanim, Y. Akrami, M. Ashdown, J. Aumont, C. Baccigalupi, M. Ballardini, A. J. Banday, R. B. Barreiro, N. Bartolo, S. Basak, R. Battye, K. Benabed, J. P. Bernard, M. Bersanelli, P. Bielewicz, J. J. Bock, J. R. Bond, J. Borrill, F. R. Bouchet, F. Boulanger, M. Bucher, C. Burigana, R. C. Butler, E. Calabrese, J. F. Cardoso, J. Carron, A. Challinor, H. C. Chiang, J. Chluba, L. P. L. Colombo, C. Combet, D. Contreras, B. P. Crill, F. Cuttaia, P. de Bernardis, G. de Zotti, J. Delabrouille, J. M. Delouis, E. Di Valentino, J. M. Diego, O. Doré, M. Douspis, A. Ducout, X. Dupac, S. Dusini, G. Efstathiou, F. Elsner, T. A. Enßlin, H. K. Eriksen, Y. Fantaye, M. Farhang, J. Fergusson, R. Fernandez-Cobos, F. Finelli, F. Forastieri, M. Frailis, A. A. Fraisse, E. Franceschi, A. Frolov, S. Galeotta, S. Galli, K. Ganga, R. T. Génova-Santos, M. Gerbino, T. Ghosh,

J. González-Nuevo, K. M. Górski, S. Gratton, A. Gruppuso, J. E. Gudmundsson, J. Hamann, W. Handley, F. K. Hansen, D. Herranz, S. R. Hildebrandt, E. Hivon, Z. Huang, A. H. Jaffe, W. C. Jones, A. Karakci, E. Keihänen, R. Keskitalo, K. Kiiveri, J. Kim, T. S. Kisner, L. Knox, N. Krachmalnicoff, M. Kunz, H. Kurki-Suonio, G. Lagache, J. M. Lamarre, A. Lasenby, M. Lattanzi, C. R. Lawrence, M. Le Jeune, P. Lemos, J. Lesgourgues, F. Levrier, A. Lewis, M. Liguori, P. B. Lilje, M. Lilley, V. Lindholm, M. López-Caniego, P. M. Lubin, Y. Z. Ma, J. F. Macías-Pérez, G. Maggio, D. Maino, N. Mandolesi, A. Mangilli, A. Marcos-Caballero, M. Maris, P. G. Martin, M. Martinelli, E. Martínez-González, S. Matarrese, N. Mauri, J. D. McEwen, P. R. Meinhold, A. Melchiorri, A. Mennella, M. Migliaccio, M. Millea, S. Mitra, M. A. Miville-Deschênes, D. Molinari, L. Montier, G. Morgante, A. Moss, P. Natoli, H. U. Nørgaard-Nielsen, L. Pagano, D. Paoletti, B. Partridge, G. Patanchon, H. V. Peiris, F. Perrotta, V. Pettorino, F. Piacentini, L. Polastri, G. Polenta, J. L. Puget, J. P. Rachen, M. Reinecke, M. Remazeilles, A. Renzi, G. Rocha, C. Rosset, G. Roudier, J. A. Rubiño-Martín, B. Ruiz-Granados, L. Salvati, M. Sandri, M. Savelainen, D. Scott, E. P. S. Shellard, C. Sirignano, G. Sirri, L. D. Spencer, R. Sunyaev, A. S. Suur-Uski, J. A. Tauber, D. Tavagnacco, M. Tenti, L. Toffolatti, M. Tomasi, T. Trombetti, L. Valenziano, J. Valiviita, B. Van Tent, L. Vibert, P. Vielva, F. Villa, N. Vittorio, B. D. Wand elt, I. K. Wehus, M. White, S. D. M. White, A. Zacchei, and A. Zonca. Planck 2018 results. VI. Cosmological parameters. *arXiv e-prints*, art. arXiv:1807.06209, Jul 2018.

[80] C. D. Porter and D. B. Tanner. Correction of phase errors in fourier spectroscopy. *International Journal of Infrared and Millimeter Waves*, 4(2):273–298, Mar 1983. doi: 10.1007/BF01008607.

[81] D.M. Pozar. *Microwave Engineering, 4th Edition*. Wiley, 2011. ISBN 9781118213636.

[82] A. M. Price-Whelan, B. M. Sipőcz, H. M. Günther, P. L. Lim, S. M. Crawford, S. Conseil, D. L. Shupe, M. W. Craig, N. Dencheva, A. Ginsburg, J. T. VanderPlas, L. D. Bradley, D. Pérez-Suárez, M. de Val-Borro, (Primary Paper Contributors, T. L. Aldcroft, K. L. Cruz, T. P. Robitaille, E. J. Tollerud, (Astropy Coordination Committee, C. Ardelean, T. Babej, Y. P. Bach, M. Bachetti, A. V. Bakanov, S. P. Bamford, G. Barentsen, P. Barmby, A. Baumbach, K. L. Berry, F. Biscani, M. Boquien, K. A. Bostroem, L. G. Bouma, G. B. Brammer, E. M. Bray, H. Breytenbach, H. Buddelmeijer, D. J. Burke, G. Calderone, J. L. Cano Rodríguez, M. Cara, J. V. M. Cardoso, S. Cheedella, Y. Copin, L. Corrales, D. Crichton, D. D'Avella, C. Deil, É. Depagne, J. P. Dietrich, A. Donath, M. Droettboom, N. Earl, T. Erben, S. Fabbro, L. A. Ferreira, T. Finethy, R. T. Fox, L. H. Garrison, S. L. J. Gibbons, D. A. Goldstein,

R. Gommers, J. P. Greco, P. Greenfield, A. M. Groener, F. Grollier, A. Hagen, P. Hirst, D. Homeier, A. J. Horton, G. Hosseinzadeh, L. Hu, J. S. Hunkeler, Ž. Ivezić, A. Jain, T. Jenness, G. Kanarek, S. Kendrew, N. S. Kern, W. E. Kerzendorf, A. Khvalko, J. King, D. Kirkby, A. M. Kulkarni, A. Kumar, A. Lee, D. Lenz, S. P. Littlefair, Z. Ma, D. M. Macleod, M. Mastropietro, C. McCully, S. Montagnac, B. M. Morris, M. Mueller, S. J. Mumford, D. Muna, N. A. Murphy, S. Nelson, G. H. Nguyen, J. P. Ninan, M. Nöthe, S. Ogaz, S. Oh, J. K. Parejko, N. Parley, S. Pascual, R. Patil, A. A. Patil, A. L. Plunkett, J. X. Prochaska, T. Rastogi, V. Reddy Janga, J. Sabater, P. Sakurikar, M. Seifert, L. E. Sherbert, H. Sherwood-Taylor, A. Y. Shih, J. Sick, M. T. Silbiger, S. Singanamalla, L. P. Singer, P. H. Sladen, K. A. Sooley, S. Sornarajah, O. Streicher, P. Teuben, S. W. Thomas, G. R. Tremblay, J. E. H. Turner, V. Terrón, M. H. van Kerkwijk, A. de la Vega, L. L. Watkins, B. A. Weaver, J. B. Whitmore, J. Woillez, V. Zabalza, and (Astropy Contributors. The Astropy Project: Building an Open-science Project and Status of the v2.0 Core Package. *AJ*, 156:123, September 2018. doi: 10.3847/1538-3881/aabc4f.

[83] T. Prouve, L. Duband, J. Hodis, J.J. Bock, C. Matt Bradford, and W. Holmes. Spica/bliss cryo-chain demonstrator. *Cryogenics*, 70:70 – 75, 2015. ISSN 0011-2275. doi: http://dx.doi.org/10.1016/j.cryogenics.2015.06.001. URL `http://www.sciencedirect.com/science/article/pii/S0011227515000788`.

[84] Thomas Prouvé, Warren Holmes, J.J. Bock, and C. Bradford. *A 1 K 4He close cycle loop precooled using a PT415 pulse tube for the BLISS test bed cryostat*. Jun 2012.

[85] Thomas Prouvé, Florian Bancel, and Laurent Clerc. Time pilot cryocooler. Technical report, CEA, Jun 2015.

[86] Anthony R. Pullen, Paolo Serra, Tzu-Ching Chang, Olivier Doré, and Shirley Ho. Search for C II emission on cosmological scales at redshift Z $\sim$ 2.6. *MNRAS*, 478(2):1911–1924, August 2018. doi: 10.1093/mnras/sty1243.

[87] I. Rana and N. Alexopoulos. Current distribution and input impedance of printed dipoles. *IEEE Transactions on Antennas and Propagation*, 29 (1):99–105, Jan 1981. ISSN 0018-926X. doi: 10.1109/TAP.1981.1142536.

[88] B. E. Robertson, R. S. Ellis, J. S. Dunlop, R. J. McLure, and D. P. Stark. Early star-forming galaxies and the reionization of the Universe. *Nature*, 468:49–55, November 2010. doi: 10.1038/nature09527.

[89] Brant E. Robertson, Richard S. Ellis, Steven R. Furlanetto, and James S. Dunlop. Cosmic Reionization and Early Star-forming Galaxies: A Joint

Analysis of New Constraints from Planck and the Hubble Space Telescope. *ApJ*, 802(2):L19, Apr 2015. doi: 10.1088/2041-8205/802/2/L19.

[90] H. A. Rowland. On concave gratings for optical purposes. *American Journal of Science*, 26(152):87–98, August 1883. doi: 10.2475/ajs.s3-26.152.87.

[91] M. C. Runyan and W. C. Jones. Thermal conductivity of thermally-isolating polymeric and composite structural support materials between 0.3 and 4 K. *Cryogenics*, 48:448–454, September 2008. doi: 10.1016/j.cryogenics.2008.06.002.

[92] Sanjay Sah, Ganapati Myneni, and Jayasimha Atulasimha. Experimental Characterization of Magnetic Materials for the Magnetic Shielding of Cryomodules in Particle Accelerators. *IEEE Transactions on Magnetics*, 52(2):2494862, February 2016. doi: 10.1109/TMAG.2015.2494862.

[93] D. Schaerer, M. Ginolfi, M. Bethermin, Y. Fudamoto, P. A. Oesch, O. Le Fevre, A. Faisst, P. Capak, P. Cassata, J. D. Silverman, Lin Yan, G. C. Jones, R. Amorin, S. Bardelli, M. Boquien, A. Cimatti, M. Dessauges-Zavadsky, M. Giavalisco, N. P. Hathi, S. Fujimoto, E. Ibar, A. Koekemoer, G. Lagache, B. C. Lemaux, F. Loiacono, R. Maiolino, D. Narayanan, L. Morselli, Hugo Mendez-Hernandez, F. Pozzi, D. Riechers, M. Talia, S. Toft, L. Vallini, D. Vergani, G. Zamorani, and E. Zucca. The ALPINE-ALMA [CII] survey. No or weak evolution in the [CII]-SFR relation over the last 13 Gyr. *arXiv e-prints*, art. arXiv:2002.00979, February 2020.

[94] P. Schechter. An analytic expression for the luminosity function for galaxies. *ApJ*, 203:297–306, Jan 1976. doi: 10.1086/154079.

[95] A. Schillaci, P. A. R. Ade, Z. Ahmed, M. Amiri, D. Barkats, R. Basu Thakur, C. A. Bischoff, J. J. Bock, H. Boenish, E. Bullock, V. Buza, J. Cheshire, J. Connors, J. Cornelison, M. Crumrine, A. Cukierman, M. Dierickx, L. Duband, S. Fatigoni, J. P. Filippini, G. Hall, M. Halpern, S. Harrison, S. Henderson, S. R. Hildebrandt, G. C. Hilton, H. Hui, K. D. Irwin, J. Kang, K. S. Karkare, E. Karpel, S. Kefeli, J. M. Kovac, C. L. Kuo, K. Lau, K. G. Megerian, L. Moncelsi, T. Namikawa, H. T. Nguyen, R. O'Brient, S. Palladino, N. Precup, T. Prouve, C. Pryke, B. Racine, C. D. Reintsema, S. Richter, B. L. Schmitt, R. Schwarz, C. D. Sheehy, A. Soliman, T. St. Germaine, B. Steinbach, R. V. Sudiwala, K. L. Thompson, C. Tucker, A. D. Turner, C. Umiltà, A. G. Vieregg, A. Wand ui, A. C. Weber, D. V. Wiebe, J. Willmert, W. L. K. Wu, E. Yang, K. W. Yoon, E. Young, C. Yu, and C. Zhang. Design and Performance of the First BICEP Array Receiver. *Journal of Low Temperature Physics*, February 2020. doi: 10.1007/s10909-020-02394-6.

[96] N. Scoville, H. Aussel, M. Brusa, P. Capak, C. M. Carollo, M. Elvis, M. Giavalisco, L. Guzzo, G. Hasinger, C. Impey, J. P. Kneib, O. LeFevre, S. J. Lilly, B. Mobasher, A. Renzini, R. M. Rich, D. B. Sanders, E. Schinnerer, D. Schminovich, P. Shopbell, Y. Taniguchi, and N. D. Tyson. The Cosmic Evolution Survey (COSMOS): Overview. *ApJS*, 172(1):1–8, September 2007. doi: 10.1086/516585.

[97] Paolo Serra, Olivier Doré, and Guilaine Lagache. Dissecting the High-z Interstellar Medium through Intensity Mapping Cross-correlations. *ApJ*, 833(2):153, December 2016. doi: 10.3847/1538-4357/833/2/153.

[98] M. Silva, M. G. Santos, A. Cooray, and Y. Gong. Prospects for Detecting C II Emission during the Epoch of Reionization. *ApJ*, 806:209, June 2015. doi: 10.1088/0004-637X/806/2/209.

[99] M. F. Skrutskie, R. M. Cutri, R. Stiening, M. D. Weinberg, S. Schneider, J. M. Carpenter, C. Beichman, R. Capps, T. Chester, J. Elias, J. Huchra, J. Liebert, C. Lonsdale, D. G. Monet, S. Price, P. Seitzer, T. Jarrett, J. D. Kirkpatrick, J. E. Gizis, E. Howard, T. Evans, J. Fowler, L. Fullmer, R. Hurt, R. Light, E. L. Kopan, K. A. Marsh, H. L. McCallon, R. Tam, S. Van Dyk, and S. Wheelock. The Two Micron All Sky Survey (2MASS). *AJ*, 131(2):1163–1183, February 2006. doi: 10.1086/498708.

[100] G. J. Stacey, N. Geis, R. Genzel, J. B. Lugten, A. Poglitsch, A. Sternberg, and C. H. Townes. The 158 Micron [C ii] Line: A Measure of Global Star Formation Activity in Galaxies. *ApJ*, 373:423, Jun 1991. doi: 10.1086/170062.

[101] Daniel P. Stark. Galaxies in the First Billion Years After the Big Bang. *ARA&A*, 54:761–803, September 2016. doi: 10.1146/annurev-astro-081915-023417.

[102] G. Sun, L. Moncelsi, M. P. Viero, M. B. Silva, J. Bock, C. M. Bradford, T. C. Chang, Y. T. Cheng, A. R. Cooray, A. Crites, S. Hailey-Dunsheath, B. Uzgil, J. R. Hunacek, and M. Zemcov. A Foreground Masking Strategy for [C II] Intensity Mapping Experiments Using Galaxies Selected by Stellar Mass and Redshift. *ApJ*, 856(2):107, Apr 2018. doi: 10.3847/1538-4357/aab3e3.

[103] BICEP Team. Zotefoam filters, 2018. URL `https://cmb-s4.org/wiki/images/Zotefoam_filters.pdf`.

[104] A. G. Vieregg, P. A. R. Ade, R. Aikin, C. Bischoff, J. J. Bock, J. A. Bonetti, K. J. Bradford, J. A. Brevik, C. D. Dowell, L. Duband, J. P. Filippini, S. Fliescher, S. R. Golwala, M. S. Gordon, M. Halpern, G. Hilton, V. V. Hristov, K. Irwin, S. Kernasovskiy, J. M. Kovac, C. L. Kuo, E. Leitch, M. Lueker, T. Montroy, C. B. Netterfield, H. T. Nguyen, R. O'Brient, R. W. Ogburn, C. Pryke, J. E. Ruhl, M. Runyan,

R. Schwarz, C. Sheehy, Z. Staniszewski, R. Sudiwala, G. Teply, J. Tolan, A. D. Turner, P. Wilson, and C. L. Wong. *Optical characterization of the Keck array polarimeter at the South Pole*, volume 8452 of *Society of Photo-Optical Instrumentation Engineers (SPIE) Conference Series*, page 845226. 2012. doi: 10.1117/12.926639.

[105] M. P. Viero, L. Wang, M. Zemcov, G. Addison, A. Amblard, V. Arumugam, H. Aussel, M. Béthermin, J. Bock, A. Boselli, V. Buat, D. Burgarella, C. M. Casey, D. L. Clements, A. Conley, L. Conversi, A. Cooray, G. De Zotti, C. D. Dowell, D. Farrah, A. Franceschini, J. Glenn, M. Griffin, E. Hatziminaoglou, S. Heinis, E. Ibar, R. J. Ivison, G. Lagache, L. Levenson, L. Marchetti, G. Marsden, H. T. Nguyen, B. O'Halloran, S. J. Oliver, A. Omont, M. J. Page, A. Papageorgiou, C. P. Pearson, I. Pérez-Fournon, M. Pohlen, D. Rigopoulou, I. G. Roseboom, M. Rowan-Robinson, B. Schulz, D. Scott, N. Seymour, D. L. Shupe, A. J. Smith, M. Symeonidis, M. Vaccari, I. Valtchanov, J. D. Vieira, J. Wardlow, and C. K. Xu. HerMES: Cosmic Infrared Background Anisotropies and the Clustering of Dusty Star-forming Galaxies. *ApJ*, 772(1):77, July 2013. doi: 10.1088/0004-637X/772/1/77.

[106] G. Wang, V. Yefremenko, V. Novosad, A. Datesman, J. Pearson, G. Shustakova, R. Divan, C. Chang, J. McMahon, L. Bleem, A. T. Crites, T. Downes, J. Mehl, S. S. Meyer, and J. E. Carlstrom. Thermal properties of silicon nitride beams below 1 kelvin. *AIP Conference Proceedings*, 1219(1):75–82, 2010. doi: 10.1063/1.3402336. URL `https://aip.scitation.org/doi/abs/10.1063/1.3402336`.

[107] Jian Wei, David Olaya, Boris S. Karasik, Sergey V. Pereverzev, Andrei V. Sergeev, and Michael E. Gershenson. Ultrasensitive hot-electron nanobolometers for terahertz astrophysics. *Nature Nanotechnology*, 3(8): 496–500, Jul 2008. ISSN 1748-3395. doi: 10.1038/nnano.2008.173. URL `http://dx.doi.org/10.1038/nnano.2008.173`.

[108] R. L. White, R. H. Becker, X. Fan, and M. A. Strauss. Probing the Ionization State of the Universe at z>6. *AJ*, 126:1–14, July 2003. doi: 10.1086/375547.

[109] Andrew T. Young. Air mass and refraction. *Appl. Opt.*, 33(6):1108–1110, Feb 1994. doi: 10.1364/AO.33.001108.

[110] B. Yue, M. Castellano, A. Ferrara, A. Fontana, E. Merlin, R. Amorín, A. Grazian, E. Mármol-Queralto, M. J. Michałowski, A. Mortlock, D. Paris, S. Parsa, S. Pilo, P. Santini, and M. Di Criscienzo. On the Faint End of the Galaxy Luminosity Function in the Epoch of Reionization: Updated Constraints from the HST Frontier Fields. *ApJ*, 868(2): 115, December 2018. doi: 10.3847/1538-4357/aae77f.

[111] O. Zahn, C. L. Reichardt, L. Shaw, A. Lidz, K. A. Aird, B. A. Benson, L. E. Bleem, J. E. Carlstrom, C. L. Chang, H. M. Cho, T. M. Crawford, A. T. Crites, T. de Haan, M. A. Dobbs, O. Doré, J. Dudley, E. M. George, N. W. Halverson, G. P. Holder, W. L. Holzapfel, S. Hoover, Z. Hou, J. D. Hrubes, M. Joy, R. Keisler, L. Knox, A. T. Lee, E. M. Leitch, M. Lueker, D. Luong-Van, J. J. McMahon, J. Mehl, S. S. Meyer, M. Millea, J. J. Mohr, T. E. Montroy, T. Natoli, S. Padin, T. Plagge, C. Pryke, J. E. Ruhl, K. K. Schaffer, E. Shirokoff, H. G. Spieler, Z. Staniszewski, A. A. Stark, K. Story, A. van Engelen, K. Vanderlinde, J. D. Vieira, and R. Williamson. Cosmic Microwave Background Constraints on the Duration and Timing of Reionization from the South Pole Telescope. *ApJ*, 756(1):65, Sep 2012. doi: 10.1088/0004-637X/756/1/65.

Appendix A

CST Consistency Checks

The work presented in this section was done in collaboration with Ahmed Soliman, Bryan Steinbach, and Roger O'Brient.

In this section I compare the output of CST 2014 to published analytical or simulated results for several cases to justify the use of CST for mm-wave slot antenna arrays. Results are repeated for both the Transient and Frequency solvers in CST.

A.1 Single Element, Free Space

Babinet's Principle

As a simple self-consistency check, I attempt to reproduce Babinet's principle $Z_{slot}Z_{dipole} = \frac{Z_0^2}{4}$ as a function of frequency for a single slot antenna in free space. I choose a slot with length $l = 0.475\,\lambda_0$ ($f = 240\,\mathrm{GHz}$) and width $w = l/25$ embedded in a 4 mm square ground plane. Open boundary conditions were used on the four edges of the ground plane, with Open Add Space boundaries on the front and back faces of the ground plane. A single discrete port drives the slot at the center. The dual to the slot, a planar dipole, is simulated with the same length and width. A small feed gap of length $\lambda_0/3000$ was added at the center to satisfy the conditions required for the discrete feed port. Open Add Space boundaries were used on all sides. The resulting impedance plots can be seen in Fig. A.2. The normalized product of the slot and dipole results, $Z_{slot}Z_{dipole} * 4/Z_0^2$, is plotted in Fig. A.3 and should be equal to 1 at all frequencies if Babinet's principle holds. For this geometry Babinet's principle holds to within $\pm 10\%$ near the resonant frequency, with a non-zero imaginary part increasing in magnitude at high frequencies in the Transient Solver.

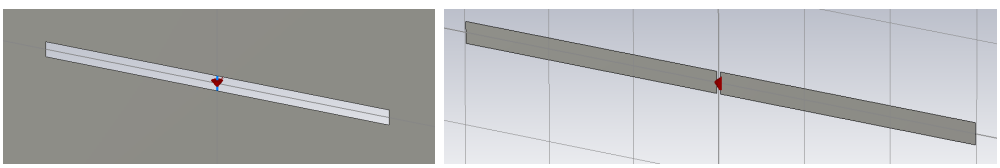

Figure A.1: A center-fed slot antenna and planar dipole as drawn in CST.

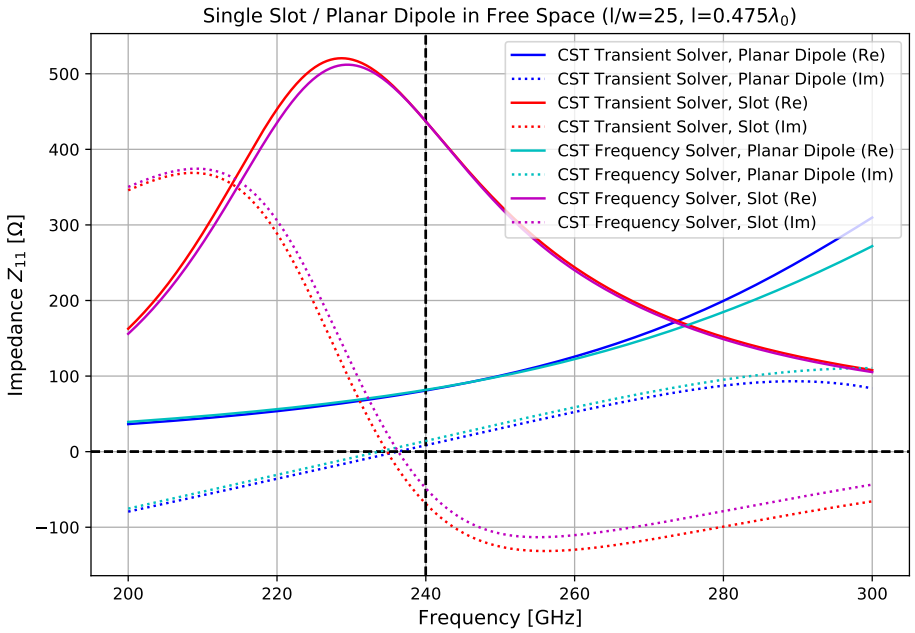

Figure A.2: Simulated impedance for a slot antenna and a planar dipole.

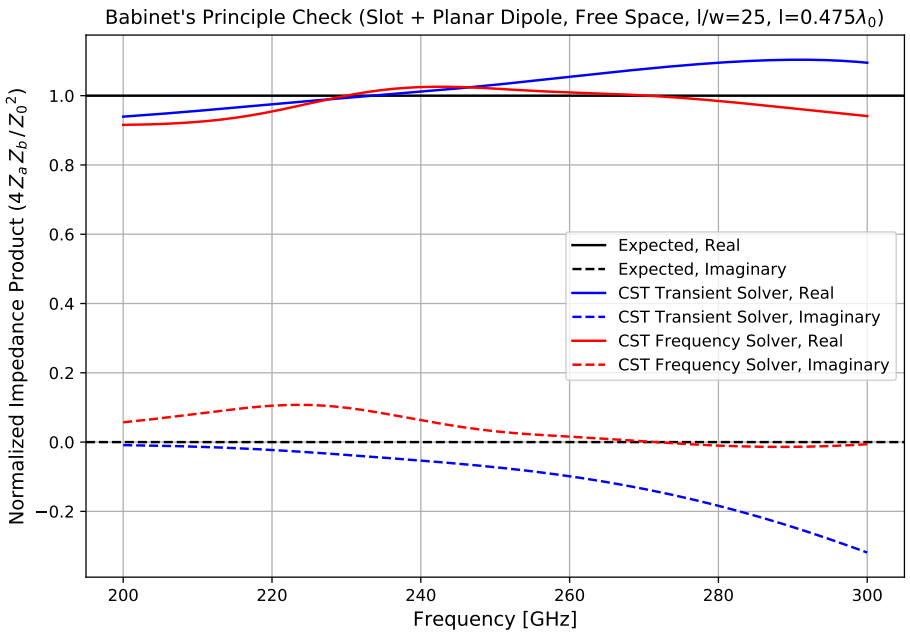

Figure A.3: Normalized impedance product of a slot antenna and its dual, a planar dipole. This metric should be equal to 1 at all frequencies according to Babinet's principle.

A.2 Single Element, Dielectric

Infinite Dielectric Half-Space

Here I compute the impedance of a single center-fed slot over an infinite half-space dielectric and compare to the results presented in Fig. 4 of Kominami et al. 1985 [59]. A slot of length $l = 0.5\,\lambda_0$ ($f = 240\,\mathrm{GHz}$) and width $w = l/50$ embedded in a 4 mm wide ground plane was placed on a dielectric slab of thickness λ_0. A single discrete port drives the slot at the center. The Open Add Space boundary condition was used on the vacuum-facing side of the ground plane with Open boundaries on the remaining five sides. Because we are simulating an infinite half space, sweeping in frequency is equivalent to scaling the slot. Thus, we can plot the results of a single frequency sweep as a sweep in slot size at fixed frequency, as shown in Fig. A.5. I find good agreement with expected results for both the Frequency and Transient solvers.

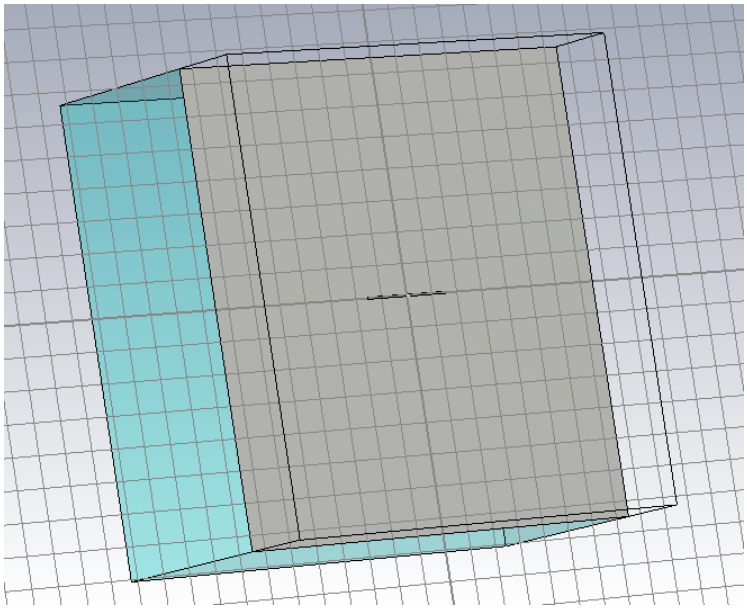

Figure A.4: A single center-fed slot antenna over an infinite dielectric half-space as drawn in CST.

Finite Dielectric with Backshort

Here I compute the impedance of a single planar dipole over a finite dielectric with a backshort and compare to the results presented in Table 1 of Rana et al. 1981 [87]. A planar dipole of variable length l and width $w = l/1500$ is placed on a dielectric slab of width 1.3 mm and variable thickness t. The dipole has a small feed gap of length $\lambda_0/3000$ ($f = 240\,\mathrm{GHz}$) at the center

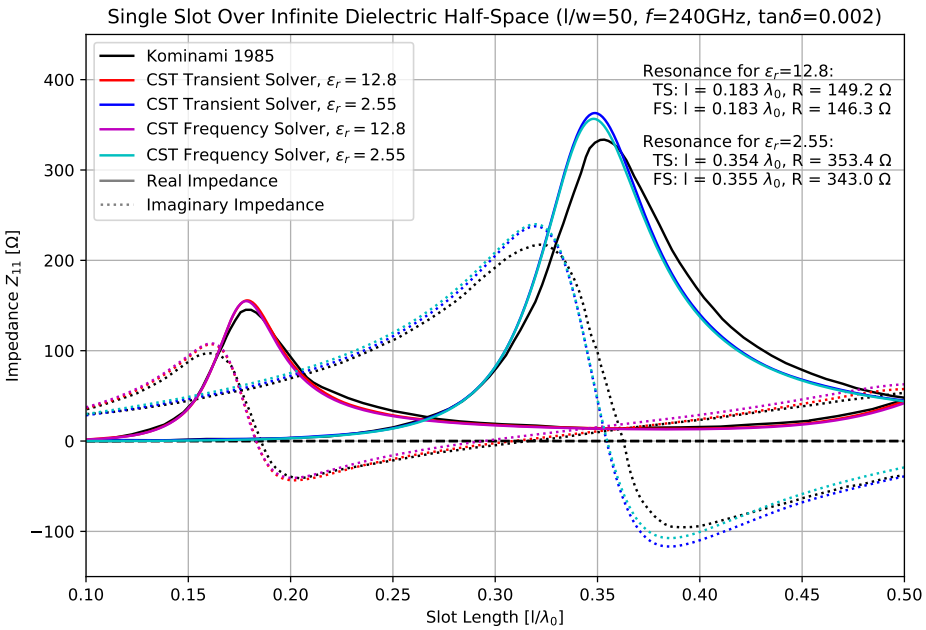

Figure A.5: Simulated impedance for a slot antenna over an infinite dielectric half-space.

and is driven by a single discrete port. The vacuum-facing side of the dipole uses an Open Add Space boundary, the bottom of the dielectric slab has a perfect electrical conductor boundary, and the four sides use Open boundaries. Results are plotted in Fig. A.7. Resonant lengths and impedances at resonance produced by CST are in good agreement with published results [87] at the chosen aspect ratio (the paper assumes a thin wire). The Transient solver achieves somewhat better agreement than the Frequency solver for this case. The computed impedance at $l = 0.5\lambda_0$, not shown, is very sensitive to the dipole width and cannot quantitatively reproduce results from Rana et al. 1981.

Comparison with HFSS and Sonnet

Here I compare results from the same simulation geometry in CST 2014, HFSS 15.0, and Sonnet 14.52. (Sonnet results were drawn and computed by Bryan Steinbach.) The "standard geometry" chosen uses uses a single planar dipole of length $l = 350\,\mu$m and width $w = 7\,\mu$m sitting on a square dielectric ($\epsilon = 3.25$) of width $w_d = 896\,\mu$m and thickness $t_d = 0.1016\,\lambda_0$ ($f = 240\,$GHz). $200\,\mu$m

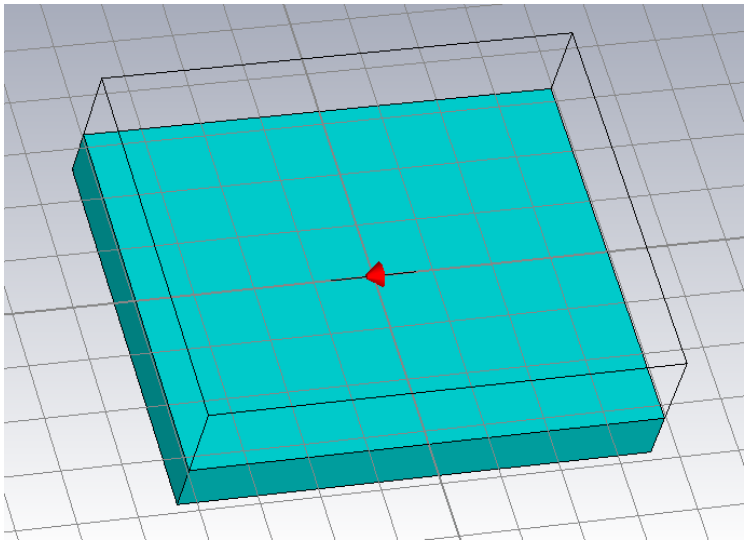

Figure A.6: A single center-fed planar dipole over a finite dielectric with backshort as drawn in CST.

of vacuum sits above the dipole. The vacuum face uses a perfect absorber boundary (Open boundary in CST), and the remaining five faces use perfect electrical conductor boundaries (required by Sonnet). A small feed gap of $\lambda_0/3000$ was used in CST and HFSS, but not in Sonnet. Results are shown in Fig. A.9, and generally agree with each other with a scatter of $\sim 10\Omega$.

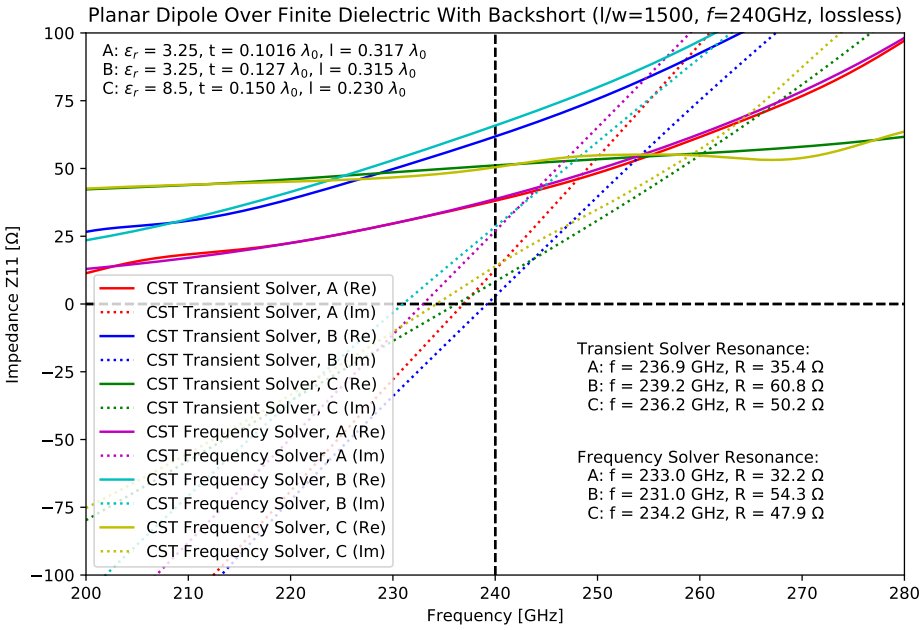

Figure A.7: Simulated impedance for a planar dipole of length l over a finite dielectric of thickness t with backshort.

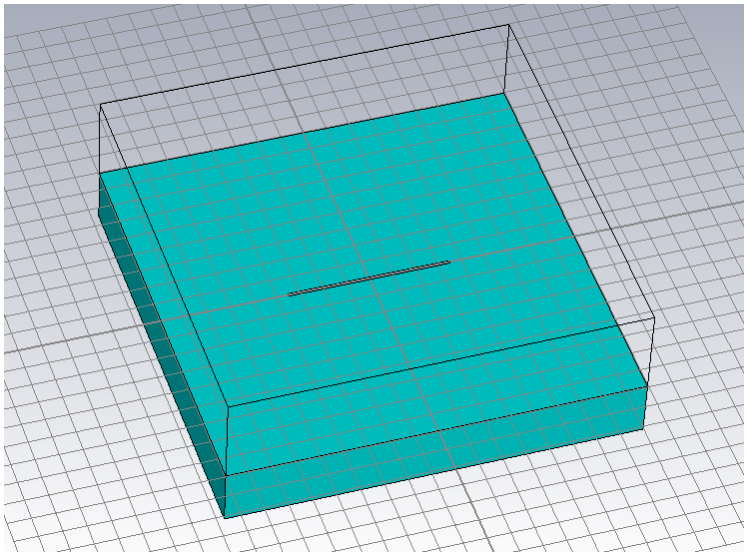

Figure A.8: The "standard geometry" planar dipole used to compare antenna simulation packages.

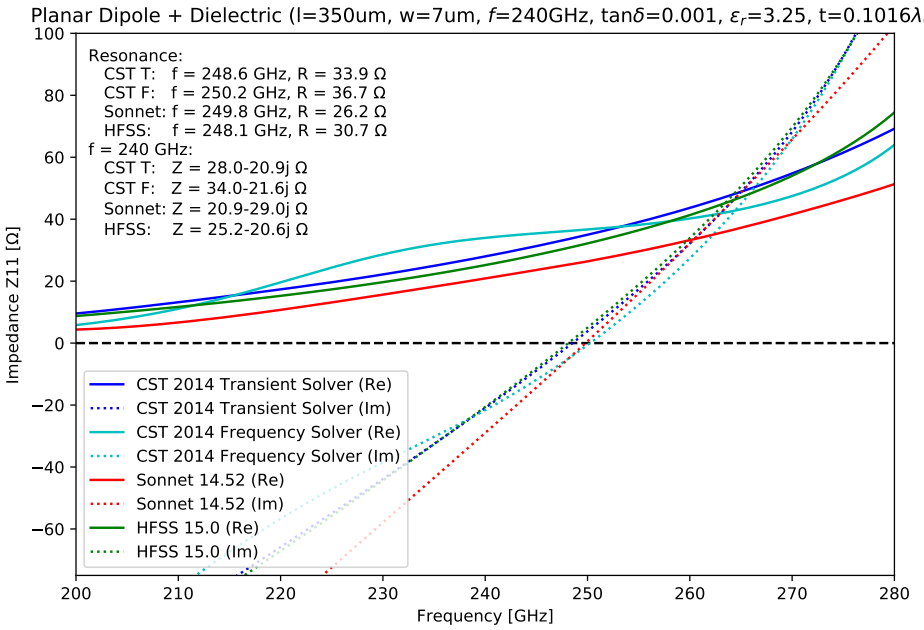

Figure A.9: Simulated impedance of the "standard geometry" planar dipole computed with CST, HFSS, and Sonnet.

A.3 Multi Element, Free Space

Two Parallel Slots

Here I compute the mutual impedance of two parallel slots oriented as shown in Fig. A.8. The two slots have length $l = 0.4\,\lambda_0$ and width $w = l/50$ and are separated by a variable distance s. Each slot is surrounded by at least 5 mm of ground plane in all directions. A discrete feed port feeds each slot at its center. Fig. A.11 shows the admittance Y_{21} as a function of slot distance computed with both the Frequency and the Transient solver; both methods are in good agreement with the results published in Rebeiz 1993 [67].

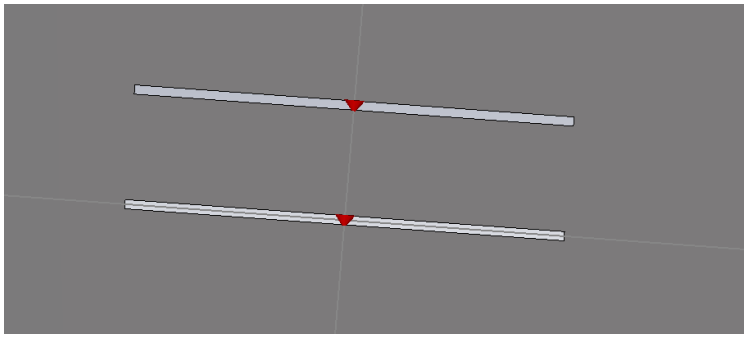

Figure A.10: A pair of parallel slot antennas in free space as drawn in CST.

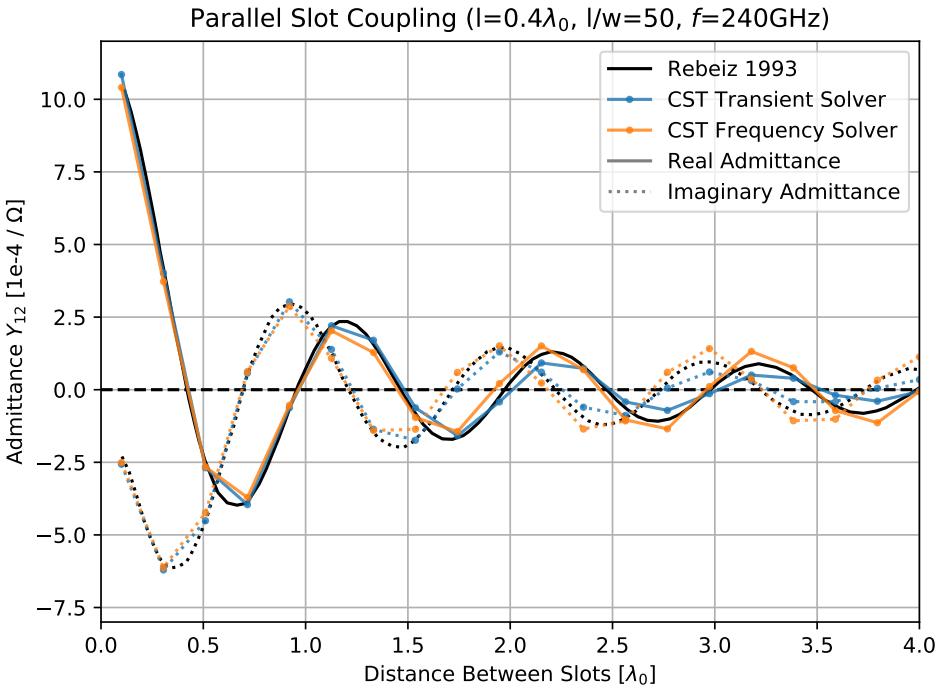

Figure A.11: Simulated admittance Y_{21} at $f = 240\,\mathrm{GHz}$ of a pair of parallel slots in free space as a function of slot-to-slot distance.

Appendix B

Automated Cable Tester

B.1 Overview

This section briefly describes the Mega Cable Tester, the Mini Cable Tester, and software used to operate them. They allow measurement of a full resistance matrix for a set of pins (up to 128x128 for the mini, 724x724 for the mega), useful for checking cryostats and modules for unexpected shorts and opens. Resistances up to $\sim$2 MΩ are supported, with best results from 0 to 1 MΩ.

Mega Cable Tester

The Mega Cable Tester includes 5 100p MDM connectors, 6 37s MDM connectors, and 2 banana jacks for a total of 724 user-accessible pins. Each pin is independently connected to two ADG732 analog multiplexer trees; one tree connects to ground through a 1 kΩ resistor, and the other to a fixed 2.5V through a 2 MΩ resistor (limiting the current to 1.3 μA). An ADS1220 24 bit ADC with 1x-128x PGA is configured to optionally use the voltage over the 2 MΩ resistor as its reference voltage, allowing ratiometric measurement of the unknown resistor when current is flowing. A Teensy 3.6 (an Arduino software compatible ARM processor) communicates with the ADC and multiplexer chips and reports results to the PC via USB.

Mini Cable Tester

The Mini Cable Tester has two sets of 128 connections, labeled Connector 0 and Connector 1. ADG732 analog multiplexer chips allow the output of a LM234 constant current source to be connected to any single pin from Connector 0 or Connector 1. Another set of analog multiplexer chips allows any single pin on Connector 0 to be connected to ground (Connector 1 cannot be connected to ground; this ground multiplexer can also be disconnected to check for ground shorts). An ADS1120 16 bit ADC measures the voltage drop over the two chosen pins (one connected to the current source, and one connected to ground). An Arduino Zero communicates with the ADC and multiplexer

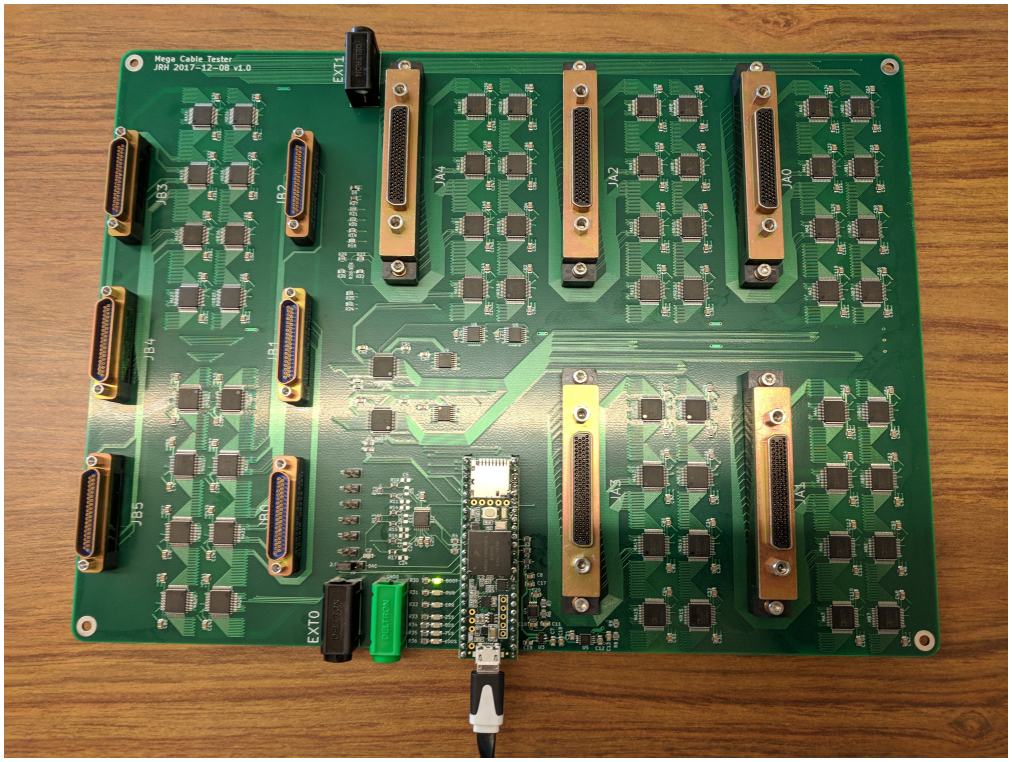

Figure B.1: The Mega Cable Tester main board removed from its protective aluminum housing.

chips and reports results to the PC via USB. A digitally programmable potentiometer allows adjusting the current in firmware.

Firmware Functional Description

An Arduino sketch waits for a start signal sent over a serial connection. The sketch then reads a set of parameters to configure the operating mode and subsequently steps through each pin combination, reporting the voltage or resistance read. To improve resolution and noise performance, the readings are repeated at higher gains for combinations that are not out-of-range at lower gains. All measurements are reported over serial as they are made, with newer measurements for a given pin combination replacing earlier ones.

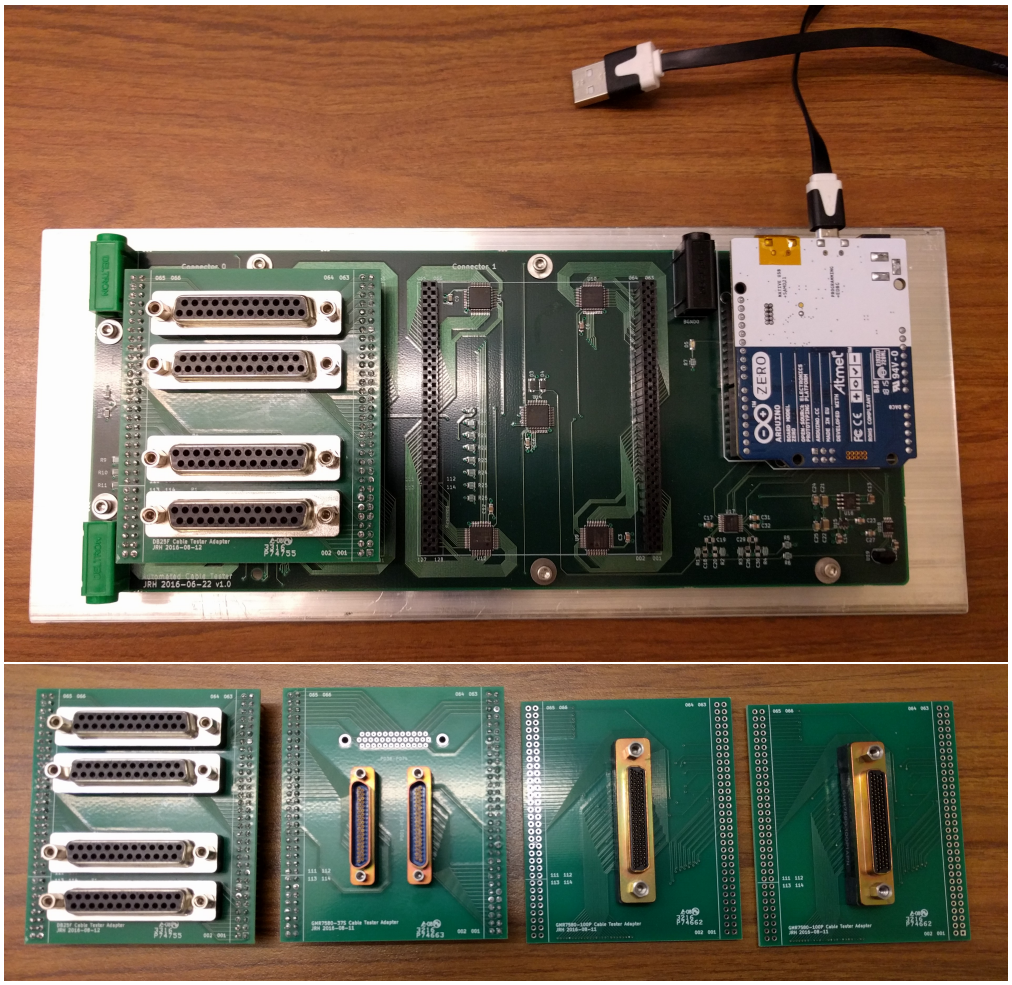

Figure B.2: The Mini Cable Tester main board and adapter modules.

B.2 Operation

`cable-tester.py` is a python script that initiates measurements and records data to a spreadsheet. As an example, the following can be used to probe out a 5 MDM MCE interface:

```
./cable-tester.py -p ./pinmap/mega-mce-mux11.txt
```

Pin mapping files allow one to configure pin names, measurement parameters, and pin resistance/voltage expectations. These expectations are verified and reported in the first tab of the output file; subsequent tabs contain the full measurement matrix. Valid pin mapping configuration lines are as follows:

- `hw [mega,mini]`
  The hardware revision this pin mapping is for.

- `j[a,b] [0-6]`
  Number of JA/JB connectors used (mega only). The first N connectors of each type are tested, others are skipped.
- `mode [half,full,block-half,block-full,cross]`
  Cable tester run mode. Block modes (mega only) measure a block-diagonal matrix, only checking combinations within connectors. Cross mode (mini only) checks from port 0 to port 1 instead of the default port 0 to port 0.
- `name [pin_id] [string]`
  Assign the name `string` to pin `pin_id`. Use double quotes around names with spaces. The order of assigned names in the pinmap file determines the order presented in the output file. Valid pin IDs for the mini tester are GND and 001-128; for the mega tester, they are GND, EXT[0,1], A[0-4]:[001-100], B[0-5]:[001-037], and CAL[614-631].
- `res [pin_a] [pin_b] [val_min] [val_max]`
  Specify that a resistor is connected between pins `pin_a` and `pin_b`. The software will check that the measured resistance is in the range [`val_min`, `val_max`]; all pin combinations without a `res` command specified have a default expectation of +inf. SI prefixes may be used if desired (ex. "1.3k", "4M"), as well as "+inf" or "-inf".
- `diode [pin_a] [pin_b] [val_min] [val_max]`
  `diode [pin_a] [pin_b] [val_min] [val_max] [rev_min] [rev_max]`
  Specify that a diode is connected between pins `pin_a` and `pin_b`, where the cathode is connected to `pin_a`. The software will check that the measured voltage is in the range [`val_min`, `val_max`]. SI prefixes may be used if desired (ex. "300m"), as well as "+inf" or "-inf". Optionally, reverse voltage limits can be specified for diodes with large leakage current; otherwise, the reverse voltage expectation is set to +inf.

Calibration

Before starting measurements, both the mini and mega cable testers short the two mux outputs to guarantee that current is flowing. They measure the voltage drop over a known fixed 1 kΩ series resistor and from that compute the current, which is assumed to be constant for all following measurements (the current is not used when computing resistance on the Mega Cable Tester,

since measurements are ratiometric). They also measure the voltage across the shorted outputs, providing a measurement of the resistance of the multiplexing tree (on the order of 10 Ω, assumed to be the same for all channels) that is removed from reported values. Additionally, a series of known resistors are mounted on the board and connected to otherwise unused pins; expected values for these resistors are included in a calibration pin mapping file provided with the software.

Timing

The mega cable tester can be limited to different subsets of connectors, affecting total run time. The 500x500 half-matrix (A to B but not B to A, sufficient for resistors only) for all 5 100p MDMs completes in approximately 2 minutes. The half-matrix for a single 100p MDM can be computed in about 10 seconds. On the mini cable tester, the full matrix (128x128) can be measured in ∼40 sec and a half-matrix in ∼20 sec.

B.3 Repositories

Everything related to the cable tester is freely available in git repositories on BitBucket.

PC-side software:

`https://bitbucket.org/jhunacek/cable-tester-software`

Firmware:

`https://bitbucket.org/jhunacek/mega-cable-tester-firmware`

`https://bitbucket.org/jhunacek/cable-tester-firmware`

PCB drawings:

`https://bitbucket.org/jhunacek/cable-tester-pcb`

Appendix C

TIME Housekeeping Electronics

C.1 Background

Legacy Housekeeping

The original TIME housekeeping (i.e. thermometry, heaters, pressure sensors, etc.) provided inadequate data rates, had an insufficient number of heater channels, lacked the ability to PID-control heaters, and lacked MCE Sync Box time stamps. The heaters and high-temperature (above 4K) thermometry were controlled with custom housekeeping equipment from prior experiments. These boxes allow for 8 diode thermometers and 8 resistive thermometers to be measured in a 2-wire configuration at high data rates. There were a total of 14 heater output channels, each with a current monitoring circuit; these monitoring circuits have a relatively small useful dynamic range and need to be tuned (by changing resistors on the PCB) to the specific heaters in questions. The low-temperature (sub-4K) thermometry was controlled with a Lake Shore 370 with a 1:16 multiplexer and a $\sim 100\mu$V AC bias. Channels were read at a 10 second cadence (160 sec revisit rate) to allow sufficient settling time for the multiplexer; it is likely this sample rate could be improved, but not to the level desired for science operation ($\sim$ 5 Hz revisit rate). Pressure sensors were read in with a LabJack U6. Critically, none of the systems described are synchronized to MCE frame numbers, and thus precise alignment with detector timestreams was not possible.

Calibration Error Propagation

For a resistive thermometer, the ratio of the fractional temperature error to the fractional resistance error is written as follows.

$$\frac{\delta \mathrm{T}/\mathrm{T}}{\delta \mathrm{R}/\mathrm{R}} = \frac{\mathrm{R}}{\mathrm{T}}\frac{\mathrm{dT}}{\mathrm{dR}} = \frac{\mathrm{d}\log \mathrm{T}}{\mathrm{d}\log \mathrm{R}}$$

This dimensionless value is a measure of the sensitivity of the thermometer, and generally varies with temperature. When the absolute value of this function is < 1, the fractional error in the measurement is reduced when converting

from resistance to temperature, thus relaxing the requirements on the resistance error required to achieve a specified temperature error.

C.2 System Requirements

Temperature Sensors

The TIME cryostat includes wiring for up to 44 thermometers in a 4-wire configuration broken across eleven 25-pin D-Sub connectors using a Lake Shore compatible pinout. Maintaining the Lake Shore pinout allows for more flexibility during in-lab testing, as alternate electronics can be swapped in without adapters.

We use a total of 12 Lake Shore Cryotronics DT-400 and DT-600 series diodes at the 50K and 4K stages. These diodes have a recommended excitation of 10 μA and a usable temperature range from room temperature to 1.4K. Above 10K the sensors use a standard calibration curve (Fig. C.1) and are interchangeable; per-sensor calibration is required to achieve sufficient accuracy at 4K (as demonstrated for one diode in Fig. C.2).

TIME uses a total of 8 carbon resistor thermometers sharing a common calibration curve (shown in Fig. C.3). These thermometers monitor the fridge gas-gap heat switches and are operated between approximately 4K and 20K.

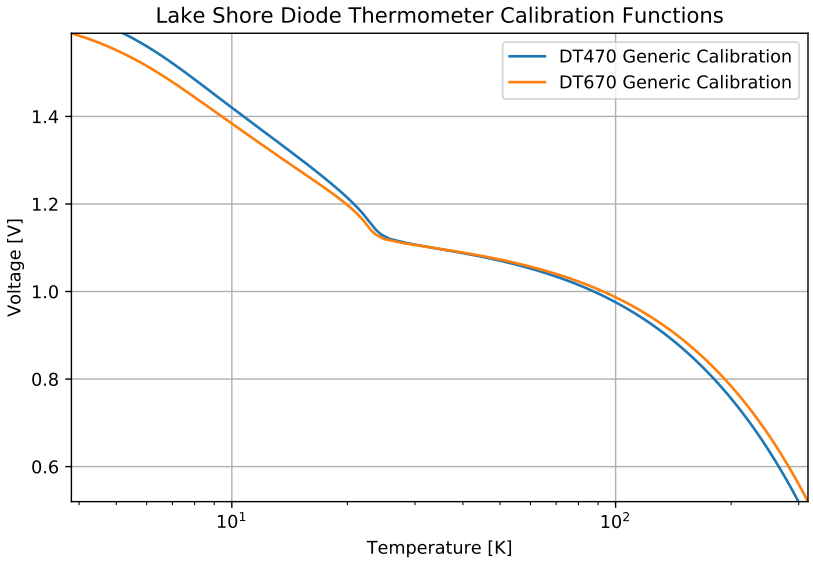

Figure C.1: Standard calibration curves provided by Lake Shore for their DT470 and DT670 diode thermometers [30].

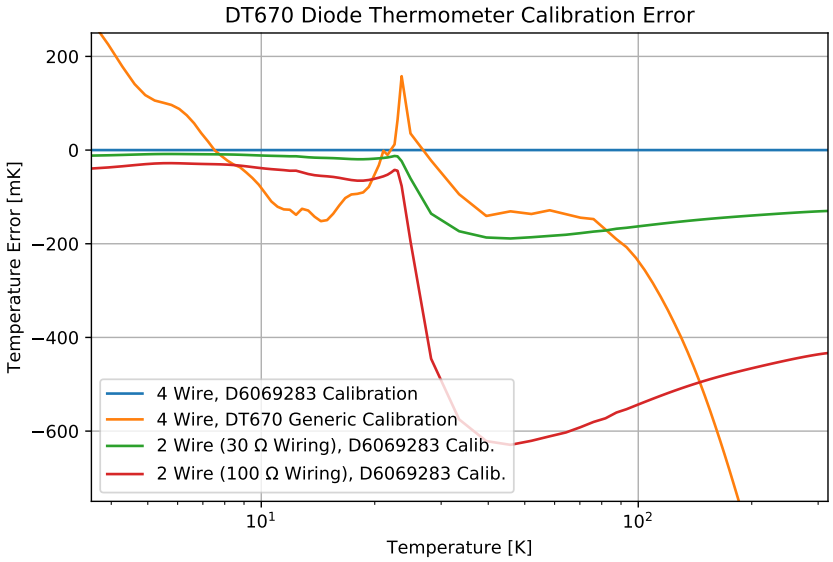

Figure C.2: Calibration errors for a particular Lake Shore DT670 diode thermometer resulting from either (*orange*) using the generic diode calibration curve instead of the known specific-sensor calibration or (*green, red*) using a 2-wire readout instead of a 4-wire readout.

We typically use a $10\,\mu A$ DC excitation current for these thermometers, which corresponds to $0.1\,\mu W$ dissipation in the sensor at 4K.

TIME uses up to 20 low-temperature Cernox thermometers, which under normal operation sit between 4K and 200mK. Figure C.3 shows the resistance curve for a representative subset of TIME Cernoxes. Figure C.4 shows Cernox resistance measured with a Lake Shore 370 as a function of AC excitation current. At high excitation currents, the thermometer self-heats and its resistance changes. Figure C.5 shows the response of two co-located thermometers at UC temperatures when the excitation current of one is stepped to $3\,\mu$A. The non-stepped sensor shows no response, indicating that the excess readout power is not heating the stage. This is likely the result of poor internal thermal conductance at 200 mK. Because the stage is not heating, it should be straightforward to determine the optimal excitation current on a per-sensor basis by checking a range of excitation currents and choosing the one with the smallest total error (low currents are dominated by readout noise, high currents are dominated by self-heating). Figure C.4 indicates that sensors at 1K or above can use $3\,\mu$A excitations, while sensors down to UC temperatures operate best at 10 nA or below.

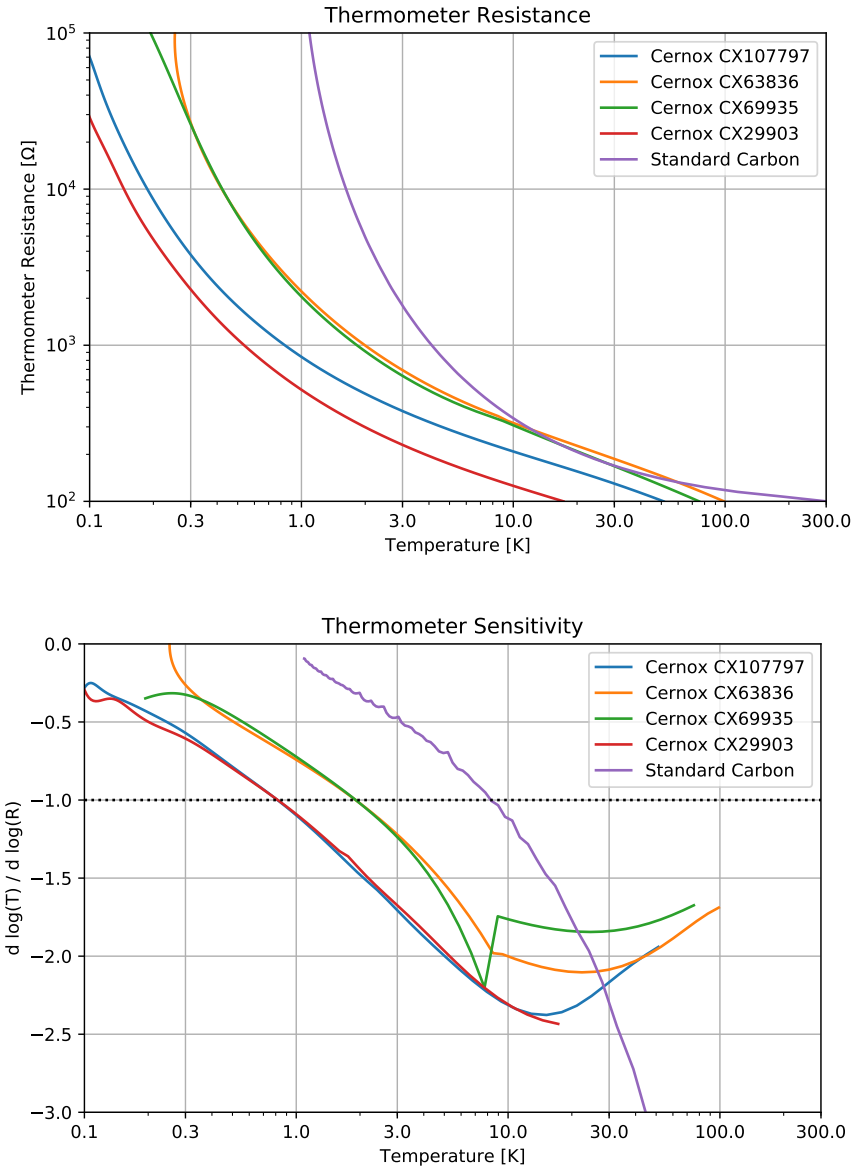

Figure C.3: Cernox resistance versus temperature for several serial numbers used in TIME. The standard carbon resistor calibration curve used for the TIME heat switch thermometers is included for comparison.

Pressure Sensors

TIME uses four analog-output pressure sensors (in addition to a fifth digital-output gauge) on the vacuum shell and the room temperature pumping cart for the 1K Joule-Thompson fridge. Absolute pressure accuracy is not critical, as we typically monitor them for large relative changes to diagnose issues. The TIME vacuum shell pressure is monitored by an Edwards AIM-S gauge at low

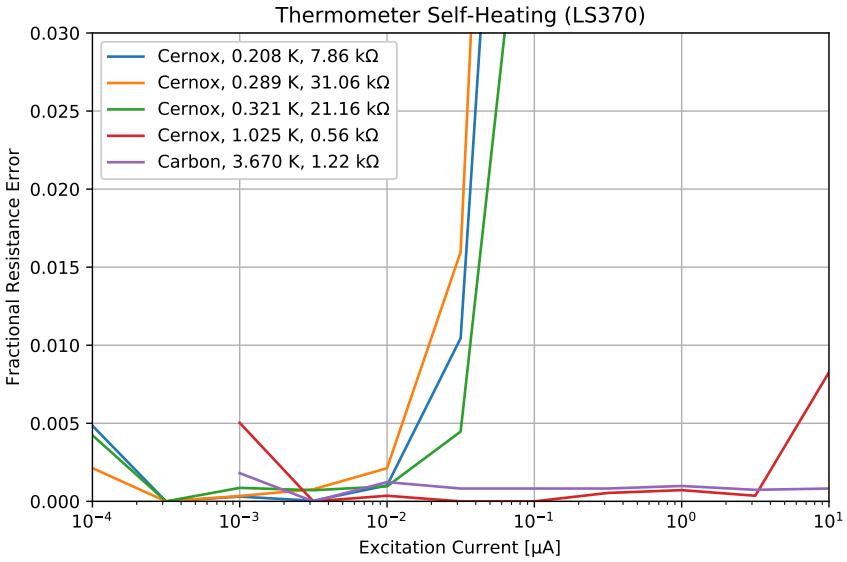

Figure C.4: Thermometer resistance measured with a Lake Shore 370 as a function of AC current bias, demonstrating thermometer self-heating at high power dissipation.

pressures ($< 10^{-2}$ mbar) and by an Edwards APG-M at high pressures (up to 1 atm). The sensor requires a 13.5-36V 3.5W (AIM-S) or 20-36V 1W (APG-M) power supply and should ideally be powered by the HK box for convenience. Each sensor outputs a 2-10V signal ($10k\Omega$ min load impedance). A digital enable line controls the low pressure sensor and should be actively toggled by the HK electronics to prevent sensor operation at unsafe pressures. An Edwards APG-L gauge powered and monitored by an analog indicator gauge on the JT cart monitors the pump line of the JT. The indicator gauge outputs a copy of the 2-10V analog output voltage that should be read in by the HK motherboard. During normal operation this gauge reads between 10^{-3} and 1 Torr. A large helium correction factor [43] results in inaccurate readings above this pressure; therefore, a parallel gauge with a gas-independent Piezo sensor (MKS 902B) is used at high pressures. A Swagelok S Model pressure transducer with a 4-20 mA output current monitors the injection line of the JT. The sensor requires a 10-30V power supply and should be powered by the HK motherboard. The maximum allowed load impedance of the current monitoring system is $(V_{cc} - 10V)/0.02A$, which is 700 Ω for 24V. During normal operation this gauge reads between 300 and 600 Torr.

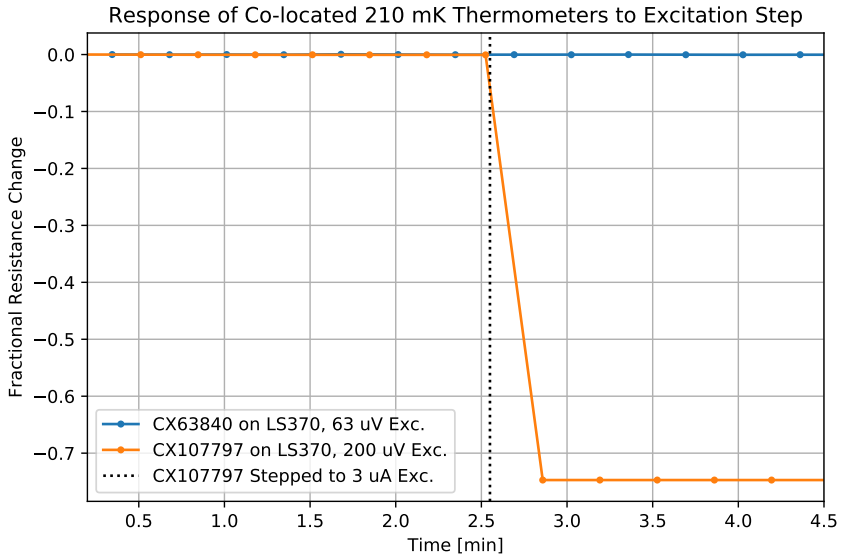

Figure C.5: The response of two co-located thermometers (on the UC at 208 mK) when the excitation for one thermometer is stepped from the nominal value to approximately 3 μA. The non-stepped sensor shows no response, indicating that the excess readout power is not heating the stage. This data is was taken with a Lake Shore 370.

Heaters

TIME has wiring for up to 27 two-wire heaters. Heater resistances range from 200Ω to 15kΩ. The two 400Ω evaporator heaters include an additional current-limiting 15kΩ in series outside of the cryostat. Voltage and current requirements are shown in Table C.1.

Type	**R [Ω]**	**R_{series} [Ω]**	**P_{max} [mW]**	**V_{max} [V]**	**I_{max} [mA]**
Heat Switches	400	50	2	0.95	2.11
^{3}He Pumps	400	50	150	8.22	18.26
^{3}He Pots	400	15050	1	3.93	0.25
Focal Plane	9000	50	1	3.01	0.33

Table C.1: TIME heater requirements (including 50Ω wiring).

Analog Input

The HK board should include a set of generic analog voltage inputs. Some subset of these inputs should be considered slow-rate precision inputs (better than 1% voltage accuracy, 1 Hz or better), useful for pressure sensors. Another

set of inputs should be considered high-speed inputs (30 Hz or better), useful for chopper references.

FTS Encoder

The TIME FTS has a linear encoder which outputs two 5V 50% duty cycle square waves with a frequency of 500 Hz at the typical 2 mm/s drive speed. Pulse counting can be used to find relative positions with up to 1 μm resolution. The measured pulse frequency can also be used to measure the drive speed directly. The HK box should provide power to the encoder (5V, max 200 mA) and should allow reading the drive speed during FTS operation.

MCE Sync Box

All measurements made by the HK motherboard should include frame index numbers provided by the MCE sync box. The fiber interface module used by the sync box is considered obsolete and is difficult to source. Therefore, the HK box should interface with the MCE sync box via RS-422, available through the 25 pin d-sub connector.

IRIG-B

All measurements made by the HK motherboard should also include time stamps synchronized to an absolute time reference. This can be done by reading an IRIG-B signal generated by a GPS or NTP timing box, which provides timing updates at 100 Hz. The IRIG-B data frame consists of 100 digital TTL pulses of variable width (2 ms for for binary 0, 5 ms for binary 1, and 8 ms for marker) with 10 ms between pulse rising edges (1 second for the full frame). These 100 bits (and markers) encode the current date and time to one-second precision, and the pulse positions correspond to 10 ms intervals within that second.

C.3 HKMBv1 – Multiplexed DC Excitation

The v1.0 TIME housekeeping main board (shown in Fig. C.6) supports 32 two-wire heaters and 36 four-wire thermometry channels multiplexed over three ADCs with software-variable DC excitations. The board is housed in a rack-mount case for easy integration with other TIME electronics systems. Power is provided by an off-the-shelf 24V DC linear power supply.

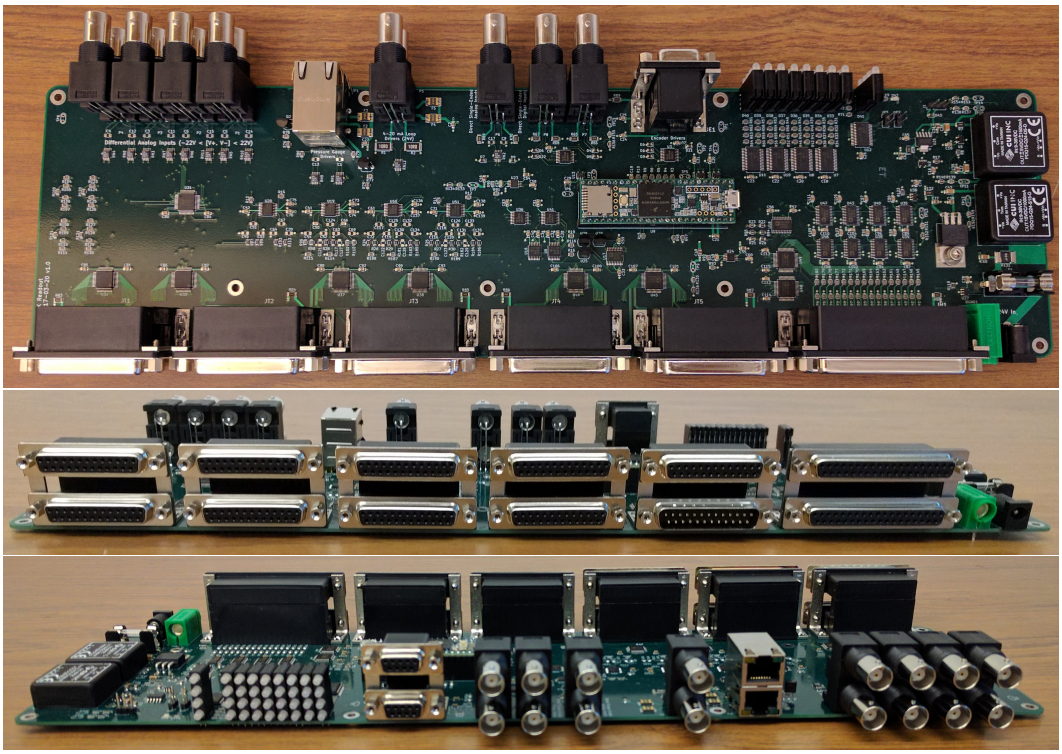

Figure C.6: The TIME housekeeping motherboard, v1.0. This board (normally housed in a rack-mount case) is responsible for the higher-temperature (4K and above) DC-excitation thermometers.

Processor

The heart of the HK board is a Teensy 3.6, an Arduino-compatible 32-bit ARM Cortex-M4F processor operating at 180 MHz that is mounted in a breadboard-friendly package. Native floating point math support and up to 58 digital IO pins makes this particularly well suited for this application. Use of an Arduino-compatible programming interface allows the firmware to leverage a rich set of existing libraries to enable rapid development while still allowing lower-level access to ARM libraries and functionality as needed. The processor communicates with the host computer via a 12 Mbit/s USB connection. (Ethernet and 480 Mbit/s USB are supported by the Teensy 3.6 and can be explored for future revisions. Note that an extreme worst case of 100 channels per motherboard all streaming at 300 Hz and sending 20 bytes per sample would only require transfer speeds of 5 Mbit/s; thus the standard USB connection should be sufficient.)

Thermometry

The v1 HK motherboard natively supports DC excitation and measurement of four-wire resistor or diode thermometers. (For sub-1K thermometers, an optional external pre-amplifier box was designed to generate AC excitations and to demodulate the resulting signal, providing a DC voltage signal to the motherboard. The pre-amplifier was not produced and has been superseded by HKMBv2.) The ADC is an ADS1220, a 24 bit delta-sigma ADC with a programmable gain amplifier (up to 128x), sample rates from 20 Hz to 2000 Hz (not including the multiplexing), and two pairs of differential inputs. One pair of inputs measures the sensor voltage while the second set measures the voltage across a fixed 75kΩ resistor to monitor the excitation current. A pair of ADG726 analog multiplexers connects pairs of current and voltage lines from 16 sensors to the excitation circuit and ADC inputs. 3 ADCs (each connected to 12 physical sensors, 4 on-board monitoring sensors, and an excitation circuit) allow for a total of 36 thermometers connected via nine Lake Shore compatible 25-pin d-sub connectors. The excitation circuit consists of an ADG734 analog multiplexer allowing connection to either a LM234 constant current source controlled with a TPL0102 digital potentiometer or to an AD5754R 16 bit DAC.

Sensitivity to voltage offsets in the ADC (or from thermocouple effects in wiring) is one of the major drawbacks of using DC excitations. Typical input voltage offsets in the ADS1220 ADC are rated at $\pm 4\mu$V at room temperature for all gains, but are actively monitored and subtracted from the sensor signals by measuring the voltage across shorted inputs. A 10μA excitation over a 100Ω sensor would produce a 1 mV signal, which should not noticeably be affected by residual voltage offset error.

The DC excitation current flowing through the fixed monitor resistor is not identical to the current flowing through the sensor due to leakage currents in various stages of the system, resulting in systematic errors in the computed resistances. Leakage due to ground shorts in the cryostat wiring is considered a system fault and should be detected (perhaps with the Automated Cable Tester presented in Appendix B) and corrected. Leakage currents in the multiplexers on the motherboard itself currently dominate the systematic error in the resistance measurements for very low excitation currents. The ADG726 multiplexer is specified to have a maximum leakage current of $\pm$0.5nA at room

temperature or ±2.5nA from −40°C to 85°C. This is a significant error for 10nA DC excitation currents, but is negligible at or above 1μA. The leakage currents in the system have been measured by checking the computed resistance of known fixed high-precision resistors across a range of excitation currents. A simple constant current offset describes the data to first order (Fig. C.7). Fit values for this current offset are approximately 0.8 nA, which is consistent with the maximum specified leakage currents for an ADG726 multiplexer. To achieve ±1% accuracy for excitation currents < 30nA, an empirical six-parameter (c_i) model with higher-order correction terms was fit:

$$\begin{aligned} \mathrm{I_{measured}} &= \mathrm{V_{monitor}}/\mathrm{R_{monitor}} \\ \mathrm{R_0} &\equiv \mathrm{V_{sensor}}/\mathrm{I_{measured}} \\ \delta &\equiv \mathrm{c_0}/\mathrm{I_{measured}} \\ \mathrm{I_{effective}} &= \mathrm{I_{measured}} * (1 - \delta^{\mathrm{c_1}} + \mathrm{c_2}\,\delta + \mathrm{c_3}\,\delta\,\mathrm{R_0} + \mathrm{c_4}\,\delta^2 + \mathrm{c_5}\,\delta^3) \\ \mathrm{R} &= \mathrm{V_{sensor}}/\mathrm{I_{effective}} \end{aligned} \tag{C.1}$$

Note that accuracy for such small DC excitations is not necessary for TIME, as AC excitation is preferred in this regime; this is simply an effort to push the limits of DC excitation in this system. Post-calibration results for the fit data are shown in Figure C.8. Additionally, a separate data set not used in the fitting (taken four weeks prior) was calibrated using these fitting results. This demonstrates that the fits found on the training data are stable on the time scale of a month and are not the result of over-fitting.

Heaters

A series of eight quad-output AD5754R 16 bit DACs drive a total of 32 heaters connected via two 37 pin d-sub connectors. Each output channel has a voltage output between 0 and 10.5V and is current-limited to 20 mA (protecting the system from short-circuits). A 10Ω resistor on the low side of the heater allows for monitoring of the current in the heater circuit, which can be used to determine the dissipated power (using the known heater resistance) or to detect shorted or open circuits. A series of 32 individually controllable bi-color LEDs on the front panel can be used to quickly indicate heater status, which is useful for software and firmware debugging.

A stress test of the DACs and power system was conducted by shorting all heater outputs and turning all of the DACs to maximum output. (Two RJ45

pressure sensors were connected and powered, and fixed resistors were installed on all thermometry channels.) Each heater channel was automatically clamped to 20 mA output as expected. Measurements of the DAC chip case temperature were made with a K-type thermocouple; results are shown in Fig. C.9. Using specified thermal parameters $\theta_{\mathrm{jc}} = 9°\mathrm{C/W}$ and $\theta_{\mathrm{ja}} = 42°\mathrm{C/W}$ of the AD5754R, one can roughly approximate the junction temperature during these stress tests.

$$\begin{aligned} \theta_{\mathrm{ja}} &= \theta_{\mathrm{jc}} + \theta_{\mathrm{ca}} \\ \mathrm{P_{dissipated}} &= (\mathrm{T_{case}} - \mathrm{T_{ambient}})/\theta_{\mathrm{ca}} \\ \mathrm{T_{junction}} - \mathrm{T_{case}} &= \mathrm{P_{dissipated}} * \theta_{\mathrm{jc}} \\ \mathrm{T_{junction}} &= \frac{\theta_{\mathrm{jc}}}{\theta_{\mathrm{ja}} - \theta_{\mathrm{jc}}}(\mathrm{T_{case}} - \mathrm{T_{ambient}}) + \mathrm{T_{case}} \end{aligned} \tag{C.2}$$

Assuming $\mathrm{T_{ambient}} = 26°\mathrm{C}$ and $\mathrm{T_{case}} = 80°\mathrm{C}$ in the steady state when all channels are on and shorted, one finds $\mathrm{T_{junction}} = 95°\mathrm{C}$. This is well within the limits specified in the datasheet ($\mathrm{T_{junction}} < 150°\mathrm{C}$). Thus it does not appear that heatsinks on the DAC chips are required (though they can easily be added later).

Analog and Digital Inputs

A set of eight BNC jacks are designated as low-speed high-precision differential analog inputs. The two conductors of each BNC are connected through precision matched 11:1 voltage dividers (110kΩ impedance to ground per side) to an ADS1220 ADC though an ADG726 analog multiplexer. Each end of the input signal can range from -22V to 22V relative to system ground. The non-infinite input impedance of the voltage dividers ensures that floating signals become ground-referenced, and the non-zero input impedance ensures that signals with sufficiently low output impedance ($< 100\Omega$) are not significantly distorted. *HKMBv2 provides larger input impedances and should be preferred over these channels.*

A pair of BNC jacks are designated as high-speed low-precision single-ended analog inputs. The shield conductor of each jack is connected to ground via a 10Ω resistor, while the center pin is connected though a precision 11:1 voltage divider (110kΩ impedance to ground) to an analog input pin on the Teensy 3.6. This allows low-precision measurements to be taken at high data rates without being limited by the system multiplexing cadence. *HKMBv2 provides larger input impedances and should be preferred over these channels.*

A set of four ground-referenced BNC connectors are connected to Teensy 3.6 digital input pins via a logic level shifter. These pins have the capability to be used for frequency measurement or as arbitrary digital inputs. *HKMBv2 provides opto-isolated digital inputs and should be preferred over these channels.*

A pair of 9 pin d-sub connectors provide 5V power and digital frequency measurement for the TIME FTS encoder, allowing monitoring of the mirror speed. *HKMBv2 provides access to a true quadrature decoder and should be preferred over these channels.*

Pressure Sensors

A pair of BNC connectors provide 24V over the center pins (with individual 300 mA trip / 100 mA hold self-resetting protection fuses) to power standard 4-20 mA output industrial sensors (such as the Swagelok S Model used in the JT cart for TIME). The BNC shield is connected to ground via a high-power rated 10Ω current monitoring resistor. The voltage over the resistor is measured by an ADS1220 ADC through an ADG726 analog multiplexer. A precision 11:1 voltage divider (110kΩ impedance to ground) protects the multiplexer and ADC inputs in the case of external short circuit conditions (the thermal fuse has a time lag).

A pair of RJ45 connectors provide 24V (with individual 300 mA trip / 100 mA hold self-resetting protection fuses) to Edwards-style pressure sensors. The 2-10V output signal is measured by an ADS1220 ADC through an ADG726 analog multiplexer with a precision 11:1 voltage divider (110kΩ impedance to ground). A digital output controlled by the processor drives the sensor enable pin through a transistor, allowing the firmware to disable the sensor in an over-pressure environment.

MCE Sync Box

Connection with the MCE sync box is made via a 25 pin d-sub connector. MAX3280E chips convert the RS-422 5 MHZ clock, data, and marker signals into 3.3V TTL signals, which are routed to Serial Peripheral Interface (SPI) clock and data inputs on the Teensy 3.6. The lines are configured as SPI slave inputs which write the continuous bit stream directly to a small circular memory buffer via a Direct Memory Access (DMA) channel. The marker pulse triggers an interrupt which extracts the current sync word from the memory buffer.

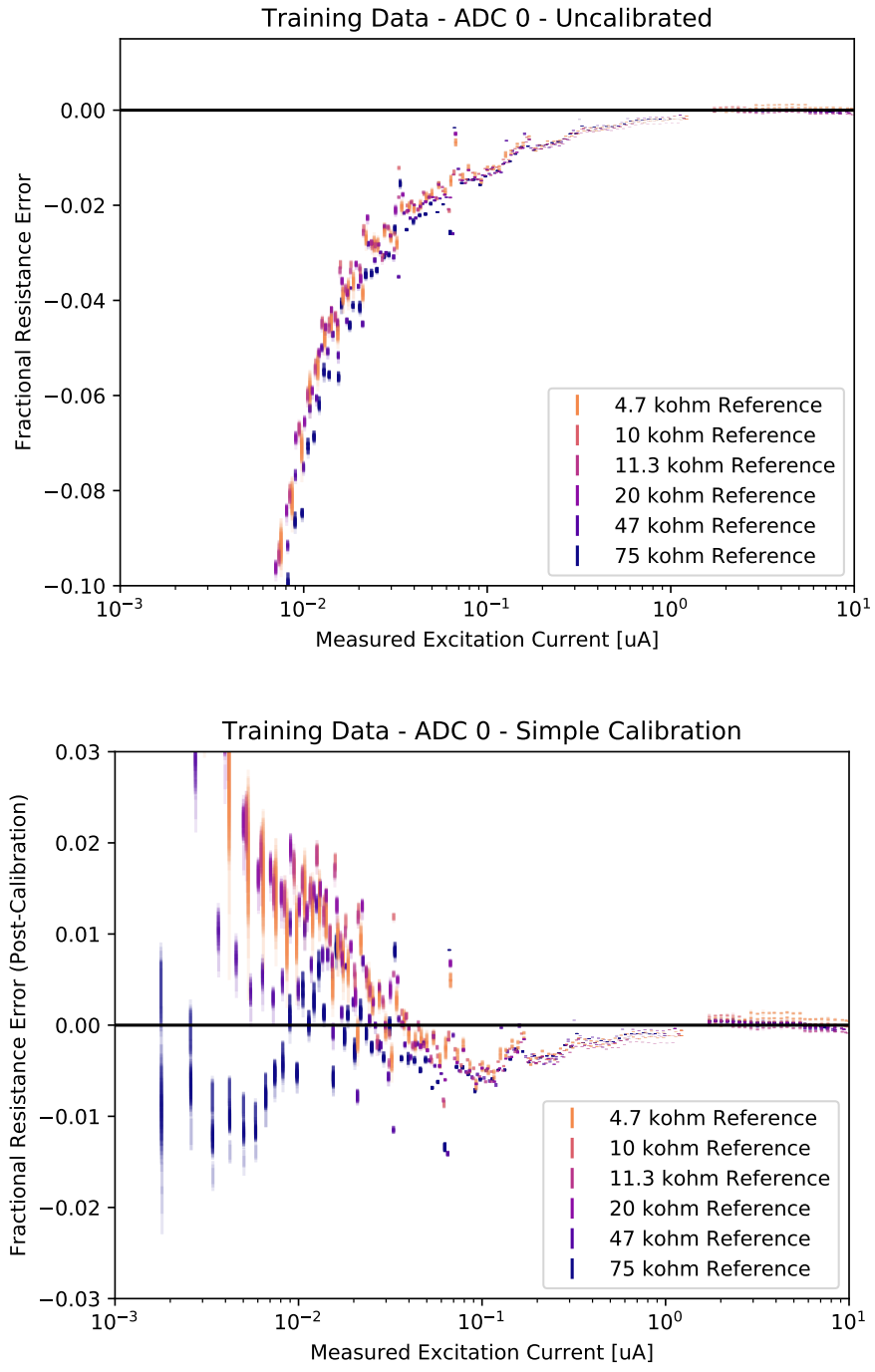

Figure C.7: Resistance calibration for ADC 0 in HKMBv1 assuming a simple current offset. This model is insufficient to describe the data to the accuracy desired for low DC excitation currents. However, for the 10 μA excitation currents currently used for TIME, calibration isn't necessary at all.

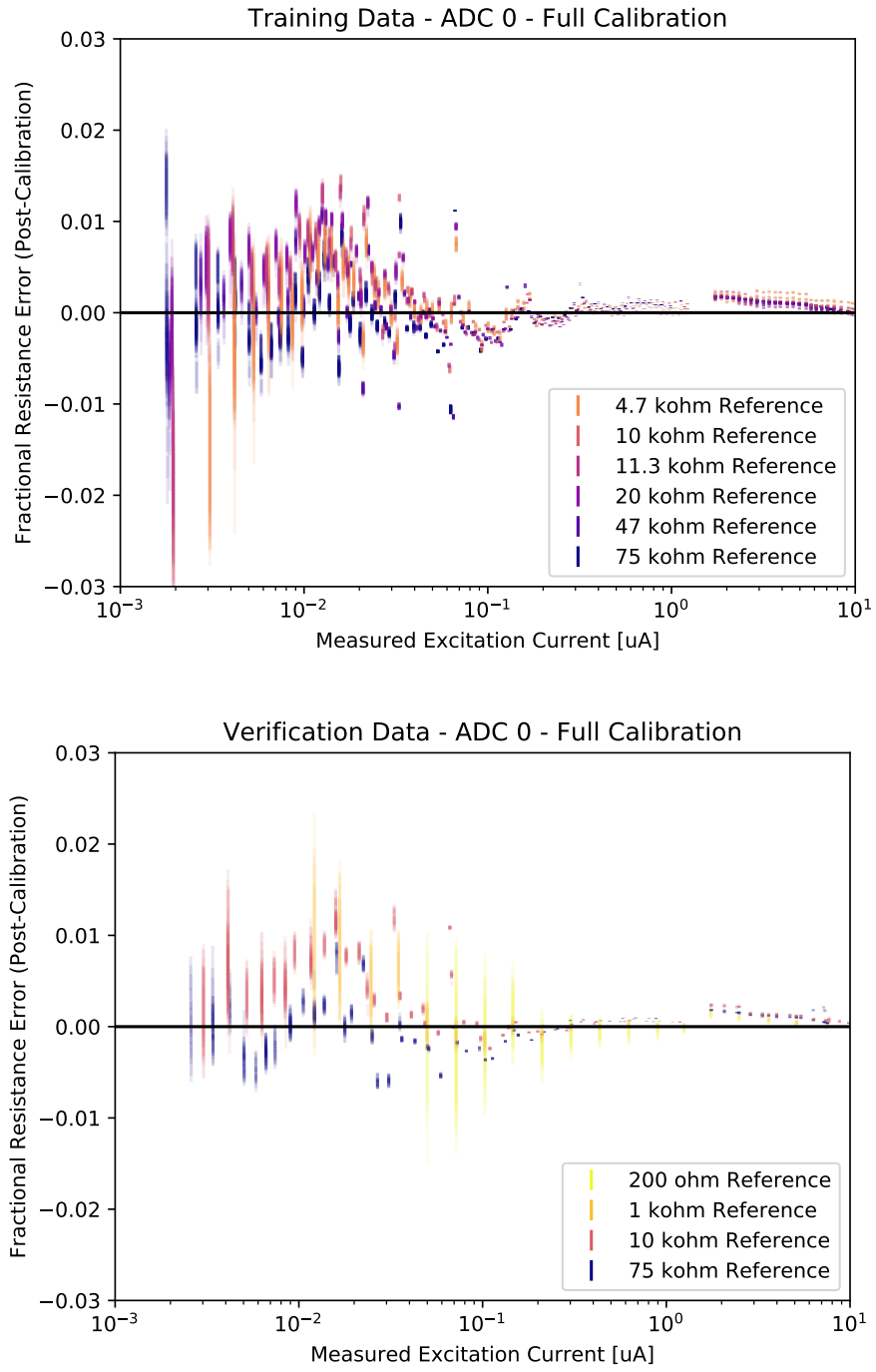

Figure C.8: Resistance calibration for ADC 0 in HKMBv2 assuming the full calibration model. Verification was data taken several weeks before the calibration data and was not included in the fitting. Note that for the 10 μA excitation currents currently used for TIME, calibration isn't necessary at all.

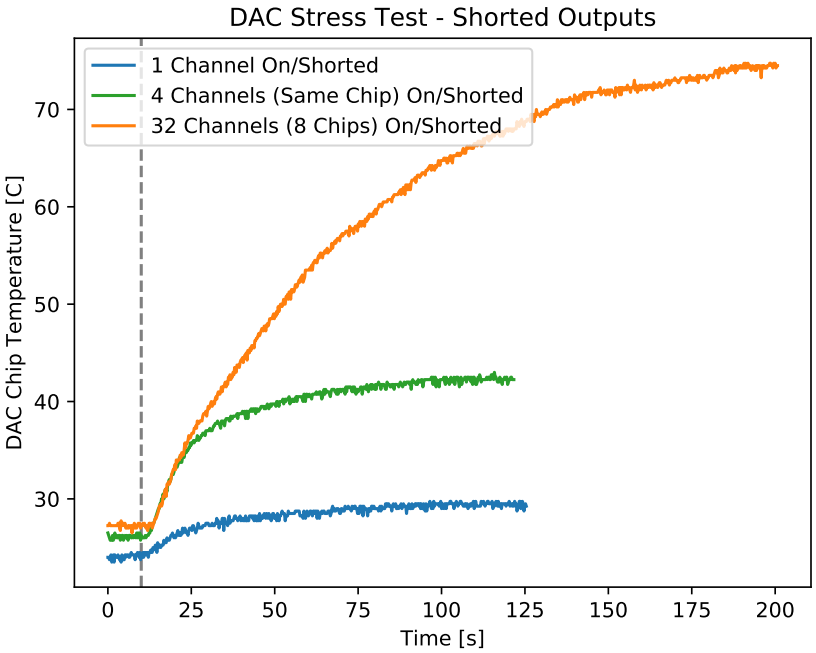

Figure C.9: Measurements of the case temperature of a DAC chip during channel output short-circuit tests.

C.4 HKMBv2 – Firmware Lock-in Demodulation

The extended math functions and high clock speed of the Cortex-M4F in the Teensy 3.6 (used in HKMBv1) make it feasible to do AC bias signal demodulation in firmware when coupled with high-rate simultaneously-sampling ADCs. The v2 TIME HK motherboard (pictured in Fig. C.10) provides two dedicated (non-multiplexed) ADS1278 ADC inputs (one for voltage measurement and one for excitation current monitoring) for each of 24 thermometer channels. Channel amplifiers are mounted on shielded replaceable mezzanine boards to allow for future upgrades.

Figure C.10: The TIME HKMBv2 box in its rack-mount enclosure. Connectors for the thermometry and heaters are found on the reverse side.

Processor

The processor and USB communication specifications are identical to HKMBv1. For HKMBv2, the NXP K66 processor used in the Teensy 3.6 has been integrated into the PCB, improving access to some of the extra peripheral lines of the chip. The Teensy 3.6 bootloader chip from PRJC is also included on the board, allowing full software compatibility with Teensy 3.6 and HKMBv1.

Thermometry

The ADS1220 ADC used in the v1 motherboard is replaced with the ADS1278. Each ADS1278 contains eight simultaneously-sampling 24-bit delta-sigma ADCs. Multiple chips are daisy-chained on the motherboard to provide up to 106 channels (64 are used) at data rates up to 10.5 kHz (depending on clock speeds set in the firmware). Thermometry and analog input channels are no longer multiplexed, and 100kΩ excitation monitor resistors in series with the thermometers allow for fully ratiometric measurement of resistive sensors. A total of 24 four-wire thermometers are supported, spread over six Lake Shore pinout

25 pin d-sub connectors

Each group of four channels is buffered and amplified ahead of the ADC on a shielded replaceable mezzanine board. The amplifier board design in current use is shown in Fig. C.11. An AD8421 differential instrumentation amplifier, chosen for its low voltage noise, amplifies the sensor voltage with a fixed gain of 496. An AD8224 differential instrumentation amplifier, chosen for its low current noise, amplifies the voltage across the on-board current monitor series resistor with a fixed gain of 10. An excitation DAC on the motherboard generates and distributes a programmable-frequency sine wave with an amplitude on the order of 1V. For each channel a pair of 200 kΩ 256 position digital potentiometers (AD5263) form a voltage divider with a fixed 200 Ω resistor, bringing the excitation into the 0.1 to 300 nA range (software variable). Excitation amplitude accuracy errors and long term drifts are suppressed by the ratiometric nature of the measurement (the current monitor resistor is sampled at the same speed as the sensor).

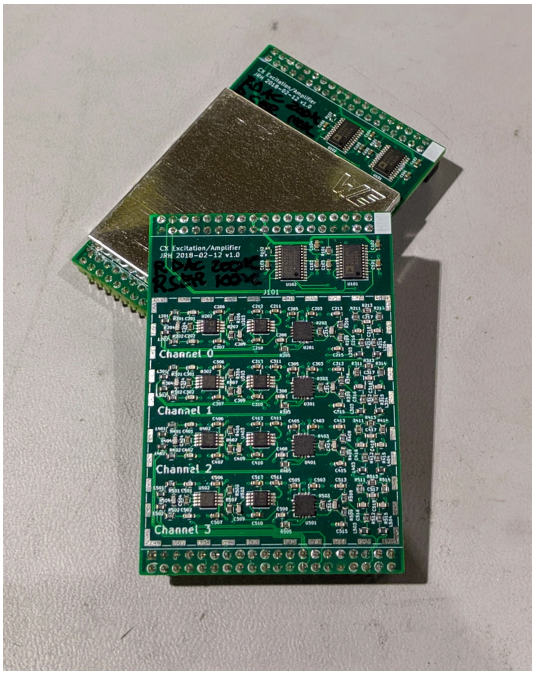

Figure C.11: Two of six replaceable thermometer channel amplifier boards for the v2 TIME HK motherboard.

Heaters

Similar to HKMBv1, a series of six quad-output AD5754R 16 bit DACs drive a total of 24 heaters connected via two 25 pin d-sub connectors. Each channel has a voltage output between 0 and 10.5V and is current-limited to 20 mA (protecting the system from short-circuits). A 10Ω resistor on the low side of the heater allows monitoring the current in the heater circuit, which can be used to determine the dissipated power (using the known heater resistance) or to detect shorted or open circuits. A series of 24 individually controllable bi-color LEDs on the front panel can be used to quickly indicate heater status, which is useful for software and firmware debugging.

Analog and Digital Inputs

A set of six BNC jacks act as precision differential analog inputs (connected to ADS1278 ADC inputs via an AD8224 instrumentation amplifier with a gain of 1). Each end of the input signal can range from -5V to 12V relative to system ground; floating inputs are also acceptable. Signals are typically reported at the thermometry data rate, but can be reported at up to the raw ADC sample rate. Inputs have a 10 MΩ impedance to ground.

A set of six BNC connectors are connected to processor digital input pins via opto-isolators. These pins have the capability to be used for frequency measurement, as IRIG-B inputs, or as arbitrary digital inputs.

A pair of 9 pin d-sub connectors provide 5V power and digital frequency measurement for the TIME FTS encoder, allowing monitoring of the mirror position and speed. This function uses the quadrature decoder built into the K66 processor.

Pressure Sensors

A pair of RJ45 connectors provides 24V (with individual 300 mA trip / 100 mA hold self-resetting protection fuses) to Edwards-style pressure sensors. The 2-10V output signal is measured by an ADS1278 ADC input via an AD8224 instrumentation amplifier with a gain of 1. A digital output controlled by the processor drives the sensor enable pin through a transistor, allowing the firmware to disable the sensor in an over-pressure environment.

MCE Sync Box

The MCE Sync Box readout circuity has been carried over from the HKMBv1 design. An additional DB-25 connector was added that acts as a signal pass-through, allowing the MCE Sync Box connection to be daisy-chained through several boxes.

Firmware Lock-in Demodulation

Lock-in demodulation uses an AC excitation signal to move the signal band of interest from DC to higher frequencies, reducing or removing the impact of low-frequency amplifier noise and DC offset errors. A sensor signal at frequency f is modulated by the excitation/carrier frequency f_c, producing signals at $f_c \pm f$. This measured signal is digitally multiplied in firmware by a copy of the pure carrier wave, producing signals at f and $2f_c \pm f$. A digital low-pass filter removes the component near $2f_c$, resulting in a demodulated output with only the f component.

An excitation frequency of 19 Hz was chosen for HKMBv2 as a compromise between 1/f noise at low frequency and parasitic losses in sensor wiring (not shared by the current monitor resistor) at high frequency. A Nyquist-sampled output bandwidth f_{out} of 5 Hz was chosen (with output data rates at or above 10 Hz), but this can easily be increased in the future if desired. Raw ADC sampling rates for HKMBv2 are firmware-variable; 562.5 Hz was chosen to reduce aliased noise arising from the cutoff frequency of the RC low pass filters at the ADC inputs (sampling slower would be possible with lower bandwidth RC filters). All data is immediately decimated by a factor of 6 to 93.75 Hz after passing though a 97-tap finite impulse response (FIR) digital low-pass filter, which is designed to have low ripple and loss in the signal band ($f_c \pm f_{out} = 19 \pm 5\,\mathrm{Hz}$). FIR filters are more resource-intensive than comparable infinite impulse response filters (IIR), but they allow linear phase filters (filters with a frequency-independent group delay) to be implemented in a straightforward way [66]; a well-defined group delay allows for proper timestamp corrections to be applied to filtered data in firmware before reporting to a computer. The FIR filter coefficients are found by starting from an ideal desired transfer function (Fig. C.12, upper) and computing its Fourier transform, producing a time domain impulse. The impulse is shifted and truncated to the desired filter coefficient count (97 taps); an odd tap count is chosen to produce a group delay corresponding to an integer number of samples (48). A Blackman

window is applied to reduce high frequency spectral leakage, producing the final filter coefficients (Fig. C.12, lower). The actual spectral response of the filter is found by transforming back to frequency space (Fig. C.13).

The raw excitation signal is directly measured in a spare ADC input channel (the phase and frequency content are important, but recall that the amplitude is not because of the current monitor channel). The measurement includes ADC noise and higher harmonics of the excitation frequency, so a narrow band pass filter is applied at the expected excitation frequency. The measured thermometer signal may in principle have some non-zero phase with respect to the carrier; in practice, due to the low frequencies involved, this is typically indicative of a wiring failure and is thus useful only as a diagnostic. Nevertheless, it is helpful to form a 90 degree phase shifted version of the excitation signal. Demodulating against both the original (in-phase, or I) and the phase shifted (quadrature, or Q) excitations produces a complex quantity $I + i\,Q$ with a magnitude and a phase. The desired 90° phase shift arises naturally from the Hilbert transform. Setting the negative frequency components of the ideal narrow bandpass filter transfer function to zero (Fig. C.14, upper) results in a complex time-domain representation. The real and imaginary parts of the resulting impulse function are shifted, truncated, and windowed (Fig. C.14, lower), forming a pair of nearly identical bandpass filters with a 90 deg phase shift between them [66]. The spectral response of these two filters is shown in Fig. C.15.

Note that each reference signal (I and Q) has now been passed through two FIR filters: the initial lowpass/decimation filter and a bandpass filter. In principle this could be accomplished with a single FIR filter; in practice, decimation between the two stages allows for much needed memory savings (fewer total filter taps) at the cost of processing time (extra multiplications). Assuming a 2-stage FIR filter with N taps per stage and decimation by a factor of M between stages, the total filter requires on the order of $2 * N$ state variables (RAM usage) and $\frac{N}{M} + N$ multiplications (CPU usage). To achieve similar performance with a 1-stage filter the total impulse length should match the effective length of the two-stage filter ($M * N$ taps), with decimation occurring at the end. This requires $M * N$ state variables and $(M * N)/M = N$ multiplications. Therefore, a 2-stage FIR filter with internal decimation results in $2/M$ times the RAM usage and $1 + \frac{1}{M}$ times the CPU usage. For $M = 6$, this

is 1/3 the RAM at the cost of 17% higher CPU usage.

Because the I and Q reference signals have been passed through filters, they each have a (known) time delay with respect to the sensor voltage and current monitor timestreams. This can be accounted for with a simple time delay on the sensor and monitor measurements. Instead, I take the opportunity to apply a (much wider) band pass filter with an identical group delay. This further reduces any DC or higher-harmonic components common with the reference measurement that would demodulate into the signal band. The response of this filter is shown in Fig. C.16 and C.17. Copies of the resulting signals are multiplied by the I and the Q reference signals, low-pass filtered (Fig. C.18 and C.19), and decimated by a factor of 8. This results in a 11.7 Hz complex timestream $I + i\,Q$ for both the sensor voltage and the voltage across the current monitor resistor. The readout phase (ideally 0 degrees) is assumed to vary slowly over time, and is taken to be the exponential moving average of the instantaneous phase. The amplitude in the readout phase for the sensor and current monitor are divided and normalized, producing a 11.7 Hz timestream of measured resistance values. The MCE Sync Box time stamps are compensated for the known filter group delays when reporting to the computer for storage.

Resistance gain errors for four channels are shown in Fig. C.20. These measurements were done with a set of relay-switched fixed resistors at the end of 12 ft of shielded twisted-pair cable. The channels were set to at most $\sim 100\mu$V excitation (lower excitation voltages were necessary at the lowest resistances due to system limitations). Raw noise for the various channel components for one fixed resistor can be seen in Fig. C.21 and mostly matches amplifier and ADC specifications (shown in dashed lines). Final output noise for fixed 300K resistors is found in Fig. C.22, demonstrating a flat frequency response and good agreement with the noise model presented in Fig. C.23. Johnson-noise limited results are achieved for 300K resistors, but the system is amplifier noise (or gain) limited for sub-Kelvin sensors. Cryogenic pre-amplifiers could be added to improve performance at the cost of increased complexity.

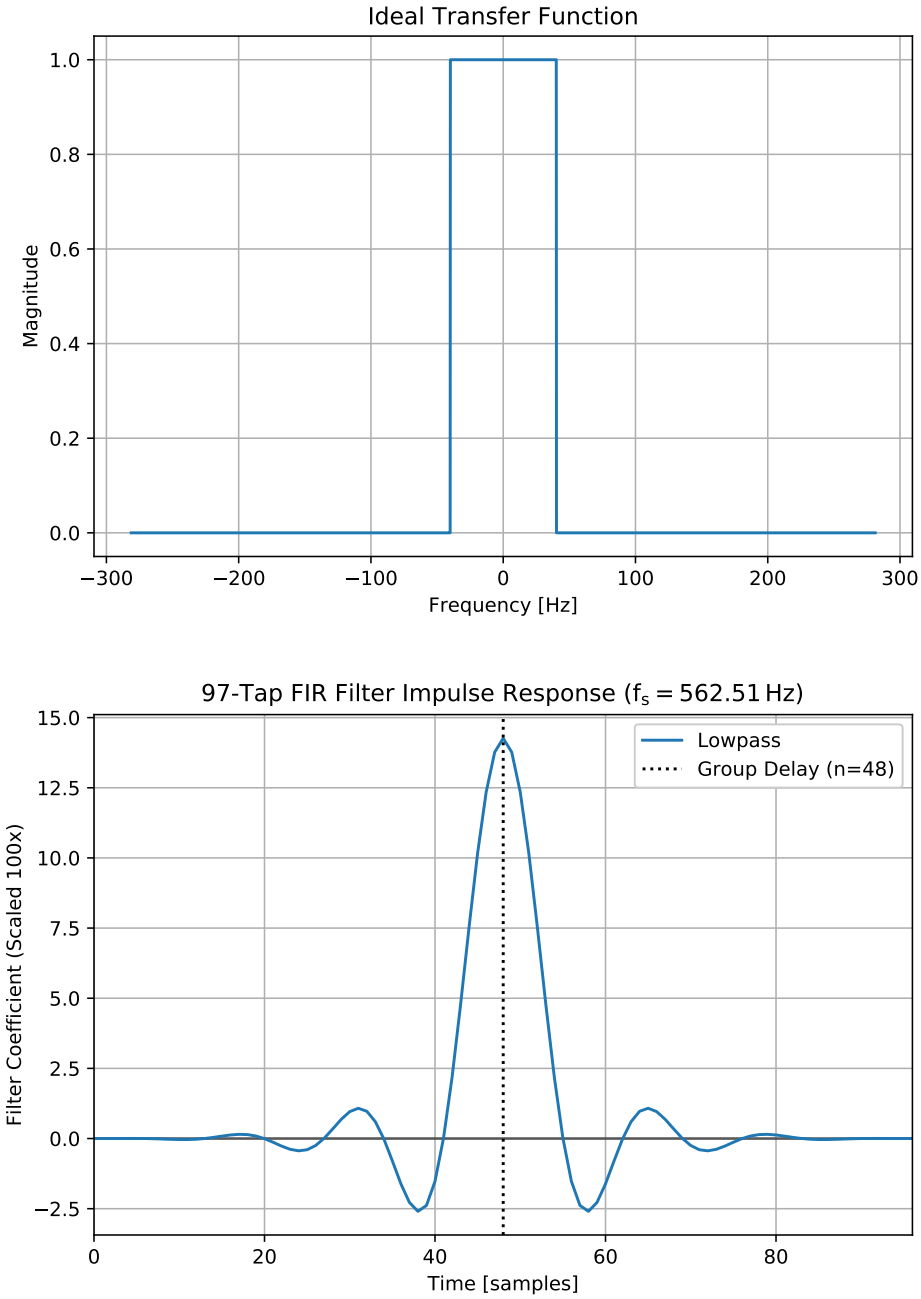

Figure C.12: Ideal transfer function and the resulting processed impulse response for the initial decimation FIR filter.

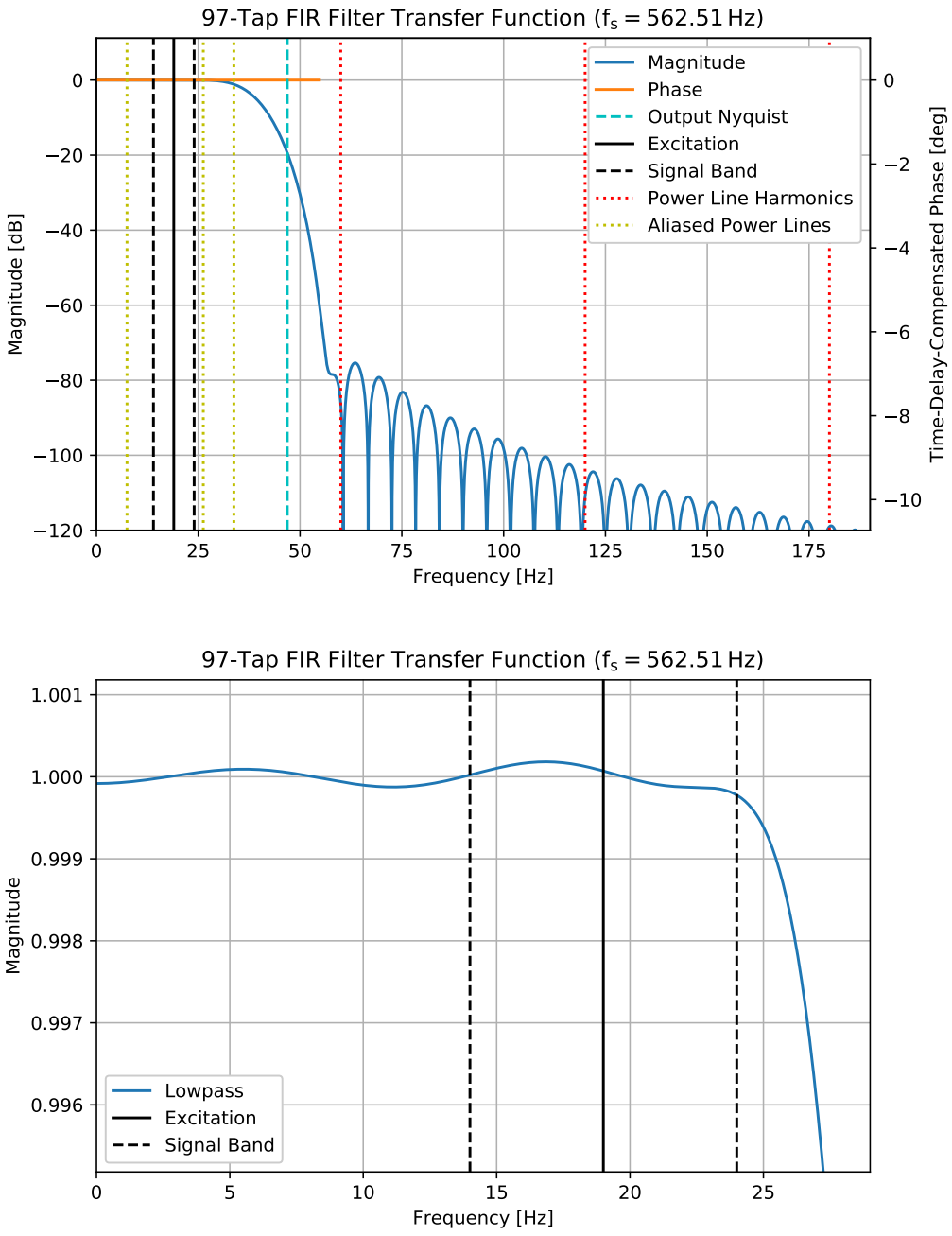

Figure C.13: Computed transfer function for the initial decimation FIR filter.

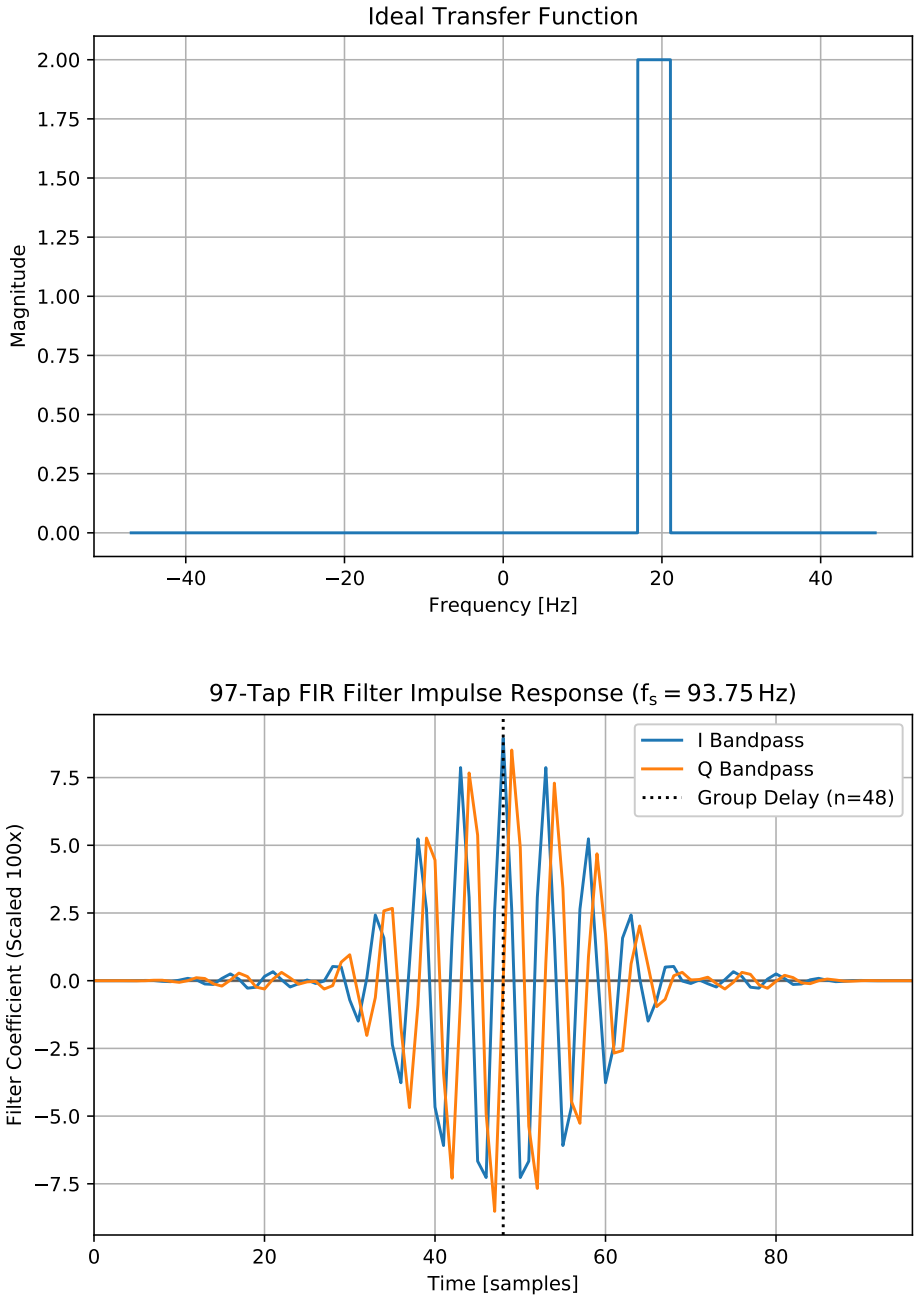

Figure C.14: Ideal transfer function and the resulting processed impulse response for the I and Q reference signal bandpass filters.

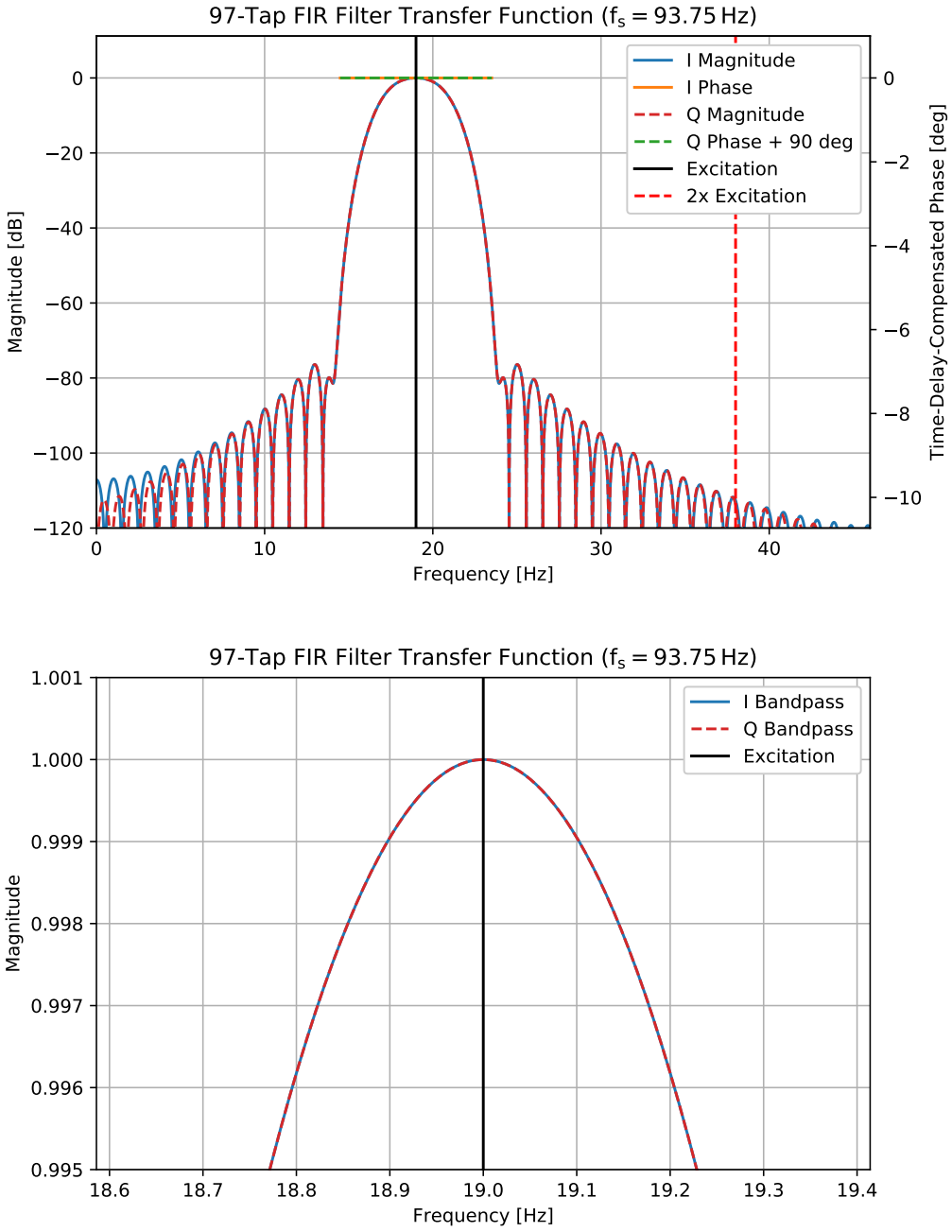

Figure C.15: Computed transfer function for the I and Q reference signal bandpass filters.

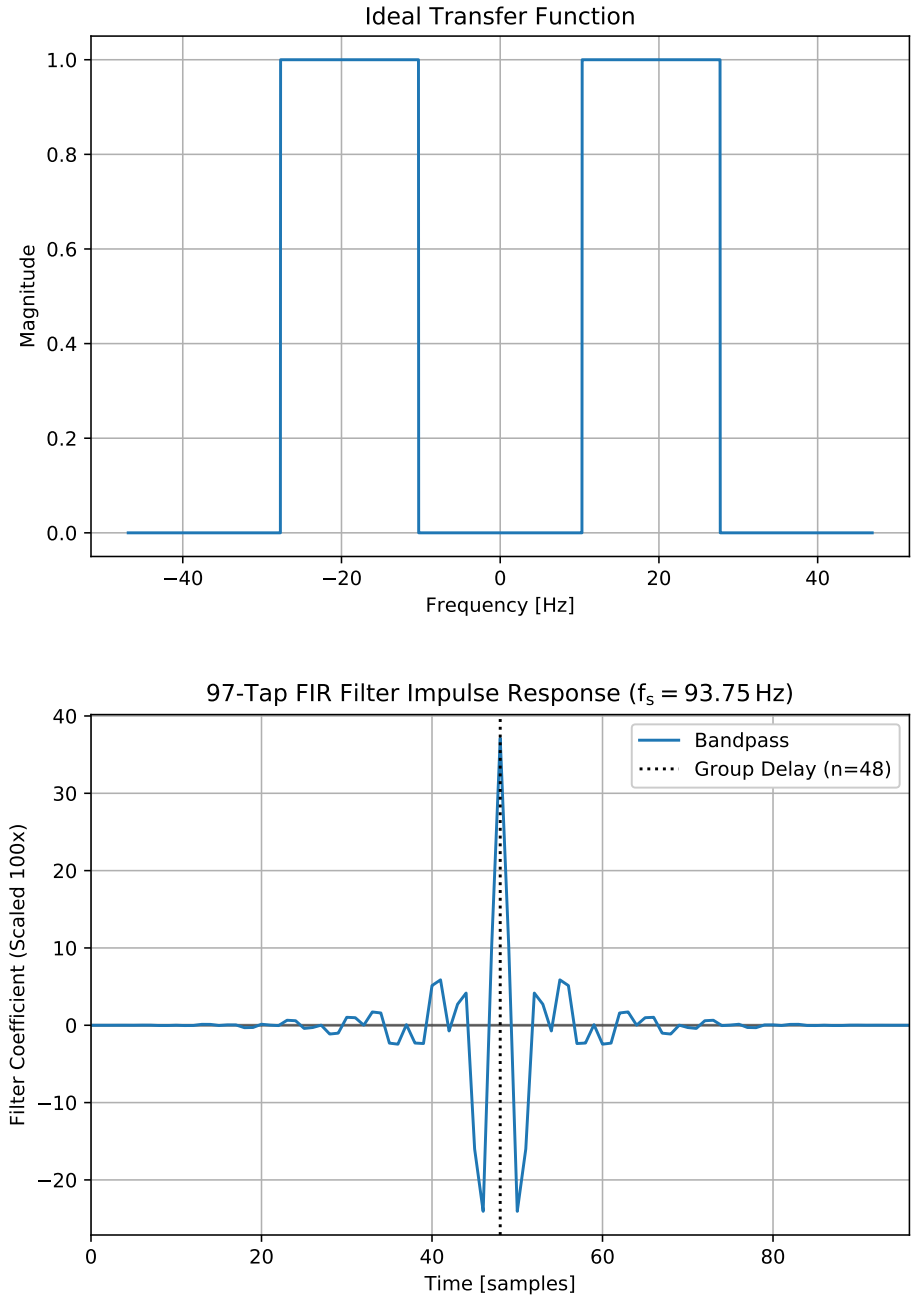

Figure C.16: Ideal transfer function and the resulting processed impulse response for the data bandpass filter.

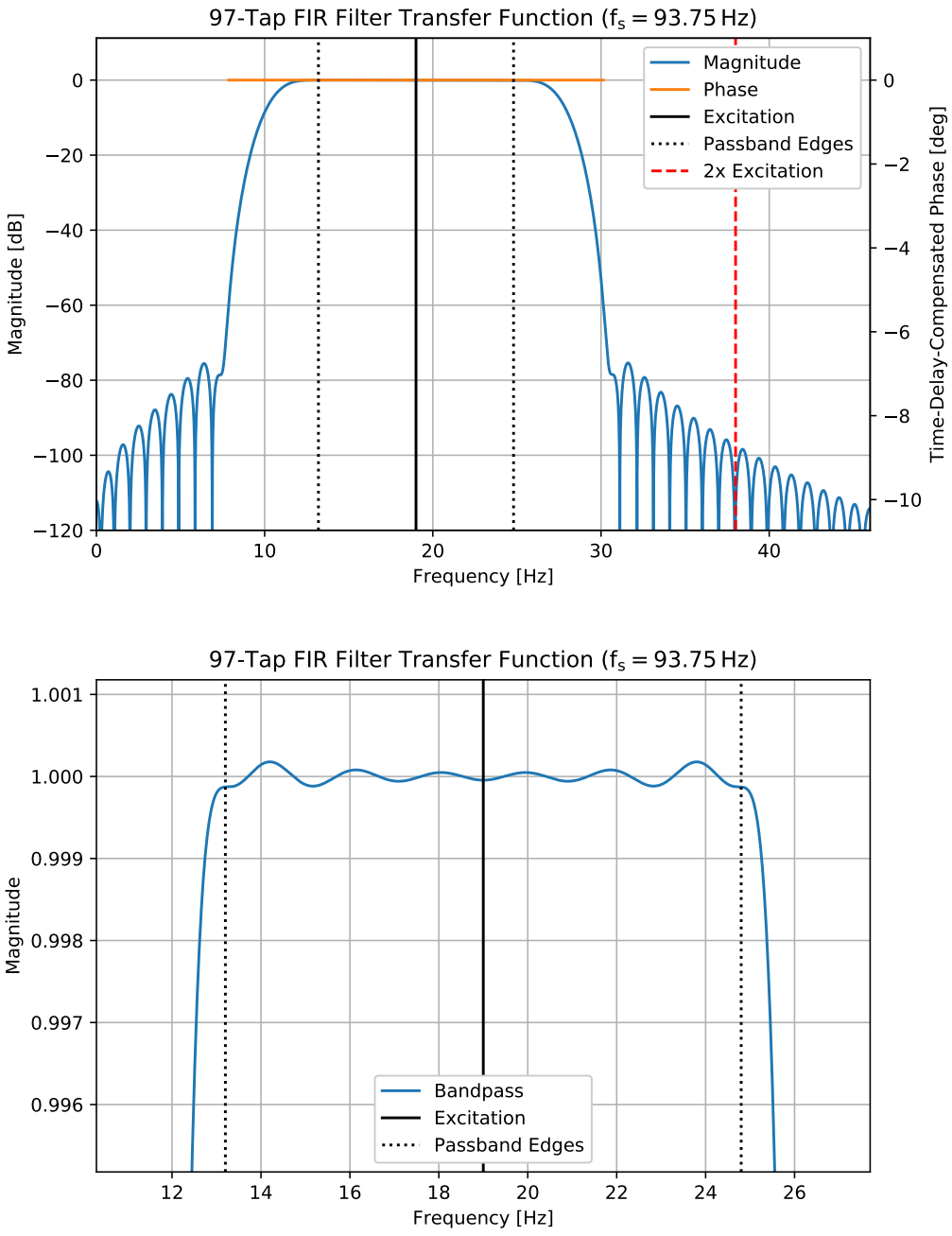

Figure C.17: Computed transfer function for the data bandpass filter.

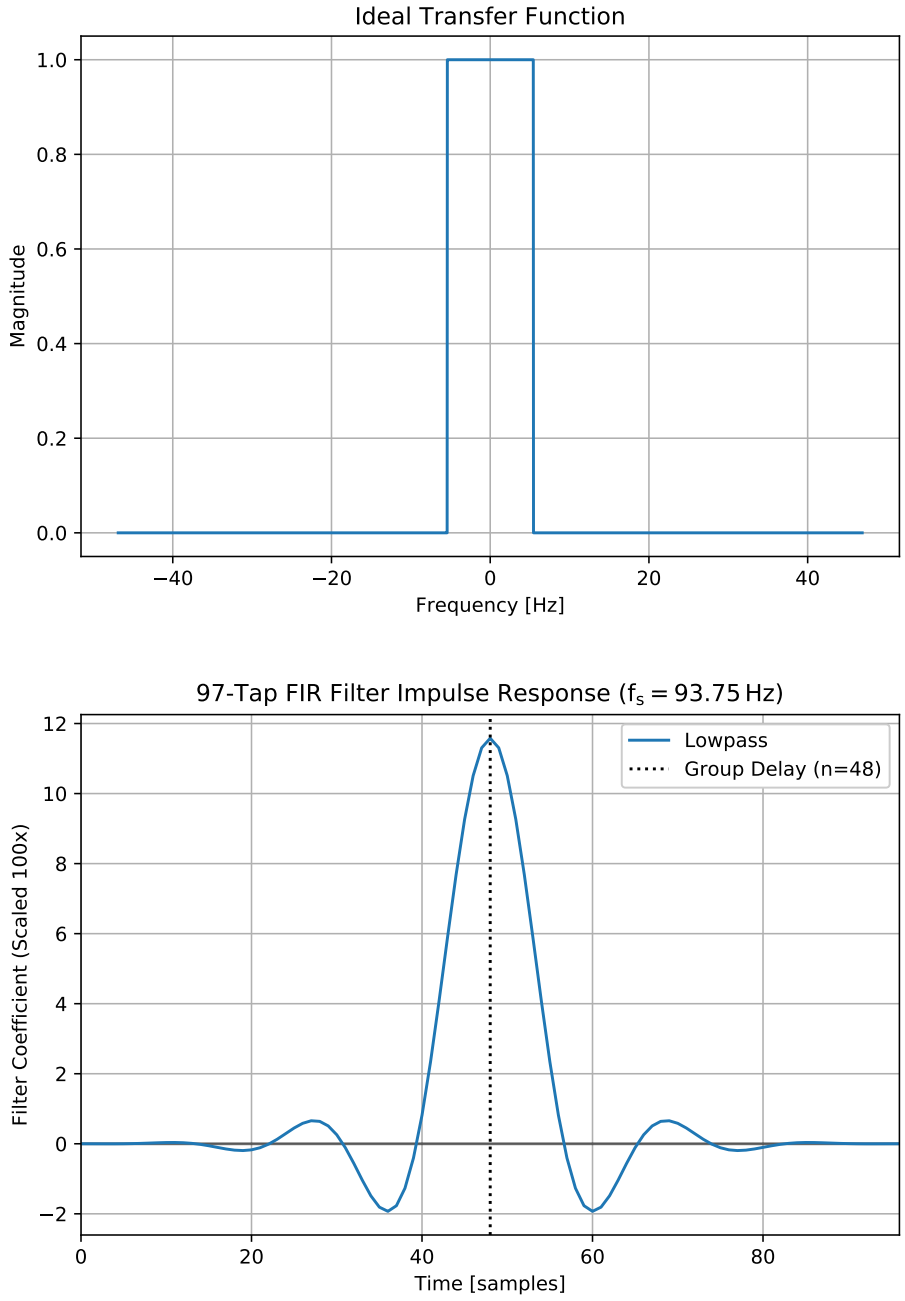

Figure C.18: Ideal transfer function and the resulting processed impulse response for the output lowpass filter.

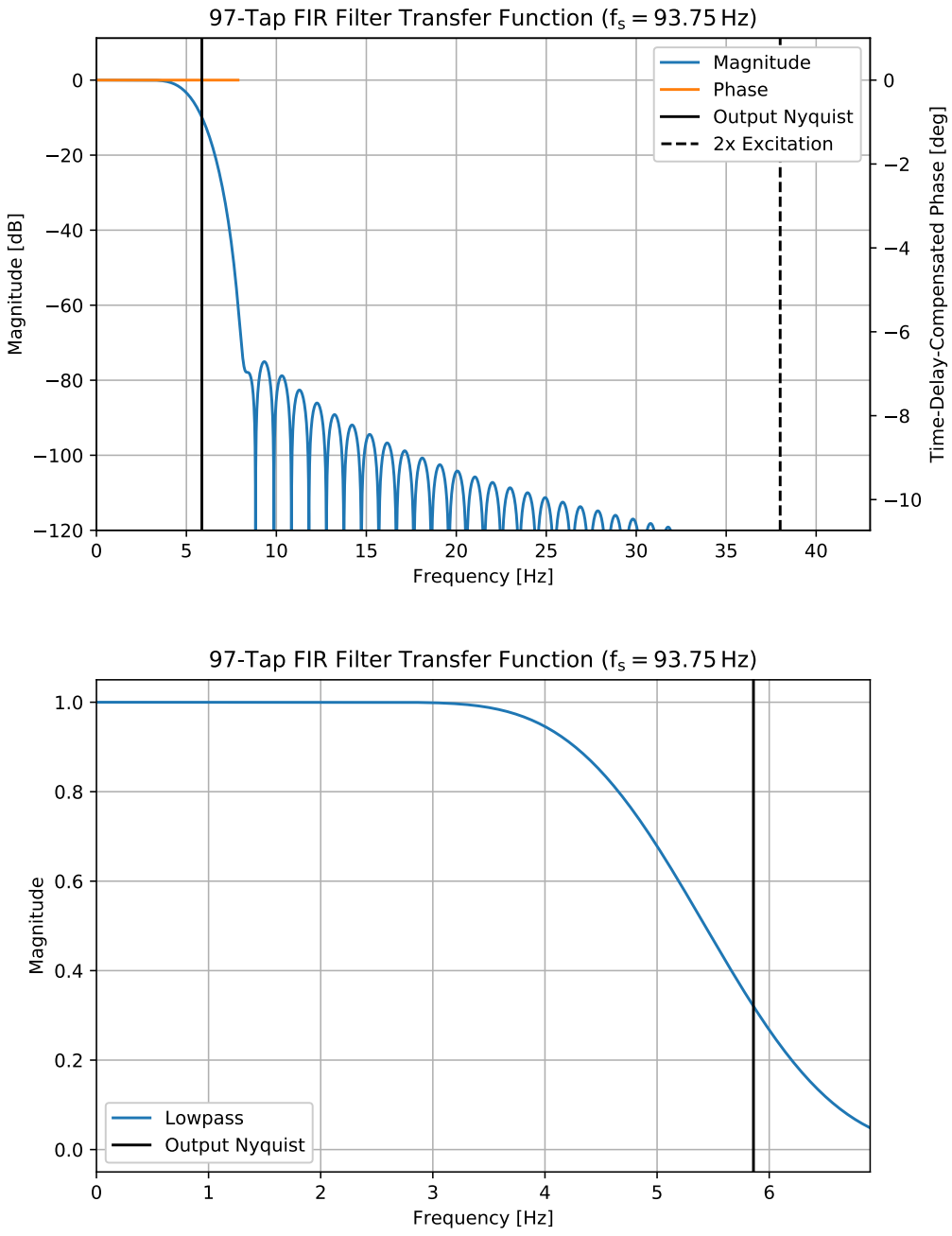

Figure C.19: Computed transfer function for the output lowpass filter.

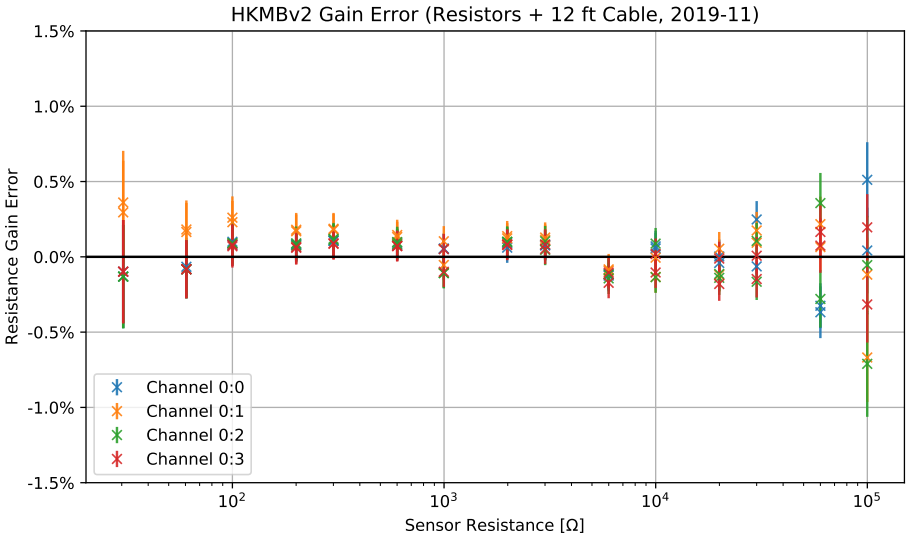

Figure C.20: Gain error for HKMBv2, measured with a set of relay-switched fixed resistors at the end of 12 ft of shielded twister-pair cable. Channels were set to $\sim 100\mu$V excitation.

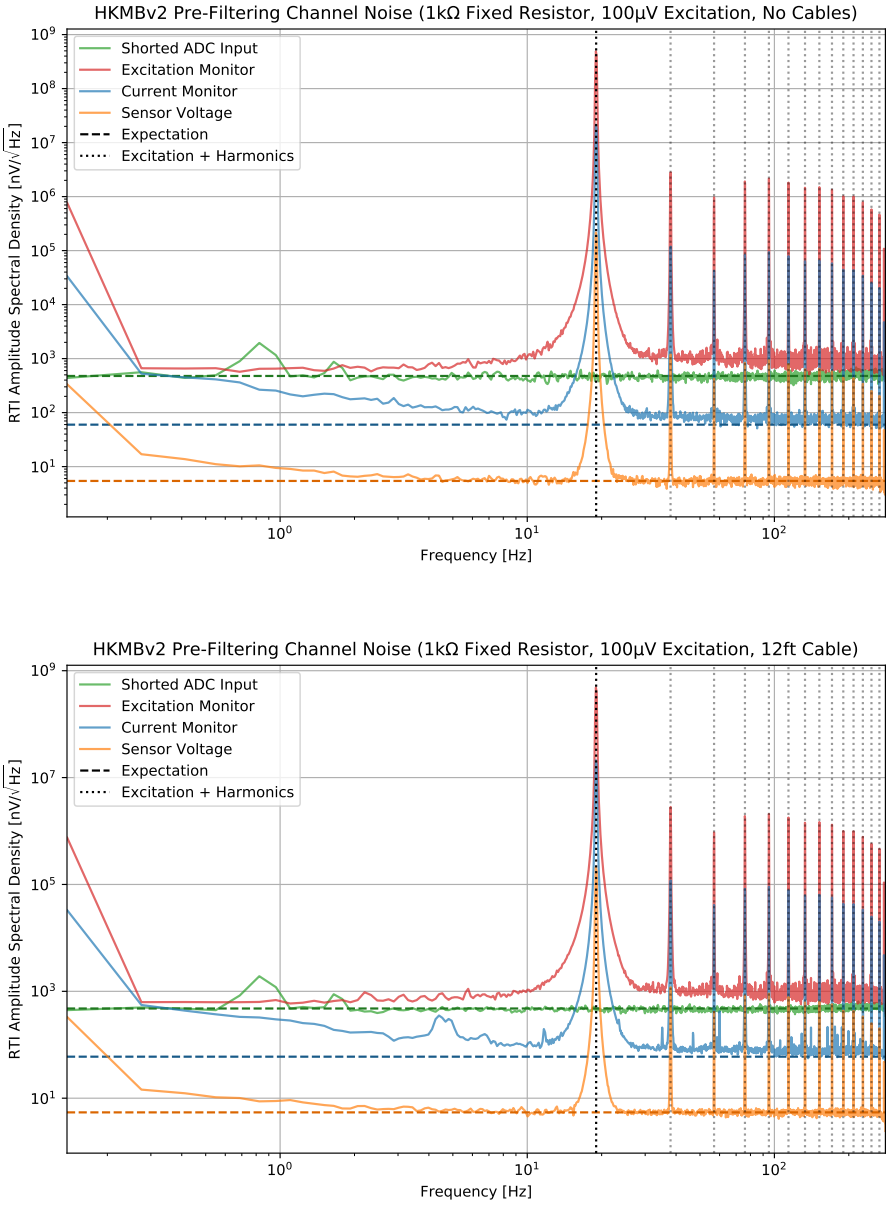

Figure C.21: Raw noise for the various channel components in HKMBv2 for a single warm fixed resistor. Results are shown with (lower) and without (upper) 12 ft cabling.

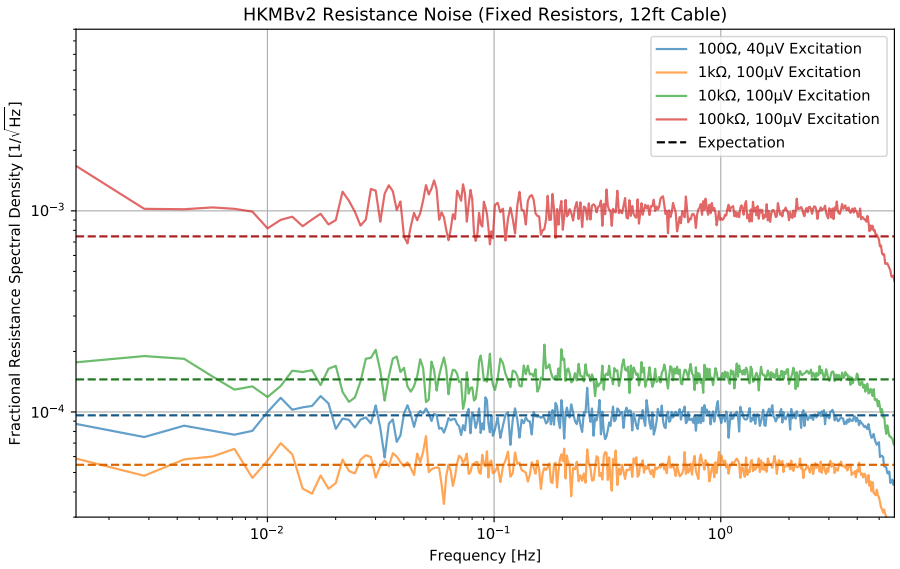

Figure C.22: Fractional resistance noise for four different fixed warm resistors (with 12 ft cabling), compared to predictions from the noise model in Fig. C.23.

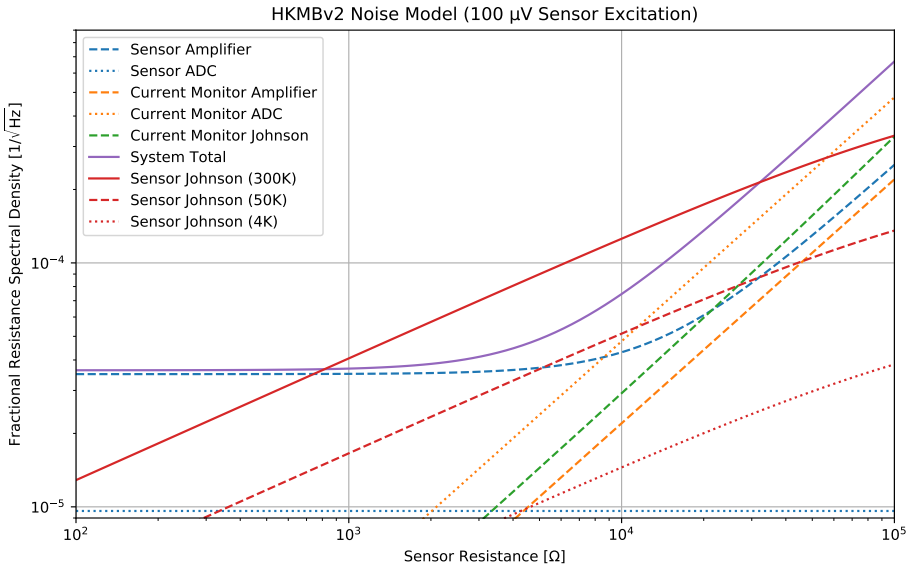

Figure C.23: The predicted fractional resistance noise for sensors at 100μV excitation in HKMBv2. Note that ADC noise on this plot depends on the fixed amplifier gains, which was chosen to provide optimal dynamic range.

	HKMBv1	**HKMBv2**
Processor	180 MHz Cortex-M4F, 1024 kB RAM	
	(Teensy 3.6, Arduino Compatible)	
Communication	USB, 12 Mbit/s	
MCE Sync Box	DB-25 Input	DB-25 Passthrough
ADC		
Part Number	ADS1220	ADS1278
Bit Depth	24	24
Raw Data Rate	90 Hz	562.5 Hz
ADC Channels	4	64
Multiplexing Factor	1:16	1:1
Amplifier	Integrated PGA	Replaceable Mezzanine
Gain	1-128	496
Thermometry		
Input Channels	36	24
Connectors	9x Lake Shore DB25	6x Lake Shore DB25
DC Excitation	10 nA - 10 μA	-
AC Excitation	-	0.1 nA - 300 nA
Output Rate	1 Hz	11.7 Hz
Aux Analog Inputs		
Input Channels	12	8
Connectors	10x BNC	6x BNC
	2x Edwards RJ45	2x Edwards RJ45
	2x 4-20mA BNC	
Data Rate	1 Hz, 2x at 20 Hz	11.7-562.5 Hz
Heater DAC		
Part Number	AD5754R	
Bit Depth	16	
Channels	32	24
Max Output	10 V, 20 mA	
Current Monitor	0.5 Hz	
Aux Digital Inputs		
FTS Encoder	2x DE9, GPIO Pins	2x DE9, Quad Decoder
GPIO	4x BNC	4x BNC
GPS Time Sync	IRIG-B via GPIO	

Table C.2: Specifications of the existing HKMBv1 and HKMBv2 TIME housekeeping boxes.

Appendix D

PyHK

D.1 Overview

PyHK is a suite of Python software developed to collect, store, and view sensor data and to control heaters and cryostat fridges remotely over the internet. It is developed with the intention of being flexible and extensible, allowing differing hardware configurations to be managed by the same platform. Versions of the code have been in use since 2014, and it is still in active development. PyHK contains several separate packages:

- `pyhkd` is the main instrument control software, which runs indefinitely collecting data and storing it to simple text files in a date-organized file structure. It is designed to run in the background as a system service, but can also be explicitly executed in a terminal. `pyhkd` listens for command packets over local TCP sockets and execute valid requests (setting a voltage, etc.).
- `pyhkweb` is a web viewer that is used in conjunction with Apache. It is the primary method for monitoring and controlling housekeeping and fridge scripts, even on the local machine. Once installed it is started automatically by Apache as needed (you never need to run pyhkweb.py yourself). You should have a DNS name (typically ___.pyhk.net) assigned to your machine, and you use that name to access the website; however, if you are running in a situation with no internet access, you can still access `pyhkweb` locally at https://127.0.0.1.
- `pyhkfridge` is responsible for the fridge cycle and other related scripts (like automated G measurement or heating fridge pumps during cooldown). It monitors the data files generated by `pyhkd` for changes and issues commands to `pyhkd` via sockets as needed. An arbitrary number of instances of `pyhkfridge` can be run simultaneously. `pyhkfridge` is designed to run in the background as a system service and to be controlled via `pyhkweb`.
- `pyhkcmd` (still in development) is a command line interface script for

PyHK. While `pyhkfridge` is the preferred method for writing scripts that read or write PyHK data (due to its integration with `pyhkweb`), `pyhkcmd` may be easier to integrate into some existing workflows.

This software has been tested on Ubuntu 16.04/18.04 with Python 3.5/3.6. Full installation instructions can be found in the PyHK documentation.

D.2 Configuration

`pyhkd` Hardware Configuration Files

The hardware configuration files define the instruments and sensors read out by `pyhkd`. Configuration data is stored in the JSON5 format, which is a superset of the JSON specification that adds human-friendly features such as comments; valid JSON is always valid JSON5, but the reverse is not true. A valid `pyhkd` hardware configuration file consists of a single list of objects, with each object corresponding to an instrument. Certain instruments acting as bus controllers also allow for lists of sub-instruments to be defined. A brief overview of supported instruments and sub-instruments is found below. For full details and configuration file examples, see the PyHK documentation.

- `prologix`: The Prologix GPIB-USB 6.0 adapter, acting as the controller-in-charge on a GPIB bus. Accepts the following sub-instruments:
  - `ls370`: Lake Shore 370 resistance-based thermometer readout instrument with a 16x multiplexer, connected via a GPIB bus.
  - `ls218`: Lake Shore 218 voltage-based thermometer readout instrument, connected via a GPIB bus (also supported over RS232).
  - `ami420`: AMI 420 magnet power supply controller.
  - `agilent_e3631a`: Triple-output HP, Agilent, or Keysight power supplies with GPIB control.
  - `agilent_e36XXa` for `XX` in [46, 47, 48, 49]: Dual-output HP, Agilent, or Keysight power supplies with GPIB control.
  - `agilent_e36XXa` for `XX` in [32, 33, 34, 40, 41, 42, 43, 44, 45]: Single-output HP, Agilent, or Keysight power supplies with GPIB control.
- `ptcompressor`: The helium compressor for a Cryomech PT410 or PT415 pulse tube. Telemetry and remote on/off are supported.

- `ls218`: Lake Shore 218 voltage-based thermometer readout instrument, connected via a RS232 (also supported over GPIB)
- `arduino`: An Arduino or Arduino-compatible device running the firmware included in `pyhk/firmware/arduino-digital-out`, which provides `pyhkd` access to the digital output pins.
- `hkmbv2`: TIME-style AC excitation housekeeping data acquisition box. Matches readings to MCE sync numbers and IRIG-B timestamps if provided.
- `hkmbv1`: TIME-style DC excitation housekeeping data acquisition box. Matches readings to MCE sync numbers and IRIG-B timestamps if provided.
- `hkmbminiv1`: TIME-style data acquisition box used for voltage measurement (no thermometer excitation). Matches readings to MCE sync numbers and IRIG-B timestamps if provided.
- `adixen_acp`: Adixen ACP40 (or compatible) vacuum pump.
- `mks_pressure`: MKS pressure sensors including 972B DualMag and 902B
- `simdata`: A fake instrument that generates a random walk output on each channel with a given frequency. Accepts any number of channels.

`pyhkd` Calibration Files

The calibration configuration files define the conversion functions between data types within a channel in `pyhkd`. For example, a piece of hardware may measure a resistance for a thermometer which is converted to temperature by a calibration function. Calibrations functions are specified on a per-channel basis. Several forms are allowed for calibration files (but only one form should be provided for a given file name). For full details and calibration file examples, see the PyHK documentation.

Interpolation Files: Files with the extension `".interp"` are text files containing a pair of numbers on each line separated by a space. The left field is the independent variable (the raw value provided by the hardware, often voltage or resistance), and the right field is the dependent variable (what we are converting into, often temperature or pressure). Python-style comments are allowed. The data is sorted by `pyhkd` when loaded, so data order in the file

is not important. Data need not be monotonic, but in many cases it should be.

Lake Shore Coefficient Files: Standard resistance or voltage `".cof"` calibration files provided by Lake Shore can be loaded directly, no changes to the file are required. If a file is found that fails to load or function as expected, please report it to the PyHK maintainer so the code can be updated (variations to the file format may occur over time).

Python Files: Any Python function that takes one argument and returns one value can be used. Place the function in a `".py"` file in the calibration folder, and be sure the function name matches the file name. Several helper functions are available to import and call for common function types, including `R2T_inverse_polylog`, `R2T_chebyshev`, and `R2T_polynomial`.

`pyhkweb` Website Configuration Files

The website configuration files define the plots, tables, and settings pages shown by `pyhkweb`. Configuration data is stored in the JSON5 format. A brief overview of supported pages is listed below. For full details and configuration file examples, see the PyHK documentation.

- `plot`: An interactive plot showing live and archived values for a provided set of sensors. Values update every few seconds without needing to refresh the page. A date-picker allows for browsing of archival data. See Fig. D.1 for a sample screenshot.
- `tables`: A set of one or more tables showing live values for a provided set of sensors. Values update every few seconds without needing to refresh the page. See Fig. D.2 for a sample screenshot.
- `pt`: A control panel that allows remote operation of a Cryomech PT410 or PT415 helium compressor. See Fig. D.3 for a sample screenshot.
- `heaters`: A basic control panel for a provided list of voltage outputs. See Fig. D.4 for a sample screenshot.
- `panel`: A custom heater/thermometer monitor and control panel. A series of "widgets" that control one heater are displayed over a static background image. See Fig. D.5 for a sample screenshot.

- `fridge`: Allows user control of any currently running instances of `pyhkfridge`, which are auto-detected. See Fig. D.6 for a sample screenshot.
- `ls370`: User-modifiable settings for a Lake Shore 370.
- `hkmb`: User-modifiable settings for one of the HKMB family of instruments (v2, v1, or v1-mini).
- `export`: A page that allows exporting of any timestream data over a provided date range. See Fig. D.7 for a sample screenshot.

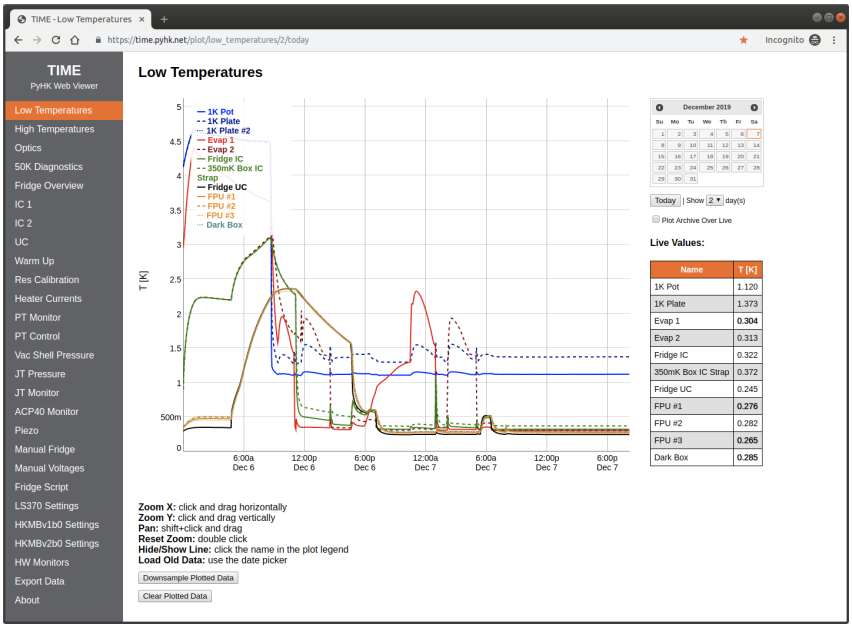

Figure D.1: A sample `plot` webpage from PyHK.

`pyhkfridge` Fridge Scripts

`pyhkfridge` script files are Python files that define a set of rules for moving between states. The main state variable of a running script is the current step index, which maps directly to a function you have written. These functions, called "steps", should be quick segments of code (executing in less than a second) that consult a series of values (time, temperature, etc.) and decide to either (A) remain at the current step index or (B) move to a different step index. Steps may also change other system state variables (voltages, etc.). Every few seconds `pyhkfridge` executes the current step function, and this is repeated until the script terminates. For full details and fridge script examples, see the PyHK documentation.

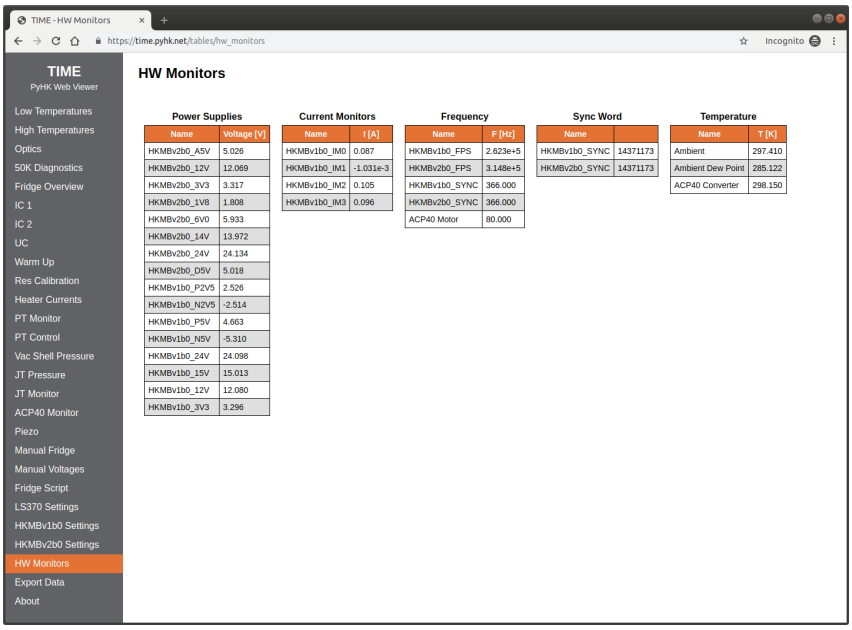

Figure D.2: A sample `tables` webpage from PyHK.

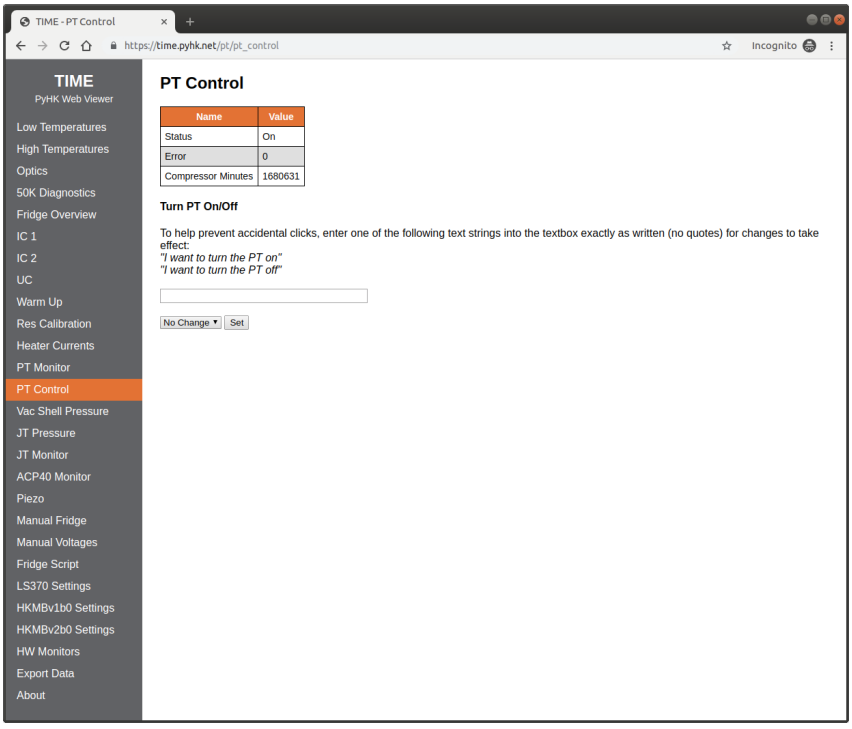

Figure D.3: A sample `pt` webpage from PyHK.

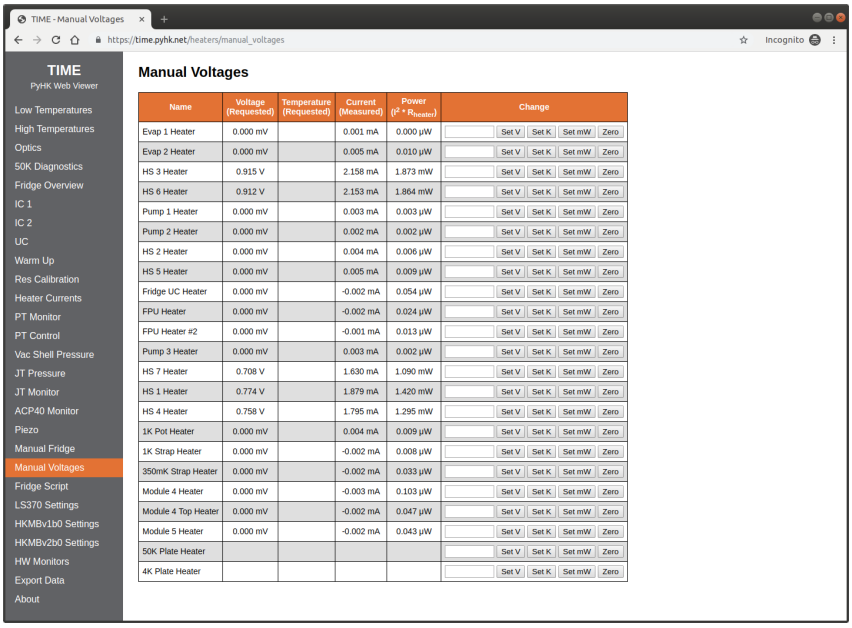

Figure D.4: A sample `heaters` webpage from PyHK.

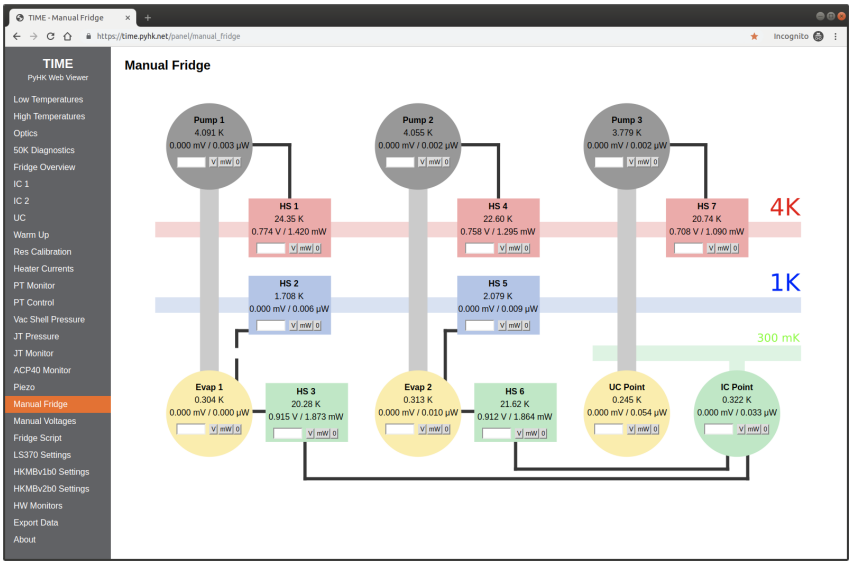

Figure D.5: A sample `panel` webpage from PyHK.

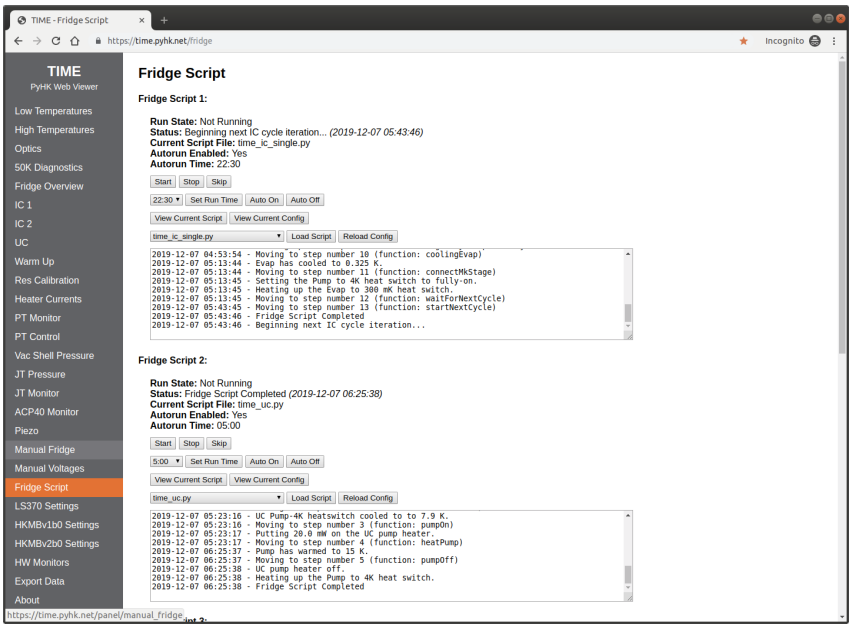

Figure D.6: A sample `pyhkfridge` webpage from PyHK.

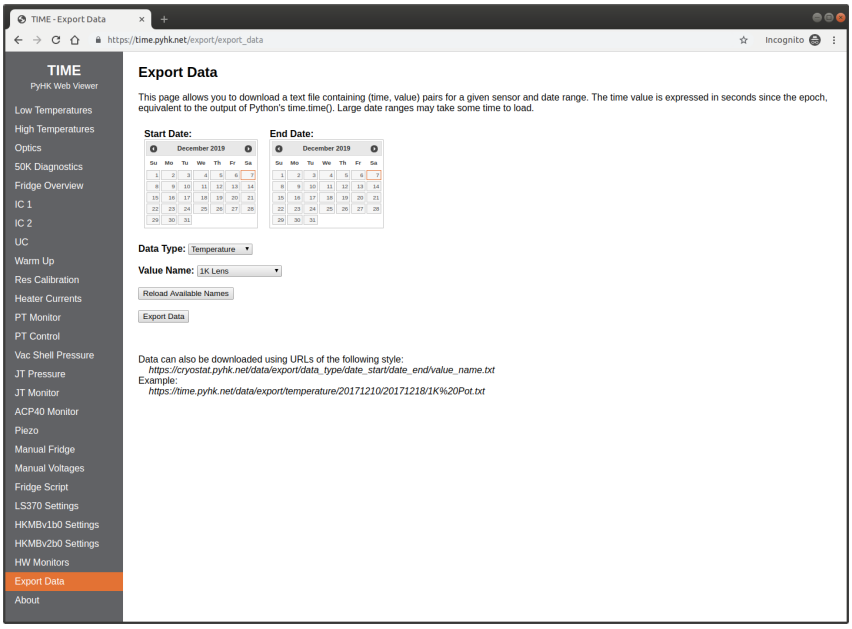

Figure D.7: A sample `export` webpage from PyHK.

D.3 Repository

PyHK is freely available in the following repository:

`https://bitbucket.org/jhunacek/pyhk`